Prediction ability of discrete modelling for the design of complex geotechnical structures

Bilal Al Tfaily

THÈSE

Pour obtenir le grade de

DOCTEUR DE L'UNIVERSITÉ GRENOBLE ALPES

École doctorale : I-MEP2 - Ingénierie - Matériaux, Mécanique, Environnement, Energétique, Procédés, Production
Spécialité :
Unité de recherche : Laboratoire Sols, Solides, Structures et Risques

Capacité prévisionnelle de la modélisation discrète pour application aux ouvrages géotechniques complexes

Prediction ability of discrete modelling for the design of complex geotechnical structures

Présentée par :

Bilal AL TFAILY

Direction de thèse :

Luc SIBILLE MAITRE DE CONFERENCES, Université Grenoble Alpes	Directeur de thèse
Abdelkrim BENNABI DOCTEUR EN SCIENCES, École Spéciale des Travaux Publics	Co-encadrant de thèse
Rodaina ABOUL HOSN ASSISTANT PROFESSOR, Australian University	Co-encadrante de thèse

Rapporteurs :

Emilien AZÉMA
PROFESSEUR DES UNIVERSITES, Université de Montpellier
Mohamed GUESSASMA
PROFESSEUR DES UNIVERSITES, Université de Picardie Jules Verne

Thèse soutenue publiquement le **19 décembre 2023**, devant le jury composé de :

Luc SIBILLE MAITRE DE CONFERENCES, Université Grenoble Alpes	Directeur de thèse
Emilien AZÉMA PROFESSEUR DES UNIVERSITES, Université de Montpellier	Rapporteur
Mohamed GUESSASMA PROFESSEUR DES UNIVERSITES, Université de Picardie Jules Verne	Rapporteur
Fabrice EMERIAULT PROFESSEUR DES UNIVERSITES, Université Grenoble Alpes	Président
Claire SILVANI MAITRESSE DE CONFERENCES, INSA Lyon	Examinatrice

Invités :

Rodaina ABOUL HOSN
ASSISTANT PROFESSOR, Australian University
Abdelkrim BENNABI
DOCTEUR EN SCIENCES, École Spéciale des Travaux Publics

"*Everything should be made as simple as possible, but no simpler.*"

Albert Einstein (1879-1955)

Abstract

Geotechnical engineering is a crucial field in the design and construction of foundations, embankments, tunnels, and other structures interacting with soil and rock. However, the description of the elastoplastic response of soil, with preponderant non-linear and non-reversible deformations together with a non-associative flow rule, is complex. The difficulty is even higher in the case of non-monotonous loading paths where phenomenological constitutive relations require ad-hoc history parameters and advanced experimental tests for their calibration.

Discrete element method has been proved to be an effective method in predicting quantitatively the constitutive response of soils, even in the case of complex loadings (with rotation of principal stress directions, or loading/unloading cycles) where conventional elastoplastic constitutive relations may fail to simulate realistic responses. For granular soils with a narrow grading, a direct representation of soil grains by polyhedral particles or with the level set method is possible, whereas for finer soils, or soils with a wider grading, alternative solutions should be considered. Spherical particles with enriched contact laws (e.g. by introducing rolling resistance at the contact) or rather simplified clumps of spheres can be used to keep the model relatively light to tackle further boundary value problems with limited computational cost. However, even if the models provide satisfying results for direct shear tests or drained triaxial compression loading paths compared to experimental measurements, their validation with respect to more complex loading paths as the isochoric compression or the path at constant stress deviator still present difficulties, in particular for initially loose granular assemblies.

First, this study aims to compare such different approaches in terms of the prediction abilities at the macroscopic scale of the constitutive responses of soils, particularly for complex loading paths. Two kinds of discrete models are considered: (i) spherical particles with rolling resistance, (ii) simple clumps made of 2 to 6 spheres. The models are calibrated from two drained triaxial compressions on dense and loose Hostun sand. They are then assessed, according to the macroscopic response, on loading paths significantly different from the calibration loading paths (isochoric compressions, circular stress paths in the deviatoric plane, constant deviatoric stress path, etc.).

Then, we investigate the importance of the description of the anisotropy of the initial fabric and of the inter-particle friction law in the simulated responses of loose granular assembly to different kinds of loading paths. It shows how the combination of both can modify importantly the simulated responses to some kinds of loading paths. This investigation is carried out for a numerical discrete model made of spheres by comparison with experimental results on sand.

Finally, the model is used to simulate the nonlinear interaction between a shallow foundation of building structure and the supporting soil during strong seismic loadings, as tested experimentally for the TRISEE project with a full scale physical model. An adaptative discretization technique is implemented to limit the number of particles in such a boundary value problem and make the computation possible with a conventional desktop computer. Numerical results are benchmarked against experimental measurements from the TRISEE project, and FEM numerical simulations or macro-element models.

Résumé

L'ingénierie géotechnique est un domaine crucial dans la conception et la construction de fondations, de tunnels, de remblais et autres ouvrages en interaction avec le sol ou la roche. Cependant, la description de la réponse élastoplastique du sol, avec des déformations fortement non linéaires et irréversibles ainsi qu'une règle d'écoulement non associée, reste complexe. La difficulté est encore plus élevée dans le cas de chemins de chargement non monotones où les relations constitutives phénoménologiques nécessitent des paramètres d'histoire ad hoc et des essais mécaniques avancés pour leur calibration.
La méthode des éléments discrets s'est avérée être une méthode efficace pour décrire quantitativement la réponse constitutive des sols, même dans le cas de chargements complexes (avec rotation des axes principaux de contraintes ou des cycles de chargement/déchargement) où les relations constitutives élastoplastiques conventionnelles peuvent conduire à des réponses simulées non réalistes. Pour les sols granulaires à granulométrie étroite, une représentation directe des grains du sol par des particules polyédriques ou à partir de level set est possible, tandis que pour les sols plus fins ou à granulométrie plus étalée, des solutions alternatives doivent être envisagées. Des particules sphériques avec des lois de contact enrichies ou des agrégats de sphères peuvent être utilisées pour conserver un modèle numérique relativement léger afin de résoudre des problèmes aux limites avec un coût en calcullimité. Cependant, même si ces modèles donnent des résultats satisfaisants pour des essais de cisaillement direct ou des compressions triaxiales drainées par rapport aux mesures expérimentales, leur validation par rapport à des trajets de chargement plus complexes tels que la compression isochore ou le chemin à déviateur de contrainte constant présente encore des difficultés, en particulier pour les assemblages granulaires initialement lâches.
Dans cette étude, nous proposons tout d'abord de comparer de tels modèles. Cette comparaison se fait en termes de capacités prédictives à l'échelle macroscopique des réponses constitutives des sols, en particulier pour des trajets de chargement complexes. Deux types de modèles discrets sont considérés : (i) des particules sphériques avec une résistance au roulement, (ii) des agrégats simples composés de 2 à 6 sphères. Les modèles sont calibrés à partir de deux compressions triaxiales drainées sur du sable d'Hostun dense et lâche. Ils sont ensuite évalués, en fonction de la réponse macroscopique, sur des trajets de chargement nettement différents des trajets de calibration (compressions isochores, chemins de contrainte circulaires dans le plan déviatoire, chemin à déviateur de contrainte constant, etc.).
Ensuite, nous étudions l'importance de la description de l'anisotropie de la microstructure initiale et de la loi de frottement inter-particules dans les réponses simulées des assemblages granulaires lâches pour différents types de chemins de chargement. Cela montre comment la combinaison des deux peut modifier de manière importante les réponses simulées pour certains chemins de chargement. Cette étude est réalisée avec un modèle numérique discret composé de sphères comparé à des résultats expérimentaux réalisés sur un sable.
Enfin, le modèle est utilisé pour simuler l'interaction non linéaire entre une fondation superficielle d'une structure de bâtiment et le sol lors de sollicitations sismiques intenses, comme testé expérimentalement pour le projet TRISEE avec un modèle physique àéchelle 1. Une technique de discrétisation adaptative est mise en œuvre

pour limiter le nombre de particules dans un tel problème aux limites et rendre le calcul possible avec un ordinateur de bureau classique. Les résultats numériques sont comparés aux mesures expérimentales du projet TRISEE, ainsi qu'à des simulations numériques par éléments finis (FEM) ou des modèles basés sur des macro-éléments.

Acknowledgements

In my thesis journey, I have encountered a range of emotions, from joy and excitement to moments of depression and lack of motivation. However, I believe this is a common experience when exploring new problems and finding new solutions. With the support of my thesis supervisors, friends, and family, I was able to overcome these challenges and achieve my goals.

I would like to extend my heartfelt gratitude to my thesis supervisors Luc SIBILLE, Rodaina ABOUL HOSN, and Abdelkrim BENNABI for their invaluable guidance and support throughout the process. They provided me with the necessary space and time to think, and try new ideas.

I would also like to thank my friends both within and outside the 3SR-Lab and IRC lab, who have been a source of encouragement and support. They have been there for me in critical moments, offering support and guidance, and discussing and sharing solutions to the problems I faced.

Finally, I would like to express my deep appreciation for my family, who have been instrumental in my academic and professional success. My parents, Ali and Samira, my brothers Hussein, Mohammad, and my sister Sarah, have been my biggest supporters and have always believed in me.

My parents' unwavering love and support has been the foundation of my success and I am forever grateful for all their sacrifices. A special thanks to my partner and best friend Rayane, who has been an unwavering source of support, love, and encouragement throughout my PhD.

Thank you all for making my thesis experience dynamic and filled with social life.

List of Publications

Journal papers

- Al Tfaily, B., Sibille, L., Aboul Hosn, R., & Bennabi, A. (2023). Prediction ability of discrete element model of loose granular media subjected to complex loadings. Powder Technology, 119251.
- Iskandar, R., Al Tfaily, B., Cornou, C., Bard, P. Y., Guillier, B., Harb, J., ... & Zaarour, R. (2023). Estimating urban seismic damages and debris from building-level simulations: Application to the city of Beirut, Lebanon. Bulletin of Earthquake Engineering, 1-42.
- Abdallah, A., Aboul Hosn, R., Al Tfaily, B., & Sibille, L. (2022). Identifying parameters of a discrete numerical model of soil from a geotechnical field test. European Journal of Environmental and Civil Engineering, 27(5), 2228-2247.
- Di Giulio, G., Cultrera, G., Cornou, C., Bard, P. Y., & Al Tfaily, B. (2021). Quality assessment for site characterization at seismic stations. Bulletin of Earthquake Engineering, 19(12), 4643-4691.

International conferences

- Al Tfaily, B., Aboul Hosn, R., Sibille, L., & Bennabi, A. A 3D discrete element model for studying soil-structure interaction on shallow foundations subjected to seismic loads. XVII International Conference on Computational Plasticity, COMPLAS 2023. 5-7 Sept. 2023, Barcelona, Spain. (2023).
- Al Tfaily, B., Sibille, L., Aboul Hosn, R., & Bennabi, A. Improving the prediction ability of simplified discrete element models on complex loading paths. VII International Conference on Particle-Based Methods - PARTICLES 2021. 4-6 Oct. 2021, Hamburg, Germany. (2021).

Contents

List of Figures

List of Tables

Dedicated to my Family. . .

Chapter 1

Introduction

1.1 Background

At the present time, soil-structure interaction problems are often modelled using elasto-plastic constitutive relationships that are easy to implement and work well with numerical methods such as finite elements and finite differences. However, these models are not suitable for complex loading paths (for example, highly non-proportional loading paths involving principal axis rotations or loading/unloading cyclic loading paths), as demonstrated by the results of the 1987 Cleveland Workshop benchmark study (Saada and Bianchini, 1988b). In such cases, the predictions produced by the elasto-plastic relations can be inaccurate, especially when modelling geotechnical structures such as wind turbine foundation piles, foundation layers of heavily loaded transport routes, or deep excavations supported by embedded walls that may be subject to loading/unloading cyclic loads in both vertical and horizontal directions. Therefore, it is important for engineers to consider the nature of the loading paths before deciding to use elasto-plastic relations, as this will affect the accuracy of the predictions.

Numerical models based on the Discrete Element Method (DEM) have been used for decades to predict the constitutive response of soils from qualitative point of view. Recent research, based on the results of the Cleveland workshop, has shown that DEM models can predict the mechanical response of soils with quantitative accuracy and not only qualitatively, even when subjected to complex loading paths (Sibille et al., 2019). This prediction capability of the DEM models is remarkable, especially when compared to the small amount of experimental data needed to calibrate the models, which often require no more than four or five mechanical parameters. In contrast, elasto-plastic relations that involve ad hoc history parameters require a much larger number of parameters and must be calibrated using cyclic tests to describe the response to non-monotonous loading paths. However, it should be noted that DEM models have some limitations, such as the inability to accurately model loose soils subjected to complex loadings paths such as a path involving a constant stress deviator or an isochoric compression loading path. Additionally, the main limitation of the DEM lies in its computational cost. Moreover, the choice of the DEM model initial state is not always straight forward. These limitations will be discussed and addressed in further detail in chapter 3.

This PhD thesis focuses on creating a discrete element model that is numerically

applicable to engineering projects on various types of soils, by limiting the computational cost. This model takes into account the structure and initial states of the granular assembly, and follows a well-defined calibration method. Finally, the DEM model is validated with a boundary value problem and a laboratory test to ensure its accuracy.

1.2 Objectives of the thesis

The thesis aims to achieve three primary objectives. In the first part, we investigate various approaches to enhance the prediction ability of the discrete element model in the case of complex loadings. In the second part of the thesis, the model is applied to a soil-structure interaction problem of a shallow foundation subjected to a seismic load, and then benchmarked against experimental measurements and previous simulations performed with the finite element method embedding phenomenological constitutive relations. Furthermore, in the third part, the discrete model is applied to a modified direct shear test to access information that is difficult to obtain experimentally: the local strain field and the local stress state. Thus presenting its practical applicability and effectiveness in real-world scenarios.

1.2.1 Objectives of part 1

This part of the thesis focuses on developing a light discrete element model that can be used to study the mechanical behavior of granular materials in geotechnical engineering project, thus by limiting the increase in computational time. The model takes into account the particle shape effect, initial states of the granular assembly, and uses a well-defined calibration method.
The following objectives are covered in this part:

- Proposing a new approach to defining the initial porosity of granular materials models.
- Examining the impact of particle shape on the mechanical behavior of granular materials through the use of triaxial tests, by comparing the behavior of spherical particles and clumps of two or more spheres.
- Introducing the possible impact of roughness by implementing a variable contact friction angle.
- Studying the effect of initial fabric anisotropy on the mechanical behavior of granular materials.

1.2.2 Objectives of part 2

In the second part of the thesis, the DEM is utilized to simulate a geotechnical application that involves a large-scale experiment within a former European Union-funded research project, the TRISEE project (Faccioli, Vanini, and Paolucci, 1999). This experiment involves a shallow foundation on Ticino sand subjected to seismic loading modeled using adaptive discretization technique. The aim of this part of the thesis is

to compare the numerical results obtained from the 3D DEM model with experimental measurements and previous simulations results from a macro-element model and other constitutive relations using the finite element method (FEM).
The following objectives are covered in this part:

- Implementation of an adaptive discretization technique to reduce the number of particles in the simulation of the shallow foundation problem to make the computation faster on a conventional desktop computer.
- Performing a 3D DEM simulation of a shallow foundation on Ticino sand subjected to seismic loading, by applying the three loading phases defined in the TRISEE project.
- Comparing the numerical results obtained from the 3D DEM model against experimental measurements and previous simulations performed with the FEM and macro-element models.

1.2.3 Objectives of part 3

In the third part of the thesis, the DEM is utilized to simulate a modified direct shear box test (Reiffsteck, 2022; Arpaia, Heintz, and Reiffsteck, 2015), where the shear plate consists of teeth with varying spacing. This modification aims to understand the behavior of the phicometer, which is a probe surrounded by steel teeth penetrating in a borehole for the measurement of mechanical characteristics such as the cohesion and the internal angle of friction. The following objectives are covered in this part:

- Modelling the modified direct shear test to understand the behavior of the soil-phicometer interaction, by testing the effect the modified plate with teeth on the behavior of soil.
- To obtain the necessary information required for defining an accurate interpretation of the phicometer, by identifying the shear surface and estimating the local shear stress.

1.3 Outline of the thesis

The thesis consists of six chapters in total. Each chapter is organized as follows:

- In chapter 2, the literature review is presented. It's divided into two parts:
  Part 1: presents a brief history of studies done to investigate and improve the prediction ability of the DEM.
  Part 2: Modeling of boundary value problems and soil structure interaction using various numerical techniques such as the finite element method (FEM), macro elements, the discrete element method, and double scale models as the FEM$\times$DEM.
  Advantages and limitations of the different methods are then discussed.
- In chapter 3, we present the development of a discrete element model, investigating the effects of particles shape, roughness, anisotropy and initial state.

The results obtained from the micro and macro scale simulations are presented and discussed.

- In chapter 4, we study the application focusing on soil-foundation interaction. The large scale experiment of the TRISEE project setup is presented. Followed by the calibration of the model on Ticino sand. Furthermore, the different steps of preparation of the discrete numerical model are described in details. Moreover, we compare the results obtained from the numerical model with experimental measurements, as well as other model based on either the finite element method (FEM) or macro elements.

- In chapter 5, the second boundary value problem is presented, the phicometer. The experimental setup, based on a modified direct shear test is discussed, along with the construction of the corresponding numerical model. The results obtained from the numerical simulations are then presented.

- Finally, in chapter 6 we provide a general conclusion summarizing the key findings and offering perspectives for future research in the field of discrete numerical models in soil mechanics and their practical applications.

Chapter 2

Literature review

2.1 Introduction

Geotechnical engineering is a branch of civil engineering that deals with the behavior of soil and their interaction with structures. It is a crucial field in designing and constructing safe and efficient foundations, embankments, retaining walls, tunnels, and many other structures. Thus, in order to design safe structures it's important to understand how soil behaves when subjected to different types of loading. Soils can be sand, gravel, silt, clay or others. It is basically composed of discrete particles interacting together at the microscopic level to sustain any applied external load. These materials can be heterogeneous and irregular (with non-uniform characteristics), which results in different behaviors characterized by stress and deformation that mainly depend on the particles shape, surface roughness, anisotropy, packing density, water content, chemo-physical interactions, and other features. The strength and deformation of soils are measured experimentally using laboratory tests such as triaxial tests or direct shear tests that measure various characteristics like the internal friction angle φ and cohesion C.

In the past decades, to model the behaviour of granular materials, phenomenological constitutive relations became the most used tool. Due to the fast development and the high computation power of computers it became possible to simulate the soil-structure interaction with different numerical methods such as: finite element method (FEM), finite difference method, and macro elements which requires the usage of phenomenological constitutive relations. Nowadays, another powerful method that have been used to simulate the mechanical behaviour of soils, and more particularly granular soils, is the discrete element method (DEM), which enables researchers to explore and understand different expects and behaviour of granular material on the micro and macro scales. In the following sections, the chapter is organized into two parts as follows: The first part begins with an introduction to the Discrete Element Method (DEM), covering its history, simulation cycle loop, contact law, particle shapes, initial state generation, and microscopic properties. Then, the second part of the chapter presents different methods for modeling Soil-Structure Interaction problems, including the Finite Element Method (FEM), Macro Elements, Discrete Element Method (DEM), and the coupling of FEM with DEM.

2.2 The discrete element method

The discrete element method (DEM), introduced by Cundall and Strack (1979b), is a numerical method that models the behaviour of assembly of particles. It's interesting, since this approach makes it possible to explicitly analyze the interactions of each particle of the assembly. These particles can represent a granular material or any industrial particles that may have different heterogeneous shapes. DEM makes it possible to monitor the data at the particle scale, which is a unique and interesting feature of this method.
In other words, in DEM, properties of each particle of the assembly (for example: contact forces, position and velocity) can be saved and are updated at each iteration. To update the properties of the particles, rotational and translational displacements are determined using Newton's 2nd law of motion, while the contact forces are computed based on a force-displacement contact law (Mindlin and Deresiewicz, 1953; Cundall and Strack, 1979b; Ristow, 1997).
To reduce the DEM simulations computational cost, and allowing the usage of large number of particles, the simplest particle shape to be used is discs or spheres in 2D (Luding, 1997; Iwashita and Oda, 1998) or 3D (Thornton, 2000) simulations respectively.

2.2.1 History of Discrete element modelling

Cundall and Strack (1978) introduced the first two-dimensional DEM program named BALL, consisting a linear spring contact law and strain/stress controlled wall boundary options, aiming to show that the DEM can realistically model the behaviour of assemblies of discs. Then in 1979, the program was upgraded into a three-dimensional version named TRUBAL by Cundall and Strack (1979a). Later, this software was extended by implementing non-linear contact laws and defining the idea of periodic cell, which allows a particle exiting a cell to move inside the opposite side of the cell, while carrying all same information except the particle position.
In recent years, both open-source DEM packages such as YADE (Šmilauer and Chareyre, 2010), MULTICOR-3D (Sanni et al., 2010), Oval (Kuhn, 2006), LMGC90 (Dubois et al., 2011), and ESyS Particle (Weatherley, Boros, and Hancock, 2011) and other commercial ones such as PFC, EDEM, and Rocky have made remarkable improvement in simulating the mechanical behavior of granular materials. These diverse packages empower researchers and engineers to explore the complex behavior of granular materials across various applications.

2.2.2 The simulation cycle loop of DEM

A typical DEM simulation loop is presented in Figure 2.1. The simulation cycle involves several engines running in a loop. After the definition of shape, material, and state of the simulation elements (particles and boundaries), these engines run in the following sequence repeatedly:
First, new contacts are detected between particles based on their positions. This step is time-consuming and requires a collision evaluation algorithm that can help filtering possible contacts, which can be done by dividing the space into a well defined grid

using the grid algorithms (Munjiza and Andrews, 1998) or by bounding boxes using the sweep and prune algorithm (Baraff and Witkin, 1992; Cohen et al., 1995) to determine any overlapping between two bounding boxes. It was later called sort and sweep in the book Ericson (2004). Then another more time-consuming step is needed to detect the exact collision. In case of two spherical particles, the contact detection computational time is significantly reduced compared to other shapes; it is detected if the distance between their centers is less than the sum of their radii (Figure 2.3.a). Then, using the force-displacement contact law the normal and tangential contact forces are computed based on relative displacements. After applying external forces (example: gravity), equations of motion are then integrated using a certain algorithm (e.g. leapfrog scheme). The velocities and positions are updated after each step and forces from previous step are then reset.

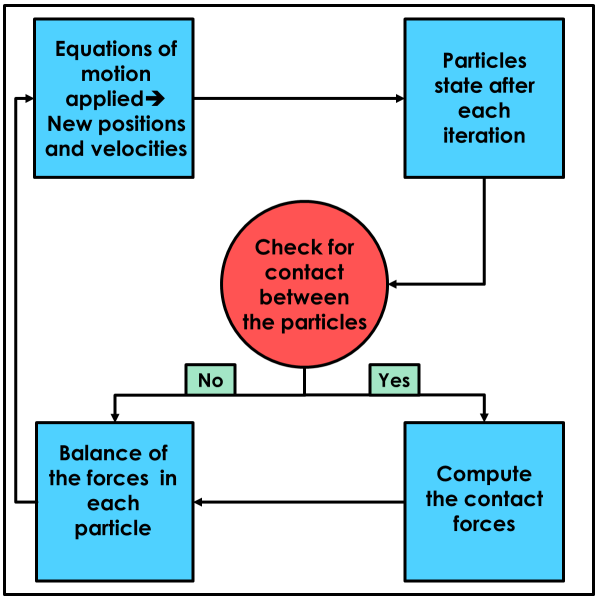

FIGURE 2.1: The typical DEM simulation loop.

2.2.3 The contact law

Many contact laws exist, but as the goal of this work is to keep the model simple, we focus in this part on the simplest contact laws taking into account spherical particles. Cundall and Strack (1979b) defined a frictional contact law (Figure 2.2) between two spherical particles of radii R_1 and R_2 (Figure 2.3.a,b) in contact with an overlap δ_n and normal $\vec{n}$ to the tangent contact plane, the normal $\vec{F}_n$ and tangential $\vec{F}_t$ contact forces are given respectively by:

$$\vec{F}_n = k_n \, \delta_n \, \vec{n} \tag{2.1}$$

$$\Delta\vec{F}_t = -k_t \, \Delta\vec{u}_t \quad \text{with} \quad ||\vec{F}_t|| \leq \mu \, ||\vec{F}_n|| \tag{2.2}$$

where k_n and k_t are the normal and tangential stiffnesses of the springs connecting the two particles (Figure 2.3.b), chosen as constant; $\Delta\vec{u}_t$ is the relative incremental tangential displacement used to compute the shear force incrementally; and μ is the friction coefficient in the tangential direction.

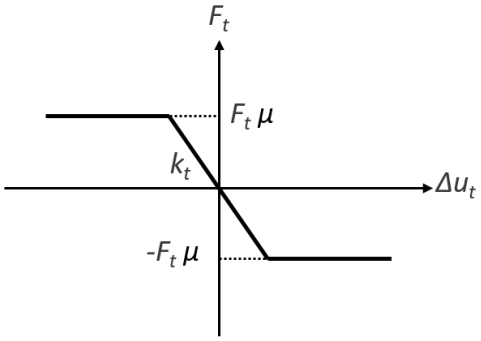

FIGURE 2.2: Perfect elasto-plastic model defined by Cundall and Strack (1979b).

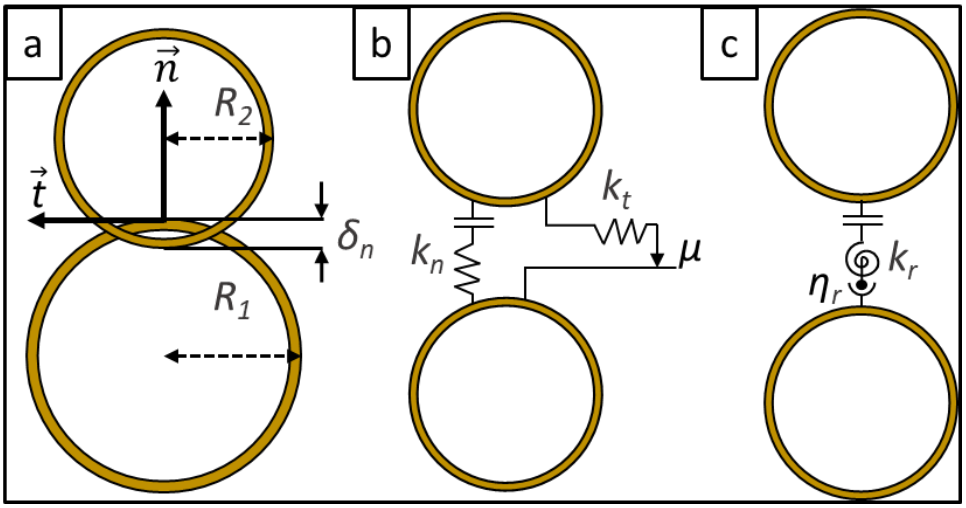

FIGURE 2.3: Contact between two spheres: (a) frame attached to the tangent contact plane and particle overlap; (b) contact model with sliders in the tangential direction and (c) with stiffness and slider acting with respect to relative rolling motion.

Another authors used a damper (Figure 2.4) defined by the Kelvin-Voigt model in parallel with the spring in the normal direction by Luding (1997) and in both normal and tangential directions by Oger et al. (1998) and Iwashita and Oda (2000) to dissipate energy.
In addition, Walton and Braun (1986) defined a normal law with irreversible normal displacement (Figure 2.5), where the normal force is given by:

$$F_n = \begin{cases} k_1 \times \delta_n & for\ loading \\ k_2 \times (\delta_n - \delta_0) & for\ unloading/reloading \end{cases} \tag{2.3}$$

where δ_0 is the residual normal displacement after unloading, with k_1 and k_2 representing the stiffnesses of loading and unloading paths respectively. This model propose a linear force-overlap relation, with the stiffness during unloading being greater than the stiffness during loading resulting in an irreversible overlap when the force diminishes to zero. This model can be used when the collision at the contact is between inelastic spheres, when plastic deformation effects should be considered.

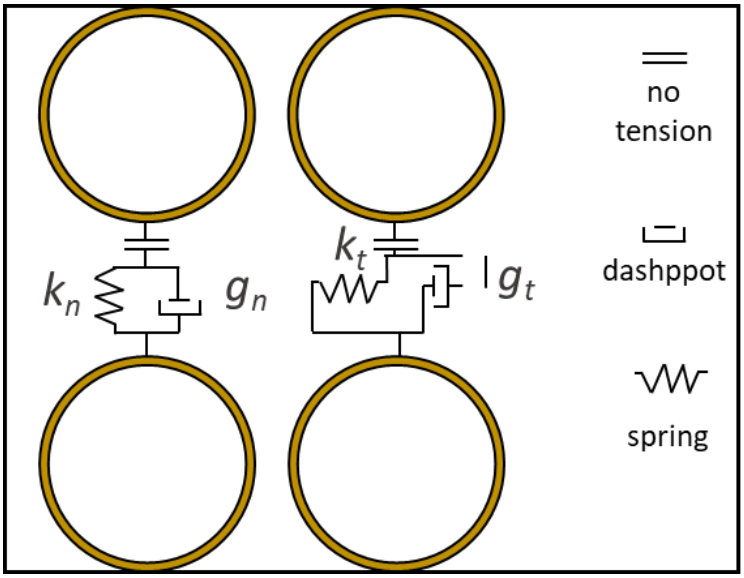

FIGURE 2.4: Contact model with damping in both normal and tangential directions

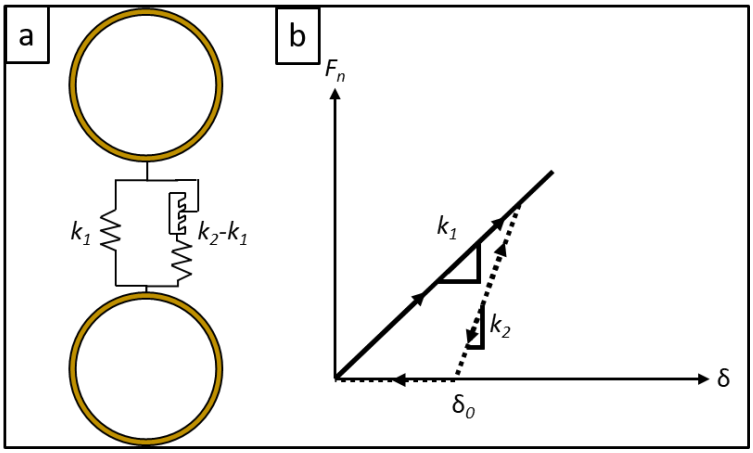

FIGURE 2.5: Normal model with irreversible plasticity by (Walton and Braun, 1986)

Rolling friction

Since contact detection of complex shapes is more complicated and requires more computation time compared to spherical particles, and since spherical particles tend to roll naturally, Iwashita and Oda (1998) implemented a contact law with rolling resistance to limit the rolling mechanism of spheres.

The rolling resistance between particles (Figure 2.3.c) is represented by a contact rolling moment $\vec{M}_r$ (Figure 2.6) defined as:

$$\vec{M}_r = -k_r \vec{\theta}_r \quad \text{with} \quad ||\vec{M}_r|| \leq ||\vec{F}_n|| \, \eta_r R_{\text{mean}} \tag{2.4}$$

where k_r is a constant rolling stiffness, $\vec{\theta}_r$ the relative rolling rotation of particles, and η_r the rolling friction coefficient.

Rolling stiffness is derived from the tangential stiffness such that:

$$k_r = k_t R_{\text{mean}}^2 \tag{2.5}$$

$$\text{with:} \qquad R_{mean} = \frac{1}{R_1} + \frac{1}{R_2} \tag{2.6}$$

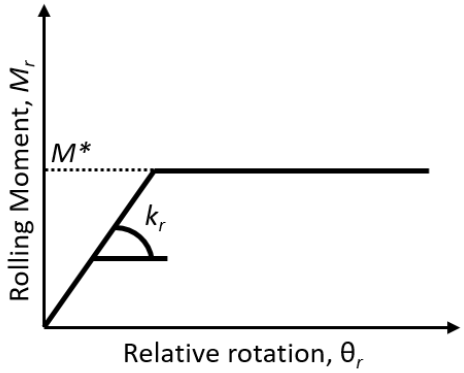

FIGURE 2.6: Perfect elasto-plastic model including rolling resistance at the contact with the yielding moment M^*

Similarly to the contact model with damping in the normal and tangential directions (Figure 2.4), the contact model proposed by Iwashita and Oda (1998) also includes rolling damping at the contact. However, Wensrich and Katterfeld (2012) showed, based on results from Iwashita and Oda (1998), Bardet (1993), and Ai et al. (2011), that the rolling damping effect is negligible in case of quasi-static conditions.

In a recent study by Rorato et al. (2021), the authors linked the rolling friction parameter to the sphericity of each grain to simplify the calibration of the model by decreasing the number of calibrated parameters. Furthermore, it introduces valuable description of the inherent variability of natural shapes within the model.

Adhesion

To simulate cohesive materials using discrete element method, it's necessary to implement an adhesion contact law at the interface between particles. This involves creating a bond between the particles in contact, that can transmit forces to resist the separation of particles in the perpendicular direction and any opposite movement in the tangential direction.

In the literature, several adhesion contact models exist. One of the most known model is the JKR model (Johnson, Kendall, and Roberts, 1971) based on the Hertz-Mindlin model (Hertz, 1896) with an attractive force introduced based on Van der Waals effects, where the contact force remains active until a surface gap threshold is reached. Another very known model is the DMT model (Derjaguin, Muller, and Toporov, 1975), where the adhesive force between an elastic sphere and a flat layer is determined by evaluating the change in surface energy as the sphere penetrates the layer.

More recently, adhesion models have been further developed. For example Luding (2005) defined a model similar to that of (Walton and Braun, 1986), but with the

addition of a "cohesive stiffness" parameter k_c for the unloading. This parameter reflects the cohesion in the contact, allowing the implementation of attractive forces.

Roughness

In an experimental study (Santamarina and Cascante, 1998), the authors investigated the effect of the soil particle surface characteristics on its behavior. They found that an increase in the surface roughness leads to an increase in the inter-particle friction. Cho, Dodds, and Santamarina (2006) used experimental databases, that include particle shape information, to show that the shape of the particle is an important soil property that should be well characterized. The behaviour does not only depend on the global form of the particles "sphericity" (defined as the ratio of the diameter of the largest inscribed sphere to the diameter of the smallest circumscribed sphere), but also on the local-scale surface curvature "roundness" (defined as the ratio of curvature of surface features relative to the radius of the largest inscribed sphere within the particle, as well as surface roughness. They proposed a hypothesis that eccentricity, angularity, and roughness contribute to increased shear resistance.
Similarly, in another study (Sandeep and Senetakis, 2018), the influence of surface characteristics was examined experimentally. The authors also observed that inter-particle friction increases with surface roughness. In addition they highlighted the importance in DEM modelling to consider the role of the surface contact area (which depend on the normal force magnitude) on the inter-particle friction. In the case of stiff soil, which intrinsically features a smaller contact area than soft soil, a corresponding decrease in inter-particle friction is observed.
In a recent DEM numerical study (Mollon et al., 2020), the authors investigate the possibility of substituting the roughness of particles by an increase in inter-particle friction in the simulations.

2.2.4 Particle shapes in DEM

Since the beginning of discrete element modelling, spherical (in 3D) and discs (in 2D) particles are the most common used particles. This is due to the easy contact detection between particles, and the limited computational time compared to other shapes.
However, several studies focus on the effect of the particle shape, on the quantitative behaviour of the assemblies. These studies lead to increase interest in understanding and developing several new DEM particle shapes as shown Figure 2.7.
In addition to spheres, simple particle shape can be a clump of two or three spheres (Salot, Gotteland, and Villard, 2009; Kodicherla, Gong, and Wilkinson, 2020), but it can also be very complex with large number of particles (Ferellec and McDowell, 2012) to overcome the underestimation of the roundness. Similarly in case of polyhedral particles, large number of vertices is needed to overcome the overestimation of the roundness (Lee, Hashash, and Nezami, 2012; Elias, 2013). PFacet particles, as described in Effeindzourou et al. (2015), are created through the Minkowski sum of a sphere, cylinders and a triangular facet. Another option is the use of superellipsoid particles (Zhao et al., 2017), but this also can overestimate the roundness. Non-uniform rational B-splines (NURBS) curves and surfaces (Lim and Andrade,

2014; Lim et al., 2016; Andrade et al., 2012), which are generalizations of both B-splines and Bézier curves, in addition to level set methods (Vlahinić et al., 2014; Jerves, Kawamoto, and Andrade, 2016; Kawamoto et al., 2018), both can accurately capture the real shape of the particle. However, these methods are computationally very expensive.
The computation time of simulations depends on the contact detection algorithm of each particle shape. For example, using a clump of spheres presents the advantage that contacts are detected using the same algorithm between two spheres, even if they belong to different clumps. In case of polyhedral particles, contacts can be detected using various algorithms and techniques, but it is more complex than spheres due to the various types of contacts, such as vertex-vertex, vertex-edge or edge-edge interactions. In addition, contact forces are calculated based on intersecting polyhedral volumes. In PFacets, contact detection includes interactions such as sphere-sphere, sphere-cylinder, sphere-PFacet, cylinder-cylinder, and cylinder-PFacet. The introduction of virtual spheres at contact points allows the application of conventional sphere-sphere interaction laws. For superellipsoids, a combination of approximate contact detection using the axis-aligned bounding box algorithm and exact detection using spherical bounding boxes is used. For level set particles, contact determination involves a master-slave approach. The surface of the master particle is discretized into nodes. Each node of the master particle is compared with the level set function of the slave particle. If the level set function value is negative for any node, contact is detected, and forces and moments are computed for each penetrating node.
Thus, there is a trade-off between the computation time and the complexity of the particles shape.

2.2.5 The initial state generation

The choice of the initial micro-structure of the sample plays a very important and crucial role in the behaviour of the DEM model. So as soil in nature and experiments exist with different porosities and fabrics (Aris, Benahmed, and Bonelli, 2012; Kodicherla et al., 2018), the same applies to numerical models depending on preparation methods.
Usually, the first step in discrete element modelling, is to generate randomly the non-overlapping particles assembly (following the same real soil particle size distribution) within a certain specified boundary conditions (rigid walls, soft boundaries, or periodic limit conditions). Then, several possible ways can be done to reach a specified initial state including, application of isotropic compression (Wang and Li, 2014), particles expansion (Plassiard, Belheine, and Donzé, 2009), multi-layer under compaction method (Jiang, Konrad, and Leroueil, 2003). These methods can influence the generation of the sample, especially the initial fabric arrangements, which can cause significant challenges in modelling the behaviour of soil. This was observed in a study (Jiang, Zhang, and Fu, 2018), where they show how the different fabric arrangements can result in different peak shear strengths and volumetric changes.
Moreover, different methods can be followed to choose the initial porosity of the numerical models, for example:

- Assigning the initial porosity of the numerical assembly similar to the one of the real reference soil. This was done in several studies such as Cui and

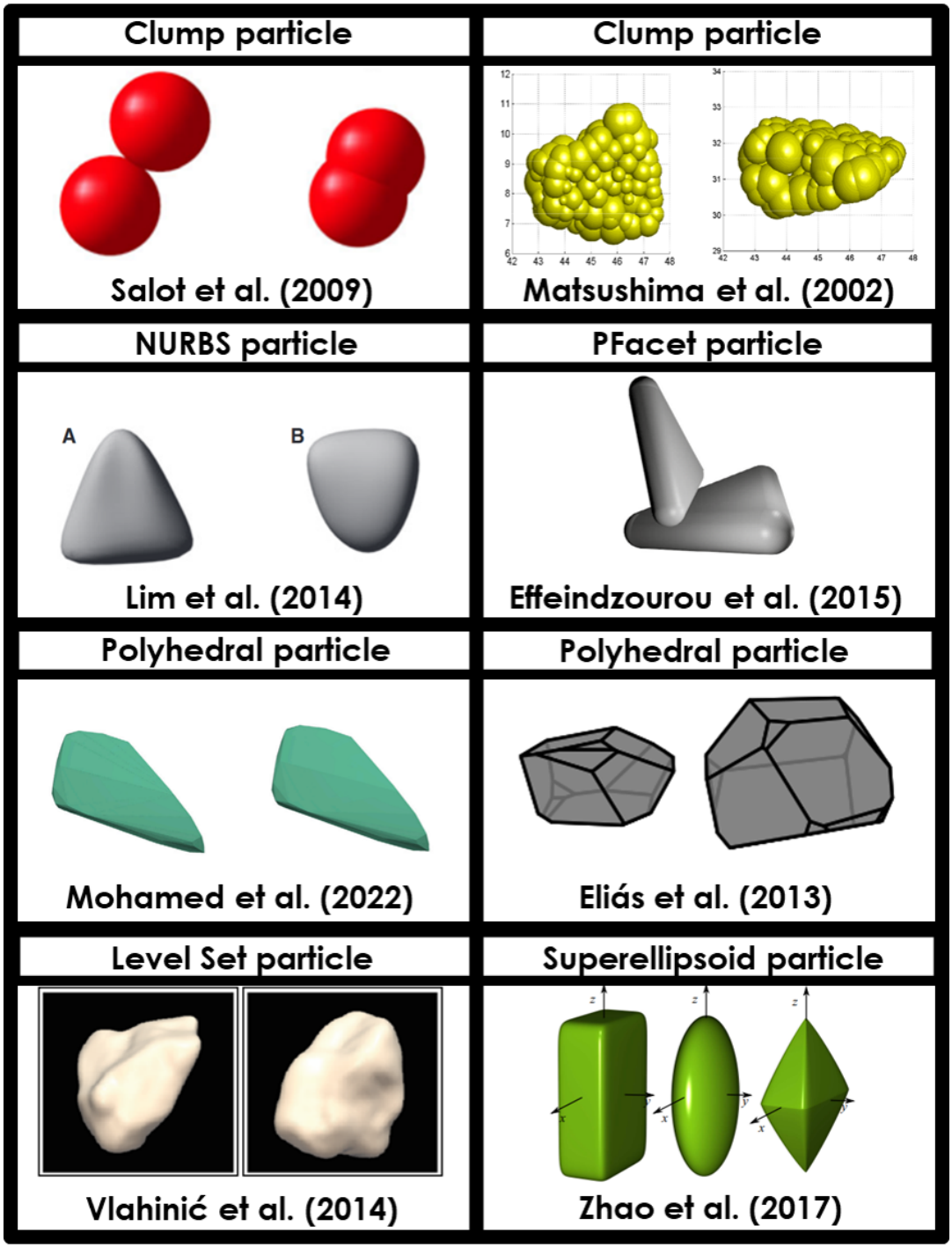

FIGURE 2.7: Various particle shapes used in DEM

O'sullivan (2006) and Mohamed et al. (2022). However, drawbacks of this method exist, especially when the shape of numerical and real particles are very different, causing different volumetric behaviour for the same initial porosity.

- Choosing the same relative density as the real reference soil (Salot, Gotteland, and Villard, 2009), which is computed with respect to a maximum and minimum initial porosity. Similarly to the previous method, it assumes that the numerical assembly and the real soil produce at the minimum and maximum porosity respectively the same volumetric response.

2.2.6 Microscopic properties

Coordination number

The coordination number Z is a microscopic quantity that represents the average of number of interactions per particle. This quantity describes the structural stability of an assembly of particles as defined in Thornton (2000) by representing the particle connectivity. It is defined by:

$$Z = \frac{2N_c}{N_p} \tag{2.7}$$

where N_c and N_p are the total numbers of contacts and particles respectively. However, in numerical simulations, particles with no contacts or only one contact do not contribute to the stable state of stress. Therefore, the coordination number Z^*, which considers only particles involved in more than one contact, is defined as follows:

$$Z^* = \frac{2N_c - N_1}{N_p - N_0 - N_1} \tag{2.8}$$

With N_1 is the number of particles involved in a single contact and N_0 the number of particles without any contact.

It was shown by O'Sullivan, Bray, and Riemer (2002) that an increase in the value of Z^* is usually related to an increase in the packing density or a decrease in the porosity. Also they show that the relation between the Z^* and the material stiffness is proportional. Thus the stiffness of a granular assembly does not depend only on its density but also on its connectivity.

Finally, in case of clumped particles, when computing the coordination number, the contacts between spheres composing the clump are ignored, so a contact is only counted in case it's between two clumps.

Fabric tensor

In 1972, (Oda, 1972) used the word "fabric" to define the particles spatial arrangement. In other terms, it could be used to quantify the structural anisotropy of a granular material (Thornton, 2000) by describing the interparticle connectivity (Satake, 1978). According to (Satake, 1978; Satake, 1982), the fabric anisotropy is

characterized by the fabric tensor F_{ij}:

$$\phi_{ij} = \frac{1}{N_c} \sum_c n_i \cdot n_j \tag{2.9}$$

where N_c is the number of contacts in the assembly, and $\vec{n}$ the normal contact vector at a contact with i,j = 1,2,3 (in 3D).

To evaluate the fabric anisotropy, the elements ϕ_{11}, ϕ_{22}, and ϕ_{33} of the fabric tensor are used. Such that if the granular sample is isotropic the following is true:

$$\phi_{11} + \phi_{22} + \phi_{33} = 1 \tag{2.10}$$

with the principal values ϕ_{11}=ϕ_{22}=ϕ_{33}=1/3, representing the average of contact orientations that are uniformly distributed in the x, y, and z directions.

Strong and weak contact forces

The study from Radjai et al. (1996) investigated the contact force networks in two-dimensional numerical simulations of rigid spheres. They found from the probabilistic distributions of the normal contact forces that forces exceeding the average of the contact forces follow exponential distribution law, while smaller ones follow a power law.

$$f_{avg} = \frac{1}{N_c} \sum_i f_i \tag{2.11}$$

where f_i is the normal force of the i^{th} contact in the sample.

$$P(f) \propto \begin{cases} f^{\alpha} & if\ f < 1 \\ exp^{\beta f} & if\ f > 1 \end{cases} \tag{2.12}$$

$$\text{with} \quad f = \frac{f_i}{f_{avg}} \tag{2.13}$$

In another study (Radjai et al., 1998), the authors divided the contact forces network into strong (when f>1) and weak (for f<1) sub-networks. They concluded that the shear stress of a assembly if mostly related to the strong force network.

2.2.7 Summary

As stated in previous parts, different aspects affect the behaviour of the DEM. One should choose the right initial state (porosity, fabric arrangement) of the assembly that allows a good representation of the granular behavior. In addition, the particle shape should be chosen depending on the complexity of the problem to be solved. For example, in case of large boundary value problems BVPs, it is very expensive computationally to use complex shapes. Finally, several contact models exist, taking into account different physical parameters (cohesion, friction, roughness and rolling resistance) of soil.

2.3 Soil-structure interaction

As mentioned earlier, different methods are used nowadays to model soil-structure interaction (SSI) problems. It is important to understand the advantages and disadvantages of each method. Therefore, several methods are discussed in the following parts.

2.3.1 Finite element method

In last decades, the finite element method (FEM) has become one of the most popular numerical methods used to model SSI problems. Usually, the physics of a problem is described by partial differential equations (the phenomenological constitutive relations) that often cannot be solved analytically. Instead, these equations are discretized and approximated, and then solved using numerical tools such as FEM to estimate the real solution of the Partial Differential Equations (PDEs). FEM involves discretizing the simulation domain into smaller finite elements to form a mesh. These finite elements are connected to each other at nodes, which represent the forces and moments transferred between elements. At these nodes, force-displacement relationships are defined. These equations are then combined to form a set of equations that can be solved to provide an exact solution. Between the nodes, the solution is interpolated and approximated.
One of the most used phenomenological constitutive relations in FEM is the hardening soil model (HSM) by Schanz, Vermeer, and Bonnier (1999), which is an advanced model to simulate the behavior of soil with its hardening behavior. It provides a very good prediction ability at least on monotonous loading path, but in case of applications involving cyclic loading paths, it may be necessary to calibrate the model based on cyclic tests (such as cyclic triaxial or cyclic simple shear tests). The Hardening Soil model requires calibration of several parameters, including the friction angle (ϕ), cohesion (c), dilatancy angle (Ψ), triaxial stiffness (E_{50}), triaxial unloading stiffness (E_{ur}), oedometer loading stiffness (E_{oed}), as well as other parameters such as the unloading/reloading Poisson ratio (ν_{ru}) and the coefficient of earth pressure at rest (K_0).
FEM has been used to model several geotechnical problems. Modeling the soil-wall interaction during excavation (Figure 2.8-a) has been performed and studied by (Faheem, Cai, and Ugai, 2004; Zdravkovic, Potts, and St John, 2005; Finno, Blackburn, and Roboski, 2007; Chugh, Labuz, and Olgun, 2016; Ahmadabadi, Hosseini, and Rezai, 2016), providing an investigation of FEM parametric studies and a better understanding of the different possible ways for modeling a retaining wall during excavation using FEM.
Another studies were done to model soil-pile interactions (Figure 2.8-b), such as (Pan et al., 2002; Khodair and Hassiotis, 2005; Maheshwari et al., 2005; Karthigeyan, Ramakrishna, and Rajagopal, 2007; Achmus, Kuo, and Abdel-Rahman, 2009; Bourgeois et al., 2010; Giannakos, Gerolymos, and Gazetas, 2012; Hamouma, Messameh, and Tallah, 2020; Cheng et al., 2021), offering a better knowledge of the behaviour of piles of different geometries under different types of loading (monotonic and cyclic). It is found that numerical results were in good quantitative agreement with experimental results. In addition, it's important to mention that in case of piles subjected

to cyclic loading, the constitutive model parameters are calibrated based on cyclic loading tests.

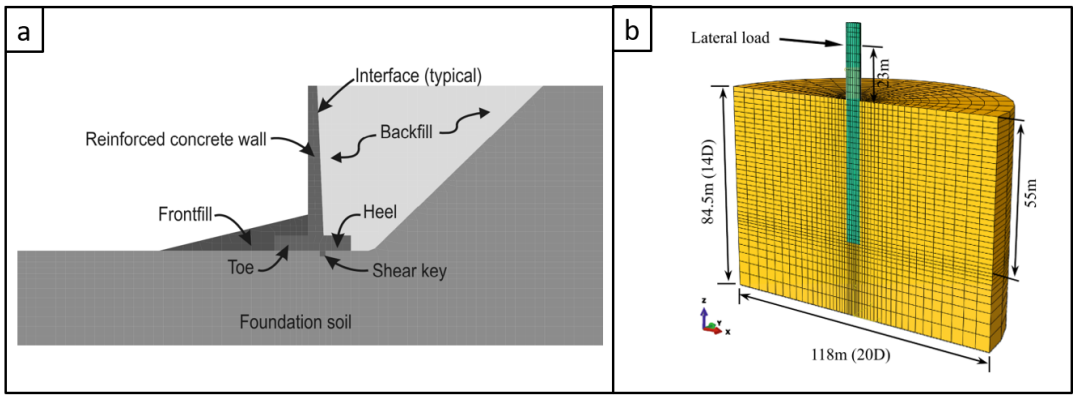

FIGURE 2.8: Finite element models of : a-soil-wall interaction(Chugh, Labuz, and Olgun, 2016) b-soil-pile interaction (Cheng et al., 2021)

2.3.2 Macro elements

Macro-element modelling is a method used across several disciplines like geotechnical engineering, structural analysis, and earthquake engineering to simulate the macroscopic behaviour of structural elements. The concept of macro-element in geotechnical engineering has been used since 1991 by Nova and Montrasio (1991) to simulate the non-linear behaviour of SSI. This method involves simplifying finite element analysis by substituting several finite elements by a single element. The main goal of this method is to reduce the number of equations solved in finite element analysis, leading to more practical analysis of large structural systems.
Nova and Montrasio (1991), investigated the settlements of shallow foundations on sand, subjected to vertical loads. In their macro-element model, they consider the soil as an homogeneous elasto-plastic material. To validate their model, a series of laboratory tests were performed on small-scale footings. The results of these tests were then compared to the predictions made by the macro-element model. The authors observed a good agreement between the experimental and the model results.
Later on, other studies were done to model shallow foundation behaviour using macro-element method by Gottardi, Houlsby, and Butterfield (1999), Cremer, Pecker, and Davenne (2001), Grange, Kotronis, and Mazars (2008), and Grange, Kotronis, and Mazars (2009). In addition, Martin and Martin (1994) applied the same concept but in case of offshore foundations. Furthermore, macro-element modelling has been applied in case of deep foundations (Taciroglu, Rha, and Wallace, 2006; Rha and Taciroglu, 2007; Li et al., 2016) by modelling the SSI of vertical single pile.

The general structure of the macro-element form (Grange, Kotronis, and Mazars, 2009) is presented in Figure 2.9. It's shown that the soil domain is divided into two domains, the near-field and the far-field, condensing the non-linear effects of the material and structure geometry in the near-field, whereas the system remains linear in the far-field.
As shown in Figure 2.9-b The total displacement of the foundation is divided into

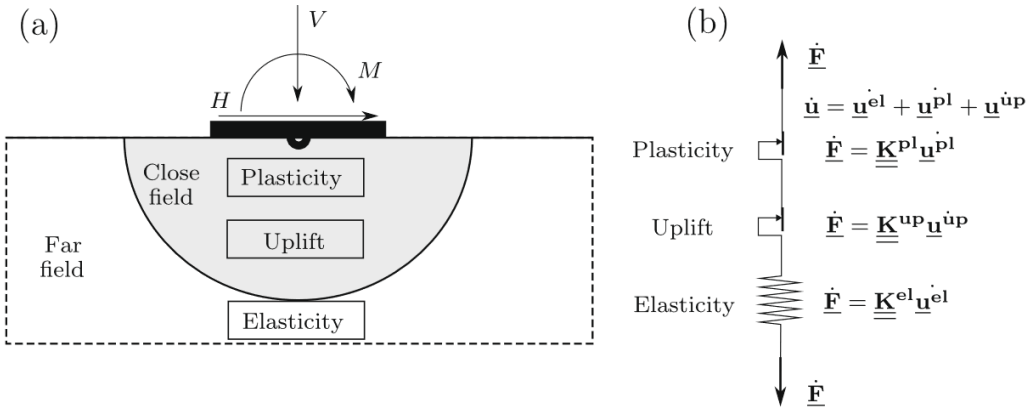

FIGURE 2.9: The general structure of macro-element from Grange, Kotronis, and Mazars (2009): a-Macro-element structure decomposition b-System analogy

three parts (elastic and plastic displacements of the soil with uplift displacement of the foundation), resulting from three mechanisms (elasticity, plasticity, and uplift, where uplift is a non-linear and non-reversible mechanism that introduces shallow foundation overturning rotations and displacements) described in details in (Grange, Kotronis, and Mazars, 2009). Using macro-element modelling usually requires the calibration of the model parameters based on the experimental results from the specific experiment to be modeled itself. For example, the macro-element in (Grange, Kotronis, and Mazars, 2009) requires the calibration of 17 parameters for one type of soil under one loading condition.

2.3.3 Discrete element method

The discrete elemnent method stands out as a versatile approach, that can serve as both a numerical method and a constitutive model representing the physical behavior of soil. The DEM simulated mechanical behavior at the scale of the Representative Elementary Volume (REV) depends not only on the contact law, but also on the geometrical shape of the grains and the microstructure of the granular assembly, like no other method.
It has been applied to several geotechnical applications and laboratory tests involving soils. Simulating laboratory tests has been done using DEM to investigate the microscopic and macroscopic behaviour of granular material. (Zhang and Thornton, 2002) investigated the deformations and development of the shear band in a direct shear test using DEM in 2D with spherical particles. Another study (Cui and O'sullivan, 2006) explored, using 3D DEM, the microscopic behaviour of spherical steel particles during a direct shear test. Recently, (Nitka and Grabowski, 2021) also investigated the shear band properties and the movement of indvidual particles during shearing in direct shear test. Similarly, the simple shear test is simulated using DEM (Asadzadeh and Soroush, 2017) under cyclic shearing were they soil behavior is studied at micro and macro scales. Results of simulations of laboratory tests in the previous studies agree with experimental results, demonstrating the efficiency of discrete element modelling in replicating laboratory tests.

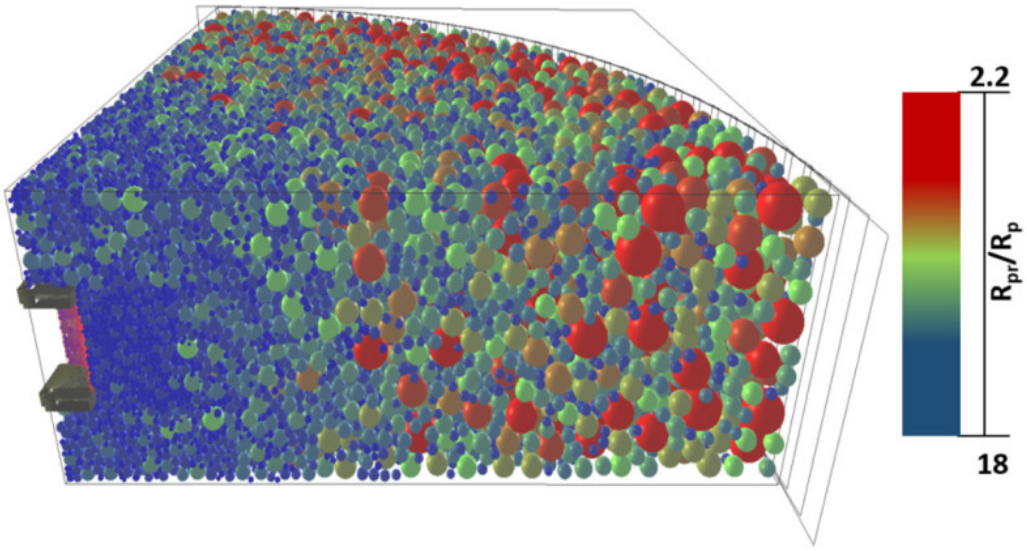

FIGURE 2.10: Discrete element model of the pressuremeter test with an adaptive size of discretization of the soil domain by (Abdallah et al., 2022)

DEM has been also used to model large scale problems in geotechnical engineering. The authors in Herten and Pulsfort (1999), simulated the earth pressure exerted on vertical shafts. Circular shafts were built as series of segments made up of small flat walls, whereas the soil domain was made up of spherical particles. They measured the lateral pressure by gradually moving the shaft wall inward. Then a comparison of the numerical simulation with experimental data was done. In a recent study (Abdallah et al., 2022), the pressuremeter test was modelled using DEM, and calibrated from experimental data from a pressuremeter test performed in a calibration chamber. The adaptive discretization technique is implemented as shown in Figure 2.10 to limit the number of particles in the soil domain. Particles with a relatively low mean size are chosen near the pressuremeter probe to capture macroscopic deformations, as the relative displacements and rearrangements of particles at the microscopic scale play a key role. As the distance from the probe increases, particle size gradually grows. Jenck, Dias, and Kastner (2009), developed a two-dimensional model to investigate the soil improvement by modelling a granular fill supported by vertical rigid piles. The DEM results were compared to results from a two-dimensional small scale model and another continuum model.The results showed that DEM was able to capture the macroscale response accurately.
A recent study (Zhang et al., 2022), investigated the bearing capacity characteristics of three foundation models (single pile, raft foundation, and single pile with raft) through discrete element models and laboratory tests. It was found that numerical results were in good agreement with laboratory tests.
The behaviour of a shallow foundation on a model slope is studied and analyzed in (Gabrieli, Cola, and Calvetti, 2009). The authors used an up-scaled grain-size curve in the DEM model to reduce the number of particles required. The authors evaluated the performance of the numerical model by comparing both the overall global results such as load-settlement curves and local results including strain field from the experiments presented in Figure 2.11. Another research (Rocha, Farias, Albuquerque,

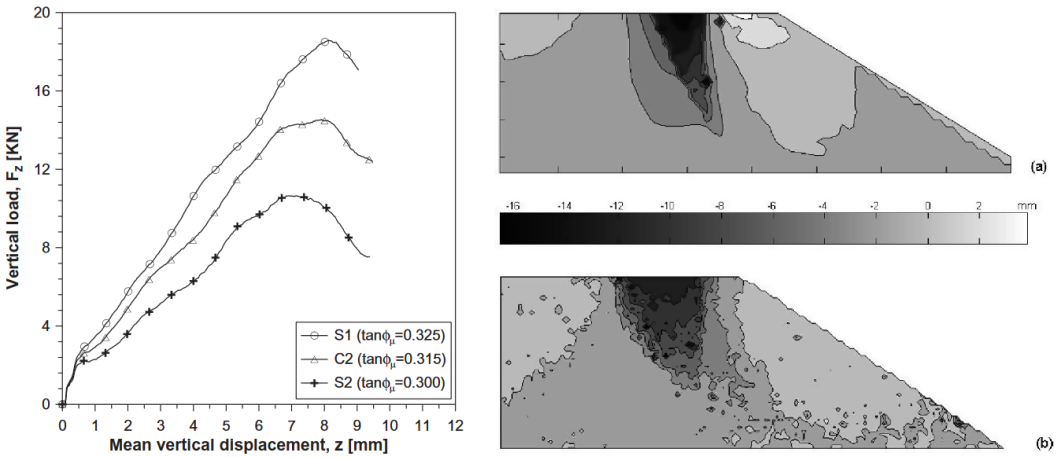

(A) load-displacement curves of the plate for different interparticle friction coefficient.

(B) Vertical displacement contour using (a) particle image velocimetry analysis and (b) DEM.

FIGURE 2.11: Global (left) and local (right) results by Gabrieli, Cola, and Calvetti (2009).

et al., 2019) conducted a numerical simulation of shallow foundations using DEM. The model parameters were calibrated from a reduced laboratory model. The discrete element method provided accurate qualitative predictions of failure surfaces and satisfactory quantitative predictions of the ultimate load capacity.

2.3.4 Coupling FEM with DEM

Finite element method and discrete element method are two different separate numerical approaches, but by using the FEM to discretize the macroscopic domain in FEM meshes and using the DEM at each integration point of the mesh, these two methods can be combined to solve problems such as BVPs, by creating a hierarchical multiscale model. Furthermore in (Guo and Zhao, 2014), FEMXDEM in Figure 2.12 is used to model the behaviour of monotonic biaxial compression test. DEM is used to capture the non-linear constitutive behaviour of the granular material at its FEM Gauss point that serves as input boundary conditions. In this way, phenomenological assumptions about the constitutive relation in traditional continuum modeling are avoided, while maintaining the computational efficiency of FEM in solving BVPs.
Similarly, Guo and Zhao (2015) employ a hierarchical coupling of FEM and DEM to solve BVPs. In this study, classical problems related to retaining walls and footings were investigated, showing that simulations could be validated and verified through analytical solutions.
In addition, Nguyen et al. (2017) used the FEMxDEM modelling to simulate the behaviour of a granular material during biaxial and pressuremeter tests.
In another study (Chaudry et al., 2021), the authors couple DEM with FEM in a different way (Figure 2.13) using a multi-domain coupling technique, inspired by the work of Wellmann and Wriggers (2012) to model the use of a granular material as a crash-absorber in ship building. This method focuses on modelling the regions where significant granular deformation occurs using DEM, while using FEM as a continuum model for other regions. They highlight that the advantage of this method

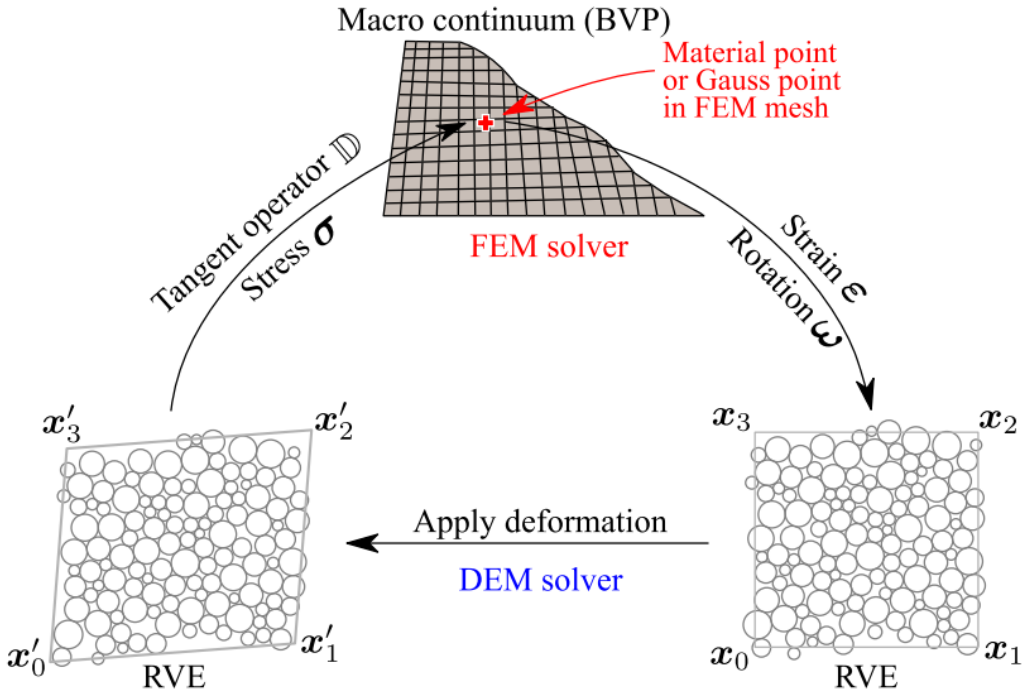

FIGURE 2.12: The FEMxDEM solution procedure in (Guo and Zhao, 2014)

is to maintain accurate numerical model results while maintaining computationally efficient simulations.

2.3.5 Summary

To summarize, different approaches can be used to model the behaviour of geotechnical problems. Continuum approaches such as finite element method solve BVPs by assuming a continuous domain. These approaches solve the problem by meshing the domain, and by relating the stresses and strains through phenomenological constitutive relations which usually require ad-hoc history parameters and advanced experimental tests for calibration in case of complex loadings. Whereas in case of cyclic loadings, calibration using cyclic tests is necessary. Another drawback with FEM is the description of large displacements, deformations, and post-failure responses. It requires the implementation of specific techniques such as remeshing. An important advantage of this method is that it is computationally cheaper than other discrete methods. In addition, phenomenological constitutive relations embedded in FEM nowadays, such as the HSM model, demonstrate excellent predictive abilities, at least on monotonous loading paths.
Moreover, modelling with macro-element is very cheap computationally; However, it is necessary to calibrate many parameters based on the experiment results of the experiment being modeled.
Furthermore, the discrete element method solve BVPs by modelling the behaviour of these problems. The overall system behaviour depends on the discrete particle interactions through simple interaction laws. The main advantages of this method is that it

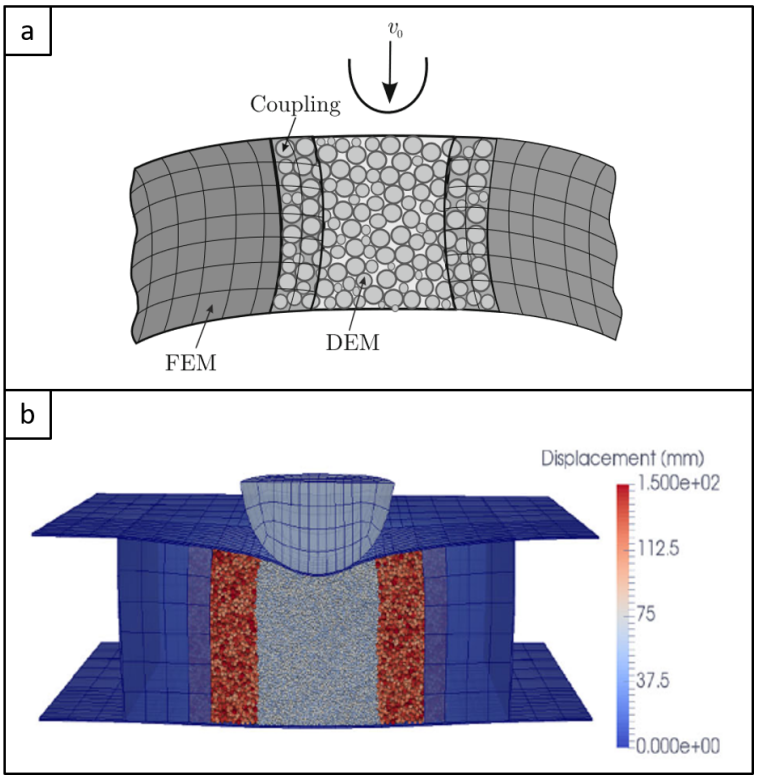

FIGURE 2.13: Coupling FEM with DEM in (Chaudry et al., 2021)
a-model scheme b-actual model

requires few parameters for calibration from simple experimental tests such as triaxial or direct shear tests. Furthermore, as discontinuities between particles are inherent in the DEM method, large displacement and post failure responses can be described without any additional ingredients. It explicitly represents the microstructure, including the entire loading history without the need for ad-hoc historical parameters when dealing with cyclic loading tests. In addition, it is very useful to understand the behaviour in the microscale. However, this method is usually computationally expensive compared to continuum methods and involves a more complex calibration process.

Coupling the FEM and DEM is possible to solve BVPs, by using the DEM to capture the non -linear stress and strain relationship of the granular material, whereas, FEM can be used to solve the large BVPs.

One can choose the method to solve a certain problem depending on the complexity and scale of investigation of the problem, taking into consideration the computation time of each method.

Although the discrete element model and coupled FEMxDEM element approaches has been used in geotechnical engineering to model BVPs, the available validation of the different approaches is still limited, especially in soil-structure interaction problems subjected to complex cyclic loadings. Therefore, it is important to model and validate complex soil-structure interaction problems such as those of a geotechnical structure subjected to a cyclic loading using DEM or FEMxDEM. Finally, we need to validate and compare these methods with respect to more conventional simulation methods and their usefulness for studying the behavior of geotechnical structures.

Chapter 3

Definition of a light discrete model for quantitative constitutive predictions

3.1 Introduction

The discrete element method (DEM) (Cundall and Strack, 1979b) has been widely used to predict the constitutive behavior of soils. However, predicting the mechanical response of some granular soil under some complex loadings can be challenging.

Loose granular soils, as loose sand, can show original constitutive responses when subjected to loading paths involving generalized loading parameters defined as linear combinations of strain or stress tensor components (Klisinski, Mroz, and Runesson, 1992; Nova, 1994; Sibille et al., 2015). In particular, this is the case of the isochoric loading where the trace of the strain tensor is fixed to zero, or the constant stress deviator loading where the difference between the major principal stress and the minor one if fixed to be constant. For an isochoric compression the loose granular medium may present a static liquefaction (vanishing of all the effective stresses corresponding to the loss of all the interparticle contacts) occurring strictly within the Mohr-Coulomb failure envelope (Prisco and Nova, 1994). For a constant stress deviator path subjected to a decrease of the mean pressure the loose granular assembly may present a plastic dilative response while the stress path is approaching the Mohr-Coulomb failure envelope (Daouadji et al., 2011).

Hence, the ability of a model to describe the mechanical response of a soil should be considered with respect to conventional loading paths as “drained” compressions (i.e compression where the radial stress is kept constant, simple compression is a particular case with a radial stress fixed to zero) but also with respect to more complex loading paths revealing some more tricky features of the constitutive response of granular medium and more discriminant with respect to model capabilities (see for instance the former benchmark of phenomenological constitutive relations realized in the late 80s (Saada and Bianchini, 1988a)). Furthermore, that such paths may representatives of some real situation, as the undrained response of water saturated soil layers for the isochoric loading path (where the isochoric constraint is indirectly imposed by the non-drainage of the pore water), or the rising of the underground water table in soil layers (after rainfalls or floods) resulting in a decrease of the effective mean pressure in the soil while the deviatoric stress is unchanged.

Besides, response of loose granular assemblies is very sensitive (probably more than dense soils) to the initial packing state in terms of porosity, distribution of porosity, initial fabric ... (Benahmed, Canou, and Dupla, 2004; Uthayakumar and Vaid,

1998). This is true for "real" granular assemblies but also for discrete numerical models, based on the discrete element method , for which the description of the constitutive response of loose granular assemblies is still challenging. Even if the DEM model is properly calibrated on a certain loading path (such as drained triaxial compression), it may fail to predict the soil's response under more complex loading pathways (Aboul Hosn et al., 2017; Sibille, Benahmed, and Darve, 2021) and for a wide range of initial soil densities (Gu, Zhang, and Huang, 2020).

The objective of the work presented in this chapter is to define a discrete numerical model and in particular a preparation process controlling the initial state to investigate how this initial state affects the model responses and what are the minimal ingredients in the constitution of the model itself, but also in the reproduction of the initial state, which are required for a faithful description of the soil responses to complex loading paths.

The particle shape (angularity – anisotropy – roughness) plays an important role in the constitutive behavior of soils. Recent studies (Kawamoto et al., 2018) offer the possibility to reproduce the real grain shape. However, such approach is very expensive in computational cost. Thus, proposing a light DEM model with the minimum required complexity is also one of the objectives in order to limit the computational cost and make possible to address easily boundary values problems such that the continuously increasing computing performance is dedicated to tackle more and more complex or extended boundary value problems and not used to integrate a complex model at the scale of a representative elementary volume. In particular, the way to describe the grain shape and roughness in a discrete model is determinant with respect to the prediction ability of the model but also with respect to the computational cost. Particle shape can be described either explicitly by complexifying the particle geometry by using clumps of spheres (Suhr and Six, 2020), polyhedral particles (Mohamed et al., 2022) or even level set based particles (Kawamoto et al., 2018), or indirectly via inter-particle contact laws representing the effect of the shape of particles. Therefore, the goal of this work is to check on one hand if more complex particle shapes than spheres (as clumps) are able to improve the predictions of the models and, on the other hand to check the trade-off between the rolling resistance, which has to be associated to spherical particles, and the use of clumps in terms of prediction ability. Effectively, it has been shown that the use of a rolling resistance contact law can represent the limitation of the relative rotation of particles in contact that would be due to their non-spherical shape (Iwashita and Oda, 2000; Martin, Thornton, and Utili, 2020; Jiang, Zhang, and Li, 2019). Furthermore, the role of a non-constant inter-particle contact friction angle is also investigated in order to represent the effect of the roughness of particles (Mollon et al., 2020) subjected to different ranges of mean pressures.

In this chapter, Hostun sand is chosen as the reference soil to assess the prediction ability of the models. Therefore, the first part of this chapter is dedicated to the presentation of the experimental data used to calibrate and validate the different numerical models. Following this, the different discrete models investigated in the chaper are presented. In particular, we detail the contact laws, the choice of the particle shapes, and the way to identify the initial porosities of the numerical assemblies. Subsequently, a first class of models, considering initial isotropic fabric and

conventional dry friction at contact (constant contact friction coefficient), is investigated and assessed with respect to the experimental data on Hostun sand. Then, this investigation is extended to a second class of models, close to the previous one but considering a non-constant friction coefficient at contact. Finally, the last part of the chapter is devoted to the particular case of describing the constitutive response of loose Hostun sand only. The impact of the initial fabric, in terms of the anisotropy of contact orientations, is examined in addition to the other factors previously considered. The analysis is performed at both the macroscopic scale and the contact scale. In conclusion, we discuss the main findings of this chapter.

3.2 Reference soil and experimental data

Calibration and validation of the DEM models in this chapter are performed with respect to experimental data on the Hostun sand "HN31" (formely referred as "RF").

3.2.1 Hostun sand "RF" description

The Hostun sand consists of sub-angular to angular grains with a uniform grain size distribution (Figure 3.1) (Flavigny, Desrues, and Palayer, 1990) characterized by a uniformity coefficient (C_u) of 1.8 and a mean grain size (D_{50}) of 0.35 mm. Depending on the technique used, it was determined that the minimum void ratio is within the range of $e_{\min} \in [0.624, 0.648]$, while the maximum void ratio was found to be in the range of $e_{\max} \in [0.961, 1.041]$.
All along this work two initial densities of sand samples are considered. An initial dense state with a relative density $D_r \approx 1.0$ and an initial loose state with $D_r \approx 0.1$. It is worth noting that the range of density between the dense and loose states is rather important which constitutes an additional challenging point for the assessment of the models discussed in this chapter.

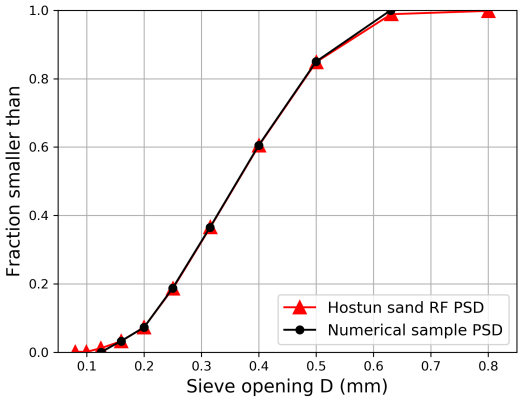

FIGURE 3.1: Particle size distribution of Hostun sand "HN31"

It is important to mention that experimentally the sand samples were prepared according to two different methods, depending on the initial density required for the subsequent mechanical loadings. Beyond the difference in terms of global porosity, these methods lead also to different sand fabrics.

- For initially dense sand samples with a relative density of approximately $D_r \approx 1.0$, which were used for drained compression tests, cyclic extension/compression tests, and circular loading path, the samples were prepared by pouring the sand into a mould and tamping it layer by layer. This preparation method resulted in samples with relatively isotropic macroscopic properties. This was confirmed in (Zitouni, 1988) through comparisons of the sand's response to drained triaxial compression tests performed in different directions relative to the direction of gravity (or tamping).

- Loose sand samples with a relative density of approximately $D_r \approx 0.1$, used for both drained and undrained compression tests, as well as constant stress deviator loadings, were prepared using the moist tamping technique. This methodology led to slightly more anisotropic sand samples compared to the denser ones described earlier (Aris, Benahmed, and Bonelli, 2012). Additionally, the moist tamping method may result in the presence of "macropores" alongside smaller inter-particle spaces (Benahmed, 2001).

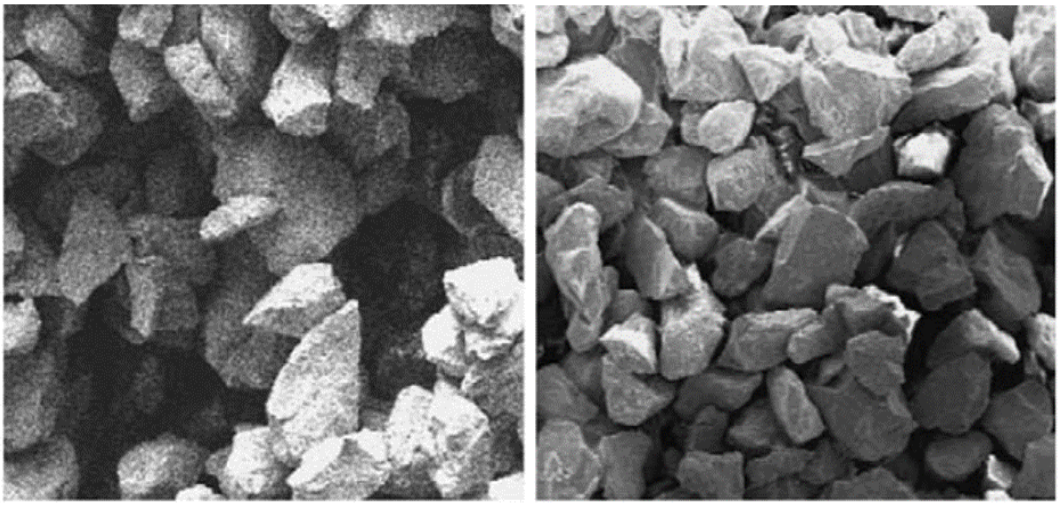

(A) Prepared by moist tamping (B) Prepared by dry pluviation

FIGURE 3.2: Microphotographs of Hostun sand RF aggregates and macropores, showing two different structures.

3.2.2 Experimental tests for calibration and validation

Triaxial tests in drained condition (Figure 3.3) performed on loose (confining pressure $p_0 = 300$ kPa) (Bousquet et al., 1994) and dense samples (p_0 = 200, 350, and 500 kPa) (Lanier and Zitouni, 1988) are used for the calibration of the model.
Cyclic compression/extension (Zitouni, 1988) and circular stress (Lanier and Zitouni, 1988) loading paths performed on dense sand samples were considered to validate and discuss the characteristics of the numerical models and their simulated responses in same conditions. Then undrained (Benahmed, 2001) (or isochoric) and constant stress deviator (Daouadji et al., 2011) loading paths performed on loose sand samples are considered in case of loose numerical samples.

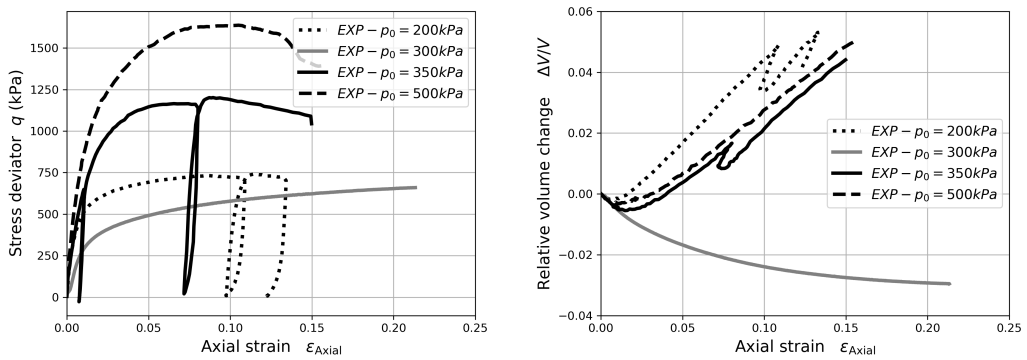

(A) (B)

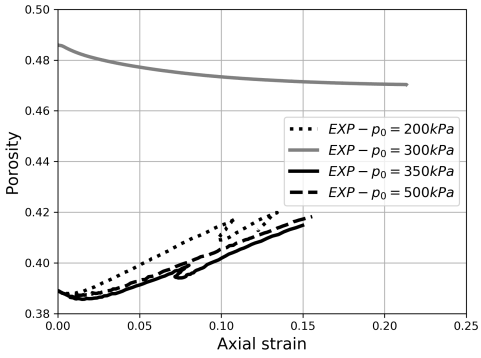

(C)

FIGURE 3.3: Drained triaxial compression tests used for calibration (grey curve represents the test on loose sand, and black curves represent the ones on dense sand).

3.3 Definition of the discrete element models

3.3.1 Inter-particle contact law

An open-source DEM software YADE is used to create the 3D discrete element models and to perform all the numerical simulations in this thesis. The 3D discrete element models in this chapter are created within periodic limit boundary conditions. The inter-granular contact law between particles is governed by a classical dry friction model characterized by a normal and tangential stiffnesses and a contact friction coefficient. As mentioned in the literature review, the simplest particle shape used in DEM is the spherical shape.

Considering two spherical particles with radii R_1 and R_2 (as shown in Figure 3.4) in contact, with an overlap δ_n and a normal vector $\vec{n}$ to the tangent contact plane, the normal contact force $\vec{F_n}$ and tangential contact force $\vec{F_t}$ are expressed as follows:

$$\vec{F_n} = k_n \, \delta_n \, \vec{n} \tag{3.1}$$

$$\Delta\vec{F_t} = -k_t \, \Delta\vec{u}_t \quad \text{with} \quad ||\vec{F_t}|| \leq \mu \, ||\vec{F_n}|| \tag{3.2}$$

where k_n and k_t are constant stiffness values in the normal and tangential directions

respectively. $\Delta\vec{u}_t$ is the relative incremental tangential displacement used to calculate the tangential force incrementally; and μ is the friction coefficient in the tangential direction.

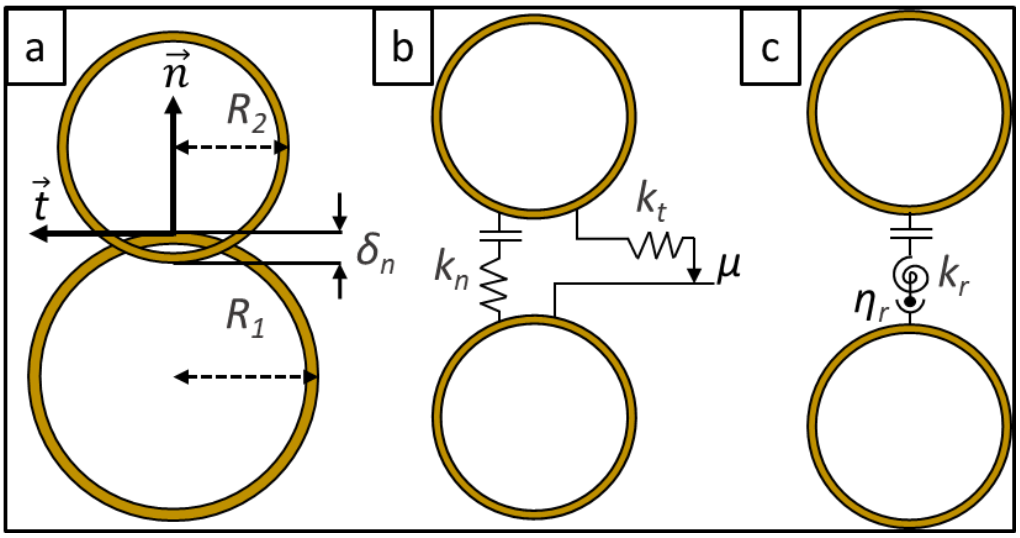

FIGURE 3.4: Contact between two spheres: (a) frame attached to the tangent contact plane and particle overlap; (b) contact model with sliders in the tangential direction and (c) with stiffness and slider acting with respect to relative rolling motion.

In this research, the contact friction coefficient μ is considered either constant (leading to a constant internal friction angle at the macroscopic scale) or non-constant and varying with the normal contact stress, as suggested in (Sibille, Benahmed, and Darve, 2021) (leading in a slightly non-linear failure surface with respect to the mean pressure at the macroscopic scale as the internal angle of friction increases with a decrease in the mean pressure). In the latter case, the contact friction coefficient μ is defined as a function that varies based on the normal contact stress σ_c which is derived from the normal contact force associated with each individual contact (Suhr and Six, 2017):

$$\mu = \mu_{min} + \frac{\mu_{max} - \mu_{min}}{\frac{\sigma_c}{\sigma_c^R} + 1} \tag{3.3}$$

$$\text{with:} \quad \sigma_c = \frac{||\vec{F}_n||}{\pi R_{mean}^2} \qquad \text{and} \qquad R_{mean} = 2\frac{R_1 R_2}{R_1 + R_2} \tag{3.4}$$

The parameters μ_{min} and μ_{max} in the contact law represent the minimum and maximum values of the friction coefficient, respectively. For a nil normal contact stress, the friction coefficient is set to its maximum value, $\mu = \mu_{max}$ and as the contact stress increases it decreases asymptotically to μ_{min}. σ_c^R is a reference contact stress chosen arbitrarily as the mean normal contact stress that would occur in an idealized isotropic granular assembly subjected to a reference isotropic confining stress of 100 kPa. Assuming a granular medium of porosity 0.4, a rough estimation of σ_c^R is then given thanks to the mixture theory by 100/(1 - 0.4) $\approx$ 167 kPa (Sibille, Benahmed, and Darve, 2021).

Considering Spherical particles can lead to excessive rolling which might affect the shear strength. Thus, rolling resistance parameter is considered to prevent excessive rotations that cause unrealistic shear strengths. The rolling resistance between particles (as shown in Figure 3.4c) is represented by a contact rolling moment $\vec{M}_r$, which is defined as:

$$\Delta\vec{M}_r = -k_r\,\Delta\vec{\theta}_r \quad \text{with} \quad ||\vec{M}_r|| \leq ||\vec{F}_n||\,\eta_r\,\min(R_1, R_2) \tag{3.5}$$

where k_r represents a constant rolling stiffness, $\vec{\theta}_r$ the particles relative rolling rotation, and η_r stands for the rolling friction coefficient.

The normal, tangential and rolling stiffness are derived from the stiffness modulus E_c by introducing dimensionless tangential and rolling coefficients α_t and α_r as follows:

$$k_n = E_c\,R_{\text{mean}}; \qquad k_t = \alpha_t\,k_n; \qquad k_r = \alpha_r\,R_1\,R_2\,k_t \tag{3.6}$$

In the following sections, different models are considered: spherical particles with rolling friction, and clumps of spheres with and without rolling friction.

3.3.2 Identification of basic particle shapes

Shear strength of granular matter at residual state (i.e. at large deformation or critical state) depends mainly on the shape of the particle and is insensitive to the initial state of the granular assembly. Hence, the choice of shapes of clumps is made by looking for clumps resulting to a realistic shear strength at residual state with respect to what is typically obtained for a sand; but also by considering that the shape of the clump can be easily tuned to fit this shear strength.
Different clumps of spheres were investigated to assess the shear strength at residual state (characterized by the residual friction angle φ_0) based on simulation of triaxial compression tests. In order to investigate the effect of particle shape only on φ_0, simulations were performed by considering identical particle size distributions (PSD) for the packings made with different particle shapes.
We followed several steps to create clumps:

1. Create an assembly of spheres of a certain PSD.
2. Define the desired geometry of the clump by clumping spheres together.
3. Replace the spheres in the assembly by the defined clump of the same volume.
4. Update the particles properties (mass, volume and inertia).
5. Verify that the assembly of clumps has the same PSD as that of spheres.

The residual friction angle of these clumps was evaluated with a constant contact friction angle of 19° (high enough to get a critical shear strength independent of the contact friction angle (Aboul Hosn et al., 2017)), and without rolling friction at contact (only the rheological model b) in Figure 3.4 is activated). The results presented in Figure 3.5 indicate that, with the exception of the clump of 6 spheres (3x2), all tested clumps exhibited a φ_0 below 30°, which is the φ_0 of the Hostun sand used for

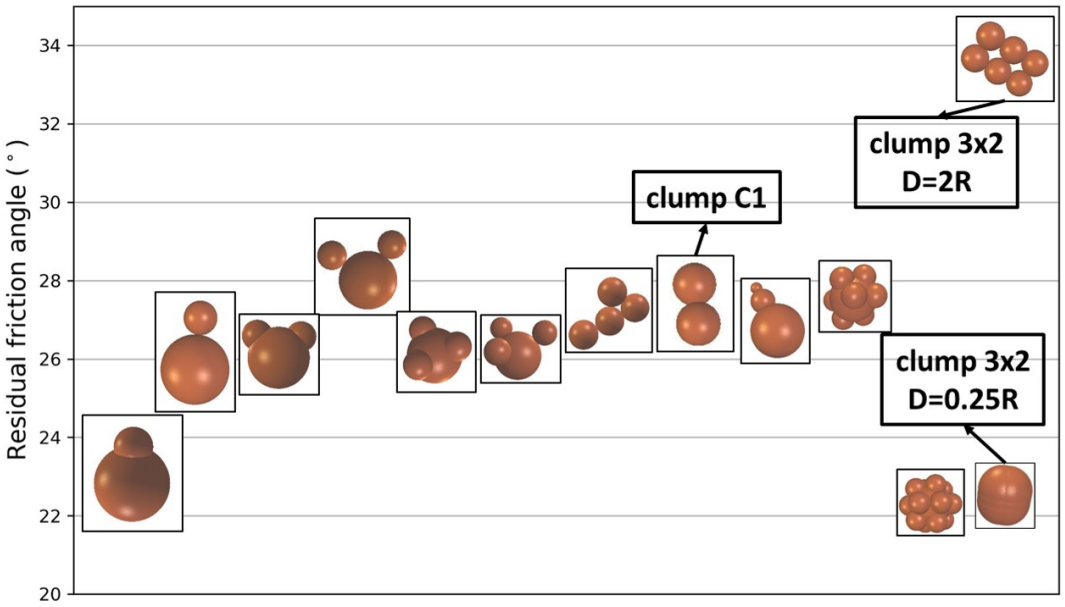

FIGURE 3.5: Comparison of residual friction angles simulated with different shapes of clumps.

calibration of the models (It should be noted that samples of spheres without rolling friction resulted a φ_0 of approximately 19.5°). In other words, it is not possible with such clumps to describe the residual shear strength of a typical sand as Hostun sand. In contrast, the clump of 6 spheres (clump 3x2) displayed a higher φ_0 of approximately 33.5°. Moreover, the shape of the clump 3x2 can be easily configured according to a single scalar representing the distance between the centres of the particles, as discussed further in this section. As a result, the clump of 6 spheres (3x2) has been chosen for further investigations to replace spheres with rolling friction. Additionally, we made the choice to consider mixing rolling resistance and clumps in order to increase the shear strength providing by clumps only. For that, we considered one of the simplest clump consisting of two non overlapping spheres (clump C1) which has already been used in several previous studies, but without rolling resistance (Villard and Chareyre, 2004; Salot, Gotteland, and Villard, 2009; Villard, Huckert, and Briançon, 2016).

Therefore, three discrete element models are considered in the following. These models vary based on the shape of the particles as illustrated in Figure 3.6 and the consideration, or not, of rolling resistance. The names of the particles (sphere, clump C1 and clump 3x2) are used to label the three different models.

The three discrete models are described as follows:

1. The "Sphere" model consists of single elementary spheres with the addition of a rolling moment at contact acting against the relative rotation of the particles.

2. The "C1" model is composed of clumps formed by two juxtaposed spheres involving in addition a rolling moment at the contact (as for the Sphere model) between two spheres of two different clumps.

3. The "3x2" model consists of clump aggragating six spheres. There is no need to introduce an inter-granular rolling moment, since the shape of the six clustered spheres is already sufficiently non spherical to overcome the issue of unrealistic shear strength as it is shown in Figure 3.5. To control the shape of the clump 3x2, we define the shape parameter D representing the distance between the particle centres, as shown in Figure 3.7. For D=0 the particle resumes to a sphere and the most elongated particle is obtained for D=2R (where R is the radius of the particles composing the clump).

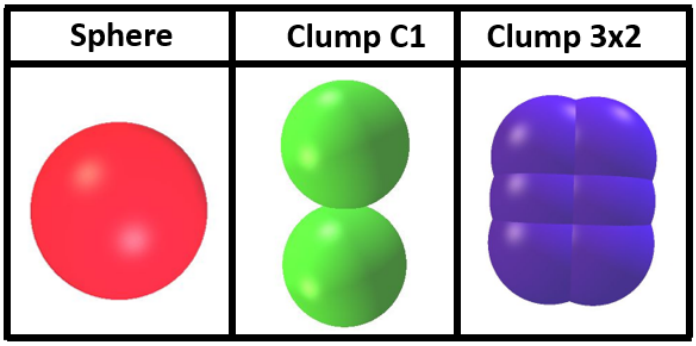

FIGURE 3.6: Particles shapes (from left to right): sphere - clump of two spheres - clump of six spheres

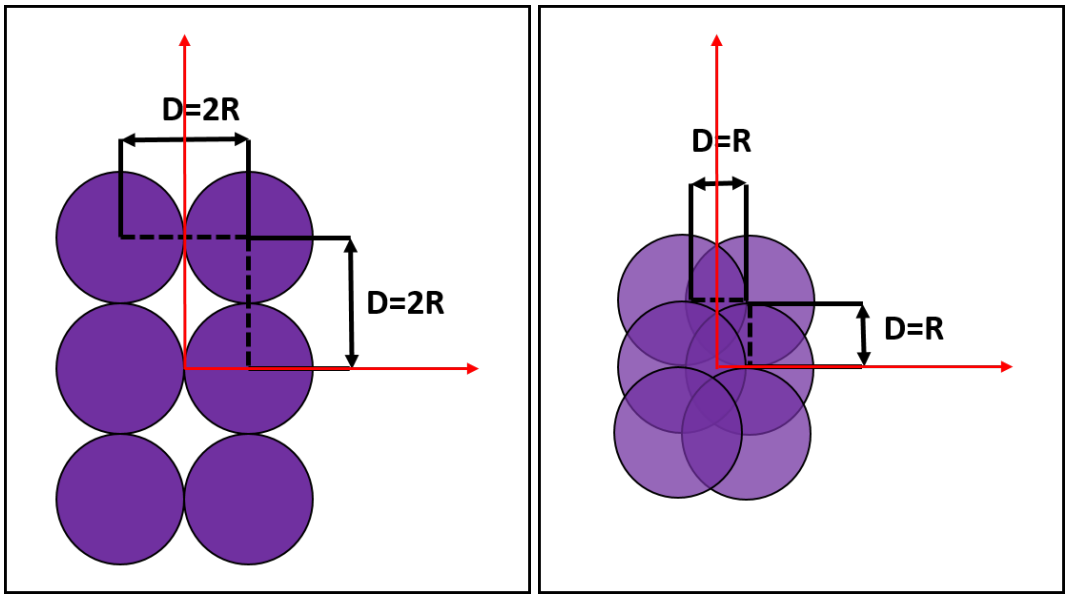

(A) D=2R (B) D=R

FIGURE 3.7: Controlling the shape of the Clump 3x2 particle with the shape parameter D (R is the radius of the spheres composing the clump).

Effect of rolling friction coefficient for Sphere and C1 models

To study the effect of the rolling coefficient, samples with spherical particles were modelled while varying η_r and μ. The critical shear strength depends only on η_r if the contact friction angle is more than 15° , i.e. $\mu > 0.268$ (Aboul Hosn et al., 2017). But this is just a particular case were $\eta_r = 0.1$ as shown in Figure 3.8. As the residual friction angle is influenced by the increase of the contact friction angle at higher η_r.

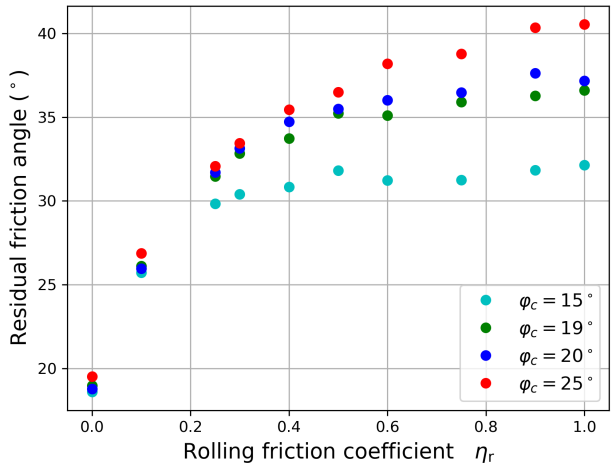

FIGURE 3.8: The variation of the residual friction angle with respect to rolling friction coefficient at different contact friction angles, based on the Spherical model

Effect of the shape parameter (for Clump 3x2 model)

To study the effect of the distance D on the critical shear strength, samples with Clump 3x2 particles were modelled while varying the distance D. These tests were done with contact friction angle equal to 19° .

3.3.3 Initial state generation and choice of the initial porosity

In this research we focus on the description of the constitutive response of dense and loose soils. Thus, the generation of initially both dense and loose numerical granular assemblies are necessary for the calibration of some of the model parameters. Consequently, two different initial porosities, loose and dense, are considered.
In practice, initially isotropic granular assemblies are generated by randomly generated non-contacting particles according to a specified particle size distribution. These assemblies are then subjected to stress-controlled isotropic compression until a desired confining pressure is achieved. The resulting porosity, denoted as n_0, is controlled by adjusting the contact friction coefficient during the isotropic compaction phase.
To achieve a denser initial state, a lower friction coefficient than the nominal value is assigned during the compaction process. This effectively lubricates the contacts

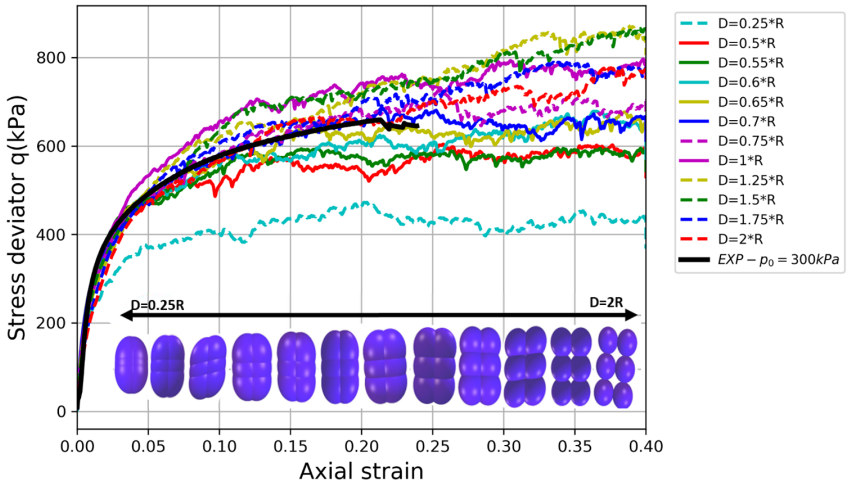

FIGURE 3.9: Calibration of the shear strength at the critical state of clump 3x2 model with respect to a drained triaxial compression on a loose Hostun sand. D represents the distance between the centres of the spheres of radius R composing the 3x2 clumps.

between particles, allowing for a more compacted configuration. However, when an initial loose state is desired, assigning the nominal contact friction coefficient during compaction (i.e. the friction coefficient that will be used after the generation of the initial state to simulate the constitutive response of the soil) may not be sufficient to achieve a very loose state. In such cases, contact adhesion can be introduced during the compaction phase to mimic the moist tamping technique used in experimental soil sample reconstitution. Subsequently, the contact adhesion is removed as proposed in (Aboul Hosn et al., 2017) to obtain the desired initial loose state before simulating the investigated loading paths.
Furthermore, the choice of the initial porosity n_0 after the compaction phase is crucial to accurately simulate the volumetric deformation observed in real soil during shearing. The numerical porosity (or void ratio) is carefully adjusted to ensure that the ratio r defined in Equation 3.7 is equivalent both experimentally and numerically. This ratio r depend on the state parameter ψ, which represents the difference between the initial void ratio e_0 and the void ratio at the critical state e_c. By appropriately tuning the initial numerical porosity, the model can replicate the same volumetric behavior during shearing as observed in real soil samples.

$$r = \frac{\psi}{(1+e_0)} = \frac{e_0 - e_c}{(1+e_0)} = \frac{\Delta V_c}{V_0} \tag{3.7}$$

The relative volume change at the critical state is represented by $\Delta V_c / V_0$. Consequently, the initial porosity (or void ratio) required for the numerical assembly is determined based on the void ratios at the critical state for both the numerical model and the real soil, as well as the initial porosity of the real soil in the specific intended state to be modeled.
The parameters of the three chosen discrete element models with their contact law used are presented in (Table 3.1).

TABLE 3.1: Parameters of the three 3d discrete numerical models

Model	Contact law	Parameters to be calibrated
Sphere	Classical dry friction model with rolling friction	E_C - n_0 - α_t - α_r - μ - η_r
C1 Clump	Classical dry friction model with rolling friction	E_C - n_0 - α_t - α_r - μ - η_r
3x2 Clump	Classical dry friction model without rolling friction	E_C - n_0 - α_t - α_r - μ - D

3.4 Calibration/validation of isotropic models with constant friction coefficient

3.4.1 Calibration Methodology

In this section, the calibration methodology followed to calibrate the different models (Spheres, Clump C1, Clump 3x2) in this work is defined. The numerical simulations are carried out by considering a parallelepipedic periodic cell made up of 10,000 particles. The particle size distribution of the numerical assembly is almost identical to that of the Hostun sand (Figure 3.1). Contact mechanical parameters are calibrated from drained triaxial compression on dense Hostun sand ($D_r \approx 1.0$) at confining pressures p_0 = 350 kPa and another on loose Hostun sand at confining pressures p_0 = 300 kPa to identify the initial porosities of the numerical models to be chosen to simulate the constitutive response of sand at these relative densities. In this part all numerical samples (dense and loose) in the three models are compacted isotropically. According to (Aboul Hosn et al., 2017), elastic contact parameters, E_c or the rolling stiffness coefficient α_r, are just set high enough in order to be sufficiently close the rigid particle assumption such that they have no effect on the macroscopic plastic properties of the granular assembly.
The calibration methodology is divided into different steps as follows:

- The first step consists in fitting the shear strength at the critical state. The latter depends on the rolling friction η_r (if used), the shape of the particles and the contact friction angle.
  The rolling friction of the sphere and clump C1 models is calibrated as shown in Figure 3.10 for Clump C1 and similarly for spheres with contact friction angle equal to 19° i.e. $\mu = 0.344$. This calibration is done without choosing high values of η_r ($\eta_r \leq 0.3$) to consider the results of the parametric study shown in Figure 3.8.
  Concerning the 3x2 model, we calibrate the distance D (Figure 3.7) between the spheres of clump 3x2 to reach the required shear strength at the critical state (Figure. 3.9).

- The peak shear strength and volumetric deformation of an initially dense granular assembly depend on factors such as rolling friction (if present), particle

shape, contact friction angle, and initial porosity. However, the rolling friction (for sphere and C1 models) and the particle shape (for the 3x2 model) have already been calibrated in the first step. Thus, the initial porosity of the numerical model (n_0) is determined in a second step to ensure that the ratio r (Equation 3.7) matches both numerically and experimentally in drained triaxial compression tests on dense sand.

- Finally, a constant contact friction coefficient (μ) is calibrated to accurately reproduce the peak shear strength observed in the drained triaxial compression tests on dense sand. It is important to note that the choice of μ can impact the value of r, and therefore, it may be necessary to iterate the last two steps (selection of n_0 and calibration of μ) to refine the calibration process and improve the accuracy of the model.

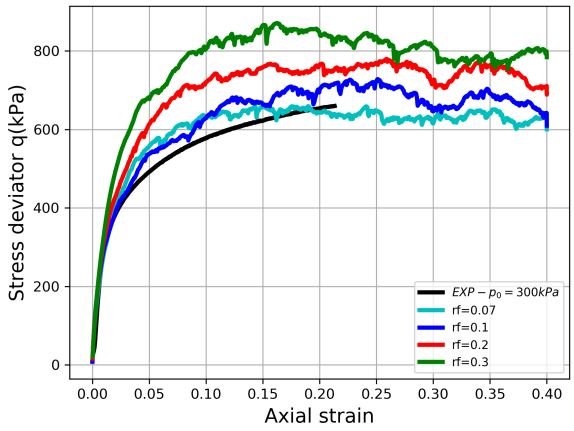

(A)

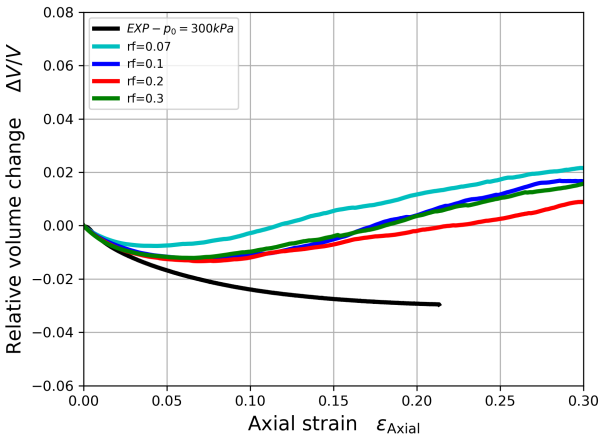

(B)

FIGURE 3.10: Clump C1 model: (a) The variation of the critical shear strength with respect to rolling friction coefficient at contact friction angle equal to 19° i.e. $\mu = 0.344$ (b) The volumetric deformation

3.4.2 Calibrated models

The calibration methodology has been applied to calibrate the parameters from the two experimental drained triaxial compression. For the three models, the particle size distribution of the numerical assemblies is almost identical to that of the Hostun sand. The identified parameters of the models are given in (Table 3.2) and simulated calibration paths are presented in Figure 3.11. By calibrating the ratio r, we are able to obtain numerical relative volumetric changes close to the experimental ones.

Note from Figure 3.11c that the numerical porosities (both initially and at the critical state) differ from the porosities measured on the sand samples. The microstructures of the numerical granular assemblies do not replicate the exact characteristics of the sand samples, including differences in grain shapes. Therefore, it is not expected for the porosities to be identical between the experiments and numerical simulations. However, the model is designed to reproduce the ability of the soil to dilate.

Finally, it is worth mentioning that the porosities of the experimental loose and dense sand samples at the critical state can vary. This discrepancy arises because, in experimental measurements, the global porosity is determined without taking into account the presence of shear bands in dense samples (Zhu et al., 2016). This is in contrast to the numerical simulations, where the porosities at the critical state remain the same for both initially loose and dense samples as no meaningful strain localization occurs.

TABLE 3.2: Parameters of the discrete numerical models identified from the calibration on dense and loose Hostun sand RF. D represents the distance between the centres of the spheres of radius R composing the 3x2 clumps (see Figure 3.9).

Model	n_0 *loose*	n_0 *dense*	$E_C(MPa)$	α_t	α_r	μ	η_r	D
Sphere	0.419	0.357	500	0.5	3	0.384	0.25	-
C1	0.467	0.407	500	0.5	3	0.767	0.07	-
3x2	0.387	0.322	500	0.5	3	0.754	-	0.7xR

3.4.3 Validation of the models for initially dense Hostun sand ($D_R \approx 1.0$)

Drained triaxial compressions for different confining pressures

The experimental results of drained triaxial compressions on dense sand used for validation are shown in Figure 3.12 and compared with the responses simulated with the model, for two confining pressures (p_0 = 200, 500 kPa). The initial porosity of each model (different shapes) identified to match the relative volumetric strain observed experimentally (ratio r) is n_0 = 0.357, 0.407, and 0.322 (Table 3.2) for sphere, clump C1, and Clump 3x2 respectively.

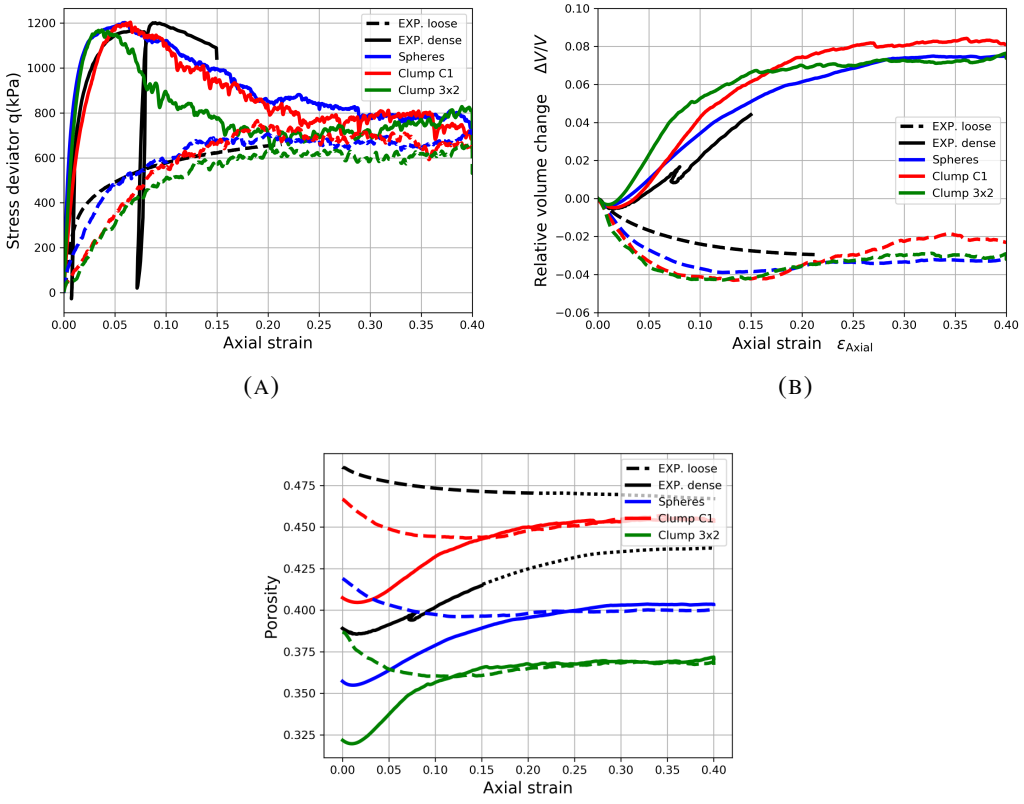

FIGURE 3.11: Calibration of the discrete element models made of particles with different shapes and based on drained triaxial compressions on dense and loose Hostun sand.

We observe an overestimation of the peak strength at 500 kPa and underestimatation at lower confining pressure 200 kPa.

Cyclic compression/extension loading path

This path involves subjecting the sample to cyclic axisymmetric ($\sigma_2 = \sigma_3$) compression/extension loading with a constant mean pressure. The mean pressure is set to 200 kPa, and the cycles are performed by controlling the axial strain ε_1. Each cycle has a strain amplitude of $\Delta\varepsilon_1 = 3.8\%$, except for the first cycle which has a larger amplitude. Therefore, the response parameter of interest is σ_1, which represents the axial stress.

The numerical response of the model, using the calibrated parameters obtained in the previous section, is compared to the experimental test conducted by (Zitouni, 1988) (Figure 3.13). The numerical results closely match the experimental data for the different particle shapes considered. However, the sphere model provides a more accurate quantitative prediction, particularly in terms of accurately capturing the volumetric deformation and estimating the overall stiffness throughout the cyclic loading. It is worth noting that conventional elasto-plastic constitutive models typically

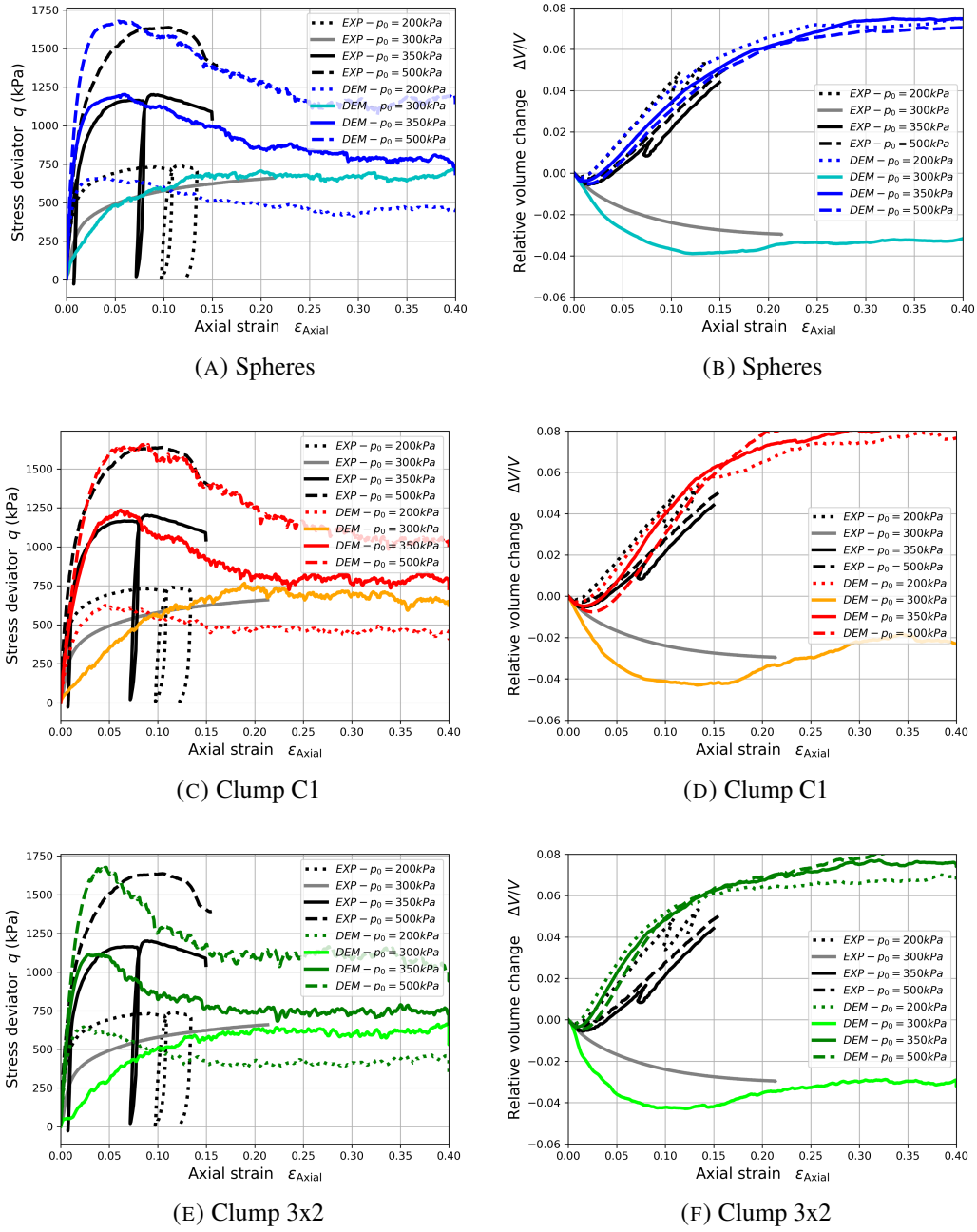

(A) Spheres

(B) Spheres

(C) Clump C1

(D) Clump C1

(E) Clump 3x2

(F) Clump 3x2

FIGURE 3.12: Validation of the discrete element models with constant contact friction coefficient on drained triaxial compressions p_0 = 200, 350 and 500 kPa on dense and loose Hostun sand at different confining pressures.

require additional historical parameters (usually calibrated based on cyclic tests) to accurately capture the soil response in such tests.

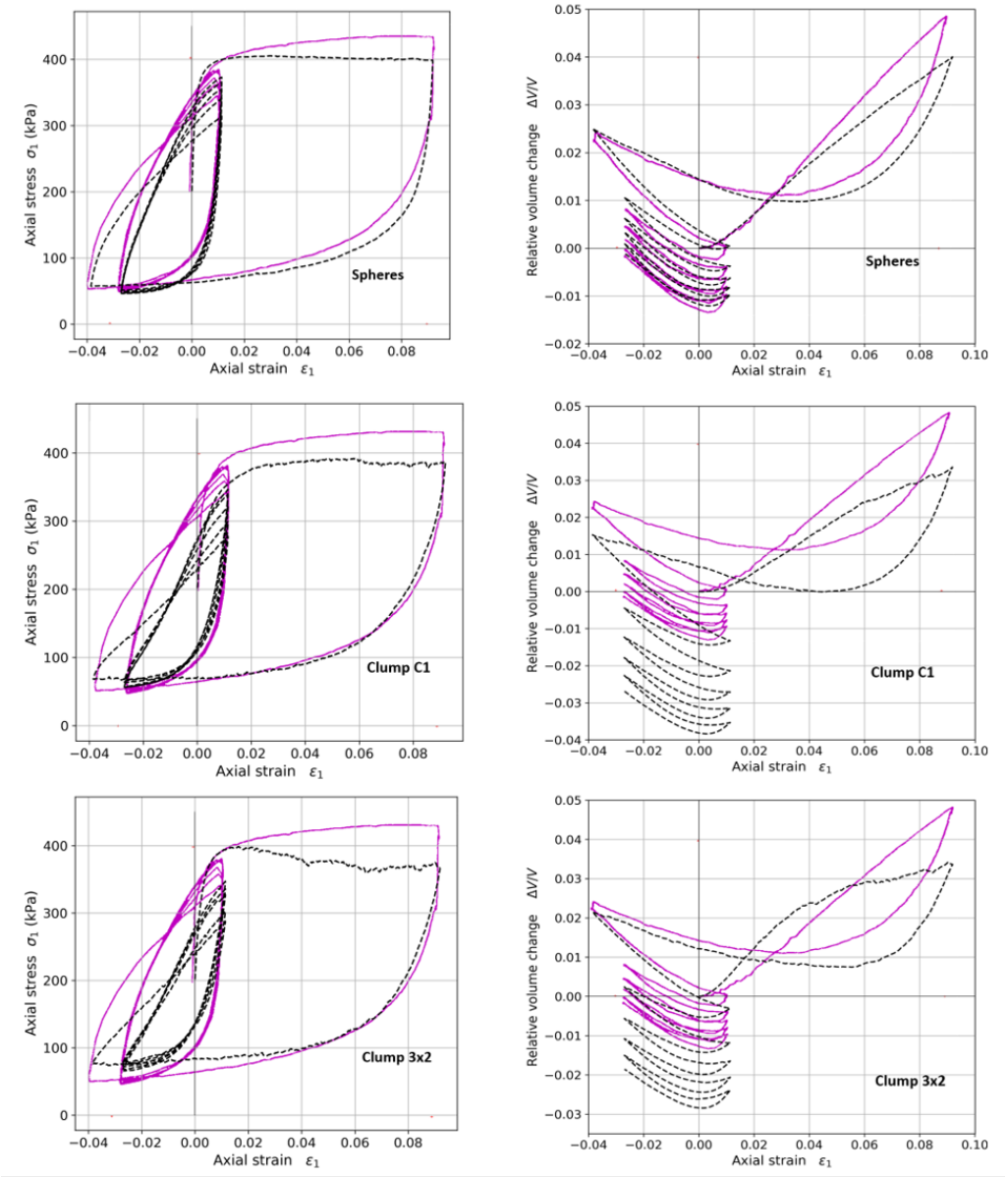

FIGURE 3.13: Validation on cyclic compression/extension paths with constant mean pressure on dense Hostun sand: experimental results are plotted with the continuous magenta lines and simulated responses are represented with the dashed black lines.

Circular stress loading path

The calibrated models are also validated on a circular loading stress path in the deviatoric stress plane, where the Lode angle φ_σ is continuously changed while maintaining constant the mean pressure and the deviatoric stress (Saada and Bianchini, 1988a). The Lode angle is defined in relation to the axis s_1, which represents the projection of the σ_1 axis on the deviatoric plane.

The intensity of the stress deviator is defined by the second stress invariant, which is given by:

$$I_{2\sigma} = \sqrt{\mathrm{tr}\left(\mathbf{s}^2\right)} \tag{3.8}$$

Where **s** is the deviatoric stress tensor.
The initial stage of the circular loading stress path involves isotropic compression of the soil sample to a mean pressure of p_c = 500 kPa. Following that, a compression is applied in the direction 3 (with $\varphi_\sigma = -120^o$) while maintaining a constant mean pressure of $p = p_c$, until the stress deviator intensity $I_{2\sigma}$ reaches a value of 420 kPa. Subsequently, the circular loading path is executed, which consists of two revolutions in the deviatoric stress plane. During this path, the Lode angle φ_σ is continuously changed between $-120°$ and $+600°$.

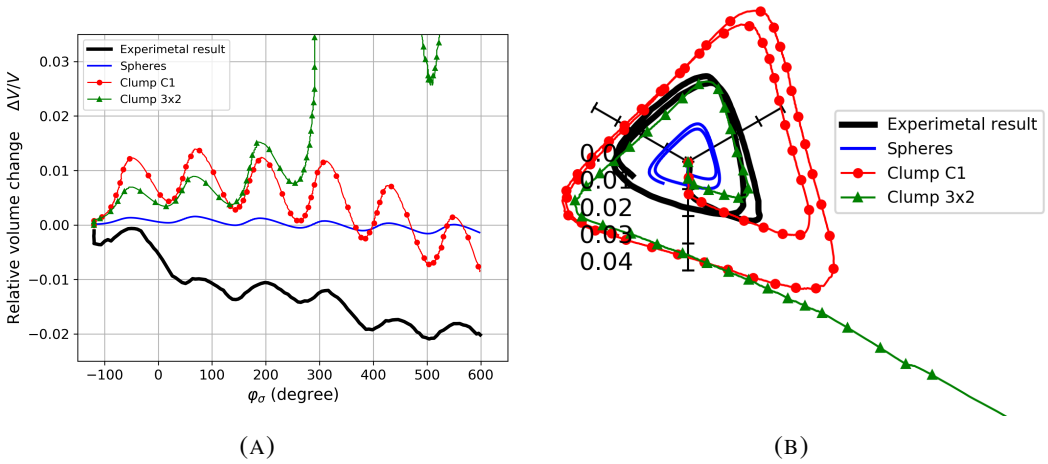

(A) (B)

FIGURE 3.14: Validation from a circular stress loading path on dense Hostun sand: the relative volume change is represented in terms of the Lode angle (top), the strain response path is projected on the deviatoric strain plane (bottom).

The responses simulated with the numerical models are compared with the experimental one obtained by Lanier and Zitouni (1988) in Figure 3.14. All models underestimate the contractancy observed experimentally, however the sphere and C1 models give a global trend of the volumetric deformations in agreement with the experimental data. The 3x2 model diverges from the experimental data by describing a strong dilation of the numerical sample leading to its failure. Finally, the sphere model underestimates the deviatoric deformations, whereas the C1 model overestimates them, but both models produce a response which is qualitatively realistic.

3.4.4 Validation of the models for initially loose Hostun sand ($D_R \approx 0.1$)

Isochoric compression

The responses simulated with the calibrated models to isochoric triaxial compressions for the loose initial state are compared to experimental data from an axisymmetric undrained compression test on loose and water-saturated sand performed by Benahmed (2001). In the experiment, the isochoric condition is achieved by preventing drainage of the pore water. In the numerical simulations, the isochoric condition is directly imposed by controlling the radial strains while compressing the sample in the axial direction. This ensures that the volumetric strain ε_V is zero, i.e.,

$\varepsilon_2 = \varepsilon_3 = \varepsilon_1/2$, where '1' is the axial direction, such that $\varepsilon_V = \varepsilon_1 + \varepsilon_2 + \varepsilon_3 = 0$. The experimental results and simulated responses are shown in Figure 3.15.

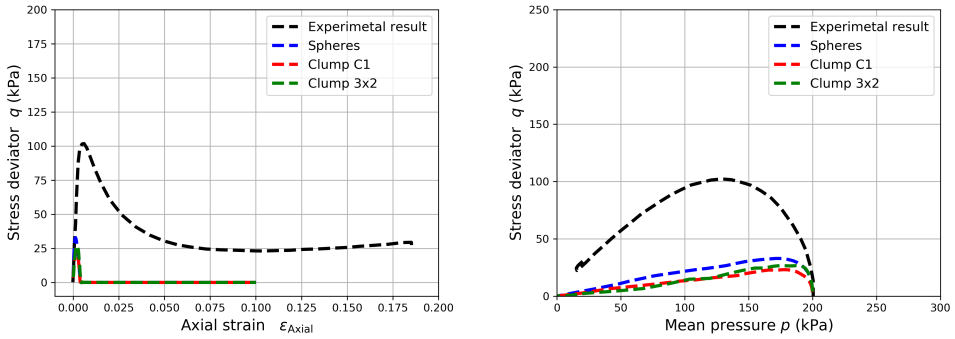

(A) (B)

FIGURE 3.15: Validation on undrained axisymmetric compressions on loose Hostun sand, comparison with experimental test with p_c = 200 kPa .

The comparison between the numerical models and the experimental data reveals that all three models are unable to accurately predict the observed experimental response. In the numerical simulations, a complete liquefaction is observed at low axial strain and the models fail to capture the peak stress deviator (q-peak) observed in the experiments. The numerical models provide unrealistic predictions of the stress deviator peak, significantly underestimating its value compared to the experimental measurement, where failure occurs at approximately $q_{\max} \approx 100$ kPa. It is worth noting that this distinction between the numerical and experimental results was not observed in the drained compression tests, as shown in Figure 3.11. Furthermore, experimentally the liquefaction occurred at a larger deformation of the samples.

q-constant path

In the constant stress deviator loading path, the stress deviator q is maintained constant while the mean pressure p is decreased, following a stress state obtained from a preliminary drained compression. We consider an experimental test performed by Daouadji et al. (2011) as a reference for this loading path. In the experiment, the initial confinement pressure was set at p_c = 300 kPa, and the stress deviator q reached a value of 119 kPa after the initial drained compression phase. It is another loading path (as for the isochoric loading path) where the range of variation in mean pressure is significant. Experimental observations show that failure occurs when the mean pressure reaches a value slightly below 150 kPa (Figure 3.16c), where the stress path intersects the Mohr-Coulomb limit surface. It is important to note that loose sand samples have the characteristic of dilating during such a constant stress deviator path. This is what is happening experimentally with the positive relative volume change observed from an axial strain slightly below 0.5% (Figure 3.16b). The preceding contractive response, resulting in a relative volume change of approximately -0.3%, corresponds to the initial drained compression of the sample.

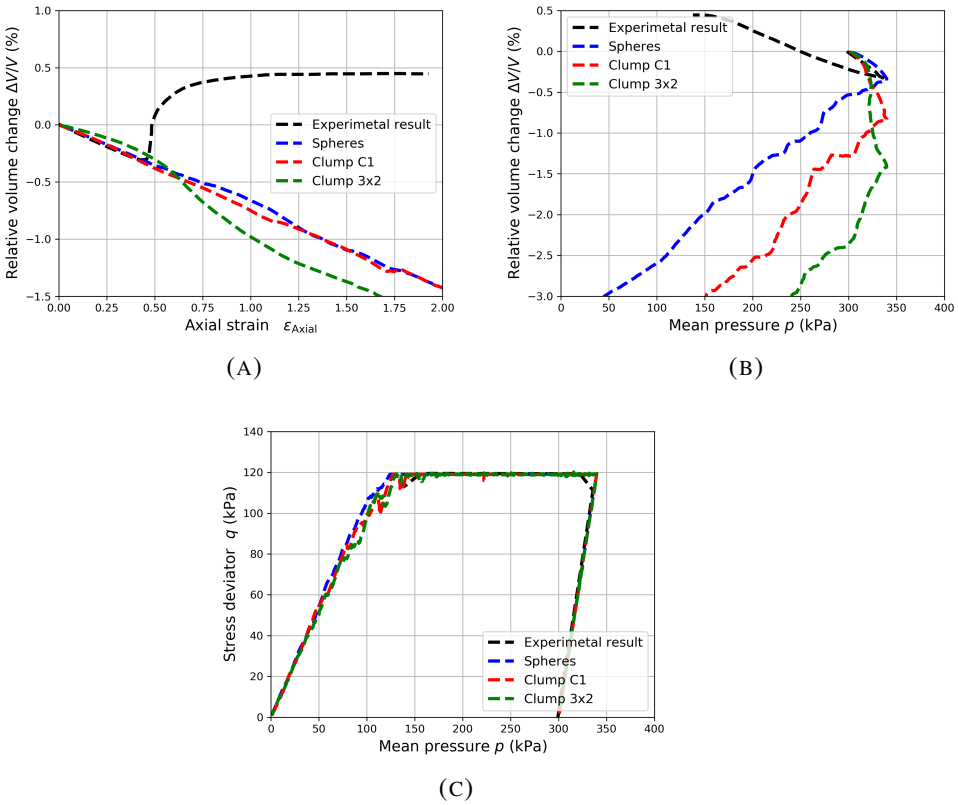

FIGURE 3.16: Validation on constant stress deviator loading paths on loose Hostun sand, comparison with experimental test with q = 119 kPa.

The comparison between the numerical and experimental responses is shown in Figure 3.16. The models reproduce correctly the initial drained compression. However, they behave opposite to the sand response along the q-constant path. The models present a contraction of the granular assemblies whereas a dilation is observed experimentally. However the failure stress state in the q-p plane is rather well predicted by the models (Figure 3.16c).

3.4.5 Summary

In this section, we investigated two options to improve upon the simplistic shape of spheres: implementing rolling friction or using non-spherical shapes (but still simple ones). We also considered a third option, which involved combining both approaches. In terms of calibration quality, all the models provided similar results, with the sphere model showing slightly better agreement. In terms of computational cost, the sphere model was the least demanding, while the 3x2 model was the most computationally expensive. However, the calibration process complexity was comparable for all the models.

The models were validated using two different initial density states. When validated against a dense initial state, the sphere model exhibited better agreement with experimental data compared to the other models, although it did not fully capture

the behavior observed in the circular stress loading path. However, when validated against loose initial states, all the models failed to accurately predict the experimental data. This could be related to the impact of the significant decrease of the mean pressure along the considered loading paths on the constitutive soil response which is not correctly taken into account in the model formulations.

Despite the limitations of the models, the sphere model with rolling resistance offered a good compromise between computational cost and predictive ability compared to the other models tested. It demonstrated better performance in terms of prediction capability with lower computation cost. Considering the significant changes in mean pressure along the loading paths, which impact the constitutive response of the soil, the next section aims to take into account the effect of the mean pressure (or the normal contact stress) on the contact friction in relation with the particle roughness (Mollon et al., 2020). This could be achieved by introducing a contact friction angle that varies as a function of the normal contact stress, thus improving the models' ability to capture the behavior along loading paths with important changes in mean pressure.

3.5 Calibration/validation of isotropic models with non-constant friction coefficient

The calibration of models with non-constant contact friction coefficient is presented here. In addition to the two drained triaxial compressions (dense state with $p_0 = 350$ kPa and loose state with with $p_0 = 300$ kPa) used in the previous part, another drained triaxial compressions at different confining pressure are needed to calibrate the non-constant contact friction parameters 3.3. Thus, Contact mechanical parameters are calibrated from three drained triaxial compressions on dense Hostun sand ($D_r \approx 1.0$) at different confining pressures (p_0 = 200; 350; 500 kPa).

3.5.1 Calibration Methodology

The calibration of models follows the methodology defined in (Sibille, Benahmed, and Darve, 2021). The first steps are similar to those followed to calibrate the models with constant contact friction angles in previous section 3.4. In addition, in this case where a non-constant contact friction coefficient is considered (Eq. 3.3) an additional step consists in substituting the calibrated constant friction coefficient by the non constant one and thus identifying μ_{min} and μ_{max} in order to match the change of the peak shear strength with the confining pressure for the three drained triaxial compressions on dense sand samples. It may be necessary to reiterate this step (with different values of μ_{min} and μ_{max}) to improve the calibration.
Figure 3.17 present the variation of the contact friction coefficient with the normal contact stress for parameters calibrated for the spherical model. (μ_{min} = 0.32 and μ_{max} = 0.76).

Parameters of the non-constant friction coefficient law calibrated on the Hostun sand are given in Table 3.3. All the other parameters, including the initial porosities of the numerical assemblies are kept unchanged, as given in Table 3.2.

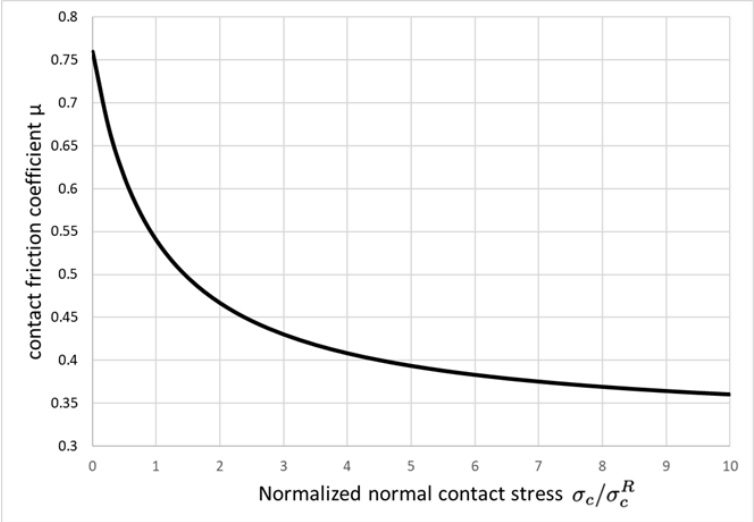

FIGURE 3.17: Dependence of the contact friction coefficient on the normal contact stress for μ_{min} = 0.32 and μ_{max} = 0.76

TABLE 3.3: Contact mechanical parameters of the discrete numerical model calibrated from Hostun sand HN31.

	μ_{min}	μ_{max}
Sphere	0.320	0.760
Clump C1	0.55	2.05
Clump 3x2	0.55	2.3

The use of a non-constant contact friction coefficient has a reduced impact only on the simulation of the drained triaxial compressions. It leads essentially to a better description of the peaks of the stress deviator q for the dense sand for the different confining pressures (Figure 3.18). For instance, the peak of q is overestimated for $p_0 = 500$ kPa for the model with a constant friction coefficient which is no more the case with the non-constant friction at the contact. For the loose sand, there is no clear difference in the simulated responses with or without non-constant contact friction (Figure 3.18).

3.5.2 Validation of the models

Cyclic compression/extension loading path

The numerical response is compared to the experimental test carried out by (Zitouni, 1988) (Figure 3.19). Predictions of the calibrated models after adding non-constant contact friction to the contact law where slightly improved in the cases of the compression/extension loading path with respect to the complexity added.

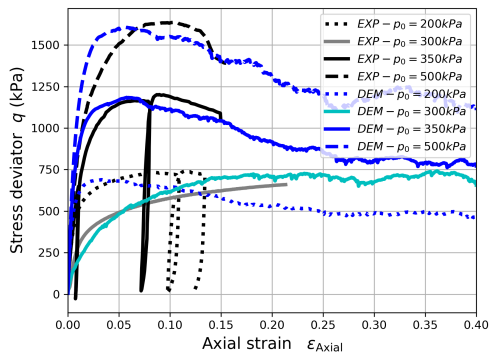

(A) Spheres

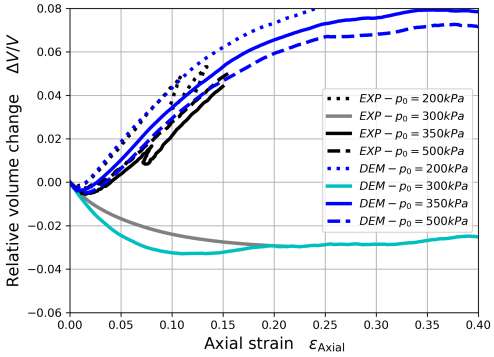

(B) Spheres

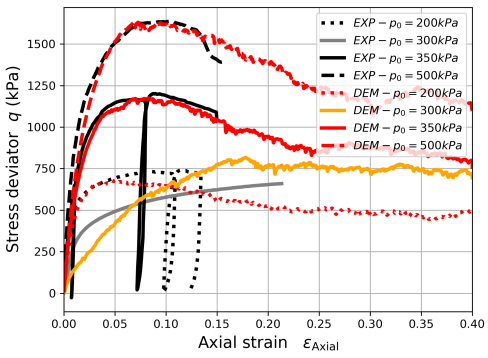

(C) Clump C1

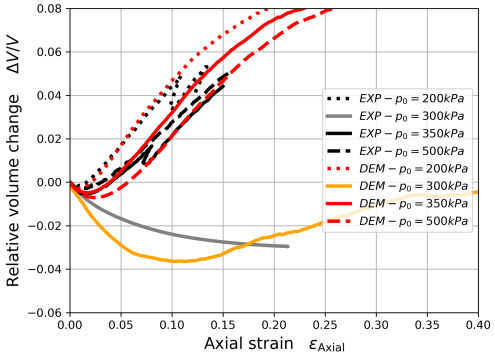

(D) Clump C1

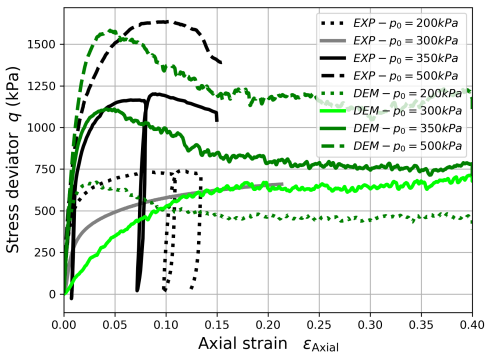

(E) Clump 3x2

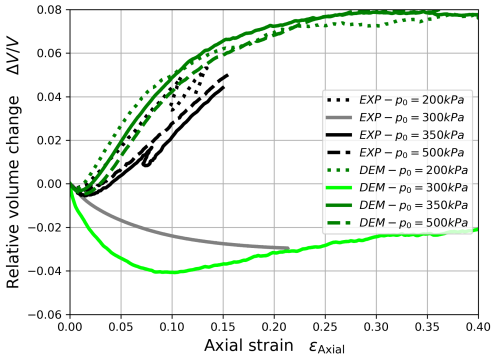

(F) Clump 3x2

FIGURE 3.18: Validation of the discrete element models with non-constant contact friction coefficient on drained triaxial compressions p_0 = 200, 350 and 500 kPa on dense and loose Hostun sand at different confining pressures.

Circular stress loading path

The models are also validated on the circular loading stress path in the deviatoric stress plane. The numerical models response is compared to the experimental one obtained by Lanier and Zitouni (1988) in Figure 3.20. Similarly to the response in the case of cyclic compression/extension, the response of the calibrated models after adding non-constant contact friction to the contact law where slightly improved in

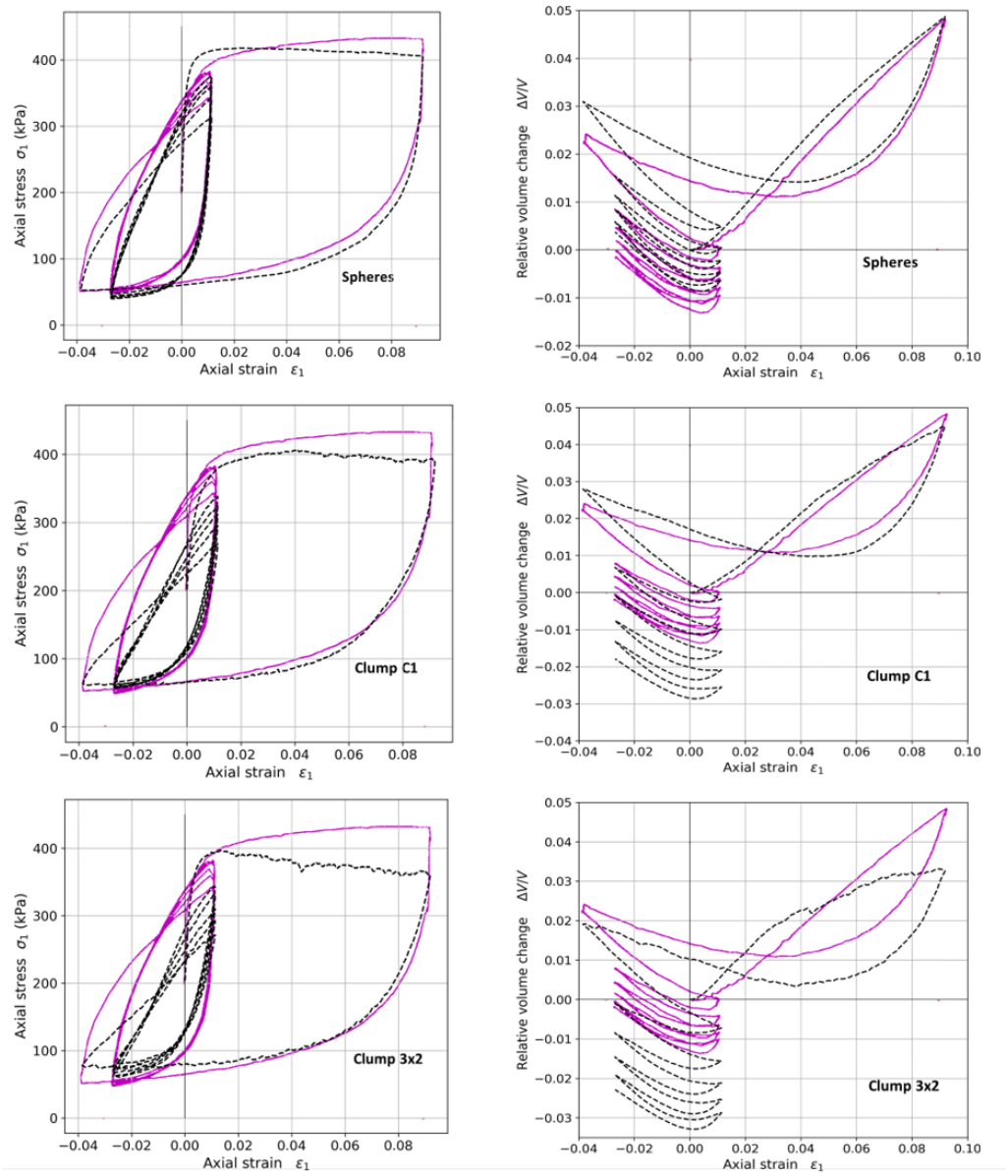

FIGURE 3.19: Validation on cyclic compression/extension paths with constant mean pressure on dense Hostun sand: experimental results are plotted with the continuous magenta lines and simulated responses are represented with the dashed black lines.

the cases of circular loading path with respect to the complexity added. In case of model C1, the deviatoric deformation and volumetric deformation improves quantitatively and qualitatively whereas the 3x2 model still diverges from the experimental measurements..

Isochoric compression

The experimental results and simulated responses of the different models are shown in Figure 3.21. Again, the consideration of non-constant contact friction contributes

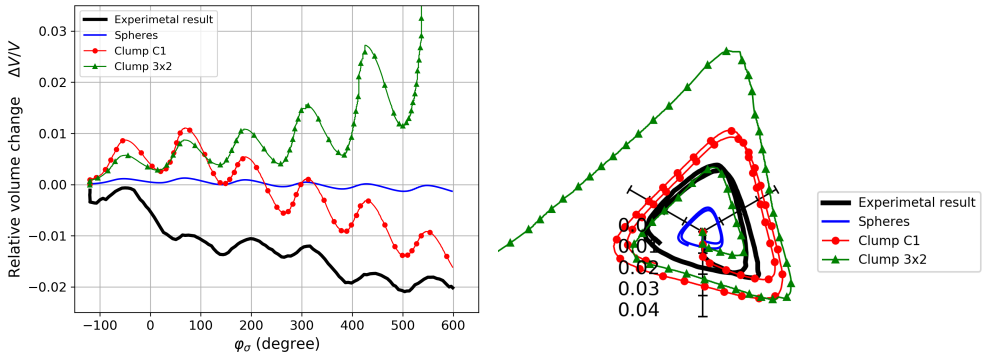

(A) (B)

FIGURE 3.20: Validation from a circular stress loading path on dense Hostun sand: the relative volume change is represented in terms of the Lode angle (left), the strain response path is projected on the deviatoric strain plane (right).

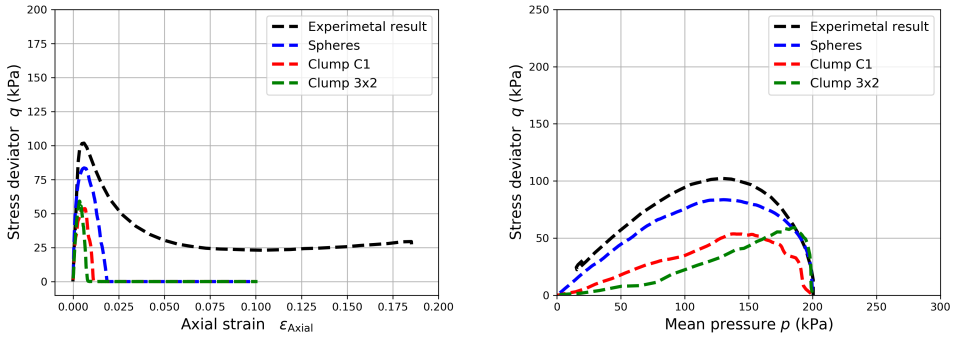

(A) (B)

FIGURE 3.21: Validation on undrained axisymmetric compressions on loose Hostun sand, comparison with experimental test with p_c = 200 kPa .

to delay the liquefaction in terms of axial strain (up to $\approx 2\%$), but still is not enough to simulate the realistic behaviour of loose Hostun sand. However the predicted stress deviator peak is now realistic with respect to the experimental measurement, in particular for the sphere model.

q-constant path

The comparison between the numerical and experimental responses is shown in Figure 3.22. The models reproduce correctly the initial drained compression. The description of the response to the q constant path still need be improved, always, in particular, concerning the dilatative volumetric response. However, we observe a slight improvement with respect to the models with constant contact friction where a small dilation is observed as the constant deviator part start, but then behaves opposite to the experiment as the numerical samples start again to contract.

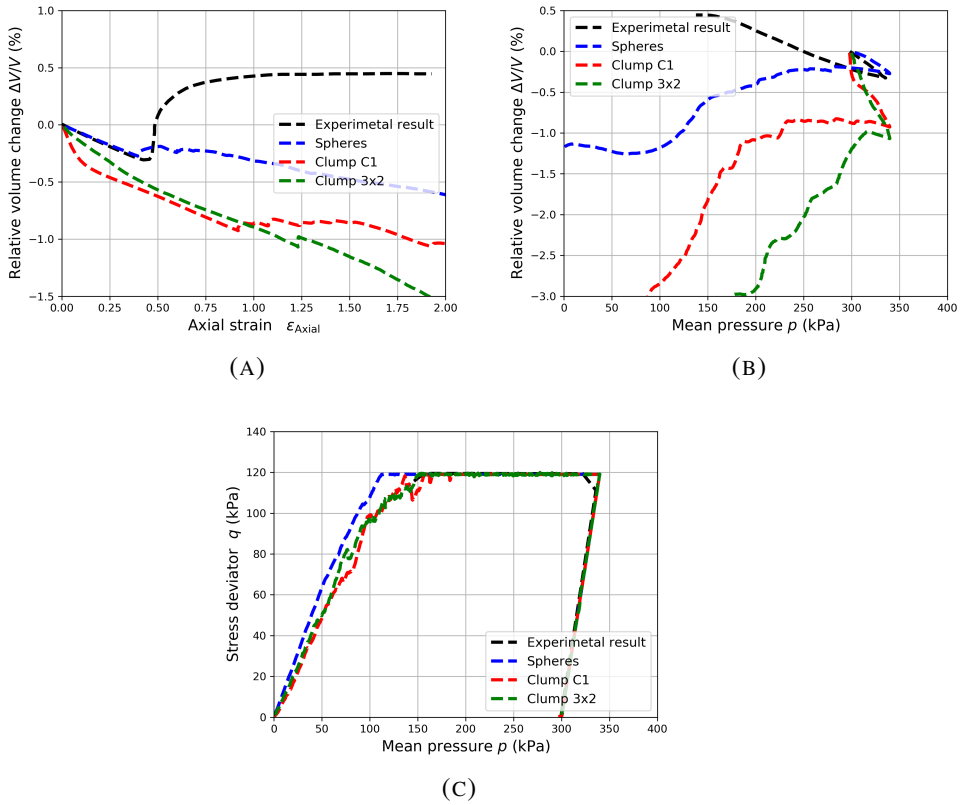

FIGURE 3.22: Validation on constant stress deviator loading paths on loose Hostun sand, comparison with experimental test with q = 119 kPa.

3.5.3 Summary

In this section to improve the prediction ability of the models, we took into account that the roughness at particle surfaces may result in different friction coefficients when the stress normal to the contact varies importantly, and in particular for very low normal contact stresses. This has been done by implementing a contact friction angle as a function of the normal contact stress.

The response of the models were only slightly improved in the case of the dense sand (cyclic compression/extension and circular loading paths) compared to the additional cost of calibrating a more complex contact model requiring additional drained compressions. In the case of the loose sand, we observe for the constant stress deviator loading path a slight improvement of the models concerning the predicted volumetric response but still not enough as the model behave opposite to the experiment when the constant stress deviator loading is pursued.

For the undrained loading path on loose sand we can see the clear improvement in the description of the peak of the stress deviator, especially for the spheres model which is much more realistic than the model with constant contact friction. However, we still observe a complete liquefaction at low axial strain with respect to the experiment.

In reality, the initial fabric is not perfectly isotropic in the case of the loose sand samples since the particles or contacts are problably oriented preferentially along a

particular direction due to their anisotropic shape and the mode of preparation (moist tamping), thus it is important to check the effect of the initial fabric anisotropy of the numerical models in the next section. Since the models with clumps 3x2 and C1 (plus rolling resistance) do not offert a better prediction ability at the macroscopic scale than the model with spheres (plus rolling resistance), only spherical particles are chosen for the investigation of fabric anisotropy due to their simplicity.
Finally, this investigation will focus essentially on the description of the loose Hostun sand because it was shown experimentally that the dense Hostun sand samples were rather isotropic and also because the worst prediction of the discrete model concerns the sand in its initial loose state.

3.6 Role of initial fabric and non-constant friction coefficient in the case of the loose sand

In the case of the loose sample, we specifically examine in this section the impact of the slight anisotropy observed in the experimental loose sand samples. In this objective, we apply anisotropic compaction to generate fabrics (i.e. distribution of contact orientations) with anisotropic characteristics.

3.6.1 Initial state generation of anisotropic models

To generate anisotropic granular assemblies, we simulated an oedometric compression process on the initial collection of non-contacting spheres generated randomly. The goal was to achieve a cubical shape for the granular assembly after the compression. To achieve this, the initial collection of particles occupied a parallelepipedic volume with a slenderness ratio (height to width ratio) of $7/3$. The oedometric compression was applied to this initial configuration until the slenderness ratio reached 1, resulting in a cubical shape for the assembly.
Following the oedometric compression, a stress-controlled isotropic compression was applied to the assembly to reach an initial isotropic stress state, but with an anisotropic contact fabric due to the previous oedometric compression. This isotropic stress state served as the starting point for the various loading paths simulated in this study.
The initial porosity, n_0, is controlled by tuning the contact friction coefficient during the oedometric compression and the subsequent stress controlled isotropic compression. In addition, adhesion is considered during the oedometric and isotropic compressions and removed afterward as proposed by Aboul Hosn et al. (2017).

3.6.2 Anisotropic calibrated models

Concerning the initial loose state, we present in Figure 3.23 a comparison between the experimental response to the drained triaxial compression under confining pressure of $p_0 = 300$kPa and the constitutive responses simulated from two different initial states obtained after either the isotropic compaction or the anisotropic one, and with constant or non-constant contact friction coefficient. The initial porosity is similar in both cases and about 0.42, as shown in Table3.4.

The implementation of an anisotropic compaction mode for the loose sample has a

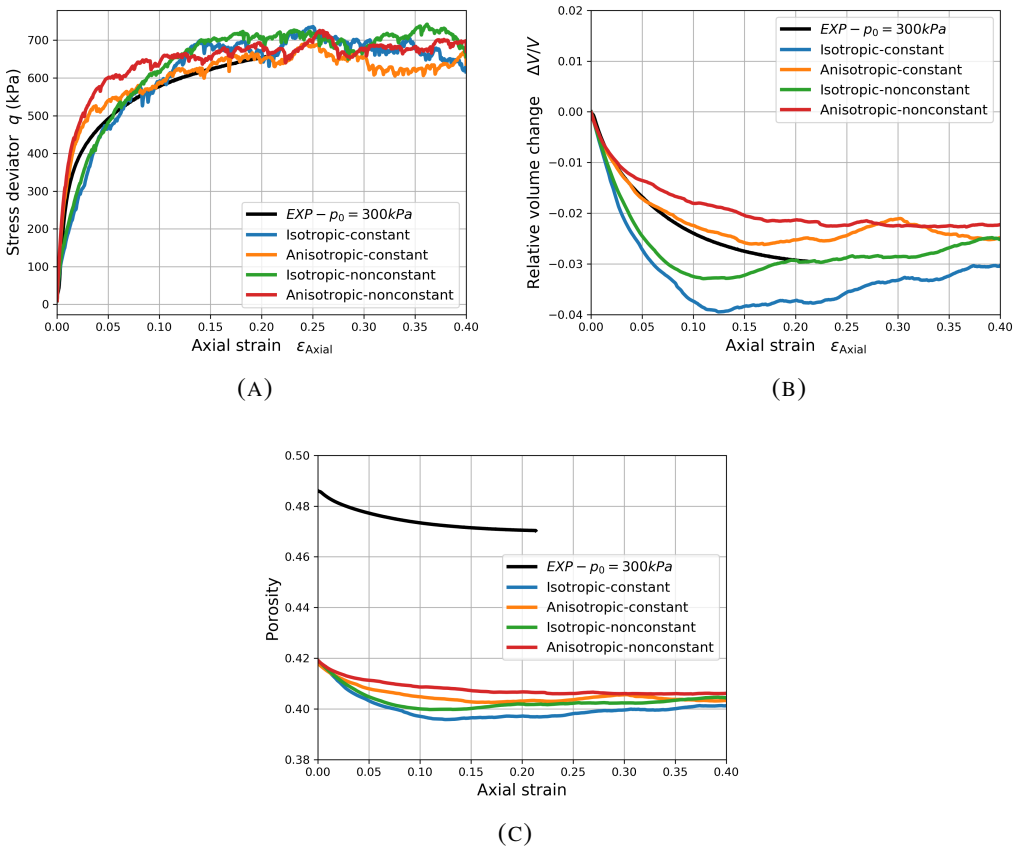

FIGURE 3.23: The discrete element models during a drained compression on loose sand of the 4 different cases.

limited impact on the overall response compared to the isotropic compaction mode. However, there are some remarkable differences. Samples with an initial anisotropy exhibit a stronger stiffness in the hardening regime, which is closer to the stiffness observed experimentally (Figure 3.23A). Additionally, anisotropic samples display a contractive behavior even for large deformations, whereas isotropic samples show a slight dilation after an axial strain of approximately 0.13, contrary to the experimental measurements. These differences indicate that the anisotropic compaction mode captures certain aspects of the experimental behavior more accurately, particularly in terms of stiffness and contractive response.

Although the benefits of using a non-constant contact friction coefficient and anisotropic compaction may be limited when considering drained triaxial compressions, their significance becomes more apparent when applied to other types of loading paths, as discussed in the subsequent sections. These modeling approaches have the potential to improve the simulation of various loading conditions and capture more accurately the behavior of granular assemblies under different stress states. Therefore, while their impact on drained triaxial compressions may be relatively small, their relevance and effectiveness in capturing the complex behavior of granular materials are discussed further in the following sections.

3.6.3 Characterisation of initial states

We provide in this section a characterization of the three initial states considered in this study: dense compaction (isotropic), loose compaction (isotropic), and loose compaction (anisotropic). The characterization focuses on three specific properties: coordination number, particle connectivity in the distribution of contact orientations, and estimation of the pore size distribution.
The particle connectivity is quantified using the mechanical coordination number Z^* as defined in Thornton et al. (Thornton, 2000). It considers only particles that are involved in more than one contact. It is defined by the equation:

$$Z^* = \frac{2N_c - N_1}{N_p - N_0 - N_1} \tag{3.9}$$

Where N_c represents the total number of contacts, N_p is the total number of particles, N_1 denotes the number of particles involved in a single contact, and N_0 represents the number of particles without any contact. The values of Z^* for the three initial states are presented in Table 3.4. It can be observed that the coordination numbers for the loose initial states, whether compacted isotropically or anisotropically, are nearly identical. However, the coordination number is higher for the initial dense state.
The anisotropy of the contact fabric in the granular assemblies is analyzed based on the distribution of the orientations of the unit normal vectors to the contacts. The distributions for the initial loose states are plotted in Figure 3.25 for the three planes: 'X-Y', 'Y-Z' and 'Z-X'. Here, the direction 'Z' corresponds to the compression direction for both the anisotropic compaction mode and the triaxial compressions used in calibrating the model. The distributions indicate a slight anisotropy in the samples compacted anisotropically, with slightly more contacts aligned in the axial ('Z') directions.

The degree of anisotropy can be quantified using an approximation of the probability distribution function $P(x)$, where the variable x represents $|\cos\alpha|$ and α is the angle formed by the contact normal with respect to the axial direction 'Z'. When $\alpha = 0$ or 1, the contact is parallel to the axial direction, while for $\alpha = \pi/2$, the contact is orthogonal to the axial direction. Previous studies (Azéma, Radjai, and Saussine, 2009; Imole et al., 2014) have shown that $P(x)$ can be adequately approximated using a Legendre polynomial based on spherical harmonics. This approximation takes into account the symmetries of the problem and is limited to the 4th order. The expression for the approximation is given by:

$$P(x) = 1 + a_2(3x^2 - 1) + a_4(35x^4 - 30x^2 + 3) \tag{3.10}$$

The coefficient a_2 provides a measure of the anisotropy along the axial direction. It is defined as follows:

$$a_2 = \frac{15}{4}(< x^2 > - \frac{1}{3}) \tag{3.11}$$

Where the value $< x^2 >$ represents the mean of x^2, which corresponds to the second moment of the probability distribution $P(x)$. For an isotropic state, $< x^2 >= \frac{1}{3}$ and $a_2 = 0$. Thus, a lower value value of $|a_2|$ indicates a more homogeneous distribution of contact orientations and a more isotropy in the contact fabric. The Legendre

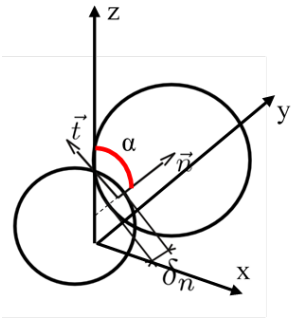

FIGURE 3.24: The contact normal inclination with respect to the axial direction of compression

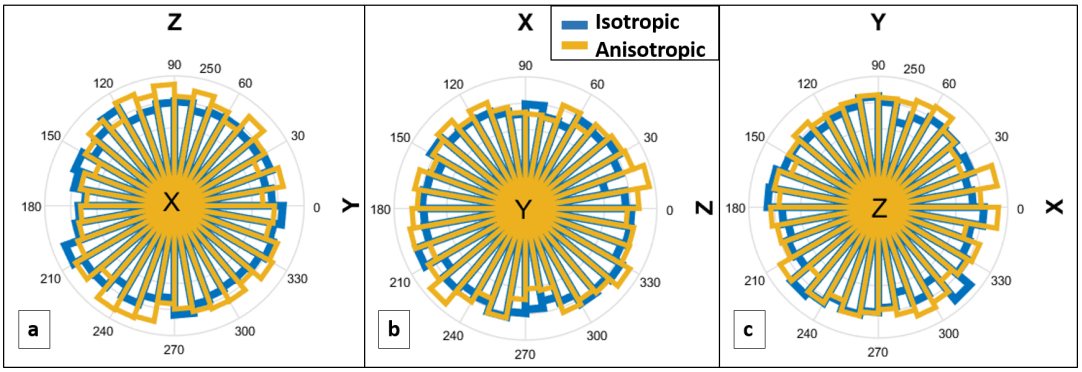

FIGURE 3.25: The contact oritentaions with respect to the three axis x,y and z

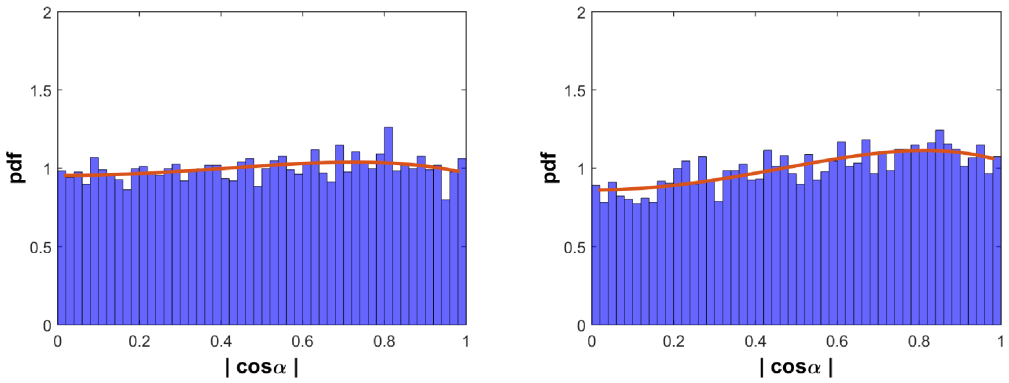

(A) (B)

FIGURE 3.26: Probability density function and approximation by Legendre polynomial of the initial orientation of contacts with respect to the direction of compression 'Z' for the loose isotropic (a) and anisotropic (b) samples; |cosα| varies from 0 to 1 for contacts orthogonal and parallel, respectively, to the direction 'Z'.

TABLE 3.4: Characteristics of the initial states of the numerical granular assemblies used to simulate Hostun sand constitutive responses.

Initial state	Compaction type	n_0	Z^*	Anisotropy a_2
Dense	Isotropic	0.357	5.4	0.0065
Loose	Isotropic	0.419	3.9	0.007
Loose	Anisotropic	0.418	3.8	0.025

polynomial approximations of the contact orientation distributions with respect to the axial direction (Figure 3.24) are shown in Figure 3.26 for the initially isotropic and anisotropic loose samples. The corresponding values of a_2 are presented in Table 3.4 for each initial state. The coefficient a_2 is very small (around 7×10^{-3}) for both the isotropically compacted dense and loose samples. In the case of the loose sample with anisotropic compaction, the value of a_2 is slightly higher at 0.025, although it is still relatively small. This indicates a low but noticeable anisotropy, which is consistent with the characteristics of the Hostun sand sample prepared by moist tamping, as observed in previous studies (Aris, Benahmed, and Bonelli, 2012) where shear wave velocities were measured in different directions.

Similarly to the impact of non-constant friction at contacts, the influence of the initial anisotropic fabric on the response to drained compression is relatively small compared to the response simulated from the isotropic fabric, as shown in Figure 3.23. The shear strength of the samples is not significantly affected by the initial fabric, and only the contractance (negative relative volume change) is slightly less important for the anisotropic initial state. In the case of the isotropic initial state, the samples shows higher contractance at low axial strain, but as the deformation progresses, they undergo a slight dilation.

As illustrated in Figure 3.23, the initial fabric anisotropy has a significant impact on the behavior of the models. Although the initial fabric anisotropy is low, it is nevertheless significant, as demonstrated by the validation of the model in the next section.

Identification of macropores

In Figure 3.27, we investigated the microstructure of Hostun sand numerical samples at varying initial states (dense, loose isotropic, and loose anisotropic). The goal was to identify "macropores" alongside smaller inter-particle spaces, as observed experimentally when moist tamping compaction is used (Benahmed, 2001). However, no specific different type of pores was detectable in loose samples compared to dense ones.

The distribution of "local" macro porosities in the samples was done using the voxel porosity function in YADE. The calculation method involves dividing the whole domain into a dense grid of voxels at a given resolution and counts voxels within

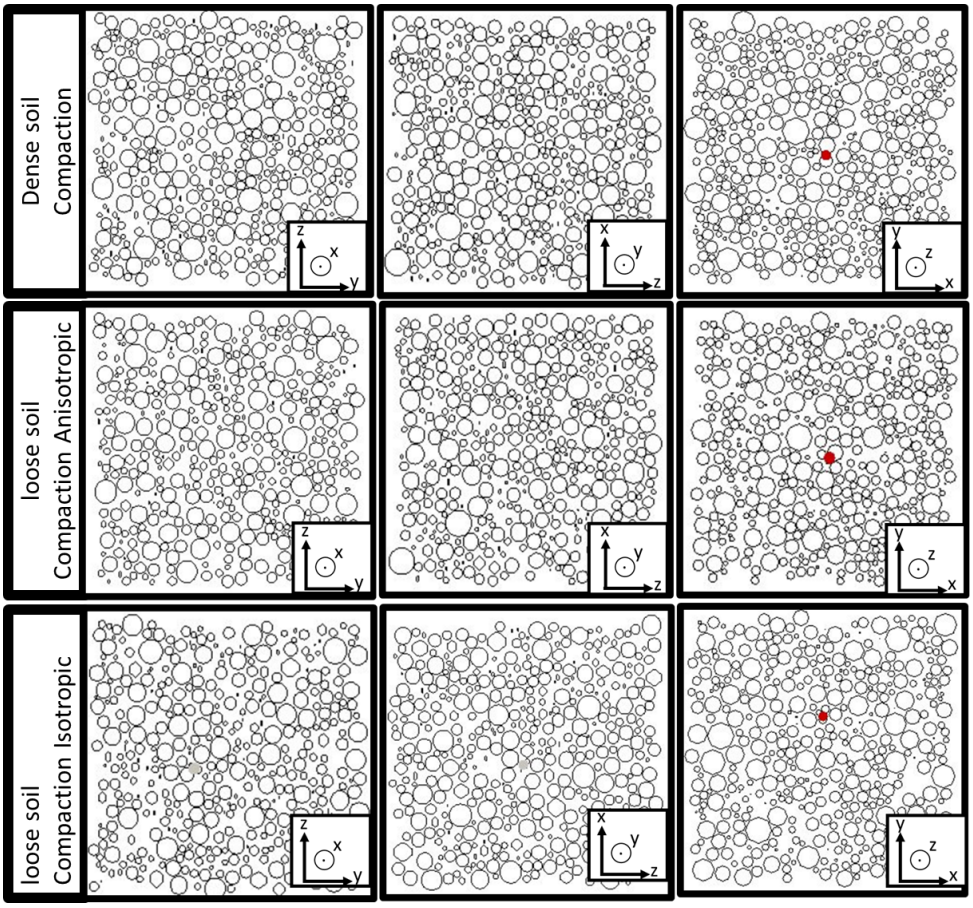

FIGURE 3.27: The microstructre of the dense, loose anisotropic and loose isotropic samples

spheres. This method allows precise porosity calculations within targeted sub-volumes and excluding parts of spheres that do not fall within the specified volume. By shifting the porosity distribution of the dense sample in order to align it with the mean porosity of the loose samples (Figure 3.28), the distributions were almost similar. This suggests that the pores in the loose samples are generally larger, which is expected due to their higher overall porosity. However, no significant macro-pores unique to the loose samples are found that were absent in the dense sample.

3.6.4 Validation on isochoric compression path

The constitutive responses of the calibrated model have been simulated for the anisotropic initial state described in Table 3.4, and compared to the responses obtained for the isotropic state for the two kind of contact friction coefficient are considered: constant and non-constant. This results in four different simulation cases: "isotropic-constant", "anisotropic-constant", "isotropic-nonconstant", and "anisotropic-nonconstant". The experimental results and simulated responses for these four cases are compared in Figure 3.29.

Firstly, in addition to the "isotropic-nonconstant" case, both anistropic cases provided a realistic predicted stress deviator peak. Then considering either an anisotropic initial state or a non-constant friction is enough to simulate a realistic shear strength.

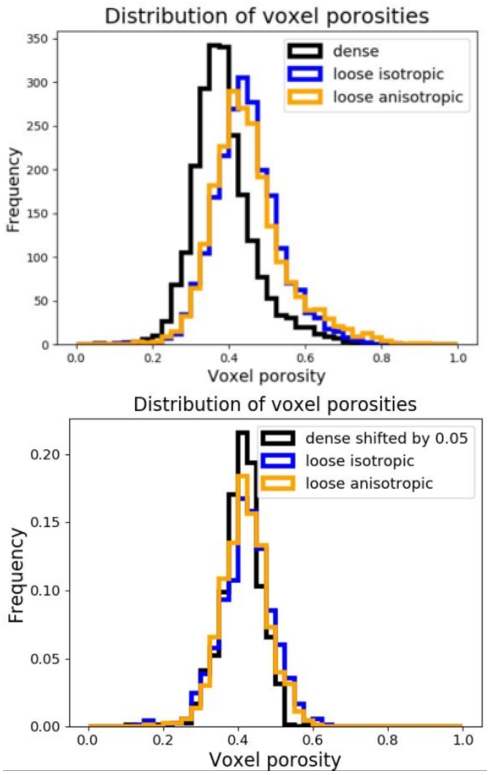

FIGURE 3.28: The distribution of porosity in samples of different initial states based on voxel porosities.

Moreover, the simulation case labeled as "anisotropic-nonconstant" exhibits a different behavior compared to the other cases in terms of the axial strain at which liquefaction occurs, which corresponds to the vanishing of effective stresses. In the experimental data, complete liquefaction is not observed, but instead a residual stress deviator of approximately 25 kPa is reached at around 7.5% axial strain.

By considering the initial anisotropic state with a constant contact friction coefficient, the liquefaction is delayed in terms of axial strain, up to approximately 1%, compared to the "isotropic-constant" case, which experiences liquefaction at around 0.5%.

Furthermore, when both the initial anisotropic state and non-constant friction coefficient are taken into account combined, liquefaction is further delayed. In this case, liquefaction occurs at an axial strain of approximately 12%. Although liquefaction still occurs at higher axial strains, this prediction is more consistent with the experimental reference. It is worth noting that a larger initial anisotropy may have completely prevented liquefaction.

It is important to highlight that achieving a more accurate reproduction of the experimental results is indeed possible by adjusting contact parameters specifically for the given initial density or by tuning the initial porosity of the numerical model. The simulated response is highly sensitive to the initial numerical porosity, especially for such low porosity values. However, such adjustments or tunings would contradict the fundamental purpose of a discrete numerical model, which aims to represent a soil with its inherent characteristics, including particle grading, shape, and roughness, regardless of its initial state. Ensuring that the model accurately represents the

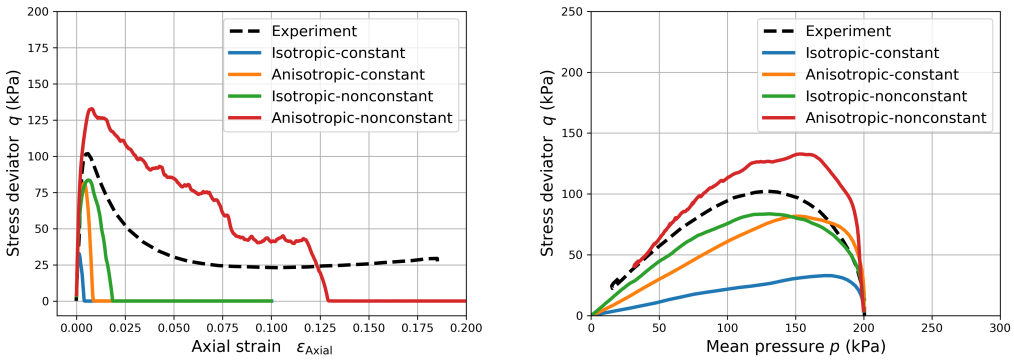

(A) (B)

FIGURE 3.29: Validation on undrained axisymmetric compressions on loose Hostun sand, comparison with experimental test with p_c = 200 kPa (sphere model).

soil's inherent properties under various loading conditions is essential to maintain the model's validity and usefulness.

The greater influence of the non-constant friction coefficient, which is dependent on the normal contact stress and hence the mean pressure, on the isochoric compression compared to the drained compression can be explained by the larger range of mean pressure p variation in the former case (from 200 kPa to 0) compared to the latter.

To provide an explanation for the observed results in Figure 3.29 and the differences between the four cases, a detailed micro-structural analysis is presented in further subsections. This analysis focuses on the fabric, including connectivity and anisotropy, as well as the mobilized friction at contacts, and the weak and strong contact networks. The analysis is carried out until the liquefaction of the samples in the isotropic-constant, anisotropic-constant, and isotropic-nonconstant cases, which occur at axial strains of 0.4%, 0.8%, and 1.8% respectively.

3.6.5 Validation on q-constant path

The simulated response using the previously calibrated models (isotropic and non-constant) with anisotropic models, are compared with the experimental results in Figure 3.30.

It is observed that the initial isotropic fabric with a constant contact friction coefficient fails to capture the characteristic dilatancy observed along the constant stress deviator path. Dilatancy is only simulated when either the initial anisotropic fabric or the non-constant friction coefficient is considered. Furthermore, it is the combination of both initial anisotropy and non-constant friction that yields the best agreement with the experimental measurements in terms of volume change. Additionally, this combined case accurately predicts the stress state at failure (near $p = 150$ kPa in Figure 3.30a). In contrast, the other cases either overestimate or underestimate the mean pressure at failure.

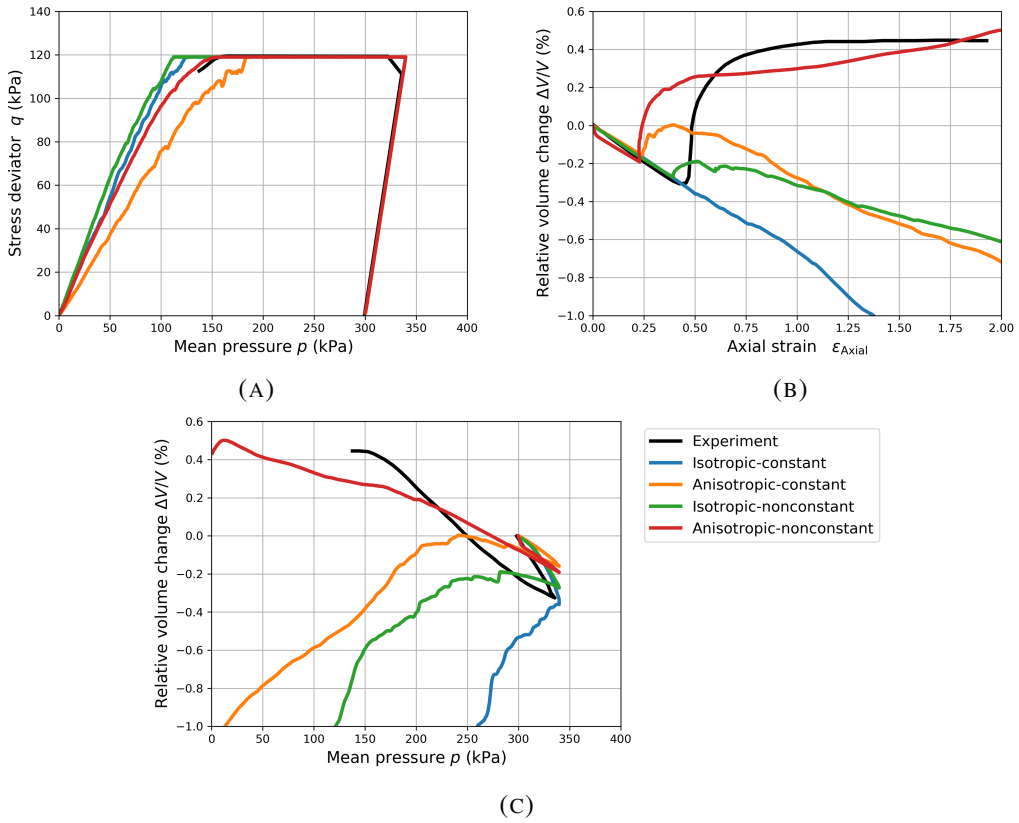

FIGURE 3.30: Validation on constant stress deviator loading paths on loose Hostun sand, comparison with experimental test with q = 119 kPa.

These findings confirm the importance of consideration of the initial fabric anisotropy and pressure-dependent friction coefficient, which are often neglected in discrete element models, for accurately describing the constitutive behavior of granular materials such as sand, both qualitatively and quantitatively. In order to better interpret the results and the effect of the anisotropy, a more refine study at the micro-scale level is done and presented in the next section based on the isochoric compression.

3.6.6 Micro-scale characterization

This micro-scale characterization has been performed in the case of the isochoric loading path. Consequently, the results discussed here after refer to the simulations and the macroscopic results presented in section 3.6.4.

Fabric anisotropy and coordination number

Figure 3.31 illustrates the evolution of contact orientation anisotropy (coefficient a_2, defined in Eq. 3.10 and 3.11) as a function of axial strain. The initial anisotropy is higher for samples initially subjected to oedometric compression compared to those initially compacted isotropically. However, during the isochoric compression, the anisotropy increases gradually at a slow rate as more contacts align parallel to the

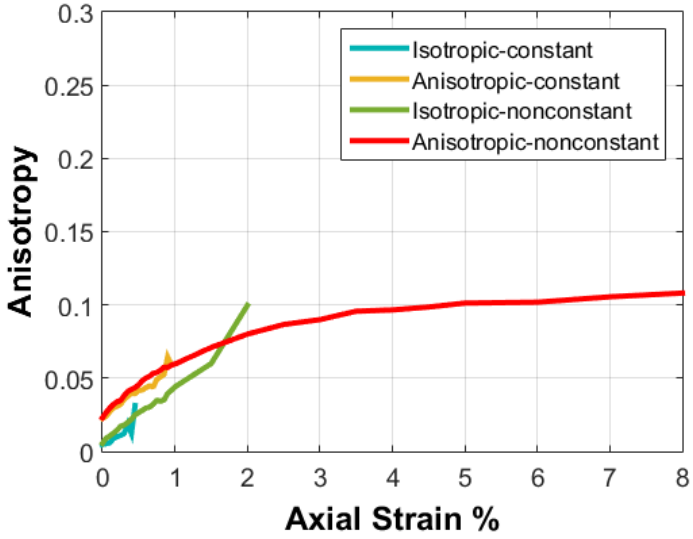

FIGURE 3.31: Anisotropy (a2) of the distribution of contact orientation in terms of the axial strain.

compression direction. This increase continues until liquefaction occurs, except for the anisotropic-nonconstant case, where the rate of increase in anisotropy gradually decreases beyond the liquefaction point observed in other cases.

Changes in microstructure as liquefaction approaches can also be observed through the evolution of the coordination number (Eq.3.9), as shown in Figure3.32. The coordination number experiences a sudden drop for all cases as the axial strain approaches the point where stress vanishes. This is consistent with the definition of liquefaction as a state where effective stress becomes zero due to the loss of interparticle contacts. However, the global loss of interparticle contacts occurs at a much larger axial strain in the anisotropic-nonconstant case.

These findings indicate that anisotropy combined with a non-constant contact friction coefficient creates a more stable initial fabric, which progressively adapts to the deviatoric stress loading under constant volume constraint. Although the observed evolutions of anisotropy and coordination number align with the macroscopic stress response computed, they do not fully explain the distinct behavior observed in the anisotropic-nonconstant case compared to other cases.

Mobilized contact friction angle and bi-modal contact network

Since the usage of constant or non-constant contact friction directly affects the sliding behavior of particles at contact, we examine the mobilized friction. Mobilized friction, for a specific contact, is defined as the ratio of the tangential contact force to the maximum tangential force resulting due to friction:

$$\frac{||\vec{F}_t||}{\mu\,||\vec{F}_n||} \tag{3.12}$$

A mobilized friction equal to 1 indicates that the frictional forces at the contact are fully mobilized, resulting in sliding between the particles with irreversible relative

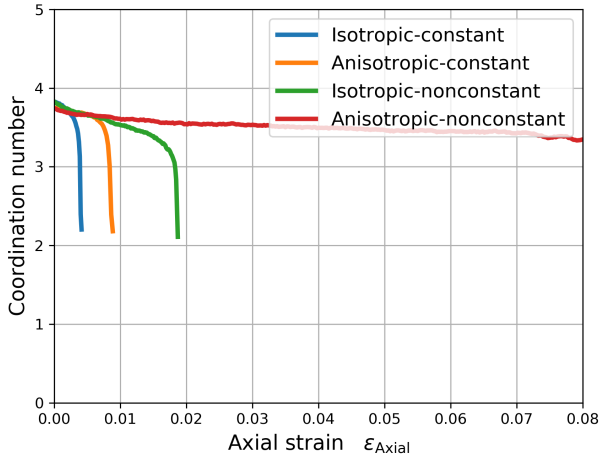

FIGURE 3.32: The coordination number of the different models as a function of the axial strain

tangential displacement.

Figure 3.33 displays the distribution of mobilized friction for the different cases at the initial state, as well as at axial strains of 0.5% and 2.0% (if liquefaction did not occur earlier).

We observe that the presence of fully mobilized contacts, indicating sliding contacts, is more notable in the cases with constant contact friction compared to those with non-constant friction, even at the initial state when the deviatoric stress is nil. Furthermore, the combination of anisotropic compaction and non-constant friction yields the lowest proportion of fully mobilized contacts, representing a more stable fabric at the initial state. Another particular observation is the presence of a local maximum number of contacts with a mobilized friction around 0.5 for cases with non-constant friction. This distribution remains relatively constant during the shearing of samples at constant volume, while nearly all contacts turn to slide (mobilized friction of 1) when the friction coefficient is constant. This point is highlighted in Figure 3.34, which shows the ratio of fully mobilized contacts (or sliding contacts) as a function of axial strain. It is clear that the failure in cases with constant friction coefficient is characterized by the sliding of the majority of contacts, whereas the ratio of sliding contacts does not exceed about 20% for non-constant friction coefficient, regardless of whether the initial compaction is isotropic or anisotropic. Furthermore, the ratio of sliding contacts decreases as complete failure is approached. These results demonstrate that the introduction of a contact friction model dependent on the normal contact stress, and thus the mean pressure, leads to a qualitatively different response of the soil microstructure to the isochoric compression path.

The analysis continues by considering the distinction between the strong and weak contact phases as defined by (Radjai et al., 1996; Radjai et al., 1998), which play different roles in the load-bearing capacity of a granular assembly. The strong contact phase consists of contacts with a contact force higher than the mean contact force, while the weak contact phase consists of contacts with a contact force lower than the mean contact force.

Figure 3.35 presents the ratios of the number of weak and strong contacts at the

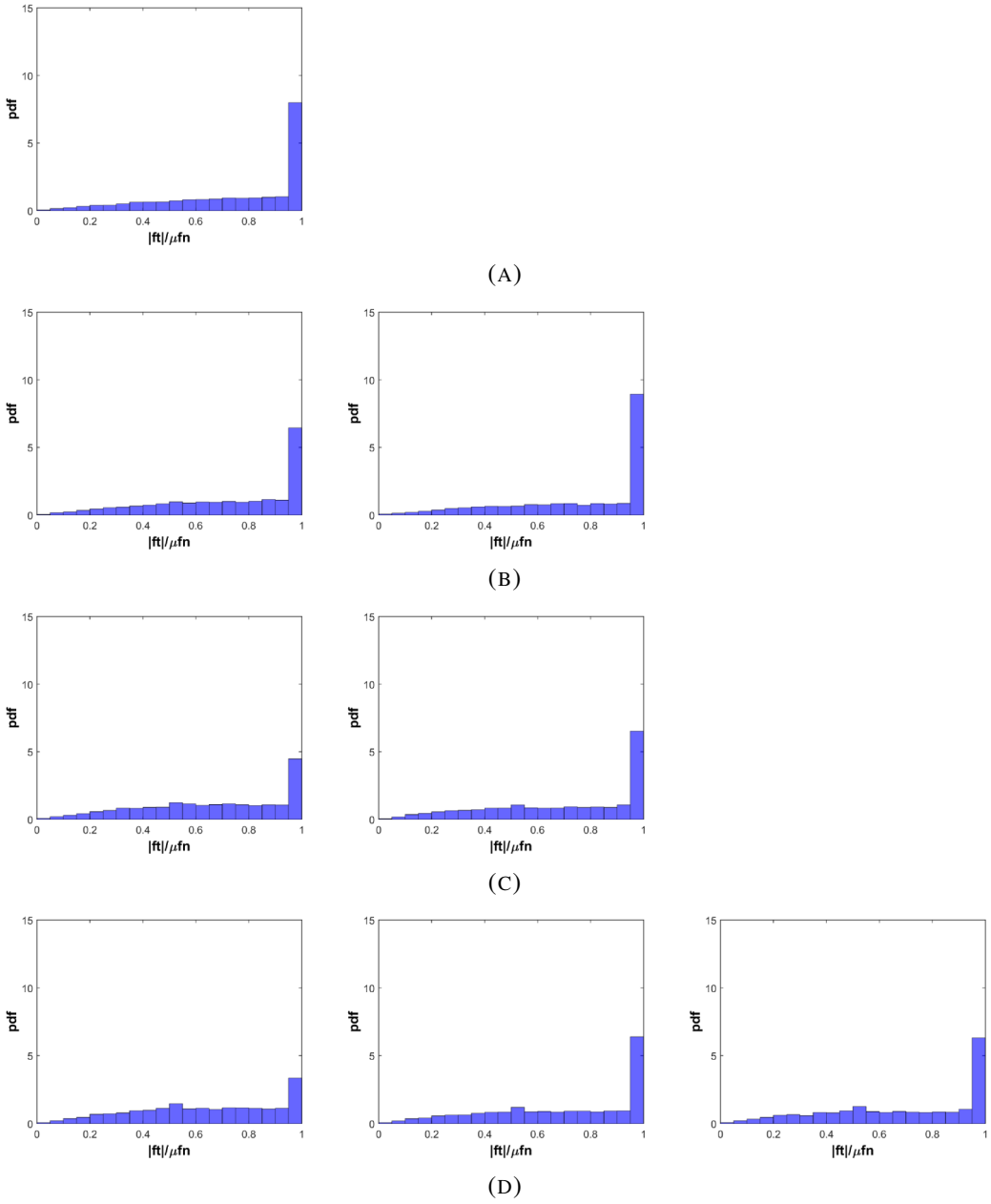

FIGURE 3.33: Probability distribution function of the mobilized friction angle. (a)Isotropic model- constant friction angle (b)Anisotropic model - constant friction angle. (c)Isotropic model - non constant friction angle. (d)Anisotropic model - non constant friction angle.
left($\epsilon = 0\%$)-middle($\epsilon = 0.5\%$)-right($\epsilon = 2\%$)

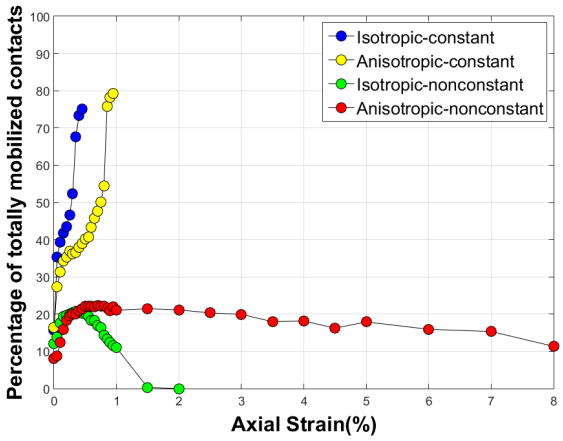

FIGURE 3.34: Percentage of totally mobilized friction contacts in the 4 models

initial state and their evolution with axial strain for each case. Initially, the ratios of strong contacts (slightly less than 40%) and weak contacts (slightly more than 60%) are similar in all cases, in agreement with the reference value given in the literature (60% of weak contacts). One remarkable difference is how the importance of each phase changes during the isochoric compression. The weak phase becomes more prominent at the expense of the strong phase, especially when the friction coefficient at contacts is constant.

As the deviatoric stress results from the strong contact forces only (Radjai et al., 1998), the reduction in the relative number of strong contacts reflects the degradation of the shear strength of the granular assembly. In cases with non-constant contact friction, the ratio of strong contacts remains closer to 40%, even if it slightly decreases. Furthermore, the decrease in deviatoric stress observed at the macroscopic scale, when the axial strain exceeds approximately 1%, is not accompanied by a reduction in the ratio of strong contacts.

Figures 3.36 and 3.37 display the distribution of mobilized friction for the weak and strong contact phases, respectively, at different axial strains. In the weak contact phase, the mobilization of friction is influenced by the choice between constant or non-constant contact friction. When the friction coefficient remains constant, a significant proportion of weak contacts are already close to the sliding condition at the initial state, and this proportion increases further during isochoric compression. In contrast, when using a non-constant coefficient of friction, the occurrence of fully mobilized contacts is relatively less common, and a significant portion of contacts fall within the half of the full range of friction mobilization. This pattern is notably distinct from the strong contact phase, where the choice between constant or non-constant friction coefficient has a lesser impact on the distribution of mobilized friction (the distribution diagrams of mobilized friction are quite similar for a zero axial strain in all cases).

In other words, the implementation of a contact friction coefficient that depends on the normal contact stress has a more significant impact on the behavior of weak contacts. This can be attributed to Equation 3.12, which describes the dependence of contact friction. The relationship has a more significant impact on the contacts

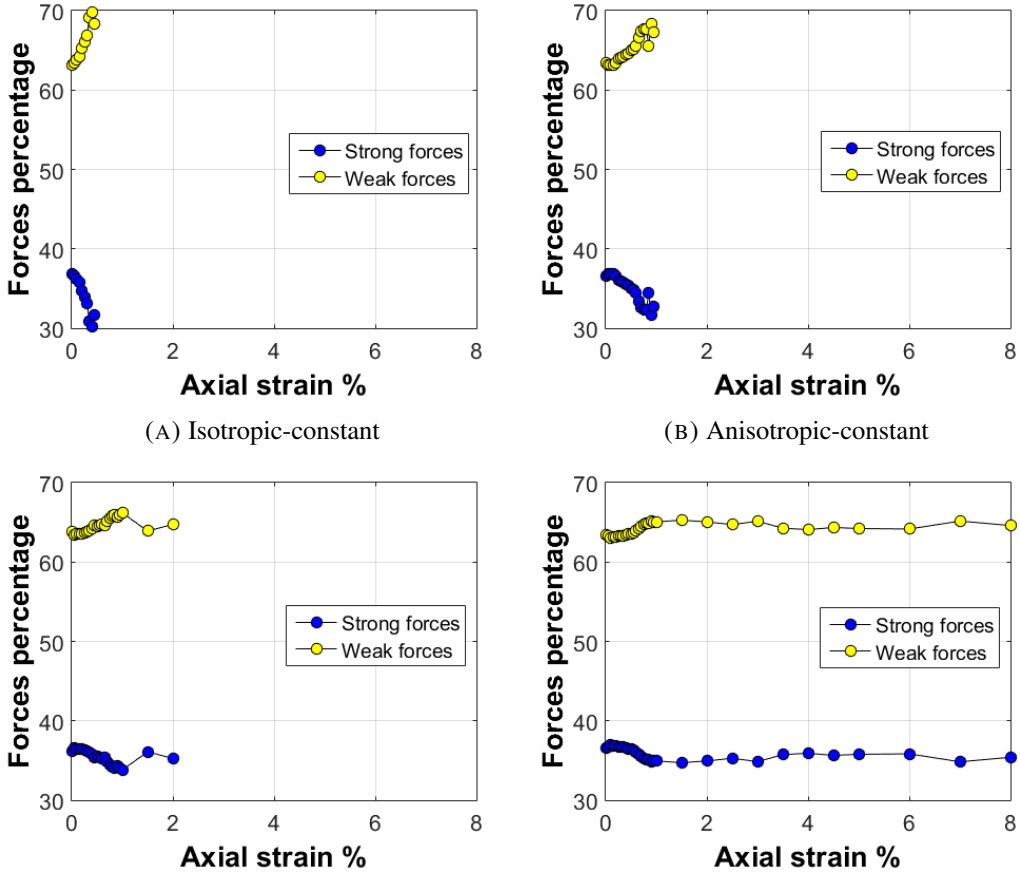

(A) Isotropic-constant

(B) Anisotropic-constant

(C) Isotropic-nonconstant

(D) Anisotropic-nonconstant

FIGURE 3.35: Percentage of strong and weak forces as a function of the axial strain

with a relatively low normal stress, particularly the weak contacts, by assigning them higher friction coefficients as represented in Figure 3.17 with respect to normal contact stress for the calibrated parameters considered here.
The role of initial fabric anisotropy can be observed by comparing the distributions of mobilized friction for initially isotropic and anisotropic samples in both the weak contact phase (Fig.3.36) and the strong contact phase (Fig.3.37). For the weak contact phase, the ratio of contacts with fully mobilized friction is slightly higher for initially isotropic fabric (Fig.3.36a,c) compared to initially anisotropic fabric (Fig.3.36b,d). Similarly, for the strong contact phase, the ratio of contacts with fully mobilized friction is slightly higher for initially isotropic fabric (Fig.3.37a,c) compared to initially anisotropic fabric (Fig.3.37b,d).

The orientations of contact, specifically the normals to the contacts, aligning with the direction of the major principal stress during compression, contribute also to the limitation of the occurrence of sliding by favouring the inter-granular force transmission between particles in the normal direction of the contact, rather than in the tangential direction.

3.7 Conclusion

In summary, the use of the model made of spheres with rolling friction for modeling dense sand has shown better predictive performance and computational efficiency compared to other simple clump models. By introducing a contact friction angle that varies with the normal contact stress, the model was able to slightly improve the response of the sand under complex loadings such as cyclic compression/extension and circular loading paths. However, this improvement came at the cost of additional complexity in the model, requiring calibration through additional drained compressions. While the calibrated model provided better predictions, the calibration process required additional computational resources. Therefore, the decision to use a contact friction angle that varies with the normal contact stress should consider the trade-off between improved accuracy and the additional effort and cost required for calibration.
In order to improve the predictions of the calibrated loose models, in addition to the implementation of non-constant contact friction, modifications were made to the sample preparation method. The latter was achieved by generating numerical samples using a technique similar to the experimental moist tamping.
The findings of the study demonstrate that a more detailed consideration of inter-particle friction, specifically related to particle roughness, plays a critical role in the response of granular materials to loading paths where the range of mean pressure is important. Simply accounting for particle shape, by implementation of rolling friction, may not be sufficient.
Indeed, the initial fabric of the granular material has a significant impact on its constitutive response. Even slight anisotropy in the distribution of contact orientations can influence the mechanical behavior of the material. Additionally, the combination of both fabric anisotropy and a non-constant friction coefficient is necessary to achieve a simulated response that closely matches experimental responses in case of

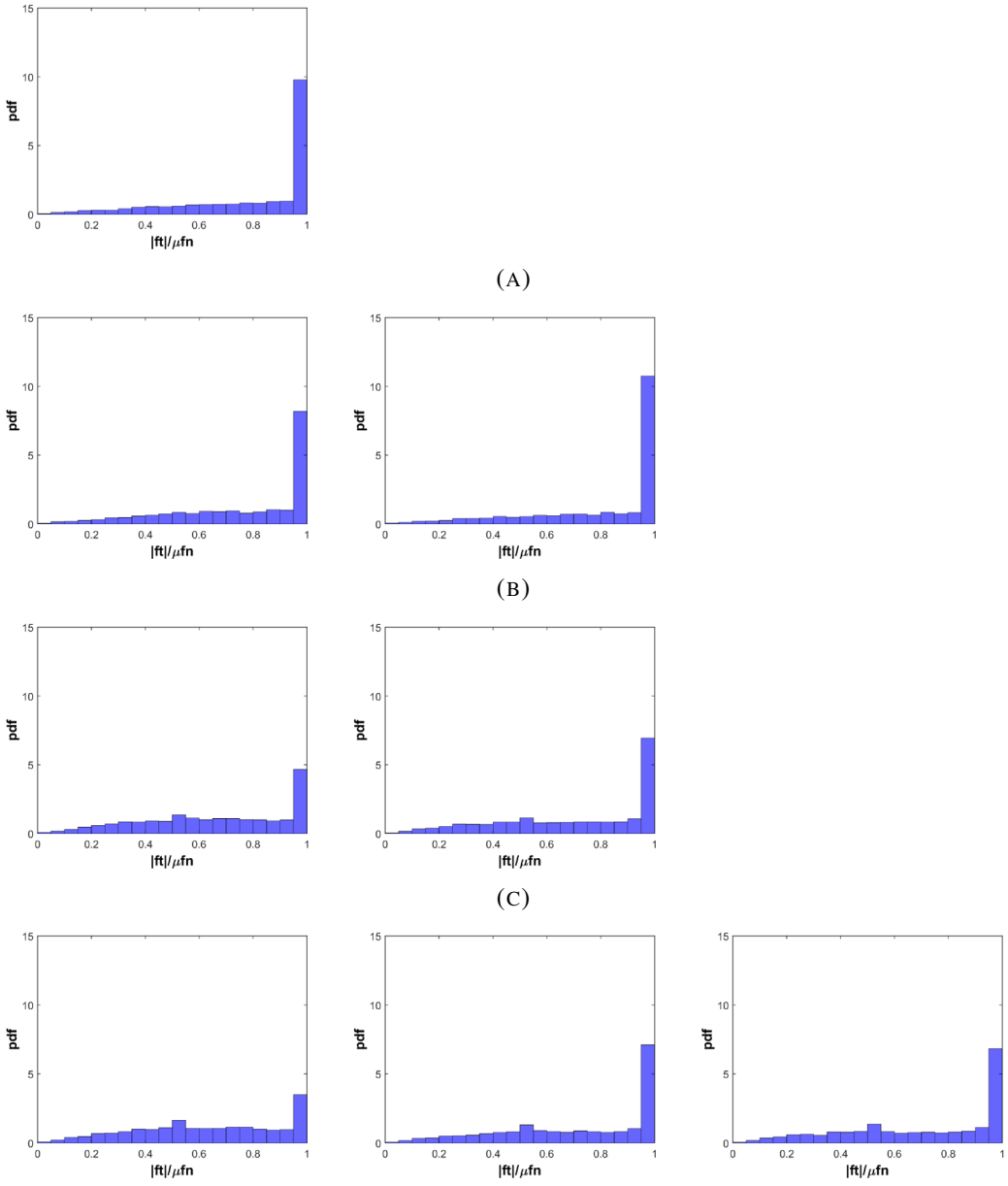

FIGURE 3.36: Probability distribution function of the mobilized friction angle of weak forces. (a)Isotropic model- constant friction angle (b)Anisotropic model - constant friction angle. (c)Isotropic model - non constant friction angle. (d)Anisotropic model - non constant friction angle.
left($\epsilon = 0\%$)-middle($\epsilon = 0.5\%$)-right($\epsilon = 2\%$)

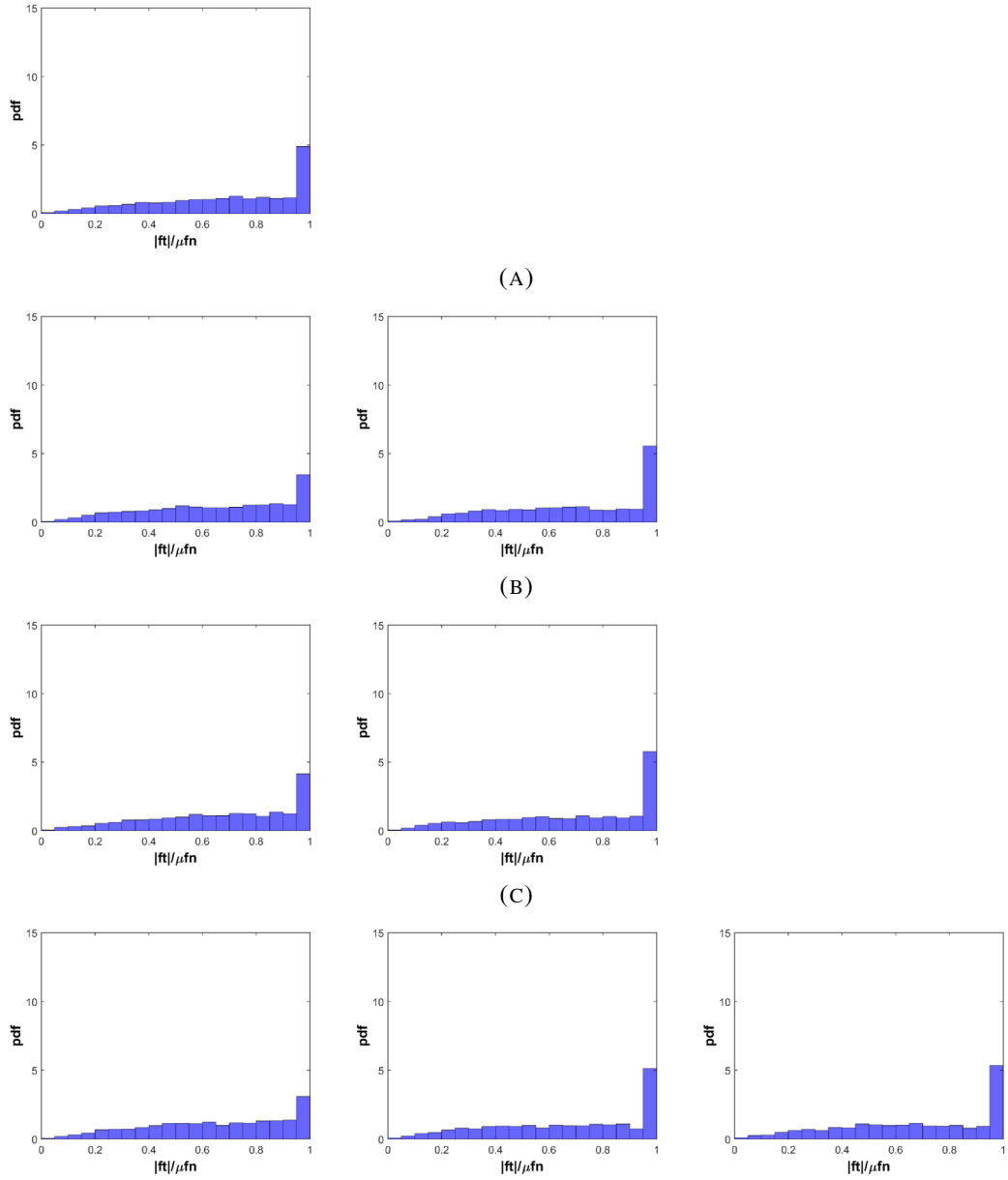

FIGURE 3.37: Probability distribution function of the mobilized friction angle of strong forces. (a)Isotropic model- constant friction angle (b)Anisotropic model - constant friction angle. (c)Isotropic model - non constant friction angle. (d)Anisotropic model - non constant friction angle.
left($\epsilon = 0\%$)-middle($\epsilon = 0.5\%$)-right($\epsilon = 2\%$)

isochoric compressions and constant deviator loading path.
A micro-scale study showed that the ratio of sliding contacts in the weak contact phase, which includes lower contact forces, is more influenced by the introduced non-constant friction model compared to the strong contact phase. However, it is important to note that the weak phase serves as a confining element for the strong contact phase and supports the contact force chains. Therefore, limiting sliding within the weak phase is crucial for the global stability of the granular assembly.
Finally, it is important to note that the effects of introducing a contact friction angle that varies with the normal contact stress and considering initial fabric anisotropy may not be essential for all loading paths. In the present study, their impact was magnified due to the significant variation in mean pressure during the specific loading conditions investigated. Different loading scenarios with smaller variations in mean pressure may exhibit different sensitivities to these factors. Therefore, their necessity and influence should be evaluated in the context of the specific loading conditions and desired level of accuracy in the model predictions.

Chapter 4

Soil-foundation interaction

4.1 Introduction

The behavior of shallow foundations under seismic loading is a complex phenomenon that is affected by various factors, including the soil properties, the foundation geometry, and the loading conditions. The description of the soil response in interaction with such a foundation is also complex due to preponderant non-linear and non-reversible deformations together with a non-associative flow rule (Darve, 1990). Furthermore, the use of continuum approaches, with phenomenological constitutive relations embedded in a finite element, or finite difference, numerical model, requires to introduce ad-hoc history parameters for a satisfying description of the soil response along the cycles of the seismic loading. Then, advanced experimental tests (including cyclic loading themselves) are necessary to calibrate these kinds of constitutive relations.

Thanks to an explicit description of the micro-structure of the soil, the discrete element method (DEM) (Cundall and Strack, 1979b) presents a good ability to describe the behaviour of granular soils under complex loadings (as cyclic loadings but not only) without the addition of specific history parameters and with a calibration performed from simple monotonous experimental tests only (as direct shear tests or triaxial compressions) (Sibille et al., 2019; Sibille, Benahmed, and Darve, 2021). In contrary to FEM, The discrete element method stands out as a versatile approach, that can serve as both a numerical method and a constitutive model when modelling boundary value problems. However, DEM usually requires higher computational cost, with respect to numerical continuum approaches, in particular when boundary value problems are considered.

This study aims to assess the relevance and the accuracy of the prediction of the response of a shallow foundation on Ticino sand under seismic loading with a numerical discrete model. The experimental data collected during the TRISEE project (a European Union-funded research project) on a physical model of the foundation carried out on both dense and medium dense sand, with relative densities of 85% and 45% respectively (at scale 1) constitutes the reference case in this study (Faccioli, Vanini, and Paolucci, 1999; Faccioli, Paolucci, Vanini, et al., 1998).

In this objective, the numerical discrete model of soil is calibrated from two experimental triaxial compressions performed on dense (D_R = 75%) and medium dense (D_R = 45%) Ticino sand and validated with triaxial compressions performed under two different confining pressures. Then, a numerical model of the foundation and the

soil system is defined with an adaptative discretization technique of the soil (Abdallah et al., 2022) to limit the number of the particles involved in the model and thus the computational cost. Finally, the ability of the model to describe the response of the foundation to the seismic loading is discussed by comparison of the simulations results with the experimental measurements from the TRISEE project. Results are also compared with simulations from the literature based either on the finite element method or the representation of the soil-structure interaction by a macro element, to highlight pro and con with respect to more conventional modelling approaches.

4.2 The TRISEE project

The TRISEE project is a European Union-funded research project conducted from 1996 to 1999 that aimed to improve the understanding of how 3D site effects and soil-foundation interaction occur during earthquakes, and the assessment of the permanent deformation development and bearing capacity of soil-foundation systems subjected to seismic loadings.
The project focused on two main areas of work: the development of mathematical tools for seismic wave propagation analysis and laboratory tests on large-scale soil foundation models. In the first area, the project aimed to create new tools for accurate calculations of 2D and 3D seismic wave propagation in heterogeneous geologic media and also explored the use of artificial intelligence methods to predict the risk levels of ground motion hazard on complex geologic configurations and identify the parameters that control it. The second area involved large-scale laboratory experiments of soil-foundation system under earthquake loading to investigate the non-linear interaction behavior during a strong earthquake. The objective was to improve the understanding of the induced motion of the foundation characterized by both the rotation of the foundation during the loading ("rocking foundation") and its permanent settlement.

4.2.1 The large scale experiment setup

The experiment was carried out at the European Laboratory for Structural Analysis (ELSA) in Italy and consisted of a shallow foundation placed on a mass of cohesionless soil (Ticino sand) with known properties, and was subjected to a time-varying horizontal force and moment. The experiment simulated the inertial forces transmitted to the foundation by the superstructure and was designed to investigate the non-linear interaction behavior between the foundation and the soil during strong earthquake loading.
The experimental setup included:

- a concrete caisson (Figure 4.1) filled with Ticino sand, with dimensions of 4.6 m by 4.6 m in plan and 4 m in height.
- a rigid mock-up of a concrete shallow foundation (Figure 4.2), 1 m by 1 m in plan, and a height of 0.2 m. It's made of steel, while the interface with the sand was made up of concrete.

- the foundation was embedded 1 meter deep in the sand to create an overburden of about 16 kPa.
- a 1-meter tall steel formwork was placed around the foundation to hold the sand in place (Figures 4.2 and 4.3).

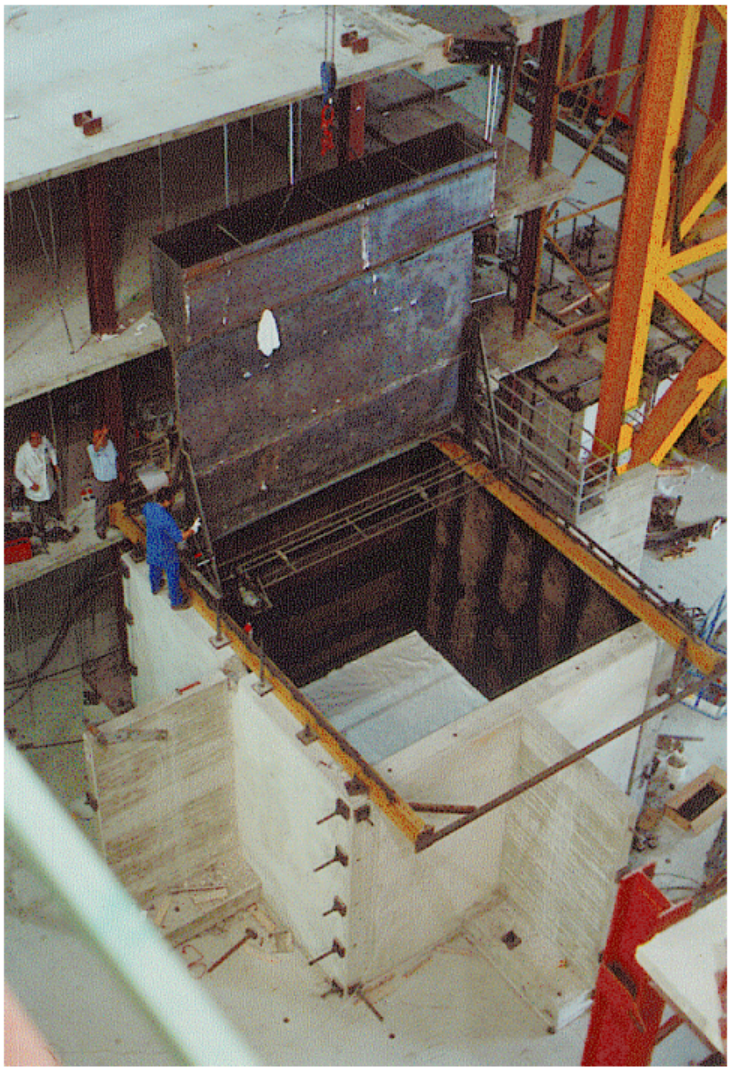

FIGURE 4.1: Filling the Caisson with the sand spreader from (Faccioli, Paolucci, Vanini, et al., 1998).

Two large-scale experiments were done using two different soil relative densities, around $D_R = 85\%$ and $D_R = 45\%$, to gather information about shallow foundation response under dense or medium dense soil conditions, respectively.
The foundation was subjected to a constant vertical force (F_V) (applied initially by steps) equal to 300 kN for the dense sand or 100 kN for the meduim dense sand using an air cushion system (Figure 4.3). In addition, before reaching the constant vertical load, an unloading-reloading was also performed as shown in Figure 4.4. During the initial application of the vertical force, the foundation settled vertically by approximately 7 mm for the dense sand and approximately 16 mm for the medium dense sand.

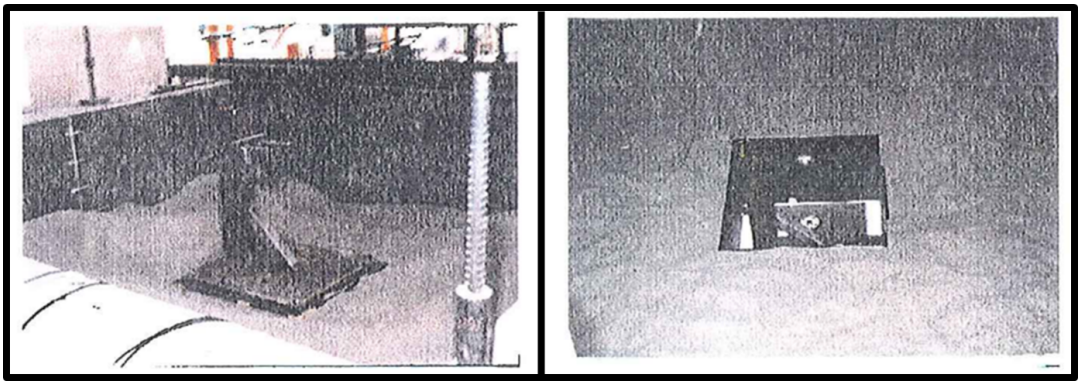

FIGURE 4.2: The shallow foundation on the underlying Ticino sand layer (Negro et al., 1999) without (left) and with (right) 1 meter top layer.

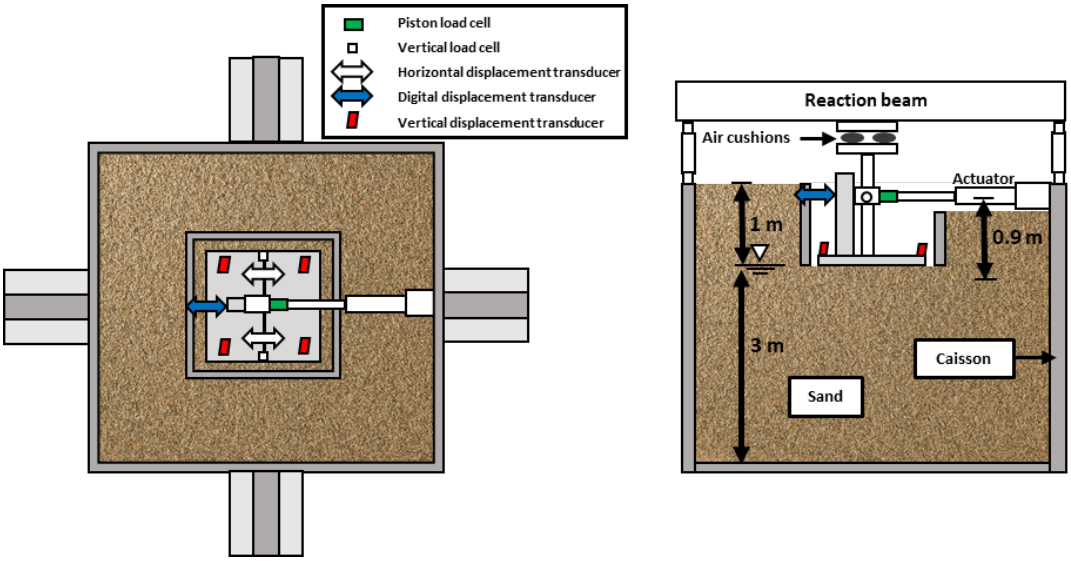

FIGURE 4.3: Scheme of the physical model of foundation with the instrumentation and the vertical and horizontal loading systems.

Then a seismic loading is simulated by a cyclic horizontal displacement or horizontal force applied by a hydraulic actuator at a height of 0.9 m from the soil/foundation interface (Figure 4.3) resulting in an overturning moment at the base of the foundation. The three following phases were applied:

- Phase I: a series of force-controlled cycles with relatively small amplitudes is applied, as shown in Figure 4.5. The amplitude of the horizontal force F_H gradually increases up to 15 kN and 5 kN (5% of the vertical load F_V) for dense sand and medium-dense sand, respectively.

- Phase II: an earthquake-like time history of the horizontal force and overturning moment as shown in Figure 4.6, with a peak of F_H equal to 60 kN and 20 kN (20% of the vertical load) for dense sand and medium-dense sand, respectively.

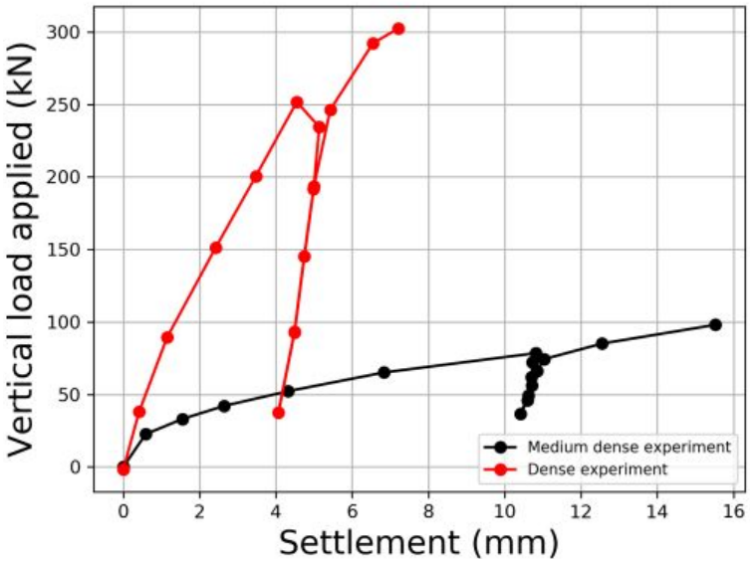

FIGURE 4.4: Monotonous vertical loading phase: vertical force vs settlement for both initial sand densities.

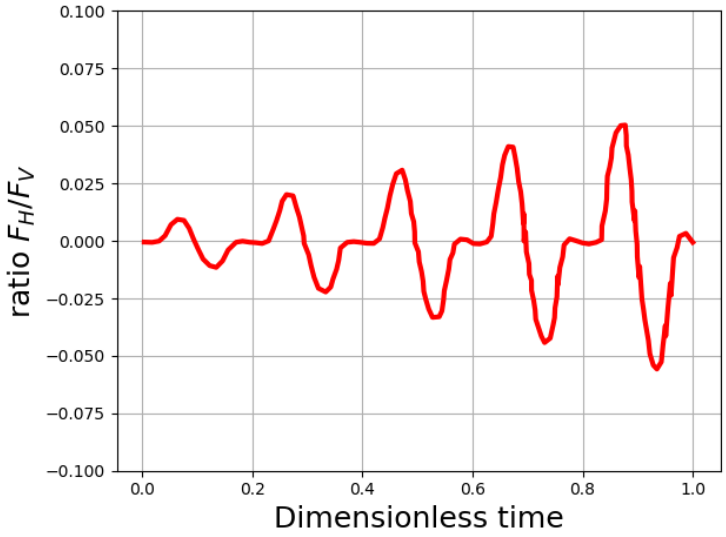

FIGURE 4.5: Cyclic loading Phase I: Horizontal force F_H normalized by vertical force F_V.

- Phase III: a controlled displacement sine-shaped cycles is applied with increasing amplitude as shown in Figure 4.7, until reaching the threshold limit of the foundation resistance. The test was done using displacement control to enable the foundation to reach its ultimate capacity without experiencing excessive movements. Pairs of cycles were used for the dense sand test, while single cycles were used for the medium dense sand test.

When subjected to such loadings, the foundation experiences settlement along with a partial cyclic rotation, commonly known as a "rocking foundation."

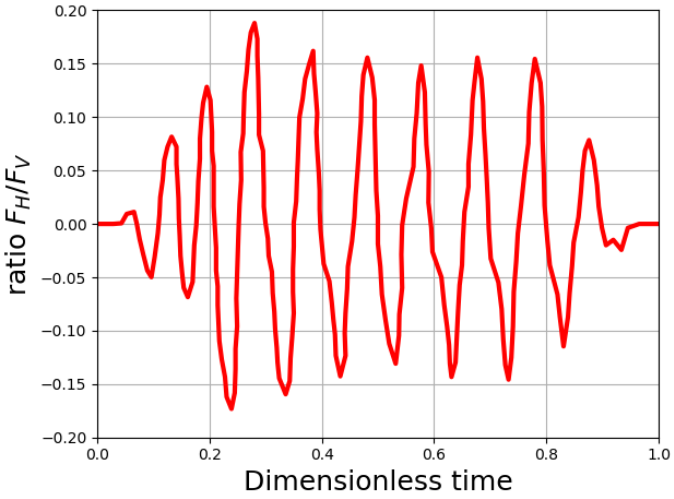

FIGURE 4.6: Cyclic loading Phase II: Horizontal force F_H normalized by vertical force F_V.

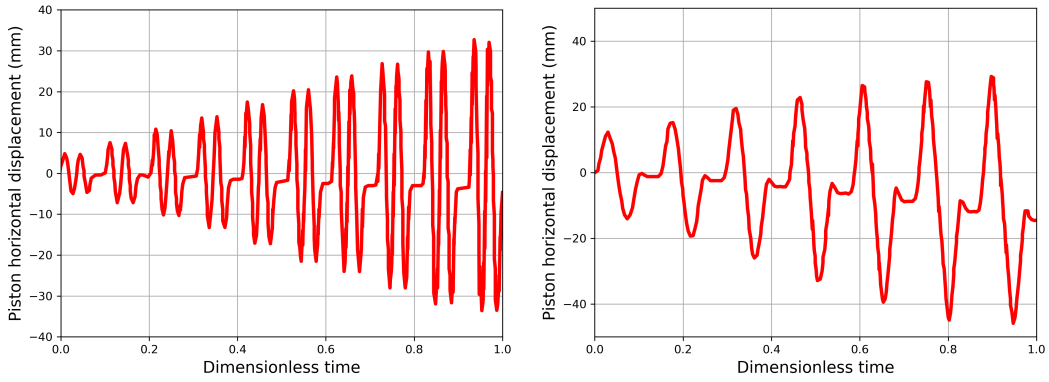

(A) Dense sand (B) Medium dense sand

FIGURE 4.7: Cyclic loading Phase III: horizontal Piston displacements for the two densities of sand.

4.2.2 Drainage conditions and loading rate

The soil was saturated up to a height of 3 meters (Figure 4.3); however, complete saturation could not be achieved (Negro et al., 2000). Consequently, the tests reflected drained conditions, where pore water drainage was possible at any point during the various loading phases. So, from a modelling point of view, solid-fluid interaction as occuring in undrained condition is discarded. Instead, only the buoyant specific weight of the soil below the foundation was considered (2690-1000=1690 kg/m^3). The experimental loading system was designed to apply relatively slow variations of force or displacement. In other words, the loading was treated as quasi-static, and both experimentally measured and simulated responses were considered as independent of the loading rate. In particular, during phase II (Figure 4.6) , the experimental signal was dilated and applied on the foundation over a period much longer than that of an actual seismic signal ((Faccioli, Vanini, and Paolucci, 1999)). The original time scale was expanded by a factor of 6 for dense sand (resulting in a duration of 80

seconds) and by a factor of 3 for medium dense sand (resulting in a duration of 40 seconds).
As the loading rate and thus time do not affect the response, experimental results are represented in terms of a dimensionless time, such that the time of application for a given phase is equal to 1 (see Figures 4.5 to 4.7). Simulated results will be presented in the same way.

4.3 Model calibration on Ticino sand

A 3D periodic discrete element model of 10,000 spherical particles have been created using the DEM software YADE to simulate the mechanical behavior of Ticino sand. The contact law involved rolling friction as defined in 3.3.1. The particle size distribution of the DEM numerical sample was chosen as that of the Ticino Sand shown in Figure 4.8. The model calibration has been performed by following the procedure defined in 3.4.1, using a constant friction angle at the contact level with an initial porosity n_0 chosen such that the ratio r, defined in 3.3.3, is equivalent experimentally and numerically so the model can accurately simulate the volumetric behavior of the soil during shearing. The soil model was calibrated using experimental data from drained triaxial compressions on Ticino sand (Calvetti, 2008) with two different relative densities (D_R=75% and D_R=45%) under a confining pressure of 300 kPa. Table 4.1 presents the calibrated parameters of the soil model. The model is then validated under two other confining pressures (100 kPa and 200 kPa). The drained triaxial compressions were simulated and the soil behavior was characterized in terms of the stress-strain behavior, the volumetric strains, and the shear strength parameters as shown in Figure 4.9. Figure 4.9a shows the results of the calibration where the model reproduces successfully the stress-strain behavior and the volumetric deformation of the Ticino sand for a confinement of 300 kPa. As can be noticed, the model succeeded in reproducing the stress-strain behavior and the volumetric deformation of the Ticino Sand at confining pressures of 100kPa and 200 kPa as shown in Figure 4.9b. As mentioned in previous sections the experiment was done using two different relative densities, D_R=45% and D_R=85%. Triaxial tests for Ticino sand calibration at D_R=85% doesn't exist. The initial porosity of the sand representing the dense sand in the TRISEE Soil-foundation experiment (D_R=85%) is chosen equal to 0.366. This value was estimated using linear interpolation based on the numerical porosities of sand at D_R=45% and D_R=75% (Table 4.1).
The calibrated parameters are used in simulating the soil-structure interaction in the TRISEE large experiment between Ticino sand and the shallow foundation in the following sections.

TABLE 4.1: Parameters of the discrete numerical model identified from the calibration on dense and medium Ticino sand.

Particle	D_R	n_0	E_C (MPa)	α_s	α_r	μ	η_r
Sphere	45%	0.411	500	0.5	3	0.477	0.35
Sphere	75%	0.381	500	0.5	3	0.477	0.35
Sphere	85%	0.366	500	0.5	3	0.477	0.35

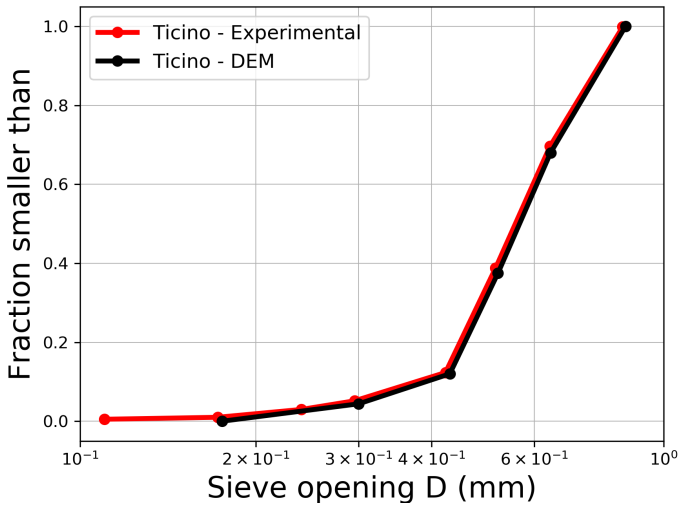

FIGURE 4.8: Particle size distribution of Ticino sand and one used in DEM model.

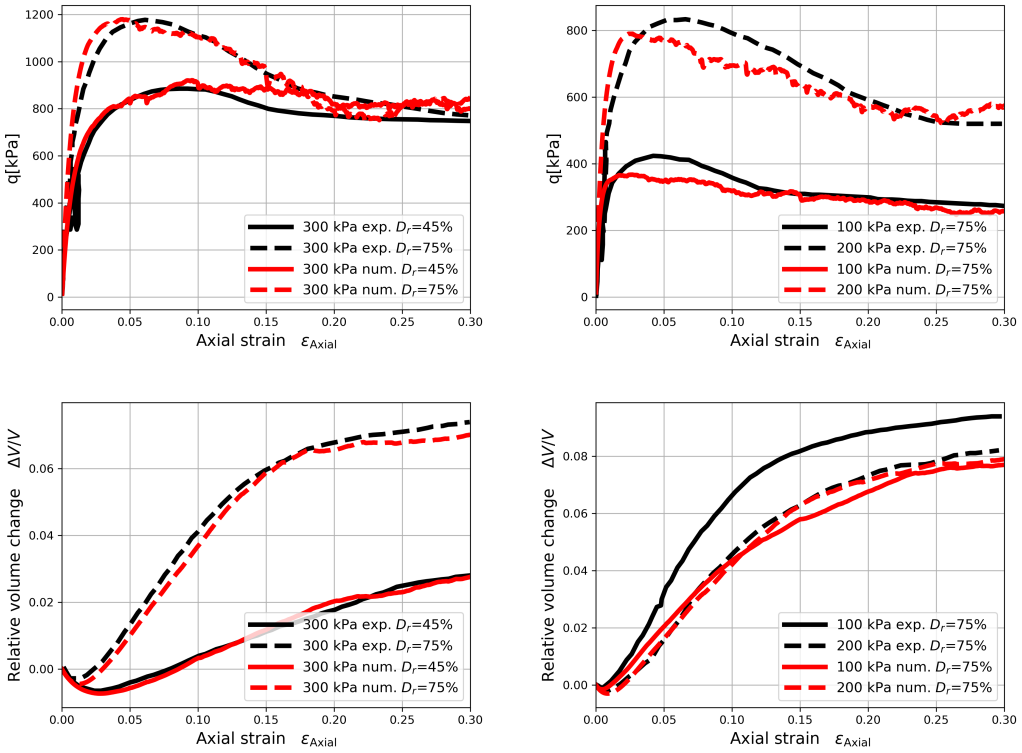

(A) Calibration: P_0 = 300 kPa (B) Validation: P_0 = 100 kPa and 200 kPa

FIGURE 4.9: Calibration and validation of the discrete element models on drained triaxial compressions on dense and medium dense sand at different confining pressures

4.4 Soil-foundation discrete model

The main difference between the experimental tests lies in the magnitude of vertical and horizontal loading. In the case of medium dense soil (D_R=45%), the constant vertical loading reaches 100 kPa, while for dense soil (D_R=85%), it is equal to 300 kPa. Moreover, the loading conditions in the different models replicate those in the experiments. In the following sections, we will present the characteristics of the Soil-foundation discrete model by describing its geometry and the process of generating its initial state.

4.4.1 Model geometry and specificities

The model geometry and specificities are defined by the following:

- the size of the caisson is identical to the experimental one (see Figures 4.3 and 4.10), where a box with six walls is created. In addition, these walls are fixed and smooth (i.e. $\mu = 0$ and $\eta_r = 0$).
- the box is filled with spheres having the buoyant weight as Ticino sand equal to 1690 kg/m^3 (specific weight equal to 2690 kg/m^3).

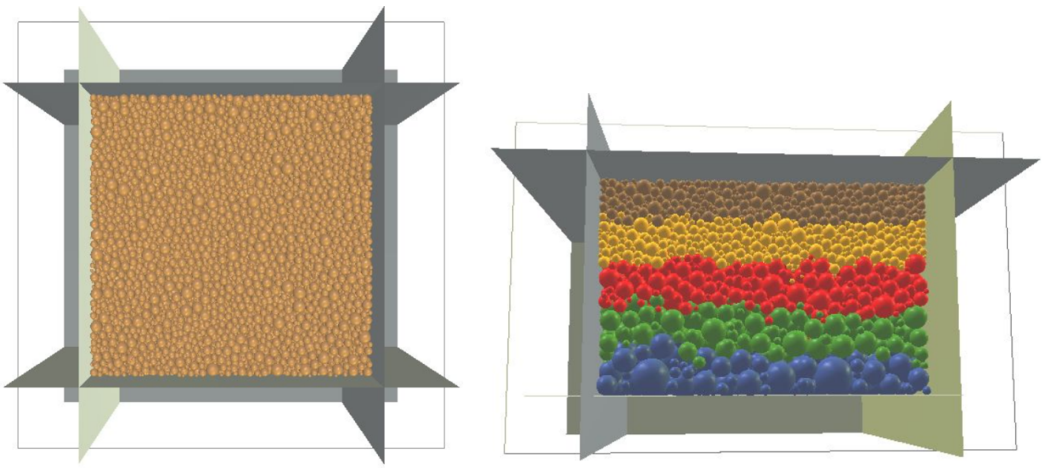

FIGURE 4.10: Top (left) and side (right) view of the DEM of the Ticino sand assemblies (increasing mean particle diameters from top to bottom).

- the foundation is also identical to the experimental one (see Figure 4.11). It is represented by a parallelepipedic structure of dimensions equal to 1m x 1m and thickness equal to 0.2m, with a density of $\rho = 4587$ kg/m^3, chosen such that the self-weight of the foundation exerts a vertical stress of 9 kPa, same as the experiment. The value of the soil-structure contact friction angle is taken as equal to 2/3 of the internal friction angle of the dense Ticino sand ($\mu = 0.511$ in case of D_R=45% and $\mu = 0.414$ in case of D_R=45%).
- the overburden soil layer is represented by a layer of large spheres with the same equivalent mass resulting in an overburden pressure of approximately

16 kPa. Moreover, instead of replicating the high steel formwork that was placed around the foundation to retain the sand, the spheres representing the overburden soil layer were not allowed to move in the horizontal plane (by blocking the translations of particles horizontally).

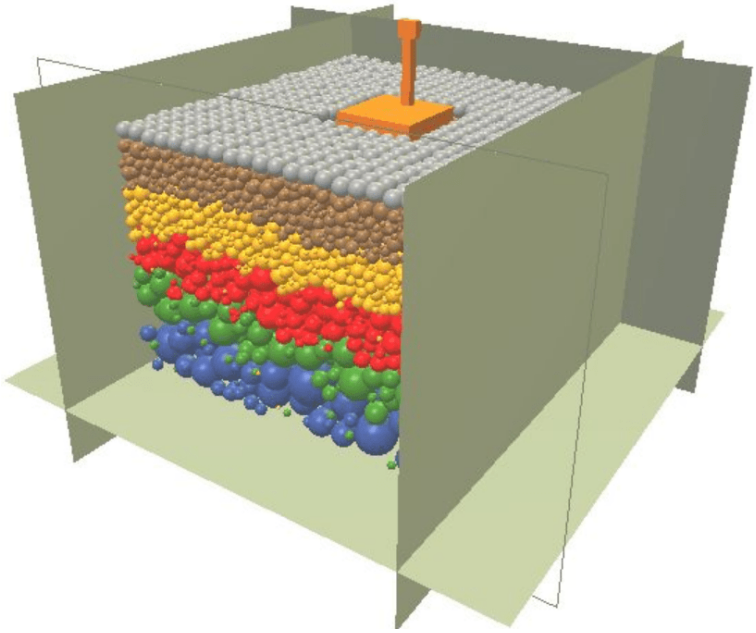

FIGURE 4.11: Global view of the discrete numerical model of the Ticino sand - shallow foundation interaction.

- an important drawback of DEM is the high computation time compared to other methods, thus to solve this issue, several strategies could be followed. Coupling DEM with FEM is possible, however we consider adaptative discretization (Abdallah et al., 2022), in order to limit the number of spheres and consequently the computational time, which consisted in dividing the domain into 4 horizontal layers (brown and yellow particles have same particle diameters) having the same relative particle size distribution and porosity but different mean particle diameters. Therefore, particles in the layers closer to the foundation were smaller than those in other layers.
  The rate at which the mean particle size changes throughout the domain is limited to ensure that the Terzaghi filter criterion is satisfied. This criterion prevents finer particles near the foundation from migrating downward, where particles are coarser. When using variable discretization of the domain, it is necessary to define contact stiffnesses as a function of the particles' radii involved in a contact (equation 3.4). Consequently, the effective macroscopic properties of the granular assembly remain unaffected by the particle sizes.
  In our models, we investigated soil discretization using different numbers of particles, ranging from about 9,000 to 100,000, where the ratio of the foundation width to the mean particle size near the foundation varied from 7.6 to 16.4.

4.4.2 Generation of the initial state

The generation of the initial state of the model involves several phases, including particle compaction, particle growth, gravity application, addition of the foundation, etc., as detailed below and shown in Figure 4.12. This figure illustrates the soil porosity, stresses at boundaries, and unbalanced forces during the whole generation process. The unbalanced force is a dimensionless parameter computed as the ratio of the mean resultant particle force to the mean contact force. In a perfect static equilibrium, this value tends to zero. It is used to assess the equilibrium of the model during the generation of the initial state. For our study, a value between 0.01 and 0.02 was considered here as representative of a state sufficiently close to static equilibrium. The generation of the initial state of the model consists of the following steps:

- The granular assembly representing the soil is generated as a cloud of particles initially not in contact. Then, the compaction of the granular assembly was done by growing the spherical particles until reaching an isotropic stress of 300 kPa (higher confining pressure resulted in more effective growing process), while controlling the initial porosity by tuning the contact friction angle during the growing particle phase (reducing the friction angle during this phase lubricates the contacts and results in higher densities). Once the particle growing is finished the contact friction angle is changed to its nominal value (i.e. the calibrated one) and the mean pressure is reduced down to 5 kPa thanks to a slight shrinking of the particles. In this process, the initial porosity remained almost unchanged (see Figure 4.12). Experimentally, there was no external confining pressure applied to the soil. However, numerically to create the sample we needed to apply at least a small confining pressure to avoid the lost of inter-particle connectivity. The local porosity at this step, for the different soil layers as represented in Figure 4.10, is shown in Figure 4.13 for a target relative density $D_R = 85\%$ and a computed average porosity for the whole sample equal to 0.366. These porosity profiles correspond to simulations performed with a number of particles ranging from 8903 to 96736. Porosity is relatively constant accross the different soil layers with a different refinement of discretization.

- The control of the mean pressure is stopped and gravity is then applied, and equilibrium of the system is checked by verifying that the vertical stress on the bottom wall equals the pressure due to the particles' weight.

- Then the top wall is removed, and the overburden top layer is added.

- Finally, the foundation is added at the middle of the top of the box domain.

Throughout the various steps, the porosity remained nearly unchanged. Moreover, the stress on the bottom wall (stress-Y) equaled the pressure resulting from the particles' weight after applying gravity. Subsequently, when the top overburden layer was added, the stress increased again due to its weight. Finally, there was a slight increase in stress after adding the foundation.
The earth pressure at rest, which represents the in situ lateral pressure of soil, is typically determined by multiplying the vertical stress by the coefficient K_0. K_0 is

referred to as the coefficient of earth pressure at rest. Jaky's formula is commonly used to calculate this coefficient.

$$K_0 = 1 - \sin\phi' \tag{4.1}$$

where ϕ' is the effective internal friction angle of the soil. Using this formula, K_0 is estimated to be equal to 0.35 ($\phi' = 40.5°$).

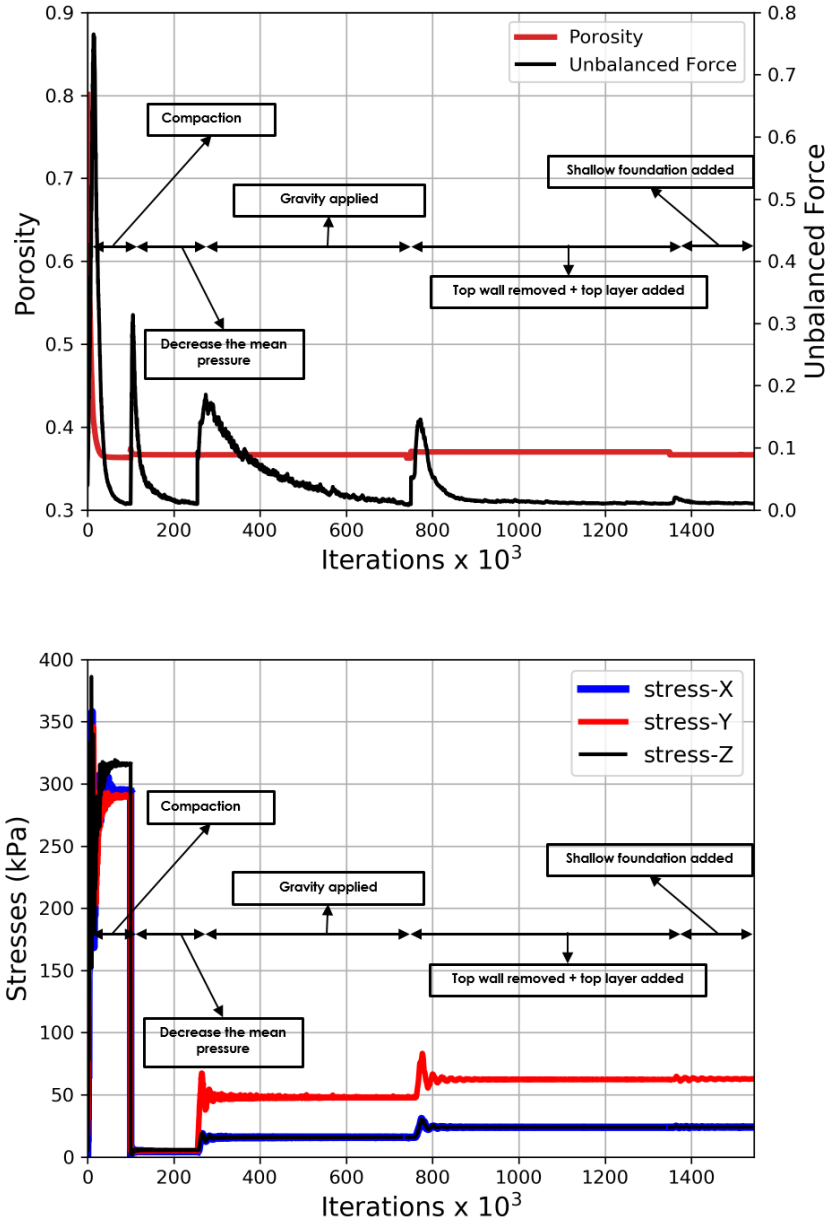

FIGURE 4.12: Evolution of the porosity, the unbalanced force (Top) and the stresses on the walls (Bottom) during the different steps (stress-Y refers to the vertical stress and stress-X and Z refer to the horizontal stresses which are equal here).

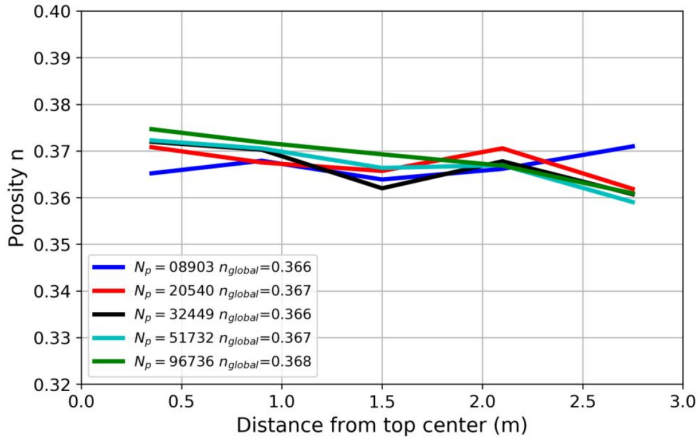

FIGURE 4.13: The local porosity of the dense granular assembly built with adaptive discretization technique along a vertical profile below the foundation down to the bottom wall (at 3 m depth).

4.5 Parametric study: soil discretization and loading rate

The objectives of this section are to determine the minimum number of particles needed to discretize the soil and to choose the appropriate loading rate for each loading phase of the foundation.
Five numerical models presented in this section are built with different numbers of particles to represent the dense sand (D_R=85%), to perform a parametric study concerning the number of particles used in order to study the feasibility of the description of the large scale experiment of the soil-foundation interaction. During the parametric study, the DEM models are prepared with spheres having a specific weight equal to 2690 kg/m^3, Whereas K_0 is around 0.76 for all models. Table 4.2 presents the number of spheres and the corresponding ratio between the width of the foundation W_{SF} and the average particle size d_{50} below the foundation for different models.

TABLE 4.2: Number of particles and W_{SF}/d_{50} ratio of the different models

Model	**Number of particles**	W_{SF}/d_{50} **ratio**
1	8,903	7.6
2	20,540	10.2
3	32,449	11.2
4	51,732	13.1
5	96,736	16.4

4.5.1 Monotonous loading

First, the shallow foundation is subjected to a vertical force equal to 300 kN for the dense sand.

Experimentally, this loading was applied by steps of 50 kN, with an intermediate unloading-reloading cycle before reaching a total of 300 kN. After each step of 50 kN, the loading procedure was paused until the creep deformations reached a state of full stabilization.
This loading protocol was similarly applied in the DEM model. The numerical load undergoes increments of 1 kN every 50 numerical iterations. After each increment of 50 kN, the simulation is run 2000 iterations by keeping the loading constant to reach complete stabilization of vertical settlement (settlement converges and shows no further increase with additional iterations). As demonstrated in Figure 4.14-B, as the number of particles increases, the model might necessitate a greater number of iterations to achieve full stabilization. This was verified by conducting tests with 5000 iterations (Figure 4.15) and similarly with 15000 iterations for each step, producing very similar results to those with 2000 iterations per step, as shown in Figure 4.15-B, where the settlement after each step clearly converges to its stable state.

Furthermore, as shown in Figure 4.14-A, it is expected that the settlement converges toward a given global value as the number of particles increases. However, this is not the case, and consequently, the minimum number of particles to consider is not known. Therefore, in Figure 4.14-C, the modulus E_S, representing the rate at which force changes with settlement is considered, showing an increasing trend with more particles during the initial loading. However, during reloading, this modulus remains relatively constant in all models. This behavior could be due to the contact between the shallow foundation and the underlying sand being less stable during the initial loading with less particles, with increased stability attained during reloading.
Numerically the settlement was measured at the middle of the foundation, whereas experimentally it is measured at the four corners. The numerical models slighlty underestimates the experimental settlement by 1 to 3 mm among the different models, which may be considered relatively small in some engineering applications.
Therefore, for the application of additional loading phases, only a comparison of the responses among models 1, 4, and 5 is being taken into consideration.

4.5.2 Cyclic Phase I

During Phase I, a sequence of force-controlled, small-amplitude cycles in the horizontal direction was applied to the foundation as shown in Figure 4.16. The cycles are sine-shaped with amplitude increasing up to 5% of the vertical load.

Model 1: In case of Model 1, four different loading rates where considered for the application of phase I loading, presented in Figure 4.17. The rate (designated as 50, 100, 200 or 300 in Figure 4.17) indicates the number of numerical iterations taken for every 1 degree of variation of the angle used as argument of the sine function defining the magnitude of the horizontal force applied at anytime on the foundation. Hence, for instance, a value of 300 represents a slower loading rate than 50. Figure 4.17-B presents the ratio of the total resultant horizontal forces computed on the foundation to the maximum applied horizontal force. In other words, as this value approaches 0, it indicates that the shallow foundation tends to a static equilibrium state. Hence, a loading rate of 200 will be considered for Phase I because the cumulative settlement

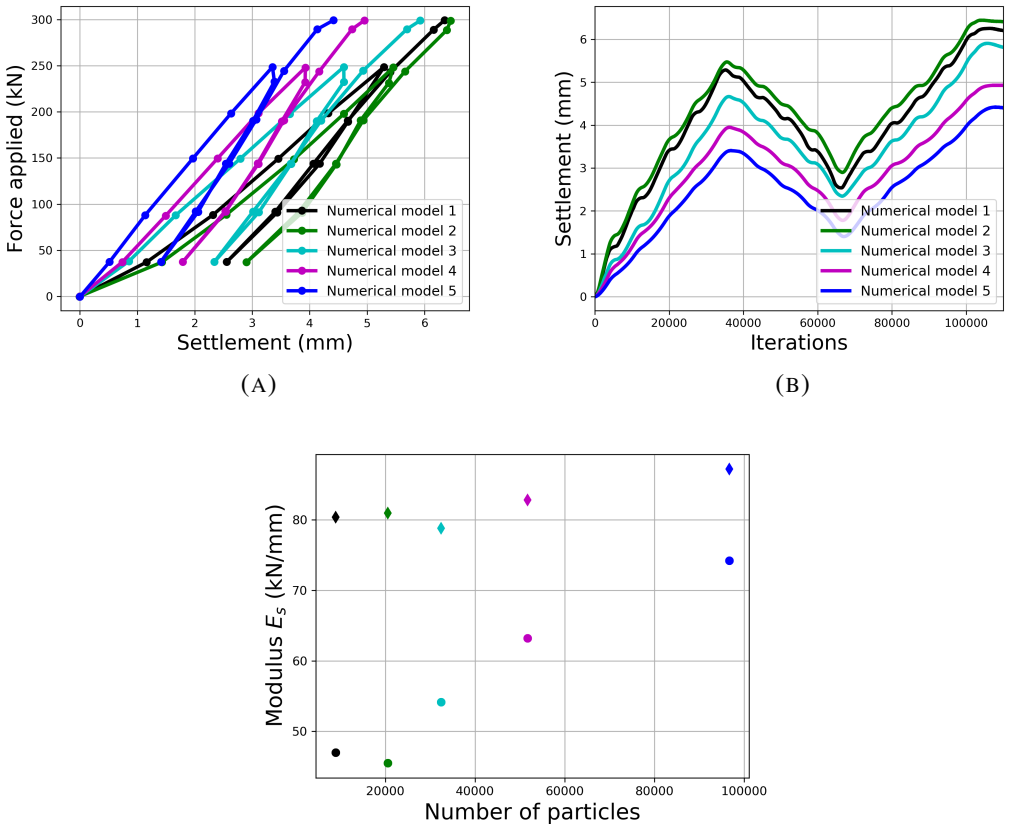

(A) (B)

(C)

FIGURE 4.14: Foundation settlement for the initial dense state during the monotonous vertical loading up to 300 kN (2000 iterations per step) computed with models 1 to 5 involving different numbers of particles.

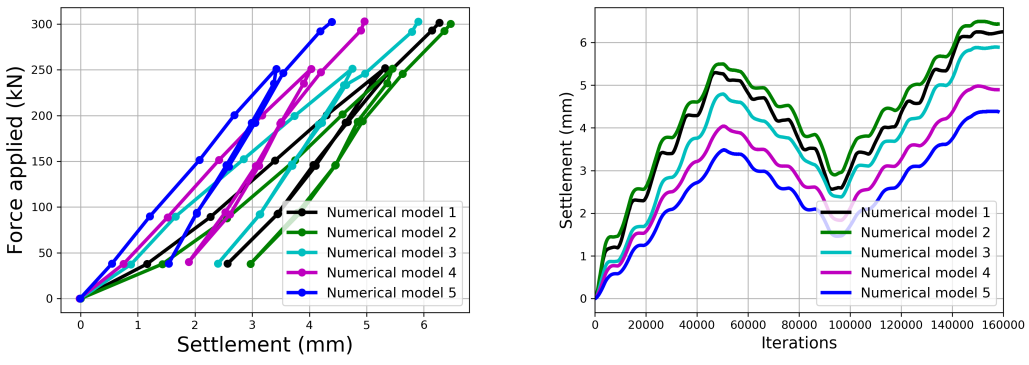

(A) (B)

FIGURE 4.15: Foundation settlement for the initial dense state during the monotonous vertical loading up to 300 kN (5000 iterations per step) computed with models 1 to 5 involving different numbers of particles.

is independent of the loading rate at lower rates of horizontal force application. Additionally, it is estimated that the ratio in Figure 4.17-B is sufficiently small at this rate.

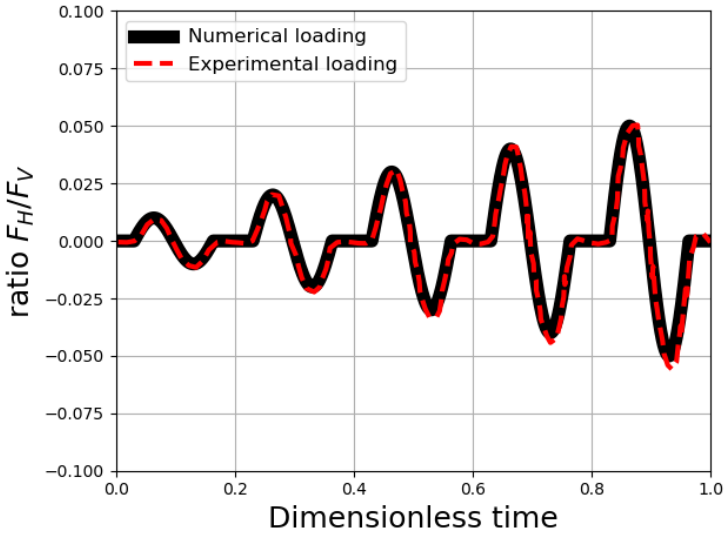

FIGURE 4.16: Cyclic loading Phase I: numerical and experimental loadings.

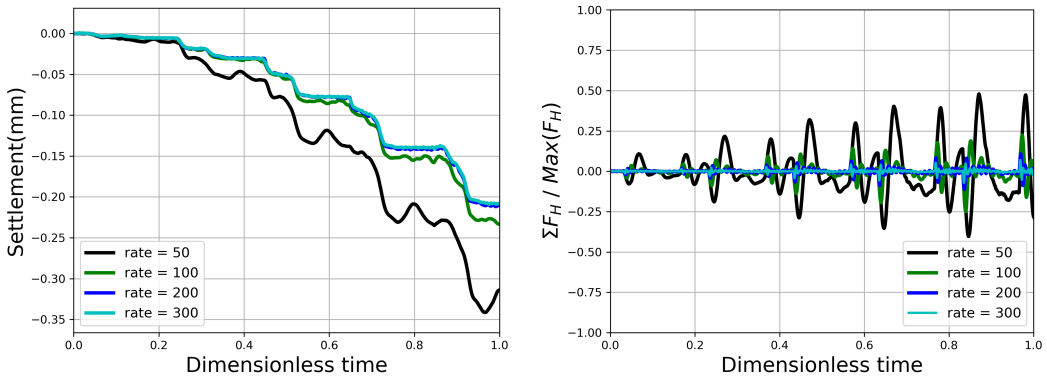

(A) (B)

FIGURE 4.17: Response of Model 1 subjected to cyclic Phase I loading

Model 4: In case of Model 4, two different loading rates (200 and 400) where considered for the application of phase I loading, presented in Figure 4.18. It is shown in Figure 4.18-B, that when the number of particles increases, a higher rate should be used to achieve a more stable simulation. This could be explained by the fact that as "information" (for instance change of the contact force due to the motion of a given particle) can be transmitted from one particle to another only in a single time step a higher number of time steps is required when there is more particles (and thus more particles to reach a given depth below the foundation for instance). Thus, a loading rate equal to 400 could be considered in this case.

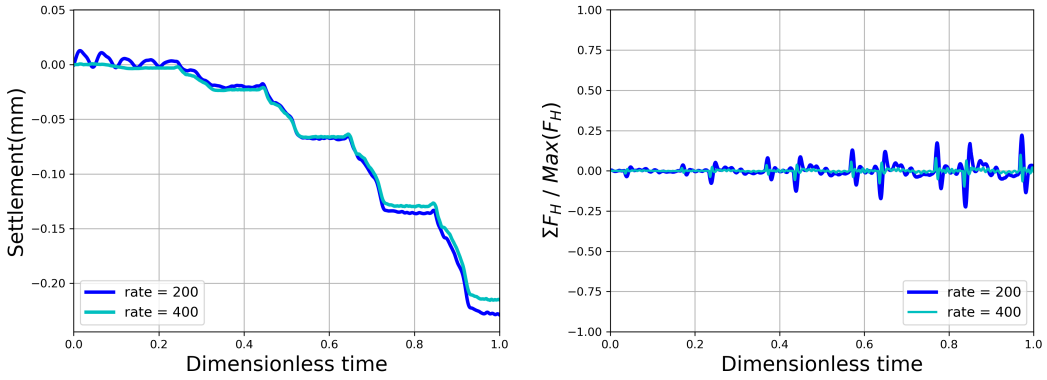

(A) (B)

FIGURE 4.18: Response of Model 4 subjected to cyclic Phase I loading

Model 5: Also in Model 5, two different loading rates (200 and 400) where considered for the application of phase I loading, presented in Figure 4.19. Figure 4.19-A illustrates that for settlement, the influence of the loading rate is somewhat more noticeable compared to Model 4, although the impact is not significant.

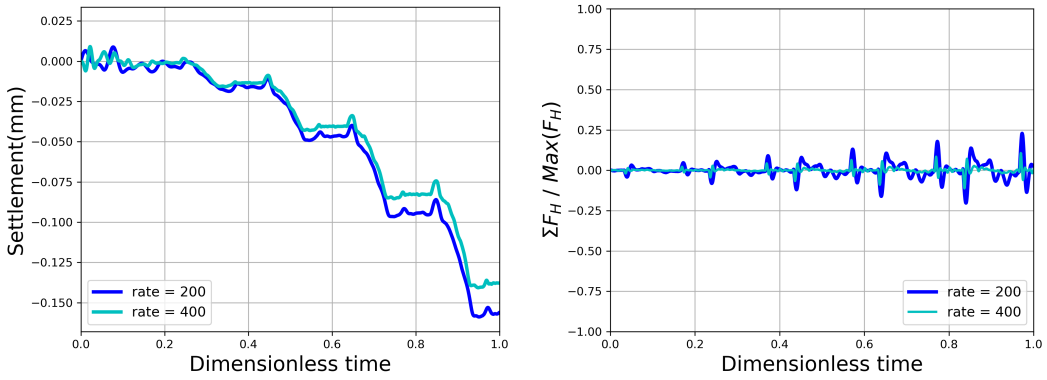

(A) (B)

FIGURE 4.19: Response of Model 5 subjected to cyclic Phase I loading

4.5.3 Cyclic Phase II

After Phase I, the shallow foundation is subjected to an earthquake-like loading in Phase II. As shown in Figure 4.20, the ratio of the horizontal force to the vertical one on the foundation reached a peak of about 0.20 corresponding to an horizontal force peak of almost 60 kN.

Model 1: In case of Model 1, four different loading rates (100, 200, 300 and 400) where considered for the application of loading phase II, presented in Figure 4.21. Similarly to phase I loading, the rate indicates the number of iterations taken for

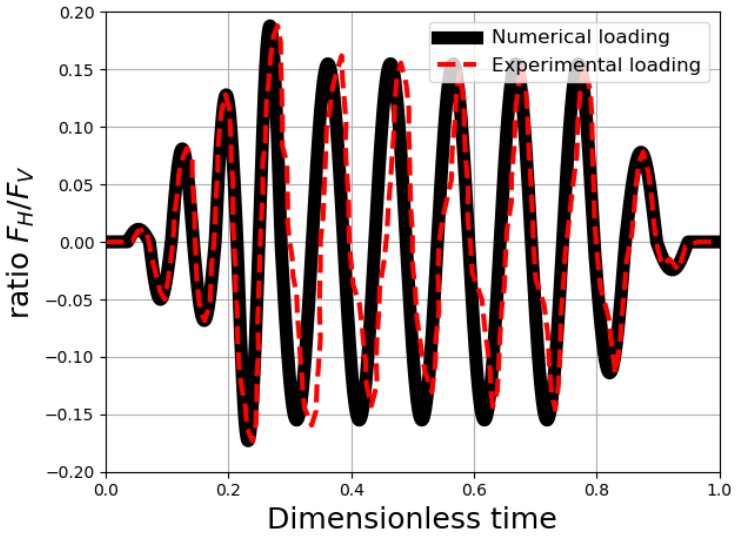

FIGURE 4.20: Cyclic loading Phase II: numerical and experimental loadings.

every 1 degree of the oscillation. Based on the same considerations as for the previous loading phases, a rate of 200 will be considered for the loading Phase II from Figure 4.21.

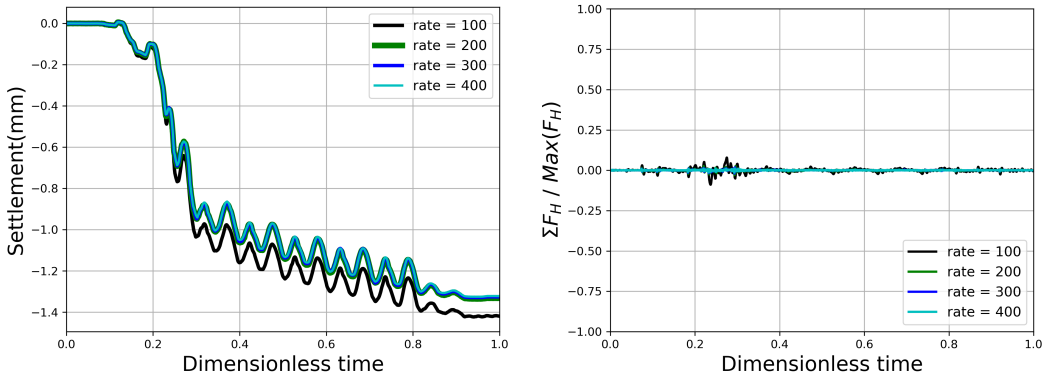

(A) (B)

FIGURE 4.21: Response of Model 1 subjected to cyclic Phase II loading

Models 4-5: In case of Models 4 and 5, a loading rate equal to 200 is considered for the application of loading phase II, presented in Figures 4.22 and 4.23 respectively. As shown in Figures 4.22-C and 4.23-C, a higher rate could be used to achieve a more stable models. But, a loading rate equal to 200 was be considered in these cases.

Likewise as in phase I, in comparison to Model 1, the settlement and horizontal displacement values in Models 4 and 5 are very similar, with no noticeable impact observed from using a larger number of particles on the response of the DEM model.

Considering these results, in cyclic loading phases I and II, only Model 1 was chosen for the application of loading phase III.

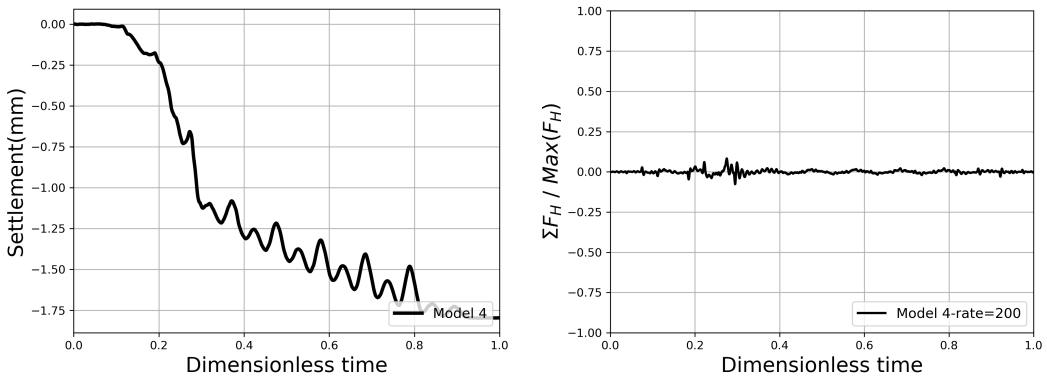

(A) (B)

FIGURE 4.22: Response of Model 4 subjected to cyclic Phase II loading

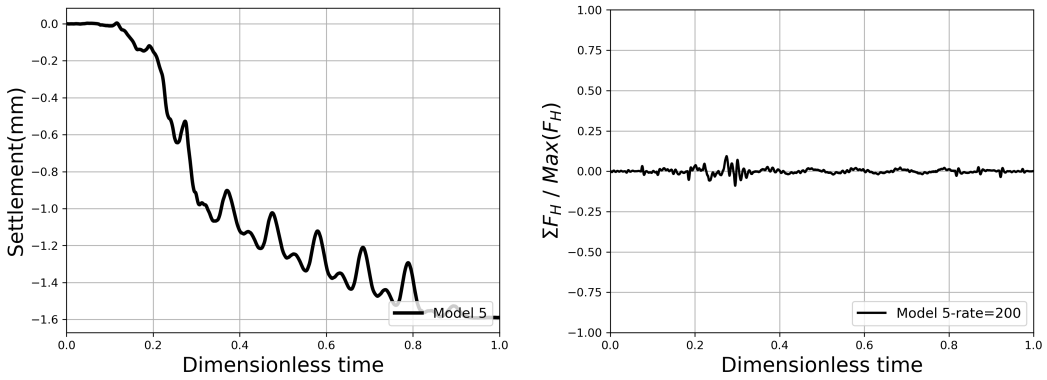

(A) (B)

FIGURE 4.23: Response of Model 5 subjected to cyclic Phase II loading

4.5.4 Cyclic Phase III

During the final experimental phase, the foundation underwent displacement controlled cycles following a sin-shaped pattern, with amplitudes progressively increasing, until reaching large settlements of the foundation (soil failure). The testing process was displacement controlled, enabling the structure to achieve its ultimate capacity without excessive foundation movements.
Numerically, since in YADE software the foundation is made up of 3 clumped parallelepipeds, it was not possible to impose a displacement on a unique member of the clump representing the top part of the pilar above the foundation (as in the experiment). Thus, we have applied to our model the experimental measured horizontal force shown in Figure 4.24 aiming to get the same horizontal displacement imposed on the top part of the foundation.

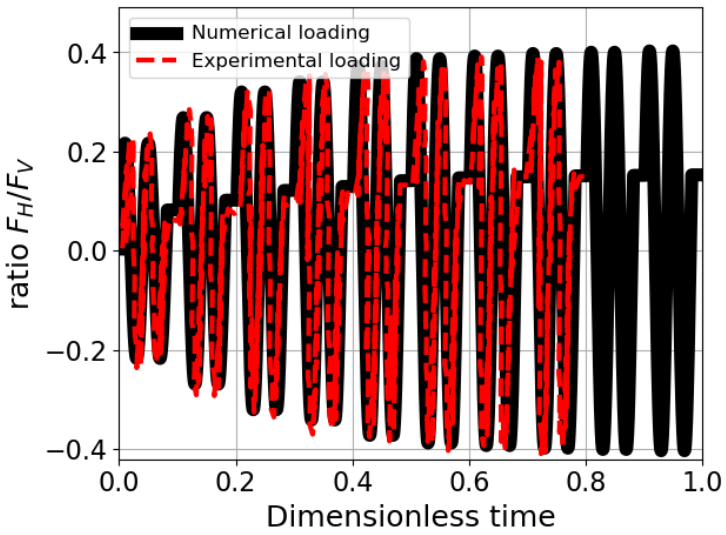

FIGURE 4.24: Cyclic loading Phase III: numerical and experimental loadings.

As previously indicated, only Model 1 is taken into account for the application of phase III loading (Figure 4.25), with four different loading rates considered (200, 500, 1000, and 2000). Just like in loading phases I and II, the rate represents the number of iterations performed for each 1-degree oscillation. As presented in Figure 4.25, a rate of 1000 was considered providing a simulated response rather independent of the loading rate in regime sufficient close to the quasi static condition.

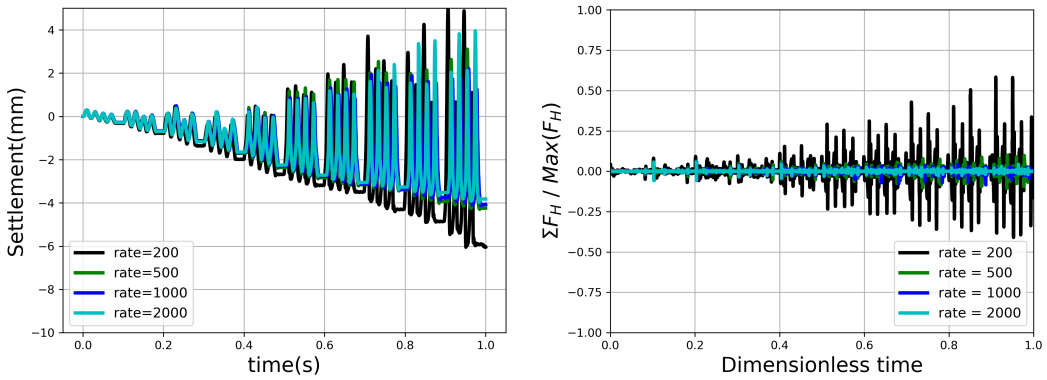

FIGURE 4.25: Response of Model 1 subjected to cyclic Phase III loading

4.5.5 Summary of the parametric study

In summary, a parametric study was conducted to determine the minimum number of particles required to discretize the soil and to select the appropriate loading rate for each loading phase applied to the foundation. The study demonstrated that the

responses of models with different numbers of particles were very similar. Consequently, we selected **Model 1 with 8903 particles** for comparison with experimental results and other numerical models.

Regarding the loading rate, it was observed that for **monotonous loading**, applying increments of **1 kN every 50 numerical iterations** and running the simulation for **2000 iterations at each 50 kN increment**, while keeping the loading constant, was sufficient. Additionally, for Model 1, a loading rate of **200** was found to be adequate **for cyclic Phase I** to achieve settlement independent of the loading rate. Similarly, a rate of **200** was sufficient **for cyclic Phase II**. **For cyclic Phase III**, a rate of **1000** was considered, providing a simulated response relatively independent of the loading rate.

4.6 Simulated response for the dense sand compared with experiments and other numerical models

In this section, we present a comparison of the discrete model's response in the case of the dense sand (D_R=85%) to both experimental data and various numerical studies, including Finite Element Models (FEM) and Macroelement Models (Table 4.3). The soil below the foundation is saturated, consequently, to represent more closely the vertical effective stress in the soil, the discrete model is prepared in this section by considering soil particles with a buoyant specific weight equal to to that of Ticino sand (1690 kg/m^3), as described in Section 4.4, resulting in K_0=0.88.
It's worth noting that previous researches have not provided complete modeling of all phases and for both densities (dense and medium dense) for a given single model. Therefore, in this section, we thoroughly examine our results for each loading phase separately and each soil relative density, comparing them to experimental data and the results of a numerical study that specifically addressed that particular phase. Thus, in the following sections, we provide a comparison of our model with other previous numerical simulations for each phase. This includes the presentation of the other numerical models, such as the constitutive model used, the number of parameters involved, and the requirements for calibration.
We then conclude by discussing the advantages and limitations of each approach.

TABLE 4.3: Summary of different models used in comparison with the discrete model for the dense Ticino sand for Phases I, II, and III

Phase I	**Phase II**	**Phase III**
Macroelement model	**Macroelement model**	**Finite element model**
Leblouba et al., 2016	Figini et al., 2012	Anastasopoulos et al., 2011
Based on the Bouc-Wen-Baber-Noori constitutive model involving 14 parameters	Based on the linear visco-elasticity, foundation uplift, and soil plasticity with 14 parameters	Based on a kinematic hardening constitutive model involving 4 parameters

4.6.1 Monotonous loading

A vertical force is applied on the shallow foundation, resulting on a vertical stress of 300 kPa below the foundation, and the induced settlement is checked as shown in Figure 4.26.
The model gives a good estimation of the final settlement of about 7 mm. During the inital loading, the inital force/settlement slope (up to 1 mm of settlement) is underestimated by the model while the subsequent slope (until the unloading-reloading cycle) is fairly well reproduced. Again, the stiffness of the soil/foundation interaction is underestimated during the unloading-reloading cycle. Initial and unloading-reloading stiffnesses of the soil/foundation interaction are probably more closely related to the elastic properties of the soil (there is almost no irreversible deformation during the unloading-reloading cycle experimentally and numerically).
The calibration of the discrete model takes particular attention to the description of the plastic response of the soil while elastic properties are not directly considered since the elastic parameters (in particular the contact stiffness) are just chosen high enough to assume the particles as almost rigid. The later may explain the underestimation of the initial stiffness of soil-foundation system.

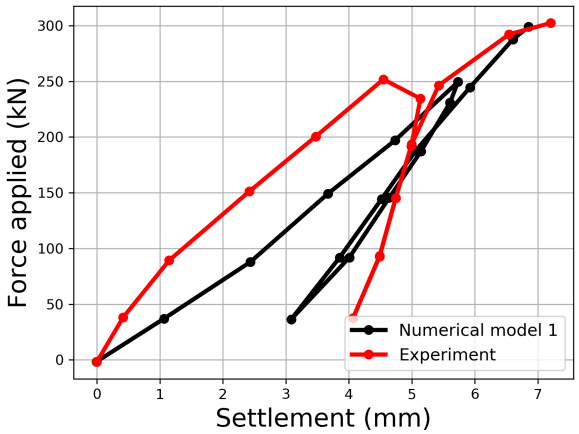

FIGURE 4.26: Monotonous loading on dense Ticino sand: numerical response of Model 1 compared to the experiment

4.6.2 Cyclic Phase I

In phase I, we compare our Model 1 response with the TRISEE experimental results and results of a macroelement model (Leblouba et al., 2016). The model's foundation representation in Figure 4.27 involves three different spring elements: nonlinear horizontal, nonlinear rotational, and linear vertical springs. In their study, they employed Baber and Noori's extension to the Bouc-Wen model, known as the Bouc-Wen-Baber-Noori constitutive model, which involves 14 parameters.
The calibration of the parameters for the macroelement model was performed by using experimental data from moment-rotation and horizontal force-horizontal displacement curves. However, the authors did not provide any specific details about these curves.

In Figure 4.28, we observe a settlement equal to 0.2 mm in the DEM model, twice the experimental settlement 0.1 mm. This differences in terms of and settlement can be considered negligible in geotechnical engineering applications. In addition, the settlement of the macroelement was not provided by Leblouba et al. (2016).

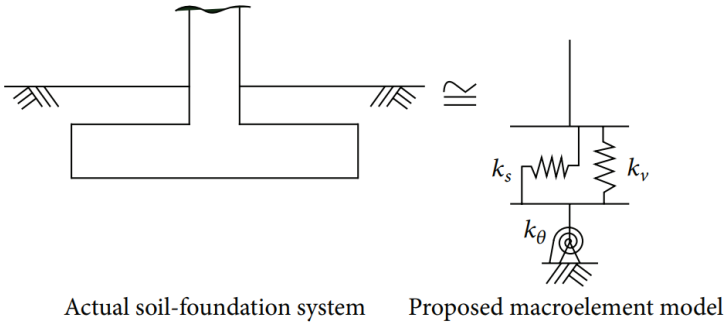

FIGURE 4.27: Rheological sketch of the Macroelement model used by Leblouba et al. (2016)

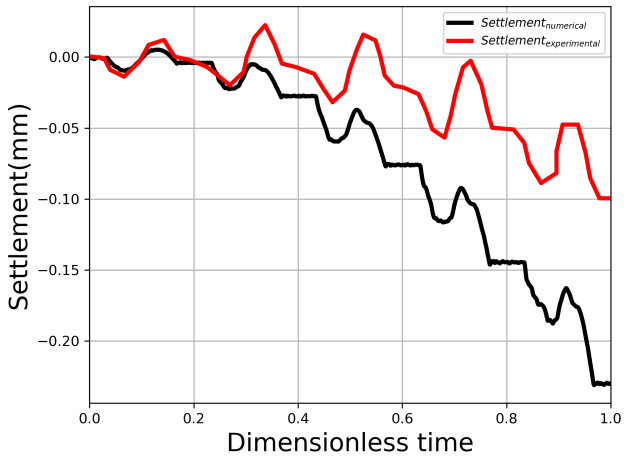

FIGURE 4.28: Cyclic Phase I loading: Comparison of numerical DEM and experimental settlement.

It's important to note that while the macro element model accurately replicates the rocking angle and horizontal displacement of the foundation, the DEM model tends to overestimate the rocking angle (Figure 4.29), with the overestimation being approximately twice that of the experimental measurements with an order of magnitude equal to 10^{-4} radians. Furthermore, the DEM model overestimates the horizontal displacement (Figure 4.29) compared to the experiment, with the DEM model showing double the displacement, resulting in an order of magnitude of approximately 10^{-1} millimeters. These differences can be considered as negligible in geotechnical engineering applications.
It's worth considering that the macro element model was calibrated using experimental moment-rotation and horizontal force-displacement curves data, whereas the discrete model was calibrated based on monotonous triaxial tests.

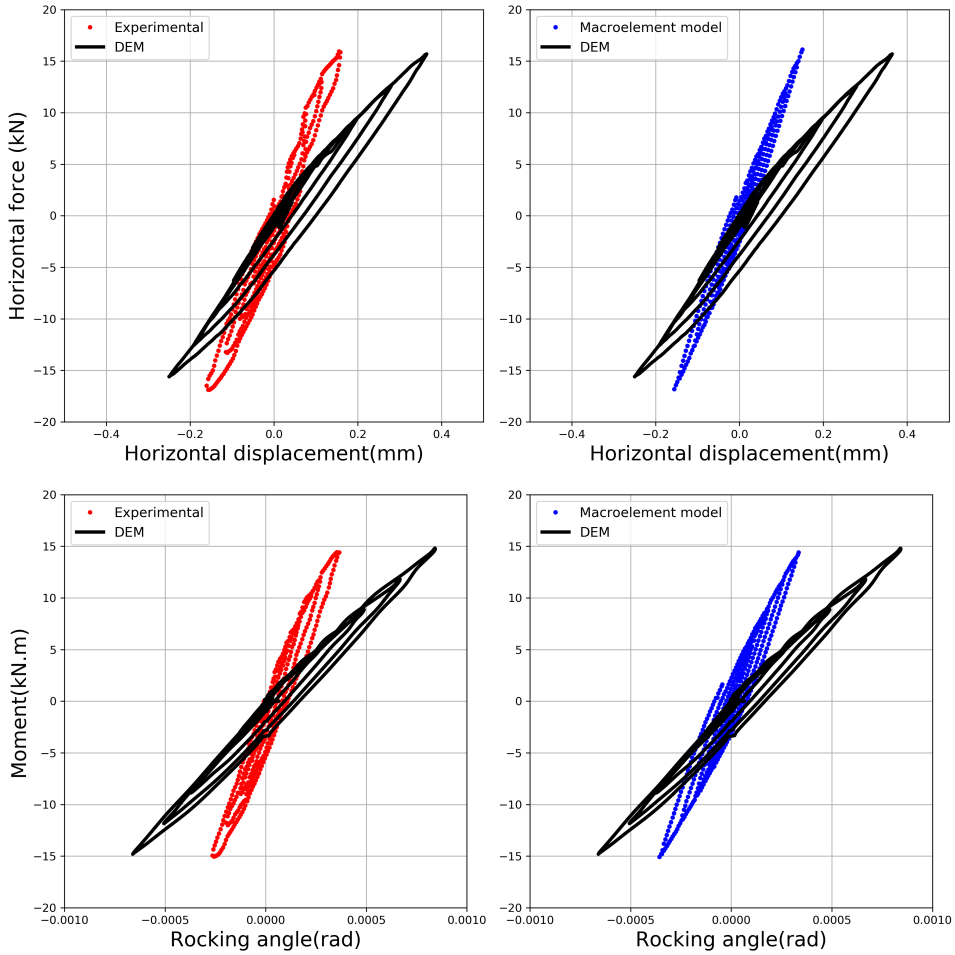

FIGURE 4.29: Cyclic Phase I loading on dense sand simulated with Model 1: Comparison with (left) the experimental and (right) the macroelement model (Leblouba et al., 2016)

4.6.3 Cyclic Phase II

In phase II, we compare our model 1 response with the TRISEE experimental results and results of the macroelement model used by Figini, Paolucci, and Chatzigogos (2012) (Figure 4.30). In this macroelement, an update of an elasto-perfectly plastic formulation of the NM91 model (Nova and Montrasio, 1991) model was intoduced, incorporating elements of bounding surface plasticity along with Wolf's (1988) uplift formulation and NM91 bounding surface. The model parameters are based on principles of linear viscoelasticity, foundation uplift behavior, and soil plasticity.
This model involves the calibration of 14 parameters based on Phase I TRISEE experimental results. Then the model is validated on Phase II.
We can observe in Figure 4.31 that the DEM model underestimated the final settlement compared to the experiment by 1 mm, whereas the macroelement model successfully predicted the final settlement. Nevertheless, the discrete model provided a good estimation of settlement until a dimensionless time of about 0.3 (i.e., until the third cycle of loading). This initial phase of settlements is almost not described by the macroelement model. Then, beyond this third loading cycle, the discrete model

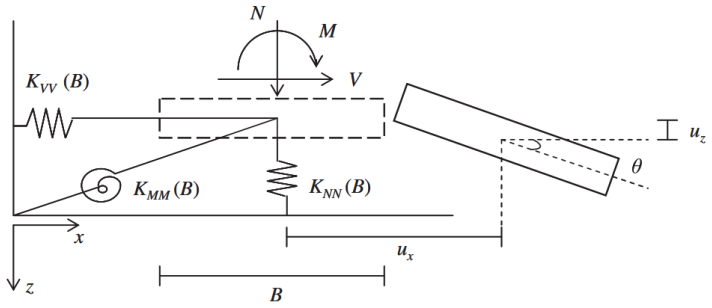

FIGURE 4.30: Rheological sketch of the Macroelement model used by Figini, Paolucci, and Chatzigogos (2012)

presents a stabilization of settlements whereas this stabilization occurs experimentally only around a time of 0.6 (so approximately after the 6th cycles over a total of nine cycles. It is worth noting such a stabilization of settlements is not predicted by the macroelement model which predicts almost constant irreversible settlements for all the cycles. To resume, even if the discrete model underestimates the final settlement, it predicts correctly the initiation of strong settlements (from a time of 0.2, during the second cycle) and the amplitude of irreversible settlements after this initiation. It also predicts settlement stabilisation but too early.
In terms of horizontal displacement (Figure 4.31-C), the model is able to capture accurately the highest and lowest peak displacements.
The DEM model precisely captured the peak values, in contrast to the macroelement model even if the differences remain rather low.
Similarly, the discrete model captured accurately the rocking angle (Figure 4.31-B-D) positive peak. However, after the third cycle the model overestimates the negative rocking angle values, but here again, the differences with the experiment or the macroelement model remain pretty small. In addition, we observe a 'sudden shift' in the rocking angle after the third cycle. However, the exact cause of this phenomenon remains uncertain. It may be due to the foundation not settling uniformly on all soil particles, causing it to tilt suddenly from one equilibrium position to another when the horizontal force vanishes. Further investigation is needed to determine the underlying reason for this behavior.

4.6.4 Cyclic Phase III

In phase III, we compare our model 1 response with the TRISEE experimental results and results of a FEM model from Anastasopoulos et al. (2011).
The FEM considers a simplified constitutive model based on kinematic hardening, utilizing the Von Mises failure criterion. This model is integrated into commercial finite element software ABAQUS. Notably, the parameters of this FEM model have been calibrated using results derived from experimental results of cyclic simple shear tests (Vucetic and Dobry, 1991; Ishibashi and Zhang, 1993).
In Figure 4.32, we can see that the horziontal force applied resulted with the discrete model in almost the same experimental horziontal displacments applied at the top piston of the shallow foundation. Nevertheless the discrete model describes a global shift of the fondation (accumulated irreversible horizontal sliding of the foundation)

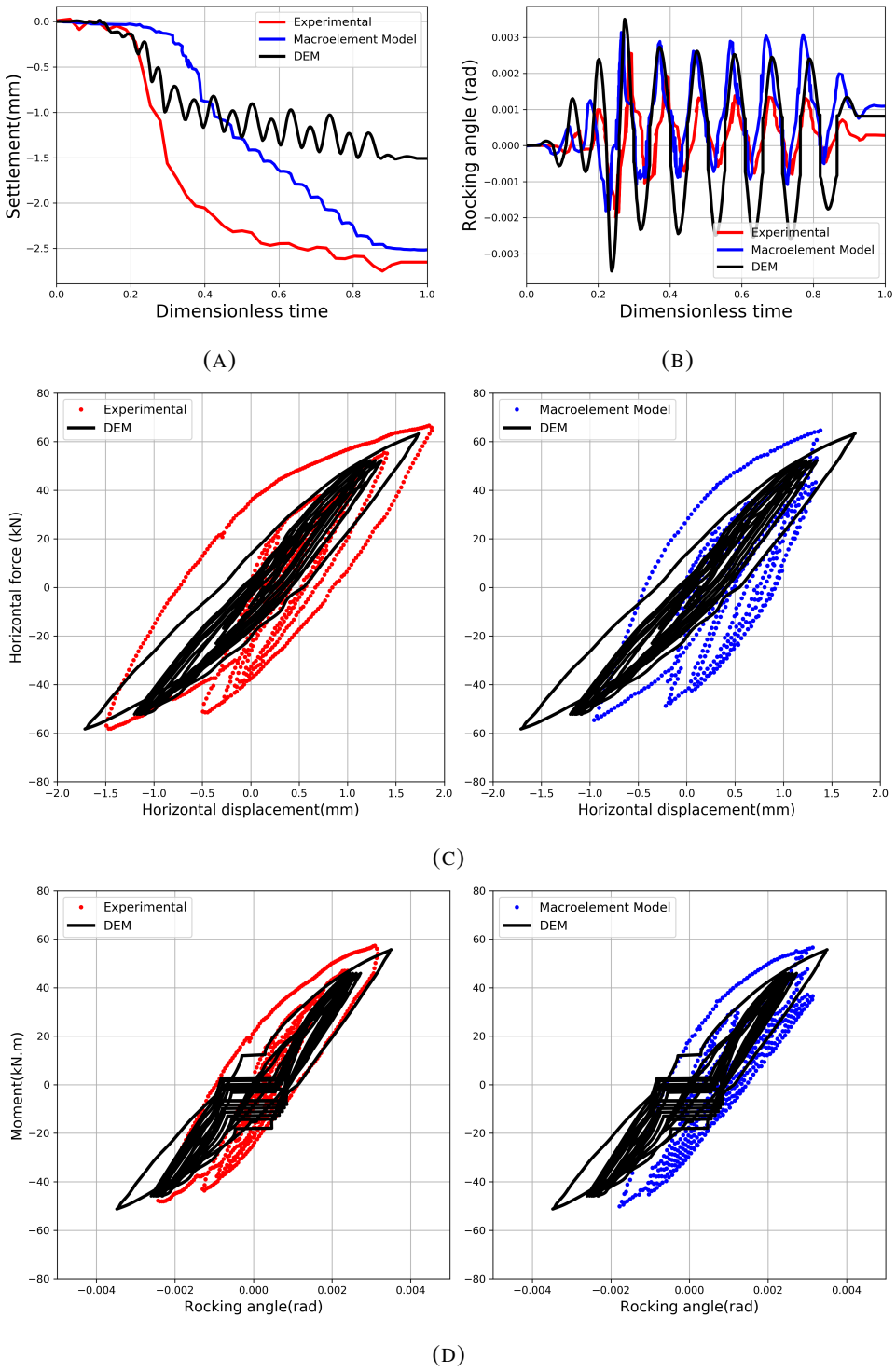

FIGURE 4.31: Cyclic Phase II loading on dense sand simulated with Model 1: comparison with (left) the experiment and (right) the macroelement model (Figini, Paolucci, and Chatzigogos, 2012)

in one horizontal direction whereas experimentally this shift is less important and measured in the other direction.

In Figure 4.33, the discrete model significantly underestimates the settlement (up to 5mm instead of 20 mm experimentally), whereas the FEM model overestimates it

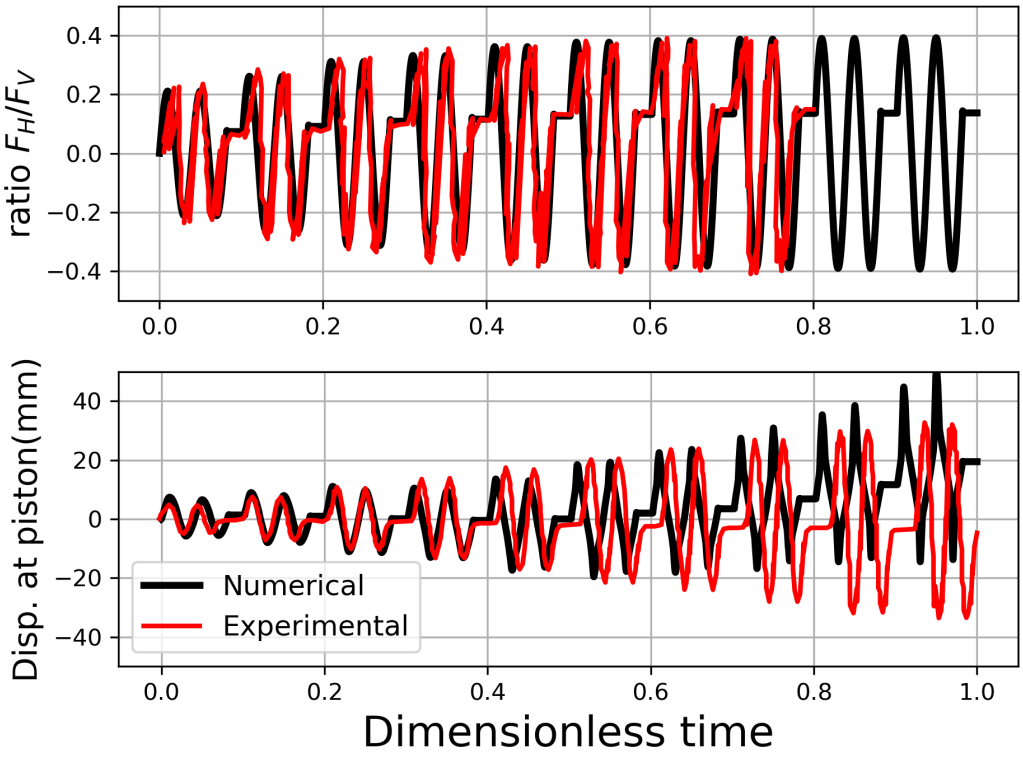

FIGURE 4.32: The horizontal force applied with the piston displacement obtained with the discrete model for the third loading phase on the dense Ticino sand.

(up to 25 mm after 7 pairs of cycles). The discrete model didn't predict accurately the experimental settlement. This discrepancy could be attributed to the numerically obtained value of K_0, which might be a contributing factor to the underestimated settlement or to the fact that the porosity of the sample was estimated by linear interpolation (a higher porosity may result in larger settlement).
Additionally, concerning the rocking angle, the DEM model successfully predicts the peak values similarly to the FEM model. However, in terms of horizontal displacement, the DEM model exhibits a sliding behavior at high horizontal loadings.
Horizontal displacement of the foundation is still described in Figure 4.34 while sliding at particle/foundation contact is locked. This means that the simulated displacement is probably the result of deformations within the soil itself below the foundation and not due to direct sliding of the foundation on the soil. However, in this latter case the simulated horizontal displacement is underestimated, while it was overestimated when sliding at soil particle-foundation contacts was allowed with a contact friction angle of 27° (Figure 4.33). Consequently, the horizontal displacement of the foundation may be the consequence of two mechanisms:

1. the sliding of the foundation on the soil.
2. the deformation of the soil below the foundation.

Thus, further investigation maybe be done on the choice of the interface contact friction.

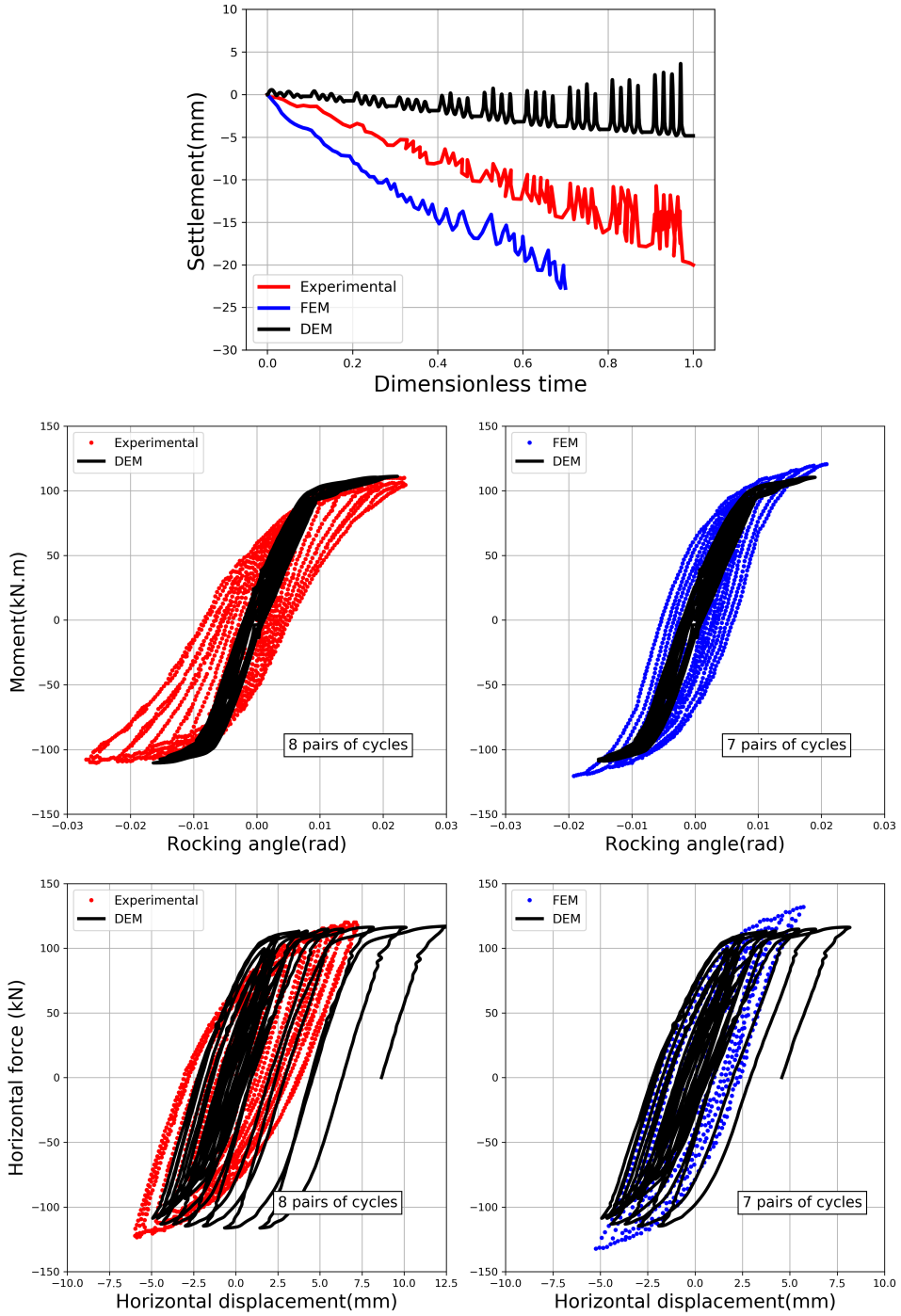

FIGURE 4.33: Cyclic Phase III loading on dense sand simulated with Model 1: comparison with the experiment and the FEM model (Anastasopoulos et al., 2011)

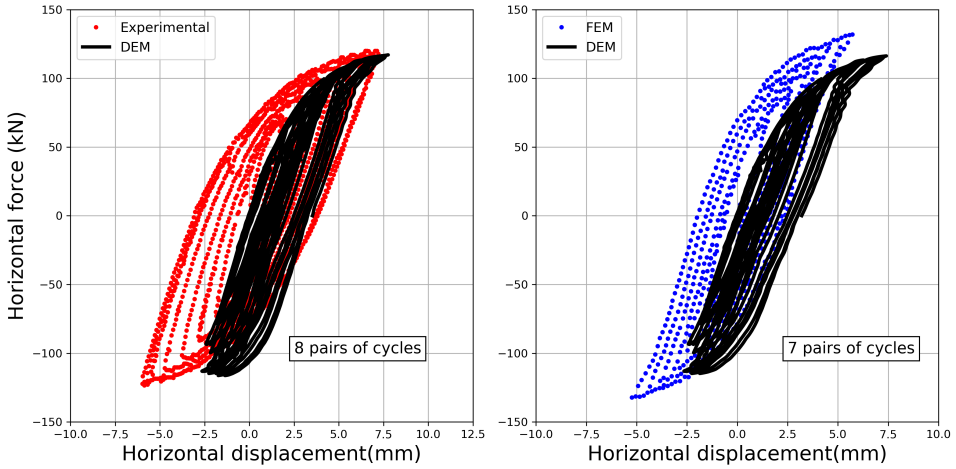

FIGURE 4.34: Simulated response to Phase III loading when sliding at particle/foundation contacts is locked.

4.7 Simulated response for the medium dense sand compared with experiments and other numerical models

In this section, we present a comparison of the DEM model's response in the case of the medium dense sand (D_R=45%) to both experimental data and various numerical studies, including Finite Element Models (FEM) and Macroelement Models (Table 4.4).

TABLE 4.4: Summary of different models used in comparison with the discrete model for the medium dense Ticino sand for Phases I, II, and III

Phase I	**Phase II**	**Phase III**
Macroelement model	**Finite element model**	**Finite element model**
Leblouba et al., 2016	Brandis, et al., 2021	Anastasopoulos et al., 2011
Based on the Bouc-Wen-Baber-Noori constitutive model involving 14 parameters	Based on the Takeda hysteretic model	Based on the kinematic hardening constitutive model involving 4 parameters

In the case of medium dense soil D_R=45%, a model was developed following a procedure similar to that used for the dense soil model, resulting in K_0=0.86. Since Model 1 (with 8,903 particles and ratio W_{SF}/d_{50} = 7.6) demonstrated promising results for dense soil with significantly lower computational time compared to other models with a finer discretization of the soil, it was chosen for the study of the medium dense sand.
We present in Figure 4.35 the distribution of the local porosity in different horizontal layers below the foundation at the initial state (i.e. just before the application of the

loading on the foundation). The vertical distribution of the porosity in the granular assembly below the foundation is rather well homogeneous.

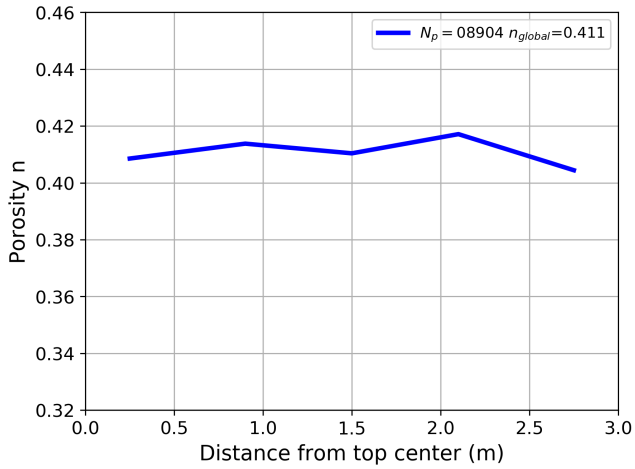

FIGURE 4.35: The local porosity of the medium-dense granular assembly built with adaptive discretization technique.

4.7.1 Monotonous loading

A vertical force is applied on the shallow foundation, resulting on a vertical stress of 100 kPa below the foundation, and the induced settlement is checked as shown in Figure 4.36. The discrete model underestimates importantly the final settlement. In particular, the model describes a linear response while the experimental one is much more non linear with an important reduction of the global stiffness of the soil-foundation system for a settlement around 1 mm. Such a non-linear response can be described by the model but for a higher vertical force (not shown in the figure). Only the slope of the unloading/reloading cycle is satisfyingly reproduced by the model.

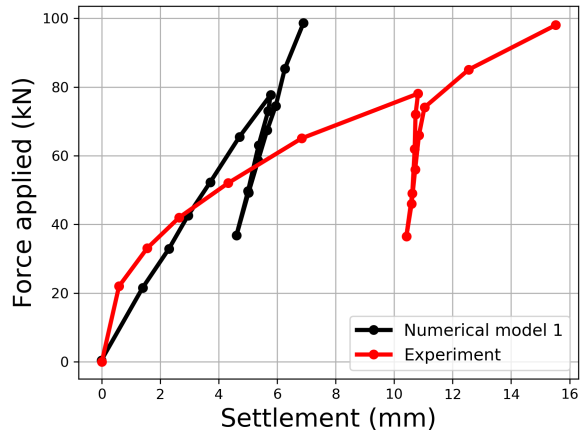

FIGURE 4.36: Monotonous vertical loading: response simulated with Model 1 compared to the one measured experimentally.

4.7.2 Cyclic Phase I

In Phase I, in case of medium dense soil, we compare our Model 1 response with the TRISEE experimental results and results of a macroelement model used by Leblouba et al. (2016) (the same model used in Phase I for dense soil in section 4.6.2) in Figure 4.37.
The discrete model globally overestimates settlement, horizontal displacement, and rocking angle. Concerning horizontal displacement, as discussed in the case of dense sand, this may be due to an inaccurate estimation of friction at the soil/foundation interface. However, these predictions remain reasonable in the context of a blind prediction. The description of the macroelement is quantitatively in better agreement with the experiments in terms of horizontal displacement and rocking angle, whereas the settlement was not provided. As mentioned previously, the macroelement model was calibrated using moment-rotation and horizontal force-displacement curves (not specified).

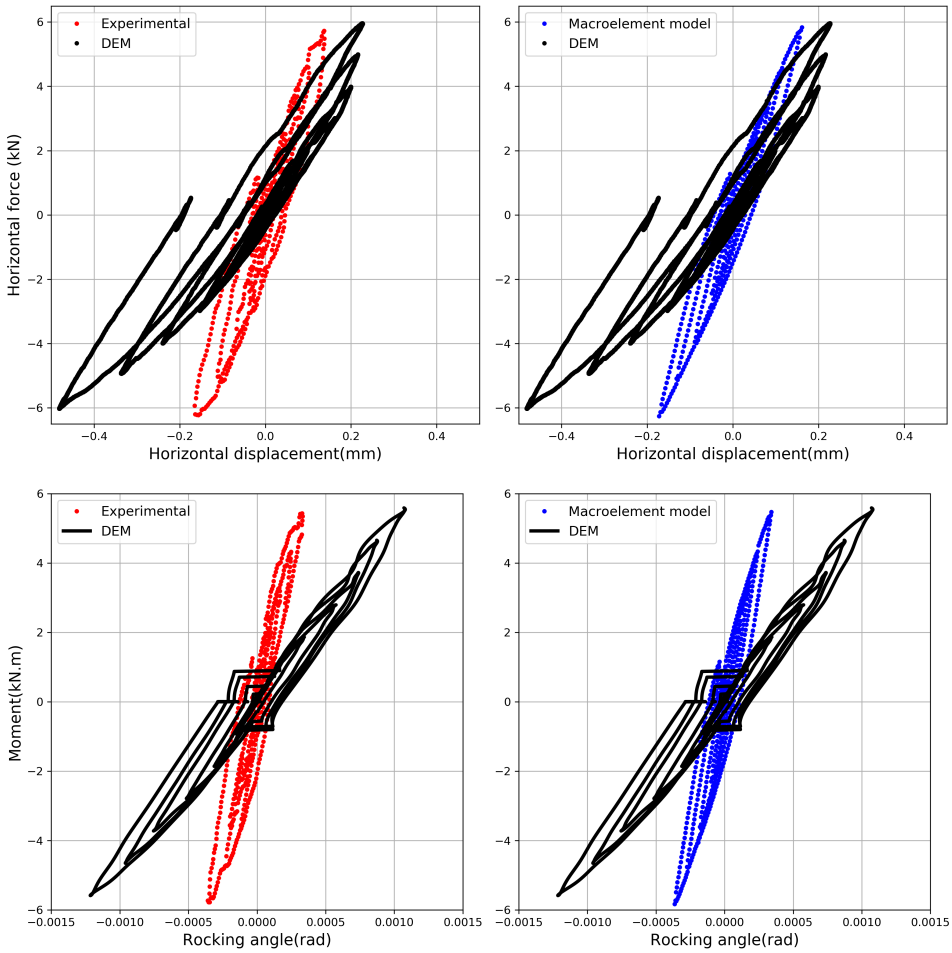

FIGURE 4.37: Cyclic Phase I loading on medium dense sand simulated with Model 1: comparison with the experiment and the macroelement model (Leblouba et al., 2016)

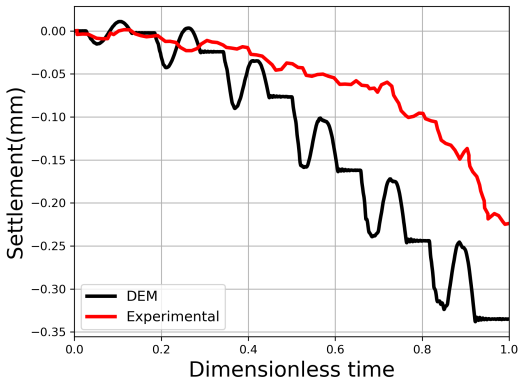

FIGURE 4.38: Cyclic Phase I loading on medium dense sand simulated with Model 1: comparison of settlement with the experiment

4.7.3 Cyclic Phase II

In the case of Phase II, we compare the response of our discrete model with a Finite Element Method (FEM) model used by Brandis, Kraus, and Petrovčič (2021). The Takeda hysteretic model (Takeda, Sozen, and Nielsen, 1970) was chosen to simulate the soil-foundation interaction in this FEM model, whereas, the shallow foundation itself was modeled using elastic frame and shell elements. In addition, it's important to mention that the Phase II from the TRISEE experiment was used for calibrating the model. However, the authors did not provide detailed information about the calibration process. The recorded loading curve is integrated into the FEM numerical model as a time history load.

In Figure 4.39, we compare the response of our DEM model with the experimental and the FEM results.

The final settlement simulated with the discrete model (up to 3.6 mm) is much lower than the one measured experimentally (of about 10 mm). The FEM model provides a closer estimation of the final settlement with 8.5 mm. However, the FEM model predicts a strong development of the settlement since the very initiation of the cycles, whereas experimentally they develop progressively during the first loading cycle (before a dimensionless time of 0.2) and more strongly after. The discrete model gives a better description of this initiation of the settlement than the FEM model. Then, as for the dense sand, the discrete model predicts a strong reduction of the development of irreversible settlements pretty early (at a time around 0.3, during the third loading cycle) compared to the experiments where the settlements continue to develop along all the cycles. The FEM model predicts a complete stop of the settlement as soon as a time of 0.3 (third loading cycle).

Concerning the horizontal displacement, as discussed previously the discrete model describes a global shift of the foundation horizontally which is not observed experimentally. However, for the FEM model, the authors do not provide information about the horizontal displacement of the foundation.

Finally, the rocking angle is fairly well estimated by the discrete model while an irreversible tilting of the foundation is described by the FEM model (the model was tilted before the loading by around 2°).

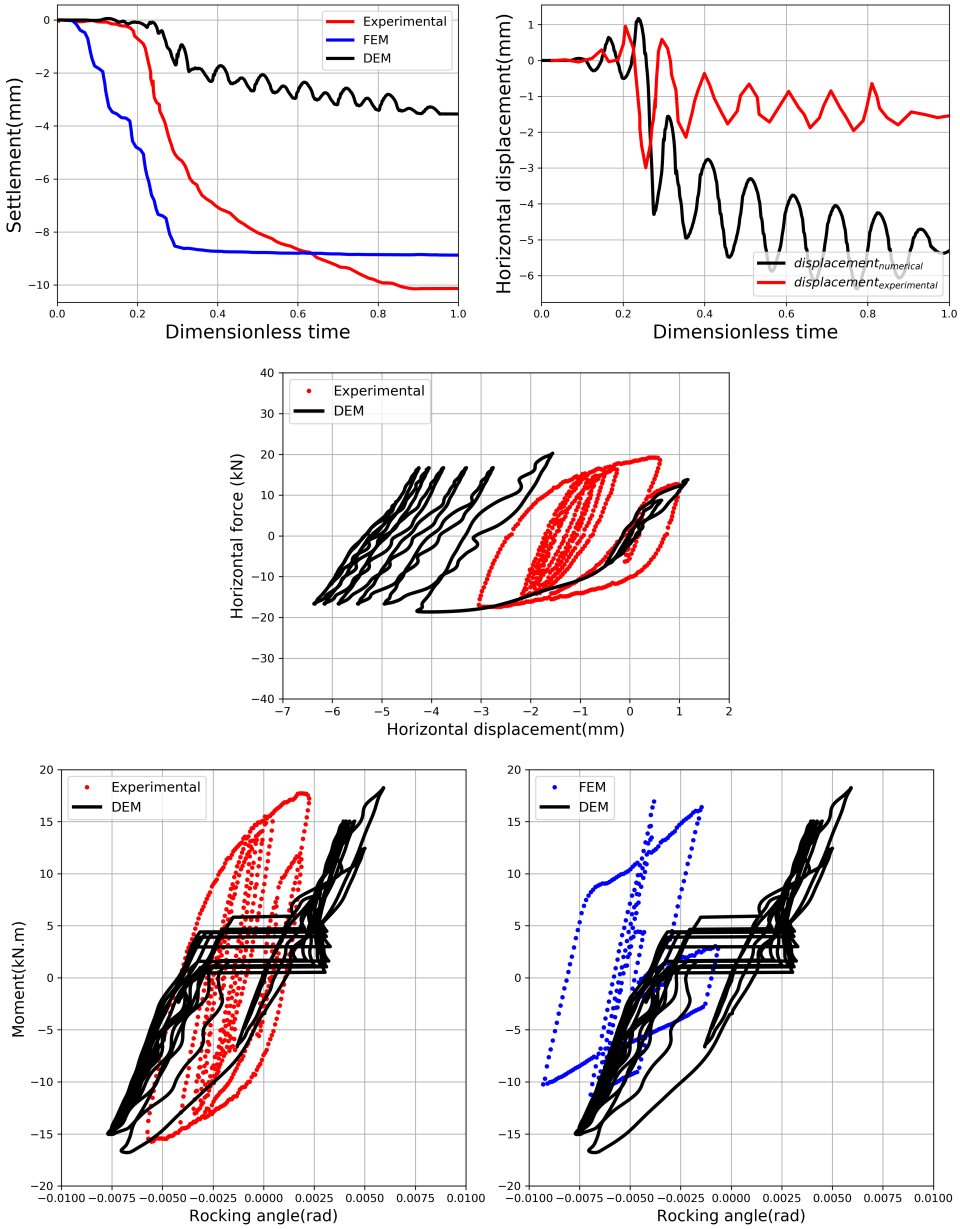

FIGURE 4.39: Cyclic Phase II loading on medium dense sand simulated with Model 1: comparison with the experiment and the FEM (Brandis, Kraus, and Petrovčič, 2021)

4.7.4 Cyclic Phase III

In Phase III, we compare our Model 1 response with the TRISEE experimental results and results of the FEM model by Anastasopoulos et al. (2011) (the same model used in Phase III for dense soil in section 4.6.4). The shallow foundation is subjected to the loading shown in Figure 4.40, with the resulting displacement (measured experimentally and simulated) at the top of the pilar above the foundation. In the discrete model, we impose the horizontal force that produces a corresponding horizontal displacement at the piston, which characterizes the system's response. However, the experimental and numerical responses were different in this case.

The response of our model is compared with the experiment and FEM in figure 4.41. In this last case, the discrete model fails to provide a reasonnable description of the response of the soil-foundation system. A final settlement of about 5 mm only is predicted while it reaches more than 60 mm experimentally. Moreover, large hysteresis were observed experimentally on the force-displacement plot and the moment-rocking angle plot. Such hysteresis are poorly recovered with the discrete model: concerning the horizontal displacement, the results are still affected by a global accumulated horizontal displacement probably due to a sliding of the foundation on the granular assembly. However, even if this global horizontal shift is discarded, only a weak hysteresis is expected on the force-displacement plot. Similarly, the hysteresis is largely underestimated for the moment-rocking angle plot. In other words, the soil below the foundation is subjected to important irreversible deformations and dissipative mechanisms that are almost discarded by the discrete model. On the contrary, The FEM model provides a very good description of the response observed experimentally.

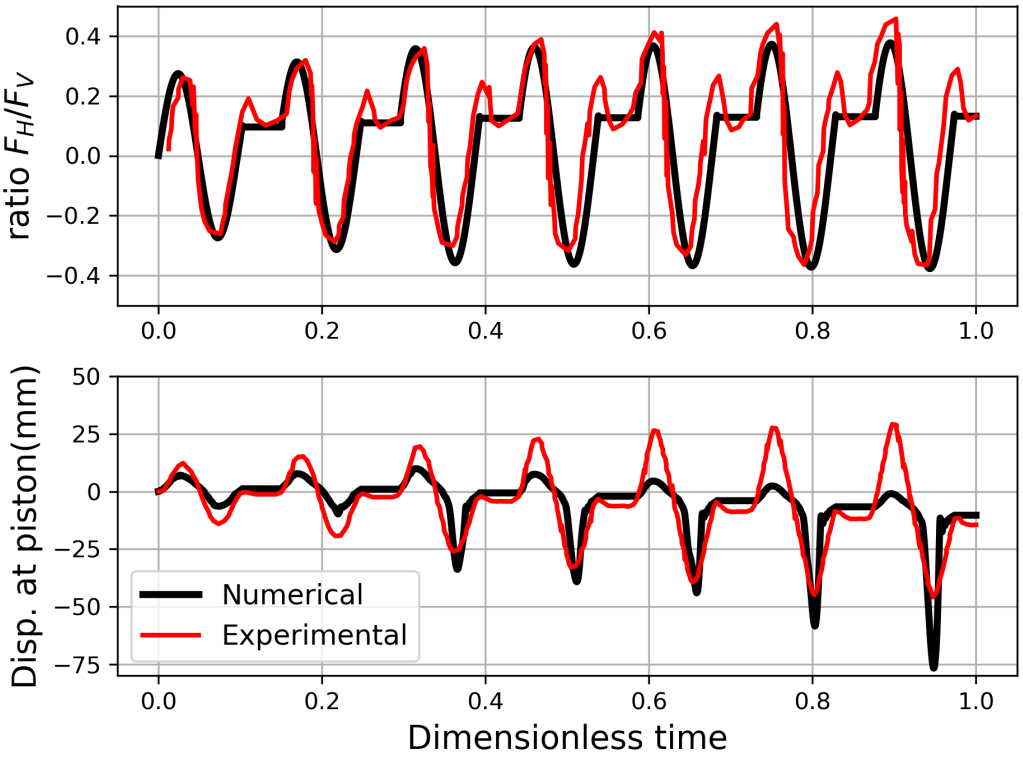

FIGURE 4.40: Cyclic loading Phase III: horizontal force applied on the system at the top of the pilar above the foundation (top) and resulting horizontal displacement at this same point (bottom).

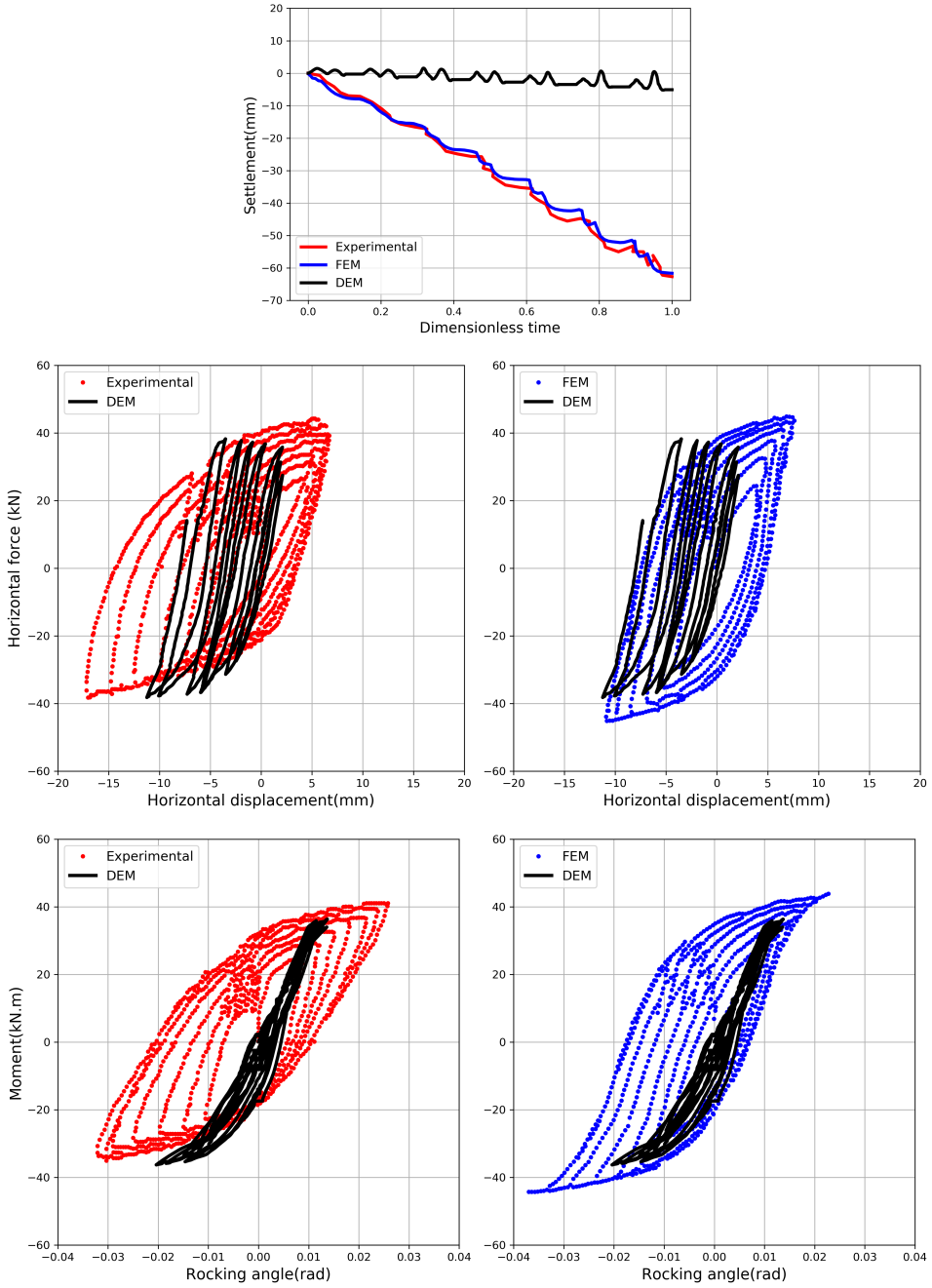

FIGURE 4.41: Cyclic Phase III loading on medium dense sand simulated with Model 1: comparison with the experiment and the FEM (Anastasopoulos et al., 2011)

4.8 Conclusion

In conclusion, the discrete model presented in this chapter has been calibrated on a single monotonous drained triaxial compression test only for the identification of the contact parameters. An additional compression test was used to identify the initial numerical porosity representing the medium dense Ticino sand. Such a calibration requires few experimental data compared to an experimental characterization of the cyclic properties of a soil, which is a significant advantage in engineering

applications. On the other hand, the Finite Element Method (FEM) often necessitates more advanced experimental tests, including the direct incorporation of cyclic loading data, to accurately calibrate constitutive relations. Moreover, macroelement models typically require an existing physical model as a reference for parameter calibration.
Additionally, the use of an adaptative discretization has made possible to address this boundary value problems for a relatively low computational cost (6 days of computation on a 3.70GHz four core of a conventional desktop computer to simulate the whole process including the generation of the initial state, the first monotonous loading and the three cyclic phases), making the approach practical for engineering applications if more advanced computational facilities are considered.
It was quite challenging objective to describe with the discrete model all the loading phases for the two initial sand densities, since numerical modellings published in the literature always focus on either some of the loading phases and/or a unique initial porosity. To summarize on dense sand, the discrete model gives the following results:

- A good description of the settlement under the application of the vertical force.
- It provides fair prediction of settlement, horizontal displacement and rocking angle for phases I and II. In particular, concerning the settlements in phase II the model predicts well the initiation of settlements and the fact that settlements stabilize after a given number of cycles despite the fact that this stabilization occurs too early with the model compared to the experiment. The macroelement model considered in this phase II fails in describing the initiation of the settlement and the final stabilization even it is assessing correctly the final settlement value.
- For phases I and II, the macroelement models could be considered as providing a better description of the experiments than the discrete model but actually it is worth noting that for phase I the response simulated is of a macroelement model that is calibrated using experimental moment-rotation and horizontal force-horizontal displacement curves. For phase II it is a true predictive simulation but for a calibration on the phase I (so a physical model, or in-situ measurement on an existing structure are necessary to calibrate the model, etc...).
- Concerning the phase III, even if the response simulated with the discrete model remains realistic, it underestimates the settlement and the hysteresis of the moment-rocking angle and the force-displacement curves. The FEM model used for comparison overestimates the settlement but provides good descriptions of those hysteresis. Nevertheless, the constitutive relation used in the FEM model was calibrated on cyclic tests, contrary to the discrete model which considers only a monotonous compression.

For the medium dense sand: the ability of the discrete model to catch the response of the soil-foundation interaction should be improved. It globally underestimates importantly the irreversible and non-linear mechanisms occurring in the soil below the foundation, except for the loading phase I.

As the way to calibrate the discrete model focuses more on the macroscopic plastic response of the Ticino sand than on its elastic properties, we expected a possible lower accuracy in the predictions for the first loading phases (when the mechanical state in the soil is far from the failure state) than for the third loading (where the loading is increased in such a way to trigger the failure of the soil).
Consequently, this unexpected trend has to be investigated and we present here after some first results obtained with investigations made in this direction. Therefore, Granular assembly with anisotropic fabric are simulated using oedometric compression, similar to the method described in Chapter 3 as illustrated in Figure 4.42. This approach resulted in granular assemblies characterized by a different K_0 value at the initial state (ie at the state just before the application of the loading program with the foundation). Specifically, in case of assemblies compacted isotropically the coefficient K_0 is equal to 0.85, while anisotropic compactions led to different K_0 values equal to 0.75 and 0.65 for two different anisotropic compactions.
From Figure 4.43, we can conclude that final settlement is highly dependent on the initial fabric of the granular assembly. Thus, further investigation of the initial fabric conditions should be carefully considered for the modeling of the foundation problem, to understand their impact on the settlement behavior.
Furthermore, we compare the response of two simulations (spheres of density equal to 2690 kg/m^3) with different n and K_0 during all loading phases as shown in Figure 4.44. We can observe how settlement increases with the increase of initial porosity, even though the K_0 value is greater for the same simulation with higher porosity. Thus, in addition to K_0, we observe that even a small change in initial porosity may affect the settlement response. Therefore, we should be careful when estimating the initial porosity. In our dense model, we estimated the initial porosity through linear interpolation since no models were calibrated for soil of $D_R = 85\%$.

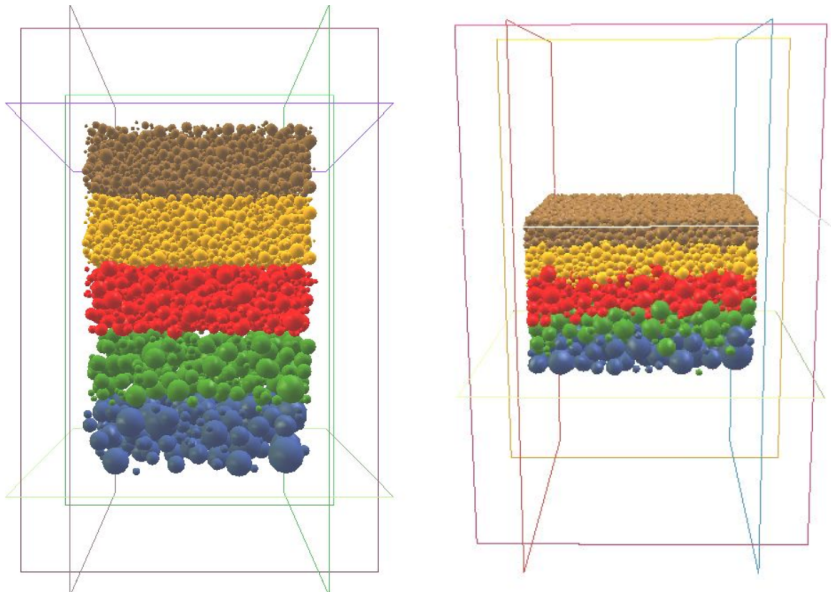

FIGURE 4.42: Sample preparation using oedometric compression to generate anisotropic fabrics

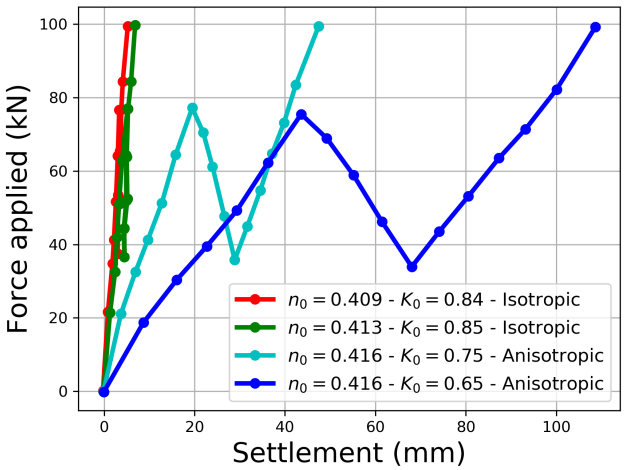

FIGURE 4.43: Monotonus load response on medium dense samples with different n and K_0.

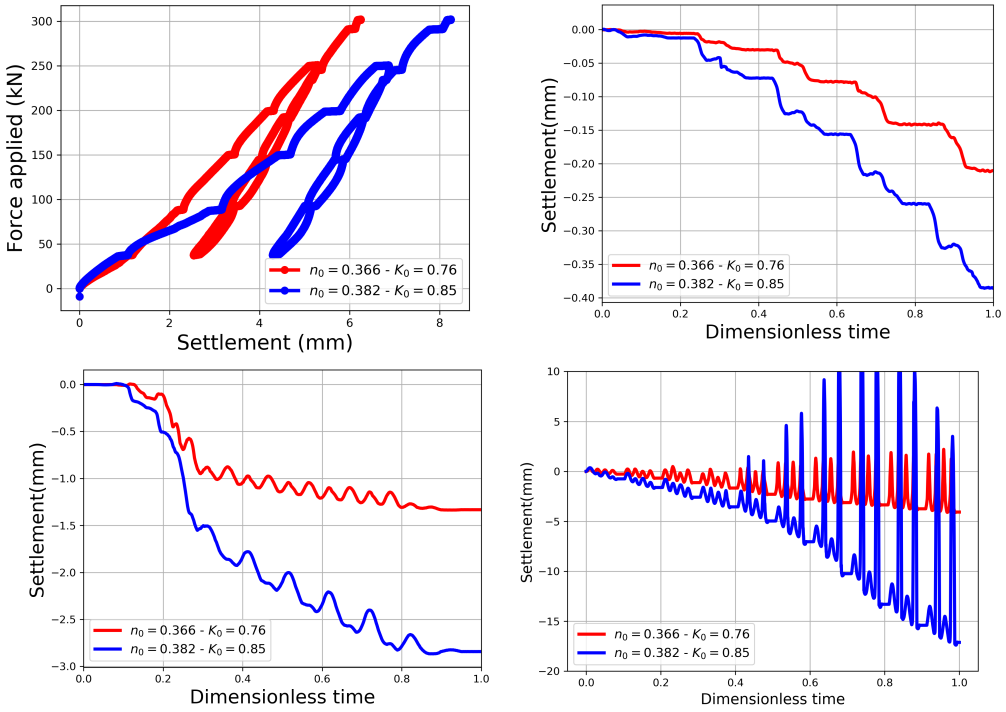

FIGURE 4.44: Settlement of the foundation simulated for different initial porosity n and K_0 for all the loading phases

Chapter 5

Numerical interpretation of the phicometer

5.1 Introduction

In geotechnical engineering, the determination of soil mechanical properties is essential when it comes to evaluating the stability of construction projects and structures. Thus, the measurement of shear resistance, characterized by both the internal friction angle and the cohesion is important. In practice, the determination of these parameters is often done using laboratory-based triaxial tests or direct shear tests carried out on field samples. However, the reliability of these measurements depends on the careful sampling, preservation, and preparation of these samples to ensure that they accurately represent the in-situ conditions.
In addition to that, it's important to mention that many types of soils and materials present challenges for geotechnical engineers because they don't meet these strict conditions. These include medium to coarse sand, chalks, sand stones, etc. Given this context, it becomes crucial to consider in-situ testing methods, which offer a valuable alternative for assessing shear resistance and other critical properties of soils and materials under realistic, field-like conditions. Classical field tests as Standard Penetration Test (SPT), Cone Penetration Test (CPT) or Pressuremeter Test, provides reliable information about the shear strength of soil but do not give directly access to the parameters defining the Mohr-Coulomb criterion.
The phicometer test (Philipponnat, 1986) offers direct access to intrinsic strength parameters: internal friction angle and cohesion. It consists of a probe constructed as a slotted tube with metal teeth as shown in Figure 5.1. These teeth designed to penetrate in the borehole when the probe is inflated as a pressuremeter probe. As the probe expands laterally, its geometry undergoes changes, specifically affecting the width of openings in between the teeth. The presence of these teeth and their complex behaviour during lateral expansion when the probe is inflated results in unknown or unidentified shear surface. Thus, Arpaia, Heintz, and Reiffsteck (2015) studied the effect of the change of the geometry of the phicometer probe on the results using a modified version of the direct shear experiment in (Reiffsteck et al., 2007), by equipping the plate with teeth and lateral grooves.
In this experimental study, the determination of the friction angle and cohesion appears to be significantly influenced by the interpretation methodology considered. In particular, different assumptions can be made regarding the shear surface at the interface between the probe and the soil. Considering this shear surface as constant or

allowing it to evolve during the test (due to probe inflation) can impact the results. However, experimentally identifying the shear surface and its shape is challenging; it would, for instance, require determining the strain field from X-ray tomographies. Alternatively, the discrete element method can be used to investigate numerically how the shear surface is affected by the radial dilation of the slotted tube and whether the locally developed shear stress in the sheared zone differs from the macroscopic one deduced by assuming a given shape of the shear surface. This investigation constitutes the main objective of this work.
The outline of this chapter is as follows: the first part is dedicated to describing the Phicometer test, including its procedure and interpretation. Following this, the experimental investigation of soil-teeth interactions is presented, involving a modified direct shear test conducted with a plate featuring teeth. Next, the numerical model of the modified direct shear test is introduced. A parametric study is performed to analyze the impact of teeth and direct shear test box geometry. Additionally, a shear surface is proposed. Finally, the local shear stress in the sheared zone is determined using different assumptions and compared with the macroscopic stress. In conclusion, the main findings of this chapter are discussed.
This work was carried out within the framework of the master internship of Merhebi (2022), which I co-supervised during this PhD.

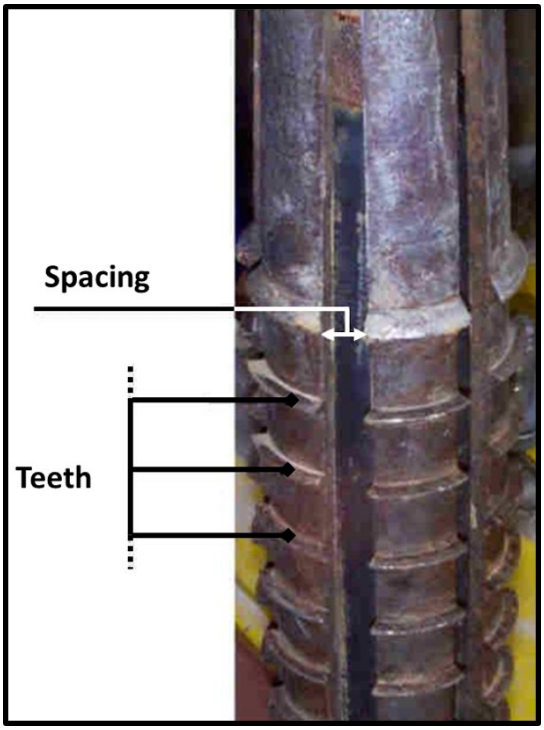

FIGURE 5.1: Phicometer: View of the expandable probe and its teeth (Arpaia, Heintz, and Reiffsteck, 2015)

5.2 Principle of phicometer test and interpretation

The Phicometer was developed in 1986 (Philipponnat, 1986) with a similar concept to the "borehole shear test". It allows in situ shearing tests to be carried out with a

pressuremeter and accessories as presented in Figure 5.2, in accordance with the **XP P94-120 AFNOR standard**. It measures the shear strength characteristics of the soil, the internal friction angle, ϕ and the cohesion, C. Its advantages are the possibility of performing tests on ground which cannot be sampled or which is difficult to sample and the low cost of this test method. Therefore the tests are faster and simpler than laboratory shear tests. A drawback of the phicometer with respect to SPT or CPT is that, as for the pressuremeter test, a borehole has to been realized prior to making the shear test, which may present difficulties for some kinds of soils.

5.2.1 Description of the Phicometer apparatus

The Phicometer apparatus, consists of three key components, as shown in Figure 5.2:

- **Phicometer Probe:** a hollow cylindrical slotted tube with a radially expandable cell. The central part of the probe features a series of annular teeth to form the cylindrical shearing surface.
- **Link and Connection Devices:** rods and tubes for connecting the phicometer probe to control and measurement equipment located at the ground surface, including fluid injection.
- **Control and Measurement Equipment:** situated at ground level, this equipment includes a pressure-volume controller to measure cell volume and control ground pressure, two bearing plates for apparatus stability, a hollow jack for applying pull-out shearing effort, and a force measuring device to measure the shear force.

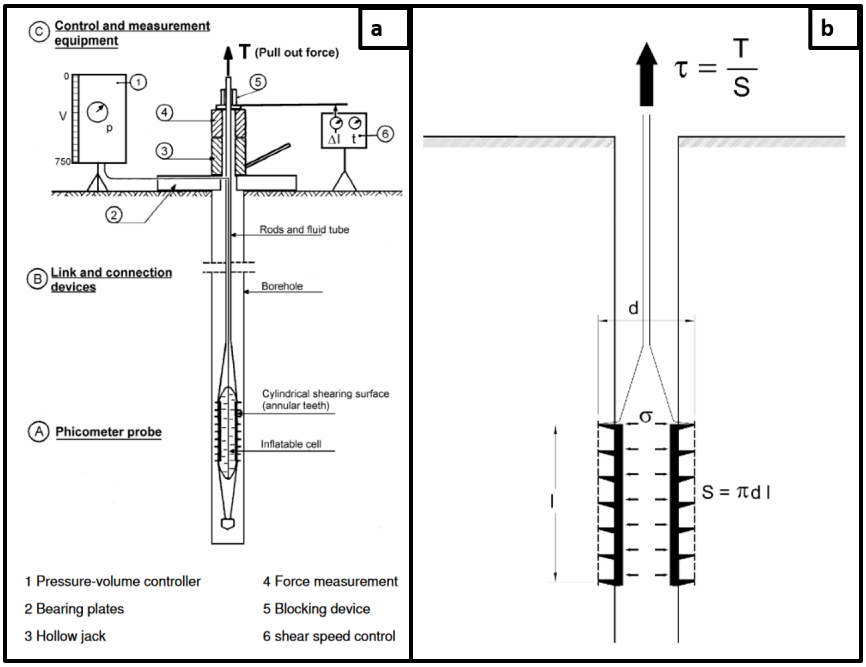

FIGURE 5.2: Scheme of the phicometer (Arpaia, Heintz, and Reiffsteck, 2015)

5.2.2 Procedure of phicometer test

The phicometer shear test involves inserting the phicometer probe into a pre-drilled borehole at a specified depth. The probe is then inflated so that the teeth penetrate into the surrounding soil in the borehole. The normal stress σ is applied to the circumscribed surface S. Afterward, the soil is sheared by pulling the probe slowly from the ground surface at a controlled speed.This results in the mobilized limit force T, which corresponds to the shear stress τ.
Throughout the pull-out shearing process, the probe's internal pressure is maintained at a constant level. The test consists of performing multiple shears at the same level and at different normal stress levels, allowing for the determination of the mechanical properties of soils, including the internal friction angle and soil cohesion from the relationship between applied normal pressure and the corresponding shearing resistance of the tested material. The AFNOR standard XP P94-120 provides detailed guidelines on the test procedure and the loading steps program.

5.2.3 Calculation of the limit shear stress

To determine the characteristics of resistance of a soil layer according to XP-94-120 standard we need to consider a shear surface area. The parameters ϕ and C are determined for each selected measurement step in the representative test zone, thanks to a key value being the shear stress τ. The conventional limiting shear stress τ is calculated using the following formula:

$$\tau = \frac{T_L}{\pi\, l_s\, d_s} \tag{5.1}$$

Where:

- T_L = Limit pull-out force.
- l_s = Conventional length of the measurement area.
- d_s = Overall outside diameter of the measurement area after the injection of a volume deduced from the calibration curve $V = f(d_s)$.

The term $\pi\, l_s\, d_s$ represents the sheared surface, which is dependent only on d_s. This means that the sheared area considered during the tests increases with the diameter of the probe d_s (which varies with the expansion of the probe).
The determination of the friction angle ϕ and the cohesion C measured in situ with the phicometer involves considering the linear regression curve (Figrue 5.3) using the least square method:

$$C = \arctan\left(\frac{n\sum\sigma^2 - \sum\sigma\,\sum\sigma\,\tau}{n\sum\sigma^2 - \left(\sum\sigma\right)^2}\right) \tag{5.2}$$

For cases where $C > 0$, we calculate ϕ as:

$$\phi = \arctan\left(\frac{n\,\sum\sigma\,\tau - \sum\sigma\,\sum\tau}{n\sum\sigma^2 - \left(\sum\sigma\right)^2}\right) \tag{5.3}$$

For cases where $C < 0$, we calculate ϕ as:

$$\phi = \arctan\left(\frac{\sum \frac{\tau}{\sigma}}{n}\right) \tag{5.4}$$

Where:

- τ: conventional limiting shear stress.
- n: number of tests.
- σ: normal stress.

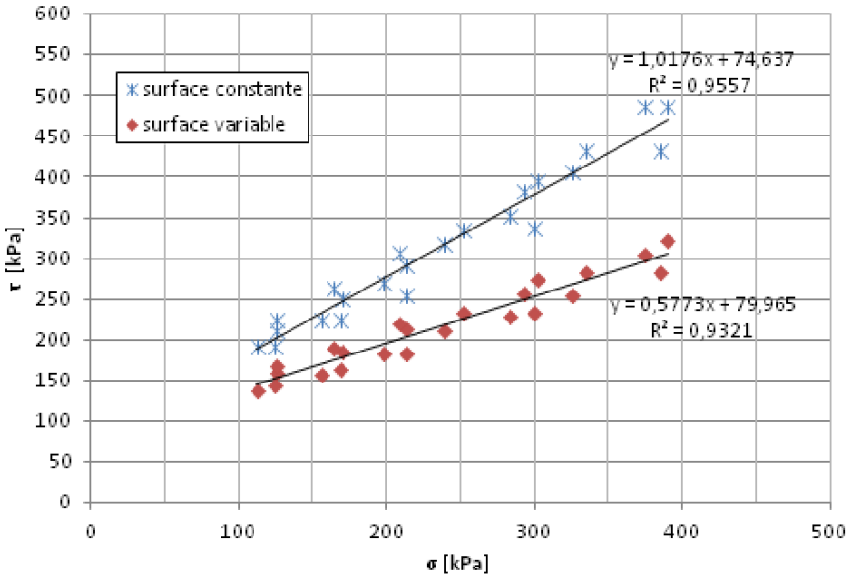

FIGURE 5.3: Interpretation of ϕ and c: constant vs variable shear surfaces

However, it's important to note that during probe inflation, the space in the teeth increases (Figure 5.1). Thus, Equation 5.1 takes into account an increasing shear area during the test, whereas a non-negligible part of it is not actually occupied by the shear expansion tube. As a result, a new formula has been proposed to consider a constant shear surface corresponding to d_{s0}, which is the surface occupied by the teeth of the probe, regardless of the injected volume.
The new formula for the conventional limiting shear stress τ is:

$$\tau = \frac{T_L}{\pi\, l_s\, d_{s0}} \tag{5.5}$$

Where d_{s0} is the overall external diameter of the unexpanded measurement zone. The results from (Heintz, 2001) show that assuming shearing only occurs on the surface of the teeth (with a diameter of d_{s0}) leads to an increase in ϕ and a decrease in C, and can even yield a negative value for C. However, limiting the shear to the teeth tends to reduce result variability. In conclusion, it is necessary to carry out reliable modeling tests of the physical phenomenon and sufficiently precise experimental verification

of the exact shearing surface, to be able to propose the modification of the XP-94-120 standard (Arpaia, Heintz, and Reiffsteck, 2015). Therefore, an experimental direct shear test done by Arpaia, Heintz, and Reiffsteck (2015) was done to understand the effect of the increase in the teeth spacing during the phicometer test and more details will be addressed in the following sections. In addition, a discrete element model could help in identifying the shape of the shear surface.

5.3 The experiment: modified direct shear test

To understand the influence of groove and teeth geometry on the measured shear characteristics of the phicometer, a study was conducted by Reiffsteck (2022), using customized version of the direct shear test described in (Reiffsteck et al., 2007). This research was carried out at the "Laboratoire Régional des Ponts et Chaussées of Rouen". The goal of this investigation was to assess the influence of various parameters, including tooth size, inter-tooth spacing, and the particle size distribution of granular materials.
To achieve this goal, a series of test plates with different configurations were created for the modified direct shear test. Two reference soils, a fine grained (Fontainebleau sand) and coarse grained (Criquebeuf gravel), were selected to stay within the device's range of applications (Reiffsteck, Nguyen Pham, and Arbaut, 2007).

5.3.1 Description of the modified direct shear test

The modified direct shear test is presented in Figure 5.4. It is made up of a large square sectioned box with dimensions measuring 500 mm in length, 500 mm in width, and a total height of 300 mm, increased by a gap between the two half boxes. The apparatus consisted of a lower half-box containing the soil and a plate with teeth placed in the top box. The shear resistance is measured at the interface between the soil and the plate with teeth.

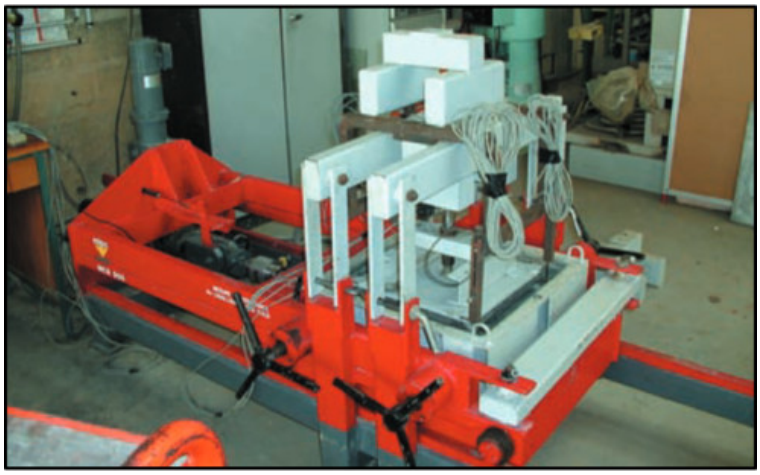

FIGURE 5.4: The direct shear test (Reiffsteck et al., 2007)

5.3.2 The geometry of the plate

The dimensions used to define the shape of the metal plates, mimicking the phicometer probe, are illustrated in Figure 5.5. According to the Phicometer standard XP P 94-120, the teeth on the plate were supposed to be shaped with trapezoidal profile. However, for the sake of simplicity, the plates were equipped with teeth with a rectangular cross section.
Four plates with different groove spacing are created. The teeth are distributed along the whole width of the plate, rather than matching the probe's unrolled perimeter.
These plates are made according to the phicometer's standard dimensions, which are as follows:

- gap between teeth: a = 22.5 mm
- tooth height: b = 5 mm
- tooth width: e = 2.5 mm
- groove spacing: s = 0, 4, 8, and 12 mm

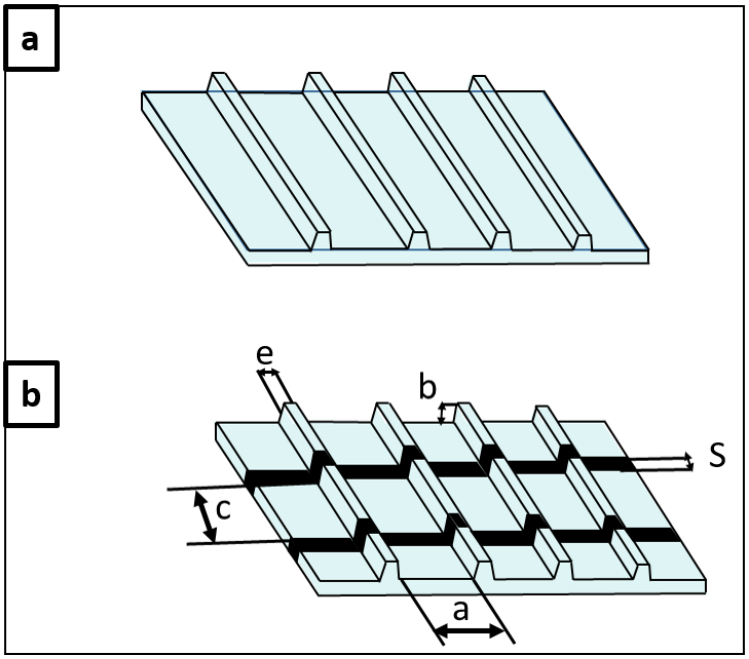

FIGURE 5.5: The plate geometry with different Groove spacing s: (a) $s = 0$ mm. (b) $s = 4$, 8, and 12 mm after Reiffsteck (2022)

5.3.3 Outcomes of the modified direct shear test

The influence of the geometric parameters of the plate, particularly the spacing of the Phicometers' grooves, showed that cohesion tended to increase while the friction angle decreased with increase in the grooves spacing. The grooves' spacing had a noticeable impact, making it seem like the probe's expansion resulted in an overestimation of cohesion and an underestimation of the friction angle. However, it's

important to note that these effects, although significant, were relatively small when considering the precision of the measurements.
In addition, significant differences are observed depending on whether a constant or variable shear surface is considered (Figrue 5.3).

5.4 Numerical model of the direct shear test

To model the modified direct shear test, a similar procedure as the experiment was followed, but instead of having the plate with teeth on the top part of the box we place it on the bottom part and gravity is not taken into account. In the simulation, the plate with teeth is defined as a rigid wall. The granular assembly of particles was modeled using spheres, and the inter-granular contact law between particles was governed by the classical dry friction model with rolling resistance limiting the relative rotation of particles. The particle size distribution of the numerical sample was chosen as that of the Fontainebleau sand and represented in Figure 5.6.

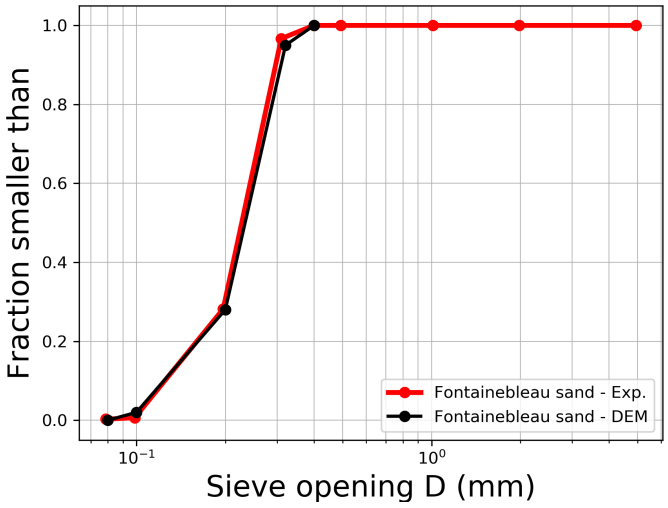

FIGURE 5.6: Particle size distribution reference soils and one used in DEM model

5.4.1 Model geometry

To numerically model the modified direct shear box based on experimental data, it's crucial to determine the appropriate number of particles for an accurate representation. Having too few particles would make the model non-representative, while an excessive number would make the simulation inefficient.
Firstly, to minimize the box's size and reduce the number of particles, we reduced the number of teeth in both horizontal directions. We configured the box initially with 5 rows of teeth (3 rows below the sample initially) with 2 spacings (if any) on a given row as shown in Figure 5.7. The specific geometry of these teeth and the box, configuration is detailed in Table 5.1.
To determine the suitability of these geometries for detecting the shear surface area

accurately, we conduct a parametric research based on strain field induced by the shearing. An initial cloud of 29,000 particles is used in the simulations.

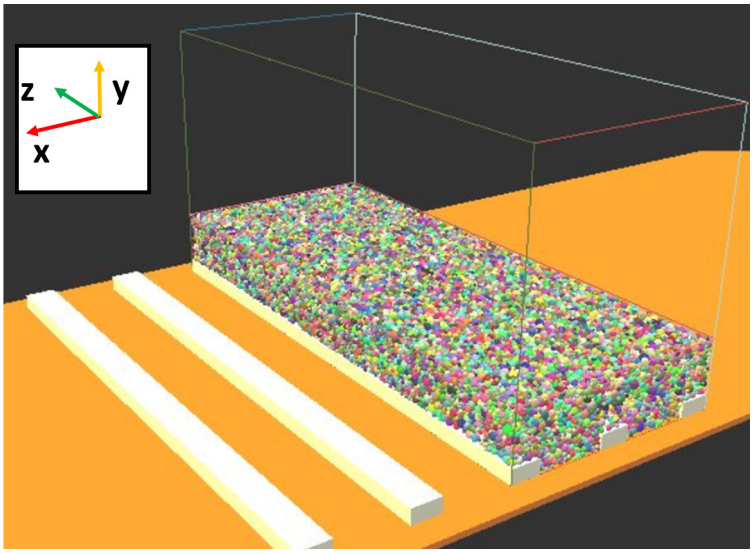

(A) Groove spacings = 0 mm

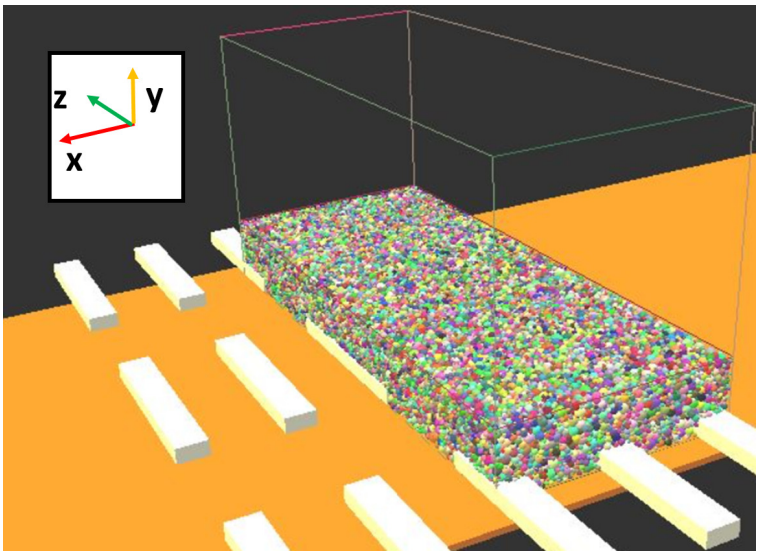

(B) Groove spacing = 4 mm

FIGURE 5.7: Discrete numerical model of the modified direct shear test

TABLE 5.1: Geometry of the teeth and box used in a modified direct shear box (DEM).

Teeth				Box		
height (b)	width (e)	gap (a)	length (c)	Height (H)	Width (W) ((3 × e)+(3 × a))	Length (L) (3 × c)
1 mm	1 mm	2.25 mm	3.04 mm	9.12 mm	7.5 mm	9.12 mm

5.4.2 Simulation procedure

The simulations included three main stages: sample preparation, application of axial stress until reaching the desired stress level, and finally shearing under a constant normal stress as shown in Figure 5.8.
First we start with the creation of a box containing a plate at the bottom, featuring rectangular-shaped teeth. Groove spacings "s" equal to 0 mm and 4 mm are considered in the model. Following this, a cloud of spherical particles is generated, with the size distribution found in Fontainebleau sand. The sample was then compacted by applying normal stress until the target normal stress equal to 50 kPa is reached, and the equilibrium is sufficiently close to the static state. This equilibrium was verified by assessing the unbalanced force which is the ratio of the mean resultant particle force to the mean contact force (Figure 5.8). The initial porosity n_0 reached after compaction is around 0.39 for all models in this chapter. Subsequently, the shearing phase is applied until a 10% displacement of bottom plate is achieved. The shear forces were computed at the plate-soil interface by dividing the sum of the forces by the total area of the plate.

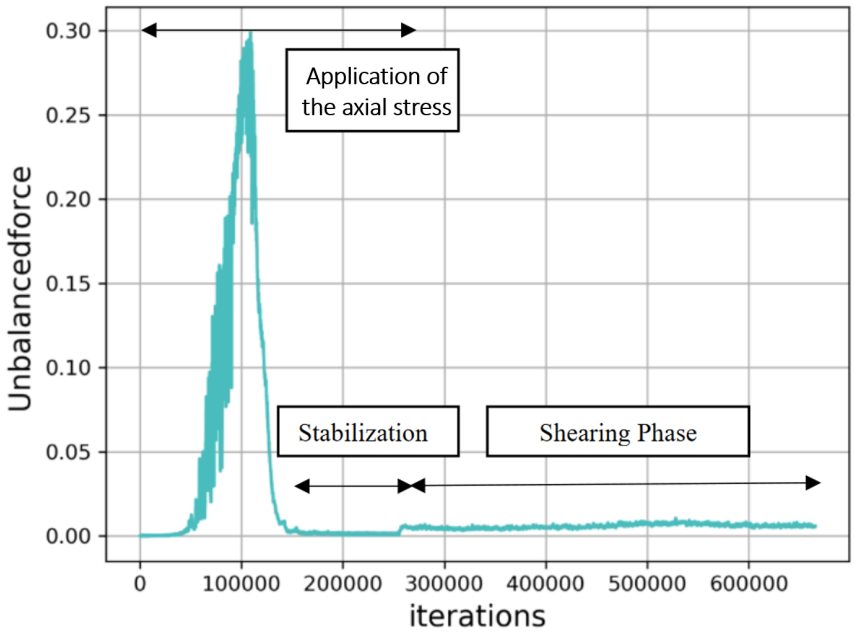

FIGURE 5.8: Evolution of the dimensionless unbalanced force

5.5 Parametric study

Selecting optimal values for various numerical parameters relevant to this application required thorough evaluation. However, it was not possible to calibrate the model as no experimental volumetric deformation data is available. Thus, the parameters in Table 5.2 served as a reference point for making these selections. Rolling friction was not considered in the contact law during the Parametric study.

TABLE 5.2: Reference parameters of the DEM model.

E_c(MPa)	α_t	ϕ_c
100	0.3	30

5.5.1 Shear velocity

During the shearing phase, the normal stress remains constant. The direct shear test starts by imposing a velocity perpendicular to the direction of the teeth (in the horizontal plane). Selecting an appropriate shearing velocity is important, as it affect the computation time and may also affect the simulated shear strength due to inertial effects. Several simulations were conducted, each with varying shearing velocity values, to determine the optimal choice as shown in Figure 5.9.

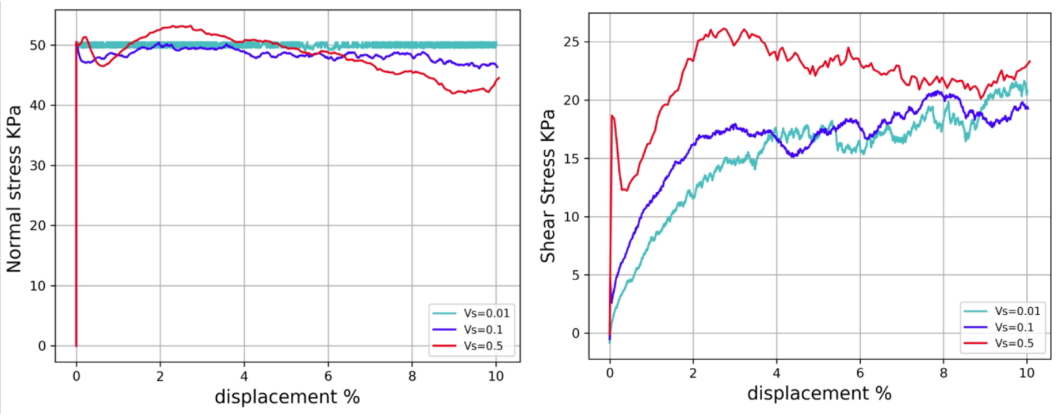

(A) (B)

FIGURE 5.9: a- variation of normal stress, b- variation of shear stress, and (for three different velocities)

During the shearing phase, a velocity of 0.01 m/s has negligible impact on the normal stress. However, velocities greater than 0.01 m/s result in a noticeable variation in the normal stress and in an overestimation of the shear stress. Thus, a value of 0.01 m/s has been selected for use in subsequent simulations.

5.5.2 Effect of the teeth and box geometry

After completing the sample preparation and applying the load, an evaluation will be performed to examine the influence of teeth and shear box size on the shear surface to identify the optimal configuration and possible effects of boundaries if the box is too small. Various scenarios were examined, considering different dimensions of teeth height, and shear box height and length. To assess their effects, the strain field resulting from these configurations was analyzed utilizing Paraview, a multi-platform open-source application designed for interactive scientific visualization. In the following subsections, we define the microstrain field and consider its application in examining these scenarios.

Microstrain definition

The microstrain is defined at the scale of particle-centered subdomains as shown in Figure 5.10 by Catalano, Chareyre, and Barthélemy (2014). The sketch in Figure 5.10 is in 2D for the sake of readability but the computation is actually performed in 3D. The microscale strain tensor for one particle is defined as a function of the displacements of the particles adjacent to that particle in the regular triangulation, which defines the polyhedral domain V_ϵ. The average displacement gradient in an equivalent continuum that would be contained in V_ϵ is given by:

$$\langle \nabla \mathbf{dx} \rangle = \frac{1}{V_\epsilon} \left(\int_{V_\epsilon} \nabla \mathbf{dx} \, dv \right) = \frac{1}{V_\epsilon} \left(\int_{\partial V_\epsilon} \mathbf{dx} \otimes \mathbf{n} \, ds \right) \tag{5.6}$$

where the displacement $\mathbf{dx}$ on the contour ∂V_ϵ is defined as a piecewise linear function equal to the displacement of the particles at the vertices and linear on each facet. Then, as the symmetric portion of the gradient, the microstrain is obtained:

$$\epsilon = \frac{1}{2} \left(\langle \nabla \mathbf{dx} \rangle + \langle \nabla \mathbf{dx} \rangle^T \right) \tag{5.7}$$

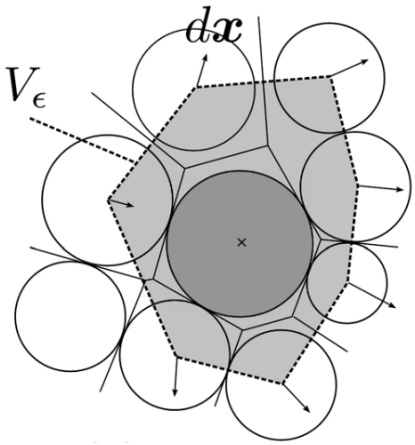

FIGURE 5.10: Domain surrounding the particle used to define microstrain from (Catalano, Chareyre, and Barthélemy, 2014).

Effect of the teeth height

To investigate how the teeth height impact the development of the shear surface, we investigated three different teeth heights (h = 0.1, 0.5 and 1.0 mm) while all the other sizes are kept unchanged and as given in Table 5.1. Enabling an exploration of its influence on the shear surface area. We maintained a fixed ratio d_{50}/e, where $d_{50} = 0.23$ mm represents the median particle size, and e is the width of the teeth.
The shear strength is importantly improved for h = 0.5 mm with respect to h = 0.1 mm (Figure 5.11). Nevertheless, considering higher teeth height, with h = 1.0 mm does not affect more the shear strength of the soil-plate interface.

To analyze the deviatoric strain field results, a cross-section is considered in the middle of the sample perpendicular to the main axis of the teeth (X-direction, see Figure 5.7), the shearing direction. Figure 5.12 presents the deviatoric strain field for three different teeth heights for a displacement of the plate of 10%. Maximum deviatoric strain values are observed at the teeth edges. Additionally, there is a noticeable decrease in shear deformation at the gap between the teeth as shown for greater teeth heights. However, a height of the teeth of h =0.5 mm is sufficient to localize the shear surface within the granular assembly and not only at the direct interface with the plate. The shear surface obtained with h=0.5 mm is rather similar with the one obtained for h=1.0 mm which explains why the shear strengths simulated for these two heights are identical. Consequently, a teeth height of 0.5 mm appears sufficient to capture the shear surface area.

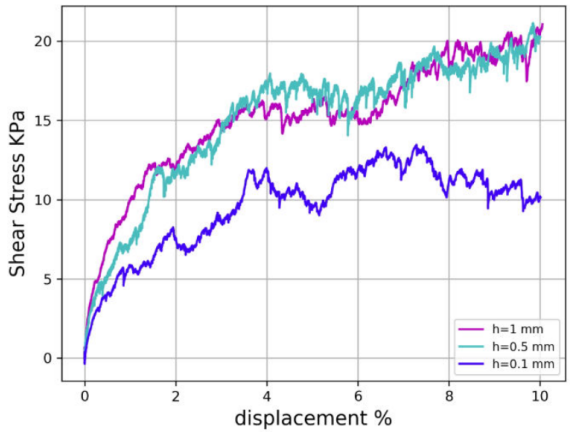

FIGURE 5.11: Simulated shear stress displacement for the three different heights of teeth h.

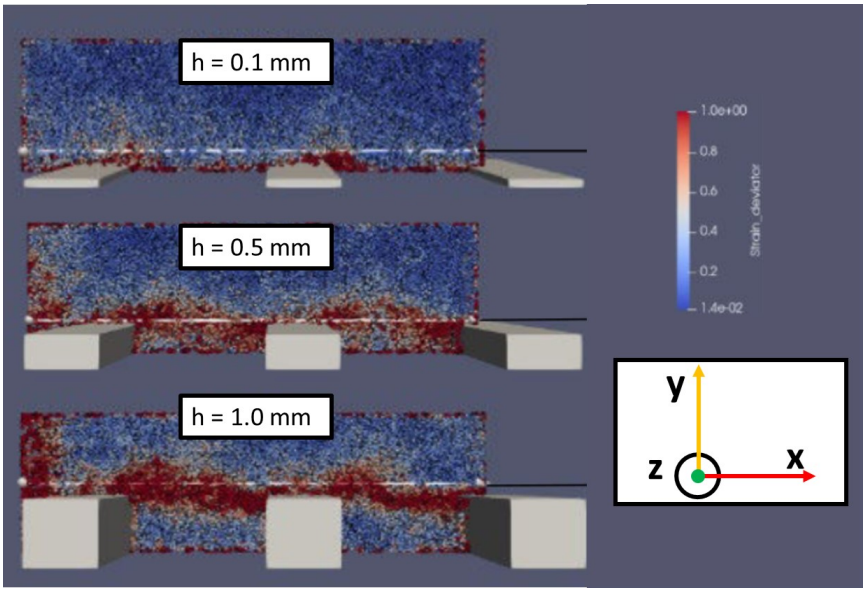

FIGURE 5.12: Deviatoric strain field identified from the discrete model for a displacement of 10% with different teeth heights.

Effect of the box height

To ensure that the development of the shear surface is not influenced by the presence of the top rigid boundary, we investigated three different box heights H = 4.56 mm (14000 particles), 9.12 mm (29000 particles), and 18.2 mm (58000 particles). The geometry for the teeth and box, as outlined in Table 5.1, was maintained, with only the box heights being varied. The height of the teeth was kept chosen equal to 0.5 mm, ensuring a fixed ratio of d_{50}/h across all simulations.
The shear surface area is shown in the region around the teeth, as shown in Figure 5.13. At the lowest height 4.56 mm, due to the proximity of the teeth to the top boundary, the shear surface area comes in contact with the later which may influence its development. However, at greater heights, the shear surface does not develop up to the top wall, and its typical shape of an inverted U is very similar for H = 9.12 mm and H = 18.24 mm. From this observation, we conclude that a height exceeding 9.12 mm is unnecessary.

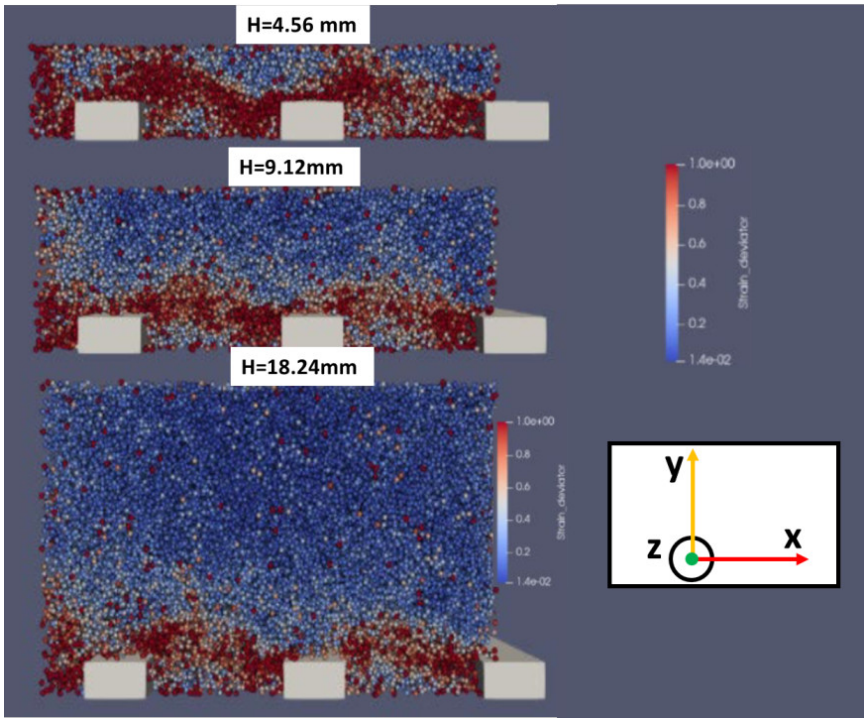

FIGURE 5.13: Deviatoric strain field simulated with different box heights for a displacement of 10%.

Effect of the box length

By maintaining a fixed box height equal 9.12 mm and a teeth height equal to 0.5 mm, and varying the length L of the box containing the granular assembly, the length of the teeth, and the spacing s between the grooves, multiple simulations were conducted to assess their impact on the distribution of the deviatoric strain in the assembly. In Figure 5.14, only one row of teeth is present at the center of the box (L= 9.12 mm) containing the granular assembly, the high strain is concentrated in this area. In contrast, when L= 18.24 mm, three rows of teeth are present (with double

teeth length), leading to a larger distribution of the shearing across the teeth. Consequently, the shearing is observed both at the middle and beyond the boundaries of the teeth.
This effect is also demonstrated in Figure 5.15, indicating that the shear stress measured at the boudaries is lower for a length of 9.12 mm compared to a length of 18.24 mm when the groove spacing is 4 mm.

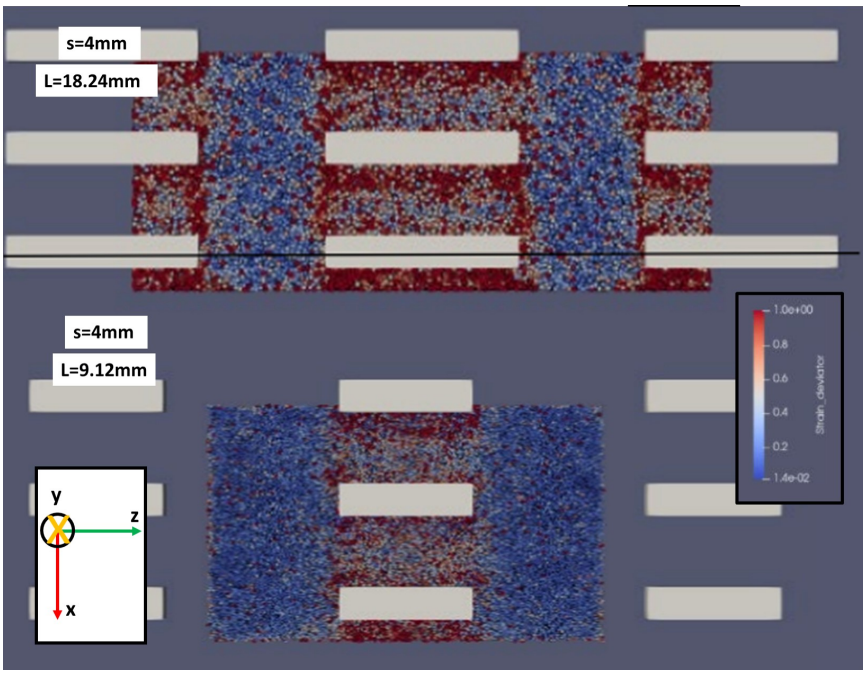

FIGURE 5.14: Strain field identified from the discrete model with different box length.

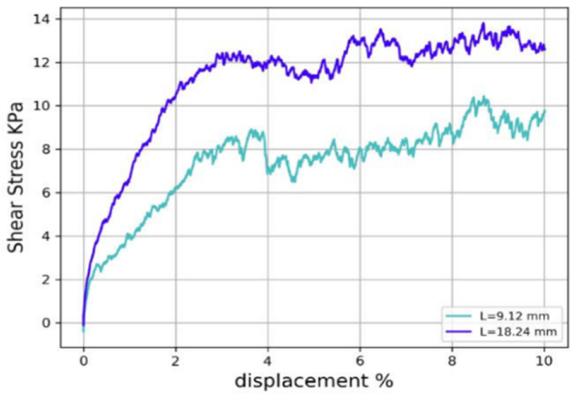

FIGURE 5.15: Simulated shear stress for the two different box length and spacing between teeth $s = 4$ mm.

The same analysis has been performed for a spacing $s = 0$ between teeth, as presented in Figure 5.16, it is evident that the shear deformation is concentrated all along the teeth boundaries, whatever the length of the box containing the granular assembly, resulting macroscopically in the same shear stress as shown in Figure 5.17.

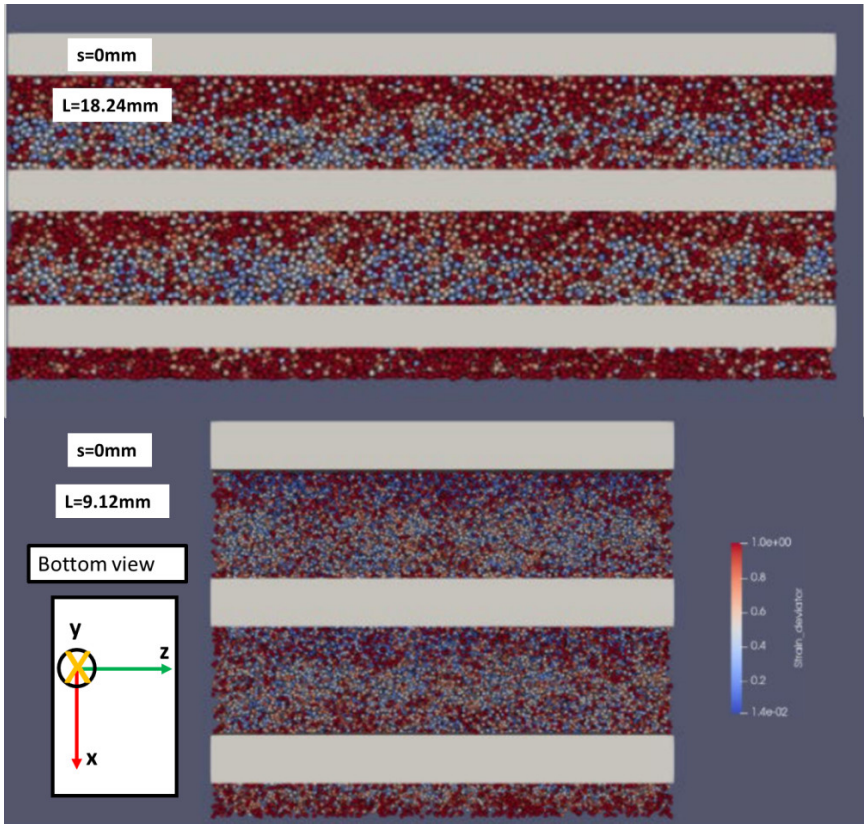

FIGURE 5.16: Strain field identified from the discrete model with different teeth heights.

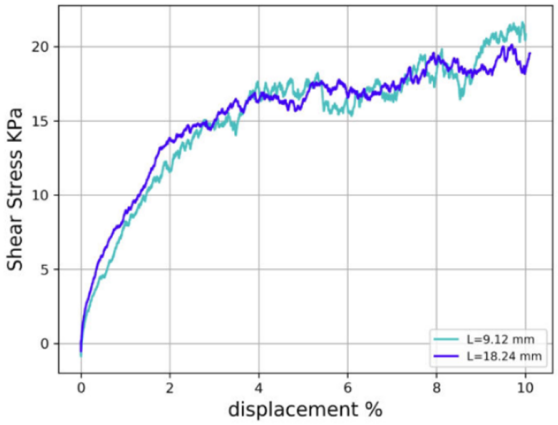

FIGURE 5.17: Simulated stress resistance with different box length and for spacing equal to $s = 0$ mm.

Summary of the parametric study

In conclusion, a parametric study was conducted to determine the dimensions of the discrete model box and teeth. Consequently, a teeth height $h = 0.5$ mm appears sufficient to capture the shear surface, not only at the soil-plate interface. Additionally, a box height $H = 9.12$ mm and length $L = 18.24$ mm are enough to identify the shear surface, resulting in 58,000 particles to be considered. This provides a good compromise between the number of particles and the computation time.

5.6 Numerical characterization of the shear surface and shear stress

Finally, after the identification of the different parameters of the teeth and box geometries through the parametric study, two simulations are done with spacing 0 mm and 4 mm between the teeth taking into account rolling friction between the particles equal to 0.25. Then, the shear surface is identified at different cross sections of the granular assembly in X, Y and Z directions.
It's shown in Figure 5.18 that the shear strength of the model with spacing s equal to 0 mm is higher than for s = 4 mm. The granular assembly is sheared all along the teeth which are continuous resulting in higher shear resistance than the case of spacing equal to 4 mm where the shearing is much limited within the spaces in between the teeth. We present in the following subsections the different cross sections of the sample in X, Y and Z directions for a displacement of 3.5%.

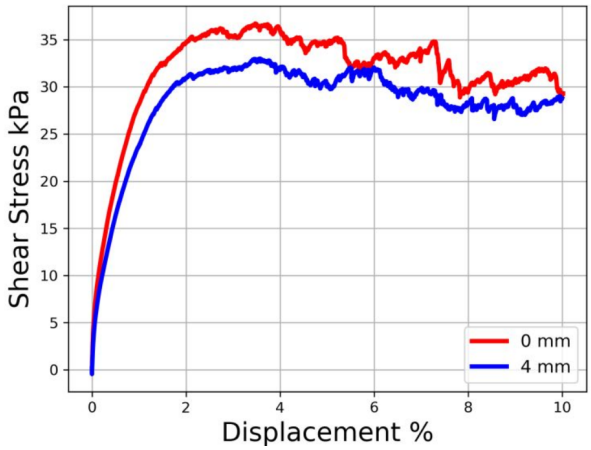

FIGURE 5.18: The modified direct shear test model behaviour with two different spacing equal to 0 and 4 mm

5.6.1 Deviatoric strain field for $s = 4$ mm

Cross section perpendicular to Z direction

Figure 5.19 presents the distribution of the deviatoric strain in cross sections normal to Z. At the teeth-soil interface, this distribution appears similar to a horizontal plane. However, between the different teeth, we can see the inverted U-shaped distribution. In addition, between the teeth it appears that no shear deformation is obtained. Thus we can propose that the shear failure area is limited in the Z-direction (perpendicular to the direction of shearing) to the length of the teeth.

Cross sections perpendicular to Y direction

It's shown in Figure 5.20 that the deviatoric strain is distributed and concentrated between the teeth in the direction of shearing (X-direction), as proposed in the previous subsection. From the bottom view, some particles with high deviatoric strain are visible, but this is limited to a few particles at the boundary. However, as the height

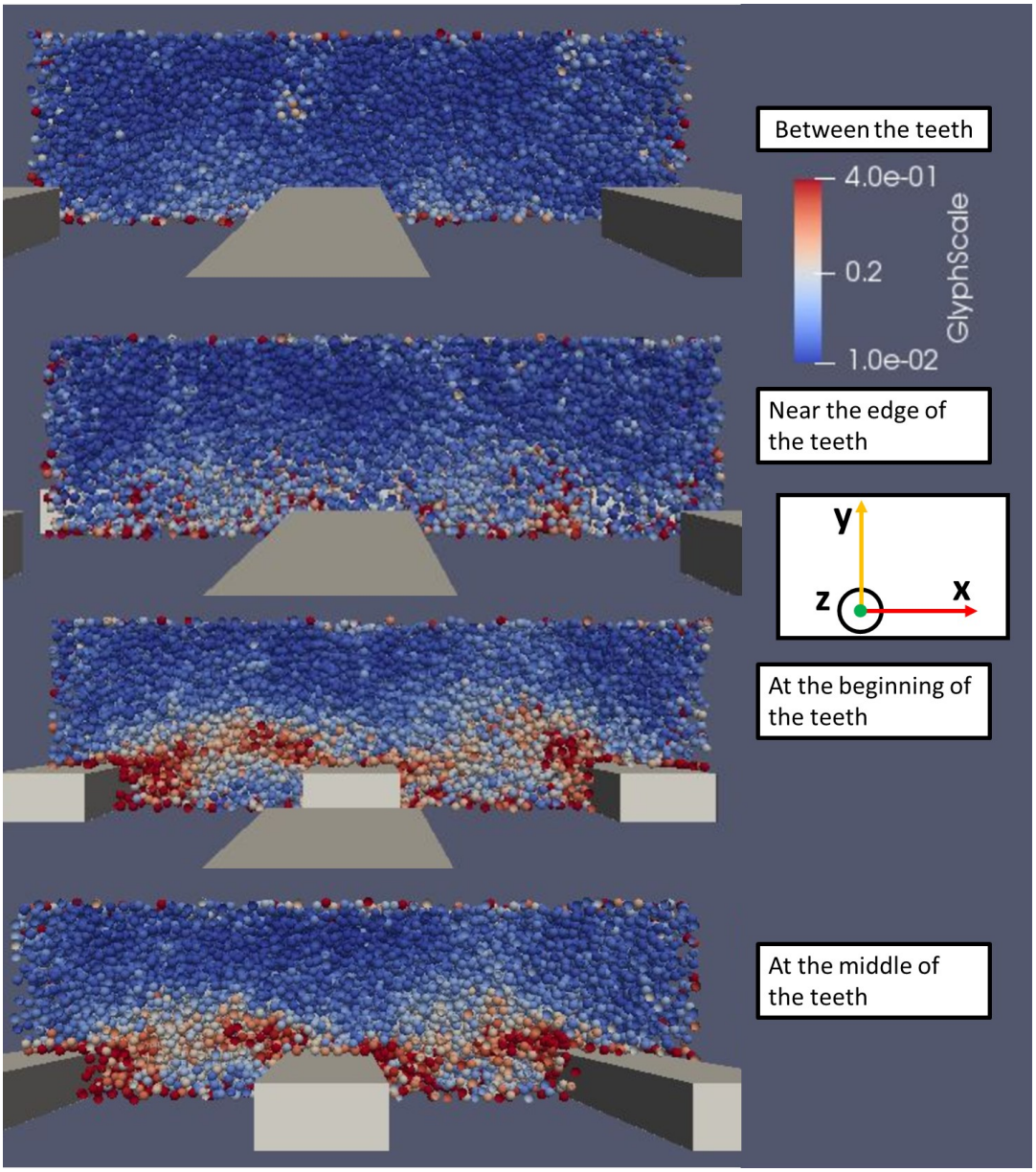

FIGURE 5.19: Deviatoric strain field computed with the numerical model in different cross sections perpendicular to Z-direction for a spacing $s = 4$ mm.

(in the y-direction) increases, no high strain appears between the teeth and the top boundary.

Cross sections perpendicular to X direction

Similar to the Z direction, we observe in Figure 5.21 an inverted U-shaped high deviatoric strain near the edge of the teeth in the direction of shearing (X-direction). At the soil-teeth interface particles with high strain form a horizontal failure surface.
To resume, in the case of a spacing between teeth of 4 mm we propose to consider the shear surface correspond to the one represented in Figure 5.22. This surface corresponds to "waves" jumping from one tooth to another in the X direction (the

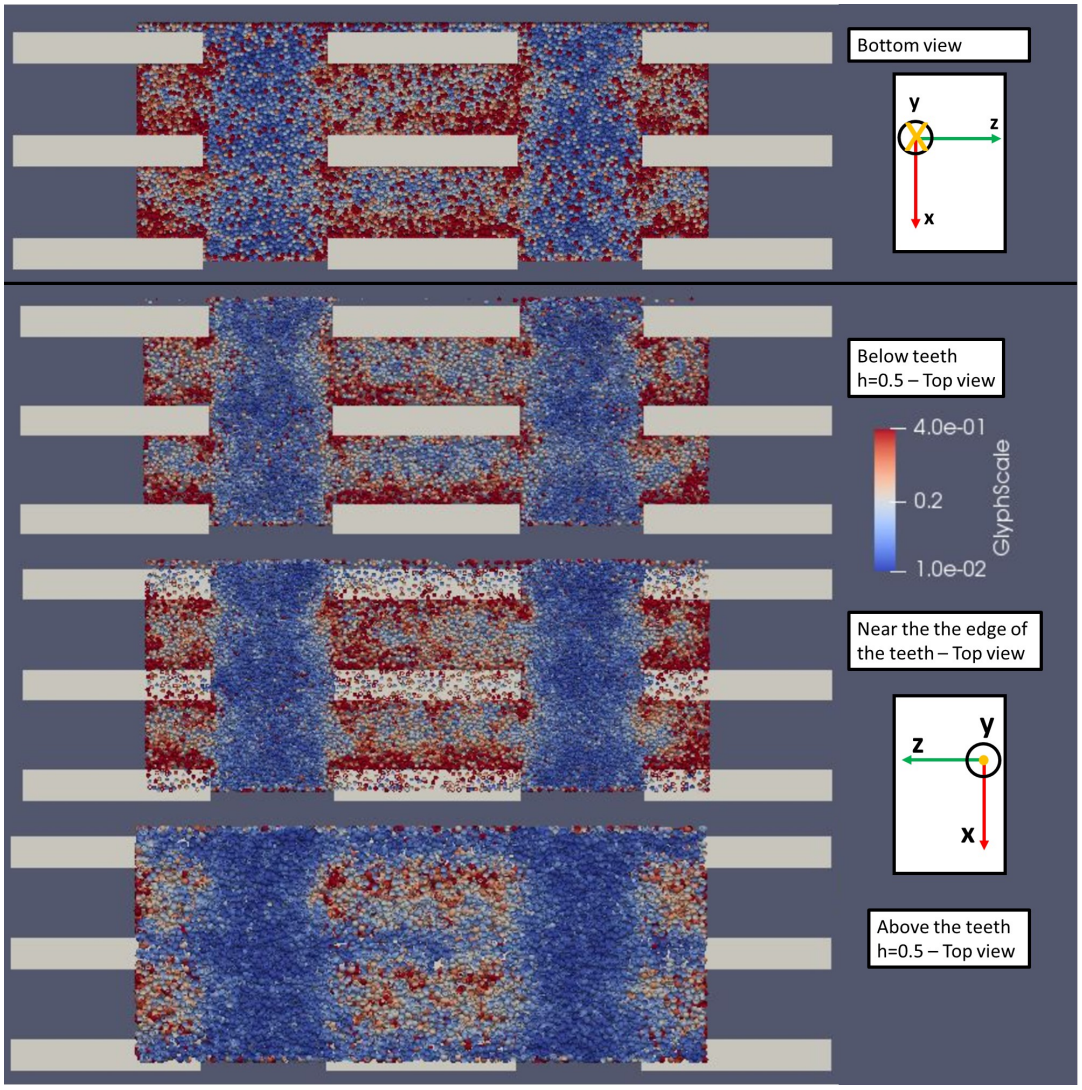

FIGURE 5.20: Simulated deviatoric strain field in cross sections perpendicular to Y-direction for a spacing $s = 4$ mm.

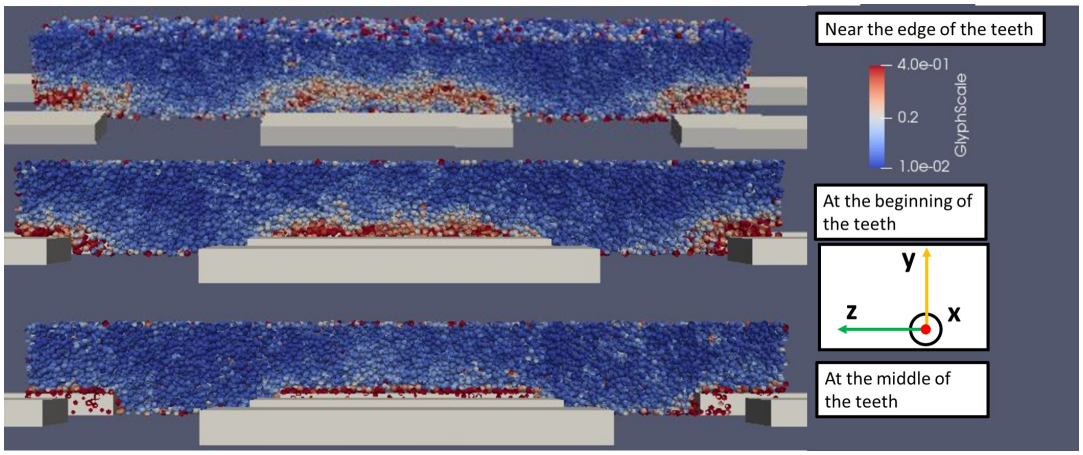

FIGURE 5.21: Deviatoric strain field in cross sections perpendicular to X direction for a spacing $s = 4$ mm.

shearing direction) while we assume there is no shearing in the zone corresponding to the spaces between the teeth in the Z direction. This result is in agreement with the conclusion given in (Arpaia, Heintz, and Reiffsteck, 2015) suggesting to consider all along the phicometer test a shearing surface constant by excluding the area corresponding to the opening of the spaces in between the teeth.

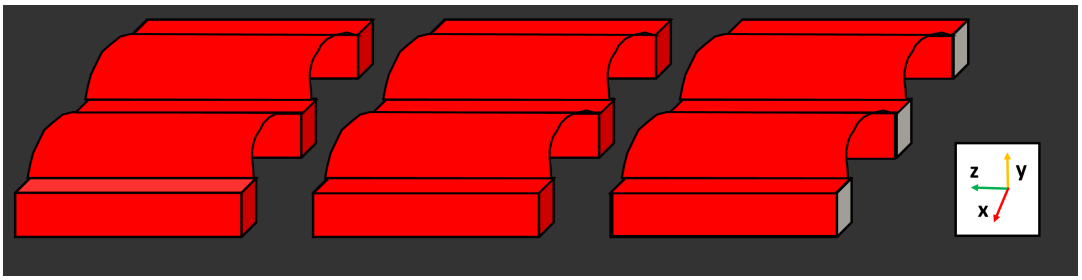

FIGURE 5.22: Shear surface proposed in the case of a spacing $s = 4$ mm

5.6.2 Deviatoric strain field for $s = 0$ mm

Cross sections perpendicular to Y direction

It's shown in Figure 5.23 that the deviatoric strain is distributed and concentrated between the teeth in the direction of shearing (X direction), similar to the distribution in case of $s = 4$ mm. From the bottom view, particles with high deviatoric strain are visible, but this is limited to few particles at the boundary. Thus, the distribution is similar to that in case of $s = 4$ mm, but as no spacing exist between the teeth , the deviatoric strain distribution is continuous in the Z-direction.

Cross sections perpendicular to X direction

We observe in Figure 5.24 at the soil-teeth interface particles with high deviatoric strain forming a horizontal failure surface. As the distance increases away from the teeth we observe that the failure surface is localized above the teeth.

To resume, in the case were no spacing exist between the teeth ($s = 0$ mm), we propose to consider the shear surface correspond to the one represented in Figure 5.25.

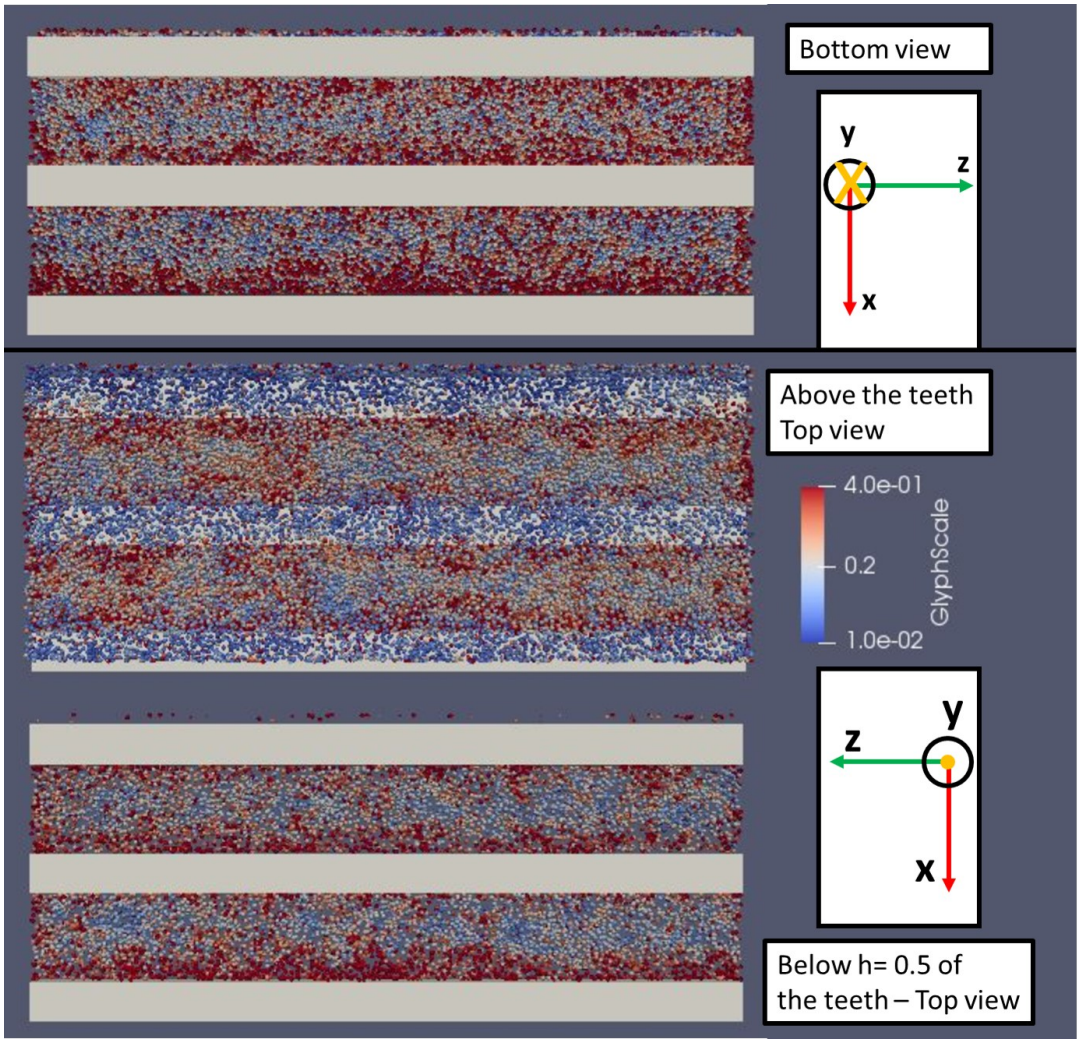

FIGURE 5.23: Simulated deviatoric strain field in cross sections perpendicular to Y-direction for a spacing $s = 0$ mm.

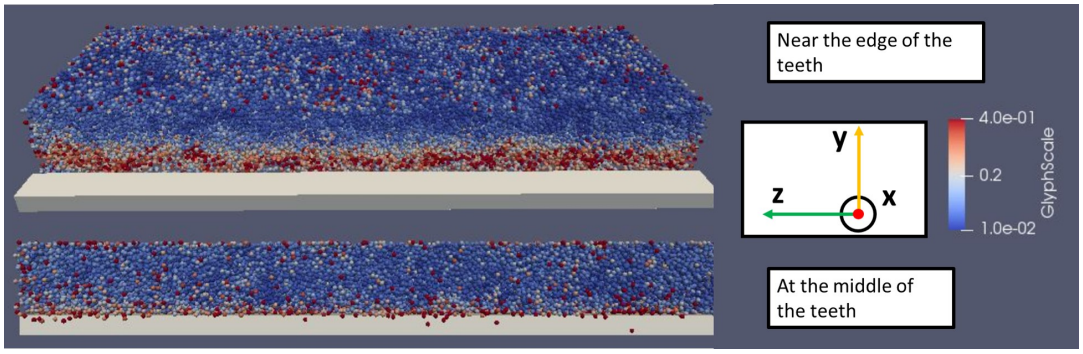

FIGURE 5.24: Deviatoric strain field in cross sections perpendicular to X direction for a spacing $s = 0$ mm.

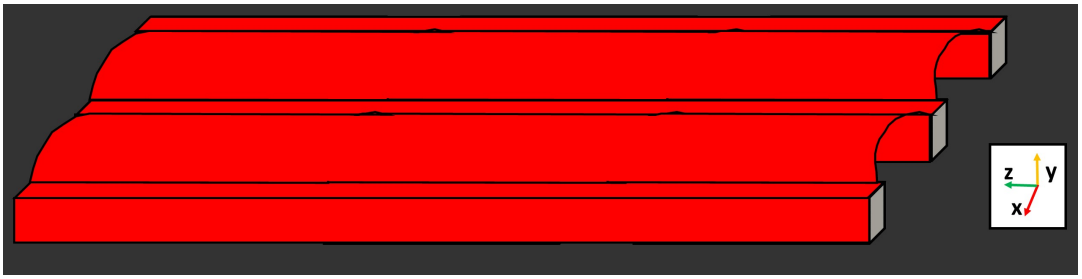

FIGURE 5.25: Shear surface proposed in the case of a spacing $s = 0$ mm

5.7 Local and global shear stress estimation

After successfully describing the shear band in the previous section, the stress deviator within the shear band will be determined and compared with the one calculated from the shear forces divided by the area of the plate.

5.7.1 Definition of the stress tensor at the particle scale

The microscopic stress associated with one particle contained in V_σ is defined as a sum over the contacts, as described (Catalano, Chareyre, and Barthélemy, 2014), and shown in Figure 5.26. It is given by:

$$\overline{\sigma} = \frac{1}{V_\sigma} \sum_k x^{c,k} \otimes f^{c,k} \tag{5.8}$$

where $x^{c,k}$ is a contact point, and $f^{c,k}$ represents the corresponding force. V_σ is the reference volume linked to the particle within the Voronoi tessellation.

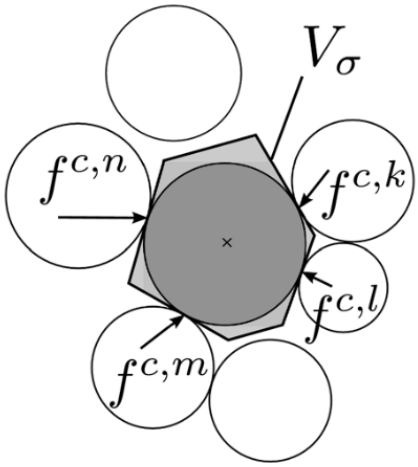

FIGURE 5.26: Domain surrounding the particle used to define microstress from (Catalano, Chareyre, and Barthélemy, 2014).

From the body stress tensor given in equation 5.8, it is possible to calculate for each

particle the maximum stress deviator and therefore compute the average stress deviator of the particles in the shear band.

5.7.2 Comparison of assumptions for the determination of the shear stress

The average microscopic shear stress is computed for an elementary volume in the shear band, shown in Figure 5.27-B and represented by the green points in Figure 5.27-A, for the case of $s = 4$ mm at displacements equal to 0.5%, 1.5%, 2.5%, and 3.5% (corresponding to the peak shear stress).
The locally computed shear stress within the elementary volume in the shear band was estimated to be 23 kPa, 34 kPa, 39.2 kPa, and 42 kPa at displacements of 0.5%, 1.5%, 2.5%, and 3.5%, respectively. In contrast, the globally computed shear stress yielded values of 16.2 kPa, 28.5 kPa, 31.5 kPa, and 32.5 kPa, assuming a constant shear surface area. However, using the proposed modified surface area, the globally computed shear stress equals 21.4 kPa, 37 kPa, 41 kPa, and 42 kPa. This comparison highlights the differences in shear stress values between the local and global scales when considering particles in the shear band. It also confirms the importance of a precise description of the shear surface to accurately calculate shear stresses.

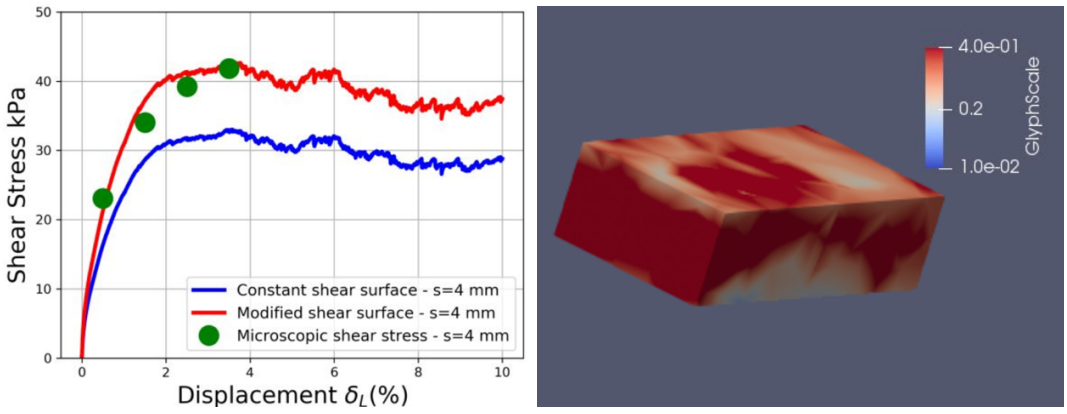

(A) (B)

FIGURE 5.27: Comparison of shear stresses: (A) Macroscopic vs. microscopic (computed within an elementary volume in the shear band) (B) The elementary volume in the shear band.

5.8 Conclusion and perspective

In conclusion, the discrete element method was used to investigate how the shear surface is affected by the expansion of the phicometer probe. We successfully identified the shear surface and made the following observations about its shape:

- In the cases of the two considered spacings, $s = 0$ mm and $s = 4$ mm, the shear surface appears as 'waves,' jumping from one tooth to another.
- When a sufficiently large spacing $s = 4$ mm is considered, there is no shearing in the zone corresponding to spaces between the teeth.

However, if the spacing between the teeth is reduced, there might be a threshold where the shear surface jumps from one tooth to another (in the direction parallel to the teeth). Thus, it is essential to consider cases with smaller spacings.

Additionally, the discrete element method provides the opportunity to estimate shear stress at both local and global scales. The shear stresses obtained for an elementary volume element in the shear band at different displacements were similar to those estimated globally using a proposed shear surface area. These results highlight the importance of considering a modified shear surface area in the interpretation of the phicometer. For future work, it is necessary to consider different ratios of particle size to teeth size.

Chapter 6

Conclusion and Perspectives

This thesis explored various approaches to enhance a light discrete element model capable of predicting complex loading paths. The model's "light" design is essential to tackle boundary value problems within acceptable computation time. Our investigation began by exploring different approaches to enhance the predictive ability of the light model. These approaches included defining a new approach for choosing the initial porosity, using more complex particles, considering the possible impact of roughness by implementing a variable contact friction angle, and the effect of initial fabric anisotropy.
Following the development of the discrete light model, it was applied to a problem involving the interaction between a shallow foundation and sand, subjected to seismic loadings. The results were benchmarked against experimental measurements and previous numerical simulations.
Additionally, the model was used to simulate a modified direct shear test, providing valuable information that is challenging to obtain experimentally.
In conclusion, the following findings can be highlighted:

To investigate **various approaches to improve the light discrete model**: We defined a new method for choosing the initial porosity based on the state parameter ψ. This allows the model to replicate the behavior observed during shearing in real soil samples.
Discrete models with simple shapes, such as a clump of 2 spheres and another with 6 spheres, were created. The model made of spheres with rolling friction for modeling dense sand, under complex loadings such as cyclic compression/extension and circular loading paths, showed better predictive performance and computational efficiency compared to other models. However, we observed when modeling loose soil under isochoric compressions and constant deviator loading paths that all models failed.
A non-constant contact friction angle was implemented into the model as a possible way to account for the complex interplay between varying normal forces (and thus the mean pressure) and the contacts frictional behavior. This adjustment led to a slight enhancement in the response of dense sand under complex loadings. However, this improvement came with increased model complexity, necessitating calibration through additional drained compressions. Furthermore, the consideration of inter-particle friction, plays a critical role in the response of granular materials to loading paths where the range of variation of the mean pressure is important. Despite a slight enhancement observed when modeling loose soil with spheres, all models still fail in predicting the response accurately
Thus, it was necessary to consider different approaches to improve the modeling of

loose soil. Modifications were made to the sample preparation method by considering initial fabric anisotropy, achieved through generating numerical samples using a technique similar to experimental moist tamping. We found that the initial fabric of the granular material significantly impacts its constitutive response. Additionally, the combination of both fabric anisotropy and a non-constant friction coefficient is necessary to achieve a simulated response that closely matches experimental results in the case of isochoric compressions and constant deviator loading paths.
A micro-scale study based on isochoric compressions shows that failure develops differently at the contact scale depending on the type of contact friction considered. When a constant friction coefficient is used, failure is characterized by the loss of connectivity of the granular assembly, together with the plastic sliding of the majority of contacts. However, with a non-constant contact friction, failure is characterized by the loss of connectivity in the granular packing alone, showing a significant impact on the weak contact phase and only a slight effect on the strong contact phase. Considering initial fabric anisotropy, when contact normals are initially oriented in the direction of the major principal stress, the inter-granular force transmission is more likely to occur along the normal contact direction rather than in the tangential contact direction. This orientation may also limit sliding at the particle contacts.

The discrete element method was used to **simulate the behavior of the shallow foundation-sand interaction subjected to seismic loading**. In contrast to other numerical methods employed for modeling soil-shallow foundation interaction, the Discrete Element Method (DEM) demonstrates notable capabilities in describing the behavior of soil-shallow foundation under cyclic loading scenarios, without the need for additional specific historical parameters. DEM achieves this with calibration based on simple monotonous compression test. On the other hand, to calibrate the Finite Element Method (FEM) often, cyclic loading data is needed to calibrate constitutive relations. Furthermore, to calibrate macroelement models, it is necessary to have a pre-existing physical model as a reference during the parameter calibration process. Moreover, using adaptive discretization has allowed for the resolution of these boundary value problems at a relatively low computational cost.
In summary, in case of dense sand, the model accurately describes settlement under vertical force and provides reasonable predictions for settlement, horizontal displacement, and rocking angle during phases I and II. In contrast, the macroelement model used in phase II fails to describe both the initiation and final stabilization of settlements, despite correctly predicting the final settlement value. During phases I and II, the macroelement models offer a better response prediction of the experiments than the discrete model in terms of rocking angle and horizontal displacement. However, in phase I, the model was calibrated based on experimental moment-rotation and horizontal force-horizontal displacement curves (the authors did not specify the phase from which these curves originate). In addition, in case of phase II, another macroelement model was calibrated based on phase I experimental data.
Furthermore, in case of phase III, the discrete model presents a realistic response but underestimates settlement and the hysteresis of moment-rocking angle and force-displacement curves. In comparison, the Finite Element Method (FEM) model overestimates settlement but accurately captures hysteresis behaviors, taking into account that constitutive relation used is calibrated on cyclic simple shear tests.

In case of medium dense sand, the ability of the discrete model to describe the response of the soil-foundation interaction should be improved. Apart from loading phase I, The model clearly underestimates the irreversible and non-linear mechanisms occurring in the soil beneath the foundation.
In perspective, granular assemblies with initial anisotropic fabrics should be explored to control the soil pressure at rest, as demonstrated in preliminary results where the settlement response clearly depended on the earth pressure coefficient at rest. Additionally, choosing the contact friction angle at the interface between the foundation and the sand should be done thoughtfully to enhance the accuracy of predicted horizontal displacement.

Finally, the discrete element method was used to **investigate the impact of the expansion of the phicometer probe on the shear surface and the assessment of the induced shear stress**. Our findings revealed different patterns within the shear surface, with 'waves' observed when considering spacings of $s = 0$ mm and $s = 4$ mm, in the direction of shearing. Moreover, for a sufficiently large spacing ($s = 4$ mm), no shearing was observed in the areas corresponding to the spaces between the teeth. However, if the spacing between the teeth is reduced, a threshold might be reached where the shear surface jumps from one tooth to another (in the direction parallel to the teeth). Thus, it becomes essential to explore cases with smaller spacings as a potential area for future research.
Moreover, the discrete element method allowed for the estimation of shear stress at both local and global scales. Specifically, we observed locally (within an elementary volume element in the shear band) at different displacements, values similar to those obtained at the global scale, assuming a modified shear surface area. This enabled the determination of shear stresses associated with the shear band. These results allow us to highlight the importance of precisely using the appropriate shear surface when calculating shear stresses and to determine a ratio that can be applied to accurately adjust the shear surface when interpreting the phicometer test.
Additionally, exploring different particle size distributions could enrich our understanding of the effect of the change of the geometry of the phicometer probe.

Bibliography

Abdallah, A. et al. (2022). "Identifying parameters of a discrete numerical model of soil from a geotechnical field test". *European Journal of Environmental and Civil Engineering*, pp. 1–20.

Aboul Hosn, R. et al. (2017). "Discrete numerical modeling of loose soil with spherical particles and interparticle rolling friction". *Granular matter* 19.1, pp. 1–12.

Achmus, M., Y.-S. Kuo, and K. Abdel-Rahman (2009). "Behavior of monopile foundations under cyclic lateral load". *Computers and Geotechnics* 36.5, pp. 725–735.

Ahmadabadi, M., S. Hosseini, and M. Rezai (2016). "Investigation of the Effect of Soil and Wall Interaction on the displacement of Retaining Walls Using Finite Element Method". *Bulletin de la Société Royale des Sciences de Liège* 85, pp. 1–7.

Ai, J. et al. (2011). "Assessment of rolling resistance models in discrete element simulations". *Powder Technology* 206.3, pp. 269–282.

Anastasopoulos, I et al. (2011). "Simplified constitutive model for simulation of cyclic response of shallow foundations: validation against laboratory tests". *Journal of Geotechnical and Geoenvironmental Engineering* 137.12, pp. 1154–1168.

Andrade, J. E. et al. (2012). "Granular element method for computational particle mechanics". *Computer Methods in Applied Mechanics and Engineering* 241, pp. 262–274.

Aris, M., N. Benahmed, and S. Bonelli (2012). "Experimental geomechanics: a laboratory study on the behaviour of granular material using bender elements". *European journal of environmental and civil engineering* 1.16, pp. 97–110.

Arpaia, J., R. Heintz, and P. Reiffsteck (2015). "Influence de paramètres géométriques sur les résultats d'essais de cisaillement effectués au Phicomètre." *ISP7-PRESSIO 2015*, 6–p.

Asadzadeh, M. and A. Soroush (2017). "Macro-and micromechanical evaluation of cyclic simple shear test by discrete element method". *Particuology* 31, pp. 129–139.

Azéma, E., F. Radjai, and G. Saussine (2009). "Quasistatic rheology, force transmission and fabric properties of a packing of irregular polyhedral particles". *Mechanics of Materials* 41.6, pp. 729–741.

Baraff, D. and A. Witkin (1992). "Dynamic simulation of non-penetrating flexible bodies". *ACM SIGGRAPH Computer Graphics* 26.2, pp. 303–308.

Bardet, J. (1993). "Rotational stiffness of cylindrical contacts". *Powder & Grains 93 Balkema*, pp. 39–43.

Benahmed, N., J. Canou, and J. Dupla (2004). "Structure initiale et propriétés de liquéfaction statique d'un sable". *Comptes Rendus Mécanique* 332.11, pp. 887–894. ISSN: 1631-0721. DOI: https://doi.org/10.1016/j.crme.2004.07.009.

Benahmed, N. (2001). "Comportement mécanique d'un sable sous cisaillement monotone et cyclique: application aux phénomenes de liquéfaction et de mobilité cyclique". *These de doctorat de l'Ecole nationale des ponts et chaussées, France*.

Bourgeois, E. et al. (2010). "Three-dimensional numerical modelling of the behaviour of a pile subjected to cyclic lateral loading". *Computers and Geotechnics* 37.7-8, pp. 999–1007.

Bousquet, H et al. (1994). "Compilation des essiais triaxiaux de révolution sur le sable d'Hostun RF". *Tech. rep., Institut de mécanique de Grenoble*.

Brandis, A., I. Kraus, and S. Petrovčič (2021). "Simplified Numerical Analysis of Soil–Structure Systems Subjected to Monotonically Increasing Lateral Load". *Applied Sciences* 11.9, p. 4219.

Calvetti, F. (2008). "Discrete modelling of granular materials and geotechnical problems". *European Journal of Environmental and Civil Engineering* 12.7-8, pp. 951–965.

Catalano, E., B. Chareyre, and E. Barthélemy (2014). "Pore-scale modeling of fluid-particles interaction and emerging poromechanical effects". *International Journal for Numerical and Analytical Methods in Geomechanics* 38.1, pp. 51–71.

Chaudry, M. A. et al. (2021). "A multiscale DEM–FEM coupled approach for the investigation of granules as crash-absorber in ship building". *Computational Particle Mechanics*, pp. 1–19.

Cheng, X. et al. (2021). "Finite element analysis of cyclic lateral responses for large diameter monopiles in clays under different loading patterns". *Computers and Geotechnics* 134, p. 104104.

Cho, G., J Dodds, and C. Santamarina (2006). *Particle shape effects on packing density, stiffness, and strength: natural and crushed sands. J Geotech Geoenviron 132 (5): 591–602*.

Chugh, A. K., J. F. Labuz, and C. G. Olgun (2016). "Soil structure interactions of retaining walls". *Geotechnical and Structural Engineering Congress 2016*, pp. 439–454.

Cohen, J. D. et al. (1995). "I-collide: An interactive and exact collision detection system for large-scale environments". *Proceedings of the 1995 symposium on Interactive 3D graphics*, p. 189.

Cremer, C., A. Pecker, and L. Davenne (2001). "Cyclic macro-element for soil–structure interaction: material and geometrical non-linearities". *International Journal for Numerical and Analytical Methods in Geomechanics* 25.13, pp. 1257–1284.

Cui, L and C O'sullivan (2006). "Exploring the macro-and micro-scale response of an idealised granular material in the direct shear apparatus". *Géotechnique* 56.7, pp. 455–468.

Cundall, P. and O. Strack (1978). "BALL-A program to model granular media using the distinct element method". *Technical note*.

Cundall, P. and O. Strack (1979a). "The distinct element method as a tool for research in granular media: part II report to the National Science Foundation". *University of Minnesota, Minneapolis, MN, USA*.

Cundall, P. A. and O. D. Strack (1979b). "A discrete numerical model for granular assemblies". *Géotechnique* 29.1, pp. 47–65.

Daouadji, A. et al. (2011). "Diffuse failure in geomaterials: experiments, theory and modelling". *International Journal for Numerical and Analytical Methods in Geomechanics* 35.16, pp. 1731–1773.

Darve, F. (1990). "Constitutive Equations and Modelling. London and New York". *Taylor and Francis books*.

Derjaguin, B. V., V. M. Muller, and Y. P. Toporov (1975). "Effect of contact deformations on the adhesion of particles". *Journal of Colloid and interface science* 53.2, pp. 314–326.

Dubois, F. et al. (2011). "Lmgc90". *10e colloque national en calcul des structures*.

Effeindzourou, A et al. (2015). "A general method for modelling deformable structures in DEM". *PARTICLES IV: proceedings of the IV International Conference on Particle-Based Methods: fundamentals and applications*. CIMNE, pp. 744–754.

Elias, J. (2013). "DEM simulation of railway ballast using polyhedral elemental shapes". *PARTICLES III: proceedings of the III International Conference on Particle-Based Methods: fundamentals and applications*. CIMNE, pp. 247–256.

Ericson, C. (2004). *Real-time collision detection*. Crc Press.

Faccioli, E, R Paolucci, M Vanini, et al. (1998). "3D site effects and soil-foundation interaction in earthquake and vibration risk evaluation". *Final Report of the European research project TRISEE, Politecnico di Milano*.

Faccioli, E., M Vanini, and R Paolucci (1999). *TRISEE: 3D site effects and soil-foundation interaction in earthquake and vibration risk evaluation*. European commission. Directorate-general 12. Science, research and development.

Faheem, H., F. Cai, and K. Ugai (2004). "Three-dimensional base stability of rectangular excavations in soft soils using FEM". *Computers and Geotechnics* 31.2, pp. 67–74.

Ferellec, J.-F. and G. McDowell (2012). "Modelling of ballast–geogrid interaction using the discrete-element method". *Geosynthetics International* 19.6, pp. 470–479.

Figini, R, R. Paolucci, and C. Chatzigogos (2012). "A macro-element model for non-linear soil–shallow foundation–structure interaction under seismic loads: theoretical development and experimental validation on large scale tests". *Earthquake Engineering & Structural Dynamics* 41.3, pp. 475–493.

Finno, R. J., J. T. Blackburn, and J. F. Roboski (2007). "Three-dimensional effects for supported excavations in clay". *Journal of Geotechnical and Geoenvironmental Engineering* 133.1, pp. 30–36.

Flavigny, E, J Desrues, and B Palayer (1990). "Note technique: le sable d'Hostun «RF»". *Revue française de géotechnique* 53, pp. 67–70.

Gabrieli, F., S. Cola, and F. Calvetti (2009). "Use of an up-scaled DEM model for analysing the behaviour of a shallow foundation on a model slope". *Geomechanics and Geoengineering: An International Journal* 4.2, pp. 109–122.

Giannakos, S., N. Gerolymos, and G. Gazetas (2012). "Cyclic lateral response of piles in dry sand: Finite element modeling and validation". *Computers and Geotechnics* 44, pp. 116–131.

Gottardi, G, G. Houlsby, and R Butterfield (1999). "Plastic response of circular footings on sand under general planar loading". *Géotechnique* 49.4, pp. 453–469.

Grange, S., P. Kotronis, and J. Mazars (2008). "A macro-element for a shallow foundation to simulate soil–structure interaction considering uplift". *Comptes Rendus Mécanique* 336.11-12, pp. 856–862.

Grange, S., P. Kotronis, and J. Mazars (2009). "A macro-element to simulate 3D soil–structure interaction considering plasticity and uplift". *International Journal of Solids and Structures* 46.20, pp. 3651–3663.

Gu, X., J. Zhang, and X. Huang (2020). "DEM analysis of monotonic and cyclic behaviors of sand based on critical state soil mechanics framework". *Computers and Geotechnics* 128, p. 103787. DOI: https://doi.org/10.1016/j.compgeo.2020.103787.

Guo, N. and J. Zhao (2014). "A coupled FEM/DEM approach for hierarchical multiscale modelling of granular media". *International Journal for Numerical Methods in Engineering* 99.11, pp. 789–818.

Guo, N. and J. Zhao (2015). "Multiscale insights into classical geomechanics problems". *International Journal for Numerical and Analytical Methods in Geomechanics* 40.3, pp. 367–390.

Hamouma, D, A Messameh, and N Tallah (2020). "Finite element analysis of soil-pile interface under cyclic loading". *International Journal of Civil Engineering and Technology (IJCIET)* 11, pp. 49–57.

Heintz, R. (2001). "Remarque concernant l'exploitation des mesures réalisées au phicomètre suivant la norme expérimentale XP 94-120, lettre 4 pages et 6 annexes".

Herten, M. and M. Pulsfort (1999). "Determination of spatial earth pressure on circular shaft constructions". *Granular matter* 2.1, pp. 1–7.

Hertz, H (1896). *Miscellaneous papers,(ed.) P. Lenard*.

Imole, O. I. et al. (2014). "Micro-macro correlations and anisotropy in granular assemblies under uniaxial loading and unloading". *Physical Review E* 89.4, p. 042210.

Ishibashi, I. and X. Zhang (1993). "Unified dynamic shear moduli and damping ratios of sand and clay". *Soils and foundations* 33.1, pp. 182–191.

Iwashita, K. and M. Oda (1998). "Rolling resistance at contacts in simulation of shear band development by DEM". *Journal of engineering mechanics* 124.3, pp. 285–292.

Iwashita, K. and M. Oda (2000). "Micro-deformation mechanism of shear banding process based on modified distinct element method". *Powder technology* 109.1-3, pp. 192–205.

Jenck, O., D. Dias, and R. Kastner (2009). "Discrete element modelling of a granular platform supported by piles in soft soil–Validation on a small scale model test and comparison to a numerical analysis in a continuum". *Computers and Geotechnics* 36.6, pp. 917–927.

Jerves, A. X., R. Y. Kawamoto, and J. E. Andrade (2016). "Effects of grain morphology on critical state: a computational analysis". *Acta Geotechnica* 11.3, pp. 493–503.

Jiang, M., A. Zhang, and T. Li (2019). "Distinct element analysis of the microstructure evolution in granular soils under cyclic loading". *Granular Matter* 21, p. 39. DOI: https://doi.org/10.1007/s10035-019-0892-8.

Jiang, M., A. Zhang, and C. Fu (2018). "3-D DEM simulations of drained triaxial tests on inherently anisotropic granulates". *European Journal of Environmental and Civil Engineering* 22.sup1, s37–s56.

Jiang, M., J. Konrad, and S. Leroueil (2003). "An efficient technique for generating homogeneous specimens for DEM studies". *Computers and geotechnics* 30.7, pp. 579–597.

Johnson, K. L., K. Kendall, and a. Roberts (1971). "Surface energy and the contact of elastic solids". *Proceedings of the royal society of London. A. mathematical and physical sciences* 324.1558, pp. 301–313.

Karthigeyan, S, V. Ramakrishna, and K Rajagopal (2007). "Numerical investigation of the effect of vertical load on the lateral response of piles". *Journal of Geotechnical and Geoenvironmental Engineering* 133.5, pp. 512–521.

Kawamoto, R. et al. (2018). "All you need is shape: predicting shear banding in sand with LS-DEM". *Journal of the Mechanics and Physics of Solids* 111, pp. 375–392.

Khodair, Y. A. and S. Hassiotis (2005). "Analysis of soil–pile interaction in integral abutment". *Computers and Geotechnics* 32.3, pp. 201–209.

Klisinski, M., Z. Mroz, and K. Runesson (1992). "Structure of constitutive equations in plasticity for different choices of state and control variables". *International Journal of Plasticity* 8.3, pp. 221 –243. DOI: http://dx.doi.org/10.1016/0749-6419(92)90049-I.

Kodicherla, S. P. K., G. Gong, and S. Wilkinson (2020). "Exploring the relationship between particle shape and critical state parameters for granular materials using DEM". *SN Applied Sciences* 2, pp. 1–13.

Kodicherla, S. P. K. et al. (2018). "Effects of preparation methods on inherent fabric anisotropy and packing density of reconstituted sand". *Cogent Engineering* 5.1, p. 1533363.

Kuhn, M. R. (2006). "OVAL and OVALPLOT: Programs for analyzing dense particle assemblies with the discrete element method". *Department of Civil Engineering, University of Portland, Portland, OR, USA*.

Lanier, J. and Z.-E.-A. Zitouni (1988). "Development of a data base using the Grenoble true triaxial apparatus-Constitutive equations for granular non cohesive soils". *Proceedings of the international workshop on constitutive equations for granular non-cohesive soils, Balkema, Rotterdam, 22-24 July 1987*.

Leblouba, M. et al. (2016). "Practical Soil-Shallow Foundation Model for Nonlinear Structural Analysis". *Mathematical Problems in Engineering* 2016. DOI: 10.1155/2016/4514152.

Lee, S. J., Y. M. Hashash, and E. G. Nezami (2012). "Simulation of triaxial compression tests with polyhedral discrete elements". *Computers and Geotechnics* 43, pp. 92–100.

Li, Z. et al. (2016). "A hypoplastic macroelement for single vertical piles in sand subject to three-dimensional loading conditions". *Acta Geotechnica* 11, pp. 373–390.

Lim, K.-W. and J. E. Andrade (2014). "Granular element method for three-dimensional discrete element calculations". *International Journal for Numerical and Analytical Methods in Geomechanics* 38.2, pp. 167–188.

Lim, K.-W. et al. (2016). "Multiscale characterization and modeling of granular materials through a computational mechanics avatar: a case study with experiment". *Acta Geotechnica* 11, pp. 243–253.

Luding, S (1997). "Stress distribution in static two-dimensional granular model media in the absence of friction". *Physical Review E* 55.4, p. 4720.

Luding, S (2005). "Shear flow modeling of cohesive and frictional fine powder". *Powder Technology* 158.1-3, pp. 45–50.

Maheshwari, B. K. et al. (2005). "Three-dimensional nonlinear seismic analysis of single piles using finite element model: Effects of plasticity of soil". *International Journal of Geomechanics* 5.1, pp. 35–44.

Martin, C and C. Martin (1994). "Physical and numerical modelling of offshore foundations under combined loads". PhD thesis. Oxford University, UK.

Martin, E., C. Thornton, and S. Utili (2020). "Micromechanical investigation of liquefaction of granular media by cyclic 3D DEM tests". *Géotechnique* 70.10, pp. 906–915. DOI: 10.1680/jgeot.18.P.267.

Merhebi, G. (2022). *Application and Validation of a Discrete Numerical Model on Geotechnical Engineering Structures*. Tech. rep.

Mindlin, R. D. and H. Deresiewicz (1953). "Elastic spheres in contact under varying oblique forces".

Mohamed, T. et al. (2022). "DEM models using direct and indirect shape descriptions for Toyoura sand along monotonous loading paths". *Computers and Geotechnics* 142, p. 104551.

Mollon, G. et al. (2020). "Can friction replace roughness in the numerical simulation of granular materials?" *Granular Matter* 22.2, pp. 1–16.

Munjiza, A. and K. Andrews (1998). "NBS contact detection algorithm for bodies of similar size". *International Journal for Numerical Methods in Engineering* 43.1, pp. 131–149.

Negro, P. et al. (1999). *3D Site Effects and Soil-Foundation Interaction in Earthquake and Vibration Risk Evaluation: Large-Scale Geotechnical Experiments on Soil-Foundation Interaction*. Tech. rep. Joint Research Centre Applied Mechanics Unit Ispra Italy.

Negro, P. et al. (2000). "Large-scale soil-structure interaction experiments on sand under cyclic loading". *Proceedings of the 12th world conference on earthquake engineering, Auckland, New Zealand*. Vol. 30.

Nguyen, T. K. et al. (2017). "FEM× DEM: a new efficient multi-scale approach for geotechnical problems with strain localization". *EPJ Web of Conferences*. Vol. 140. EDP Sciences, p. 11007.

Nitka, M. and A. Grabowski (2021). "Shear band evolution phenomena in direct shear test modelled with DEM". *Powder Technology* 391, pp. 369–384.

Nova, R. (1994). "Controllability of the incremental response of soil specimens subjected to arbitrary loading programmes". *J. Mech. behav. Mater.* 5.2, pp. 193–201.

Nova, R and L Montrasio (1991). "Settlements of shallow foundations on sand". *Géotechnique* 41.2, pp. 243–256.

Oda, M. (1972). "Initial fabrics and their relations to mechanical properties of granular material". *Soils and foundations* 12.1, pp. 17–36.

Oger, L et al. (1998). "Yield and deformation of an assembly of disks subjected to a deviatoric stress loading". *Mechanics of materials* 27.4, pp. 189–210.

O'Sullivan, C., J. D. Bray, and M. F. Riemer (2002). "Influence of particle shape and surface friction variability on response of rod-shaped particulate media". *Journal of Engineering Mechanics* 128.11, pp. 1182–1192.

Pan, J. et al. (2002). "Three-dimensional analysis of single pile response to lateral soil movements". *International Journal for Numerical and Analytical Methods in Geomechanics* 26.8, pp. 747–758.

Philipponnat, G (1986). "Le phicomètre: essai de cisaillement direct in situ". *Revue française de géotechnique* 35, pp. 49–65.

Plassiard, J.-P., N. Belheine, and F.-V. Donzé (2009). "A spherical discrete element model: calibration procedure and incremental response". *Granular Matter* 11.5, p. 293.

Prisco, C. di and R. Nova (1994). "Stability problems related to static liquefaction of loose sand". *Localisation and Bifurcation Theory for Soils and Rocks* Chambon, Desrues, Vardoulakis (eds), Balkema, pp. 59–70.

Radjai, F. et al. (1996). "Force distributions in dense two-dimensional granular systems". *Physical review letters* 77.2, p. 274.

Radjai, F. et al. (1998). "Bimodal character of stress transmission in granular packings". *Physical review letters* 80.1, p. 61.

Reiffsteck, P. (2022). "Laboratory study of factors influencing borehole shear test with Phicometer apparatus". Personal communication.

Reiffsteck, P., P. T. Nguyen Pham, and J. Arbaut (2007). "Influence de la rèpartition granulomètrique sur le comportement mècanique d'un sol". *Bulletin des Laboratoires des Ponts et Chaussèes* 268-269, pp. 83–104.

Reiffsteck, P. et al. (2007). "Mesures en laboratoire du comportement mécanique des sols hétérogènes". *Bulletin des Laboratoires des Ponts et Chaussèes* 268-269, pp. 59–82.

Rha, C. and E. Taciroglu (2007). "Coupled macroelement model of soil-structure interaction in deep foundations". *Journal of Engineering Mechanics* 133.12, pp. 1326–1340.

Ristow, G. H. (1997). "Critical exponents for granular phase transitions". *Europhysics Letters* 40.6, p. 625.

Rocha, J., M. Farias, B. Albuquerque, et al. (2019). "Shallow foundation analysis using the discrete element method". *Material Sci & Eng* 3.4, pp. 136–139.

Rorato, R. et al. (2021). "Image-based calibration of rolling resistance in discrete element models of sand". *Computers and Geotechnics* 131, p. 103929.

Saada, A. S. and G Bianchini (1988a). "Constitutive equations for granular non-cohesive soils". *Proceedings of the international workshop on constitutive equations for granular non-cohesive soils, Balkema, Rotterdam, 22-24 July 1987, Cleveland*. AA Balkema.

Saada, A. and G. Bianchini (1988b). *Constitutive equations for granular non-cohesive soils - Proceedings of the international workshop on constitutive equations for granular non-cohesive soils*. 22-24 July 1987, Cleveland: Balkema, Rotterdam.

Salot, C., P. Gotteland, and P. Villard (2009). "Influence of relative density on granular materials behavior: DEM simulations of triaxial tests". *Granular matter* 11.4, pp. 221–236.

Sandeep, C. S. and K. Senetakis (2018). "Effect of Young's modulus and surface roughness on the inter-particle friction of granular materials". *Materials* 11.2, p. 217.

Sanni, I. et al. (2010). "A reliable algorithm to solve 3D frictional multi-contact problems: application to granular media". *Journal of computational and applied mathematics* 234.4, pp. 1161–1171.

Santamarina, C and G. Cascante (1998). "Effect of surface roughness on wave propagation parameters". *Geotechnique* 48.1, pp. 129–136.

Satake, M (1978). "Constitution of mechanics of granular materials through the graph theory". *Proc. US-Japan Seminar on Continuum Mech. Stat. Appr. Mech. Granul. Mater., Sendai*, pp. 203–215.

Satake, M (1982). "Fabric tensor in granular materials". *IUTAM-Conference on Deformation and Failure of Granular Materials, 1982*, pp. 63–68.

Schanz, T, P. Vermeer, and P. G. Bonnier (1999). "The hardening soil model: formulation and verification". *Beyond 2000 in computational geotechnics* 1, pp. 281–296.

Sibille, L. et al. (2015). "Granular plasticity, a contribution from discrete mechanics". *Journal of the Mechanics and Physics of Solids* 75, pp. 119–139. DOI: 10.1016/j.jmps.2014.09.010.

Sibille, L., N. Benahmed, and F. Darve (2021). "Constitutive response predictions of both dense and loose soils with a discrete element model". *Computers and Geotechnics* 135, p. 104161.

Sibille, L. et al. (2019). "Quantitative prediction of discrete element models on complex loading paths". *International Journal for Numerical and Analytical Methods in Geomechanics* 43.5, pp. 858–887.

Šmilauer, V. and B. Chareyre (2010). "Yade dem formulation". *Yade Documentation* 393.

Suhr, B. and K. Six (2017). "Friction phenomena and their impact on the shear behaviour of granular material". *Computational particle mechanics* 4.1, pp. 23–34.

Suhr, B. and K. Six (2020). "Simple particle shapes for DEM simulations of railway ballast: influence of shape descriptors on packing behaviour". *Granular matter* 22.2, pp. 1–17.

Taciroglu, E., C. Rha, and J. W. Wallace (2006). "A robust macroelement model for soil–pile interaction under cyclic loads". *Journal of geotechnical and geoenvironmental engineering* 132.10, pp. 1304–1314.

Takeda, T., M. A. Sozen, and N. N. Nielsen (1970). "Reinforced concrete response to simulated earthquakes". *Journal of the structural division* 96.12, pp. 2557–2573.

Thornton, C. (2000). "Numerical simulations of deviatoric shear deformation of granular media". *Géotechnique* 50.1, pp. 43–53.

Uthayakumar, M and Y. P. Vaid (1998). "Static liquefaction of sands under multiaxial loading". *Canadian Geotechnical Journal* 35.2, pp. 273–283. DOI: 10.1139/t98-007. URL: https://doi.org/10.1139/t98-007.

Villard, P. and B. Chareyre (2004). "Design methods for geosynthetic anchor trenches on the basis of true scale experiments and discrete element modelling". *Canadian Geotechnical Journal* 41.6, pp. 1193–1205.

Villard, P., A. Huckert, and L. Briançon (2016). "Load transfer mechanisms in geotextile-reinforced embankments overlying voids: Numerical approach and design". *Geotextiles and Geomembranes* 44.3, pp. 381–395.

Vlahinić, I. et al. (2014). "Towards a more accurate characterization of granular media: extracting quantitative descriptors from tomographic images". *Granular Matter* 16.1, pp. 9–21.

Vucetic, M. and R. Dobry (1991). "Effect of soil plasticity on cyclic response". *Journal of geotechnical engineering* 117.1, pp. 89–107.

Walton, O. R. and R. L. Braun (1986). "Viscosity, granular-temperature, and stress calculations for shearing assemblies of inelastic, frictional disks". *Journal of rheology* 30.5, pp. 949–980.

Wang, X. and J. Li (2014). "Simulation of triaxial response of granular materials by modified DEM". *Science China Physics, Mechanics & Astronomy* 57, pp. 2297–2308.

Weatherley, D, V Boros, and W Hancock (2011). "ESyS-particle tutorial and user's guide version 2.1". *Earth Systems Science Computational Centre, The University of Queensland*.

Wellmann, C. and P. Wriggers (2012). "A two-scale model of granular materials". *Computer Methods in Applied Mechanics and Engineering* 205, pp. 46–58.

Wensrich, C. and A Katterfeld (2012). "Rolling friction as a technique for modelling particle shape in DEM". *Powder Technology* 217, pp. 409–417.

Zdravkovic, L, D. Potts, and H. St John (2005). "Modelling of a 3D excavation in finite element analysis". *Geotechnique* 55.7, pp. 497–513.

Zhang, L. and C. Thornton (2002). "DEM simulations of the direct shear test". *15th ASCE Engineering Mechanics Conference*. Columbia University New York, pp. 2–5.

Zhang, X. et al. (2022). "The macroscopic and mesoscopic study on strengthening mechanisms of the single pile with raft under pile-soil-raft combined interaction". *Computers and Geotechnics* 144, p. 104630.

Zhao, S. et al. (2017). "Particle shape effects on fabric of granular random packing". *Powder technology* 310, pp. 175–186.

Zhu, H. et al. (2016). "On a common critical state in localized and diffuse failure modes". *Journal of the Mechanics and Physics of Solids* 95, pp. 112–131.

Zitouni, Z.-E.-A. (1988). "Comportement tridimensionnel des sables". PhD thesis. Université Joseph Fourier (Grenoble).